Contribution à la modélisation, à l'optimisation et à l'étude expérimentale d'un lanceur à rails augmenté et du projectile

Mieke Ineke Rik Coffo

N° d'ordre : 135 Année 2011

THESE

pour obtenir le grade de

DOCTEUR
de l'Université de Franche-Comté et de l'Ecole Royale Militaire

Ecole Doctorale : Sciences Pour l'Ingénieur et Microtechniques
Spécialité : Sciences Pour l'Ingénieur

Mieke COFFO
Ingénieur de l'Université de Gand

Contribution à la modélisation, à l'optimisation et à l'étude expérimentale d'un lanceur à rails augmenté et du projectile.

Contribution to the Modeling, Design, and Experimental Study of an Augmented Railgun and its Projectile

soutenue le 16 juin 2011 devant le jury composé de

M. Frans ABSIL	Président
M. Markus LÖFFLER	Rapporteur
M. Abderrezak REZZOUG	Rapporteur
M. Marc PIRLOT	Examinateur
M. Markus SCHNEIDER	Examinateur
M. Johan GALLANT	Co-directeur de thèse
M. Jean-Marie KAUFFMANN	Directeur de thèse

Thèse préparée à l'Ecole Royale Militaire (Bruxelles), à l'Institut Franco-Allemand de recherche de Saint Louis (ISL) et à l'Institut FEMTO-ST département ENYSIS, UMR (CNRS 6174), dans le cadre d'un accord de cotutelle

Summary

This thesis was supervised by Professor Jean-Marie Kauffmann of the University of Franche-Comté. The co-director at the Royal Military Academy was Dr. Johan Gallant and the experiments at French-German Research Institute ISL were directed by Dr. Markus Schneider.

A conventional electromagnetic railgun is composed of two conducting rails connected by a projectile. The magnetic field generated by the current in the rails interacts with the current in the projectile resulting in an electromagnetic force accelerating the projectile. The projectile used in this thesis is a two brush projectile. For a conventional railgun the most efficient way to increase the force on the projectile is to increase the current in the rails. But the current density is limited. The heating of the sliding contacts between the brushes and the rails due to the Joule losses and the friction can cause the contacts and can result in contact transition which we want to avoid. One way to reduce the heating is to add more current brushes to obtain a better current distribution between the brushes. Another way is to add an extra pair of rails and create an additional magnetic field. This augmenting field allows us to increase the electromagnetic force without increasing the current through the projectile. In this thesis the current and heat distribution in a two brush projectile in a parallel augmented railgun is studied through simulations and experiments. Because the current brushes and the inner rails form a closed loop, the augmenting field will induce a loop current and influence the current distribution between the brushes.

The first simulation model is a global model of the railgun in PSpice which allows us to predict the global currents as well as the average temperature in the brushes, the force on the projectile and the position and the velocity of the projectile. The model takes into account the velocity skin effect and was validated based on experiments. The second model is a finite element model in ANSYS for a fixed projectile. This model allows a local study of the current and temperature distribution in the projectile. A model for the contact between the rails and the projectile is introduced. The local model is used to calculate the time-dependent coefficients for the force equation used in the global model. Both simulation models are compared and a good correspondence is found.

The LARA railgun of ISL with a length of 1.5 m and a square caliber of 15 mm has been used for the experiments. A maximum of three capacitor banks was used for the non-augmented and the augmented configuration. The muzzle velocities obtained in the experiments vary between 48 and 214 m/s. To determine the current distribution between the brushes a technique proposed by [SCH05a] has been used. It is based on the measurement of the voltage between two pins in the rails in combination with the voltage in a loop. When applied to this velocity range, the eddy currents in front of the projectile hamper the interpretation of the signals and the results are not what we expected. An analytical method for the determination of the current distribution based on the voltage in the loop was introduced. The results are then compared with the results of the simulations. The maximum current in the rails found with PSpice shows a good correspondence with the experiments, the calculated decrease of the current is slightly overestimated. The errors on the velocities are less than 10 %. Both simulation models and experiments show that the brush towards the breech carries the greater part of the current for the non-augmented as well as the augmented railgun.

In the last part a parametric study is carried out with ANSYS for the preliminary design of an augmenting circuit for an existing railgun. The influence of the geometry and the position of the outer rails on the forces on the rails and on the projectile is discussed. Also a parametric study with PSpice for LARA is presented for the optimization of the projectile and for the feeding of the railgun.

Keywords : augmented railgun, two brush projectile, current distribution, temperature distribution, contact model, time-dependent force model

Résumé

Cette thèse a été dirigée par le Professeur Kauffmann de l'université de Franche-Comté. Le co-directeur de l'Ecole Royale Militaire était le Docteur Johan Gallant et les essais à l'Institut franco-allemand de recherches de Saint-Louis (ISL) étaient encadrés par le Docteur Markus Schneider.

Un lanceur à rails conventionnel est composé de deux rails conducteur connecté par un projectile. L'interaction entre le champs magnétique induit par le courant dans les rails et le courant dans le projectile résulte en une force électromagnétique accélérant. Dans cette thèse on utilise une projectile avec deux ponts de courant. Pour un lanceur à rails conventionnel la méthode le plus efficace pour augmenter la force sur le projectile est d'augmenter le courant dans les rails. Mais le densité de courant est limité. L'échauffement des contacts entre les rails et les ponts de courant par l'effet Joule et la force de frottement, peut résulter dans la transformation d'un contact solide dans un contact plasma, ce qui est à éviter. Une possibilité d'adresser ce problème est d'ajouter des ponts de courant pour améliorer la distribution de courant. Une autre possibilité est d'appliquer un champs magnétique extérieur généré par un circuit extérieur qui nous permet d'augmenter la force électromagnétique sans augmenter le courant dan le circuit intérieur. Dans cette thèse l'objectif est d'étudier la distribution de courant et de température dans un projectile à deux ponts de courant pour un lanceur augmenté. Comme les deux ponts de courants et les rails du circuit intérieur forment un circuit fermé, le champs augmenté va induire un courant de circulation qui influence la distribution de courant entre les brosses.

Le premier modèle de simulation est un modèle global du lanceur en PSpice qui nous permet de déterminer les courants globaux, la force électromagnétique, la position et la vitesse du projectile et la température moyenne des brosses. Le modèle global prend en compte l'effet de peau dû à la vitesse et est validé par des résultats expérimentaux. Le deuxième modèle est un modèle local en ANSYS, un code à elements finis, pour un projectile fixe. Ce modèle permet une étude locale de la distribution de courant et de température. Un modèle pour la zone de contact entre les rails et les brosses est introduit. Le modèle local est utilisé pour calculer les coefficients de l'équation de force dans le modèle global. Les résultats des deux modèles de simulation sont cohérents.

Le lanceur LARA, utilisé pour les essais, a une longueur de 1.5 m et un calibre carré de 15 mm. On disposait de trois bancs de condensateurs pour l'alimentation du lanceur en configuration non-augmenté et augmenté. Les vitesses à la bouche obtenues varient entre 48 et 214 m/s. Pour la détermination de la distribution de courant nous avons utilisées une méthode proposée par [SCH05a]. Cette méthode est une combinaison d'une mesure de tension entre deux pins dans les rails et dans une boucle. Nous avons constaté que les signaux obtenus avec cette méthode, appliquée dans ce régime de vitesse, sont perturbée par les courant de Foucault induits avant le projectile et les résultats ne répondent pas à nos attentes. Une méthode analytique basée sur la mesure de tension dans la boucle a été développée. Les résultats expérimentaux sont comparés avec les simulations. Nous avons constaté une bonne correspondance entre les valeurs des courants maximaux dans les rails calculés avec PSpice et les valeurs expérimentales, mais le courant calculé avec PSpice est plus faible dans la phase décroissante du courant. Les erreurs sur la vitesse sont inférieures à 10 %. Les deux modèles de simulations et les essais montrent que la brosse avant porte la plus grande partie du courant.

La dernière partie de cette thèse est une étude paramétrique avec Ansys pour l'avant-projet du circuit extérieur d'un lanceur à rail existant. L'influence de la géométrie et de la position des rails extérieurs sur les forces sur la projectile et les rails est examinée. D'autres études paramétriques sont effectués avec PSpice pour LARA pour l'optimisation du projectile et pour l'alimentation du lanceur.

Mots clés: lanceur à rail augmenté, projectile à deux ponts de courant, distribution de courant, distribution de température, modèle de contact, modèle de force en fonction du temps

To Peter Permentier

Acknowledgments

This thesis would not have been possible without the support of many people. I would like to thank:

Prof. Jean-Marie Kauffmann, Professor at the University of Franche-Comté and director of this thesis, for his advice and guidance from the initial to the final version of this work.

Dr. Johan Gallant of the Royal Military Academy of Belgium, co-director of this thesis, for introducing me to railgun research and for his support throughout the years.

Dr. Markus Schneider, head of the electromagnetic launchers research group at ISL, for his technical advice and his encouragements and for providing the facilities to perform the experiments.

Prof. Abderrezak Rezzoug of the University of Nancy and Prof. Markus Löffler of the Gelsenkirchen University of Applied Sciences for accepting the task of reviewer and for their suggestions to improve this work.

Prof. Frans Absil of the Netherlands Defence Academy and Prof. Marc Pirlot of the Royal Military Academy of Belgium for accepting to participate in my jury.

I'm grateful to my colleagues of the Department Of Ballistics at the RMA for their support throughout the years, their suggestions and the many discussions we had. I also want to thank the members of the Electromagnetic Launchers group at ISL for their advice and technical insight and especially Thorbjörn and Laurent for assisting me during the experiments.

My gratitude goes to Fred en Adriaan for guiding me around at conferences and for their advise to improve my presentation skills.

I want to thank my family and friends for their support that kept me motivated. And last but not least I want to thank my fiancé Peter for his understanding, encouragements and patience during the last long months.

Contents

List of Symbols

	unit	
a	m	Distance between the current brushes
a_0	1/s	Decay constant current equation
a_{spot}	m^2	A-spot size
b	m	Distance between the two inner rails
b_0	Rad/s	Angular frequency current equation
$\vec{B}$	T	Magnetic field
$\overrightarrow{B_{ext}}$	T	Magnetic field of the outer circuit
$\overrightarrow{B_R}$	T	Magnetic field of the inner circuit
c	m	Position of the outer rail
C	F	Capacitance of a capacitor bank
d	m	Contact layer thickness
D	m	Position of a point of measuring from the breech
D’	m	Position of a point of measuring from the muzzle
e	m	Distance between the optic fibers of the light barrier
E_m	J	Magnetic energy
E_m’	J/m	Magnetic energy per meter
$\vec{F}$	N	Force
F_{EM}	N	Electromagnetic force
$F_{N,EM}$	N	Normal component of the electromagnetic force
F_f	N	Friction force
F_{mech}	N	Mechanical force
$F_{N,mech}$	N	Normal component of the mechanical force
F_N	N	Normal force
F_{proj}	N	Force on the projectile
F_P	N	Electromagnetic force on the brush towards the breech
F_Q	N	Electromagnetic force on the brush towards the muzzle
g	m	Gap between the inner and outer rail
h	m	Height of the outer rail
HGen	kW/mm^3	Heat generation
i_{loop}	A	Circulating current in the armatures
I	A	Current
I_A	A	Current in the outer rail (augmented)
I_{Am}	A	Maximum of the fitted current in outer rail
I_{AB}	A	Current in the section AB of the rails
I_R	A	Current in the inner rail
I_{Rm}	A	Maximum of the fitted current in inner rail
I_1	A	Current in the brush on the breech side
I_2	A	Current in the brush on the muzzle side
$\vec{J}_R$	A/m^2	Current density in the projectile
k		Ratio K_{fiber}/K_{cu}
k_1		Upper limit ratio K_{fiber}/K_{cu}
k_2		Lower limit ratio K_{fiber}/K_{cu}
K_{Cu}	J/(m.K)	Thermal conductivity of copper
K_{fiber}	J/(m.K)	Thermal conductivity of the fibers
L	m	Length of the first segment of the railgun
L_A	H	Self inductance of the outer rail
L_{AB}	H	Self inductance of the section AB of the rails
L_b	H	Self inductance of a brush

L_B	H	Self inductance of the conductors
L_I	H	Inner self inductance of a capacitor bank
L_{pr}	H	Self inductance of the projectile
L'_R	H/m	Self inductance gradient of the inner rail
L_R	H	Self inductance of the inner rail
L_S	H	Self inductance of the switch
L_T	H	Total inductance
Δm	g	Mass loss
m_{pr}	g	Mass of the projectile
$m_{pr,0}$	g	Mass of the projectile before the shot
$m_{pr,b}$	g	Mass of the projectile after the shot
M'	H/m	Mutual inductance gradient between outer and inner rails
n		Number of turns in the loop of the measurement device for the current distribution
q	C	Electric charge
r	m	Radius of current brush
R_A	Ω	Resistance of the outer rail
R_{AB}	Ω	Resistance of the section AB of the rails
R_b	Ω	Resistance of a brush
R_B	Ω	Resistance of the conductors
R_c	Ω/m^2	Contact resistance per unit area
R_I	Ω	Inner resistance of a capacitor bank
R_{pr}	Ω	Resistance of the projectile
R'_R	Ω	Resistance gradient of the inner rail
R_S	Ω	Resistance of the switch
R_T	Ω	Total resistance
s	m^2	Section of the loop
t	s	Time
t_{0A}	s	Time corresponding to the maximum of the fitted current in the outer rail
t_b	s	Time the projectile reaches the muzzle
t_c	s	Time discharging time second capacitor bank
t_d	s	Time delay for the augmenting current
t_P	s	Time where a plasma was detected
t_r	s	Rise time of the current
T	°C	Temperature
T_{end}	°C	Temperature at the end of the shot
T_h	°C	Average temperature
T_{max}	°C	Maximum temperature
T_P	°C	Temperature at plasma time t_P
U_0	V	Initial charge capacitor bank
$U_{R,C}$	V	Voltage at the breech of inner rails
$U_{A,C}$	V	Voltage at the breech of outer rails
v	m/s	Velocity of the projectile
v_1	m/s	Velocity at the first measurement point
v_2	m/s	Velocity at the second measurement point
v_3	m/s	Velocity at the third measurement point
v_{muzzle}	m/s	Muzzle velocity of the projectile
V	m^3	Volume of the projectile
V_m	V	Muzzle voltage
V_{pins}	V	Voltage measured between the pins of the measurement devices for the current distribution

V_{loop}	V	Voltage measured in the loop of the measurement devices for the current distribution
w	m	Width of the outer rail
W_m	J	Magnetic coenergy
z	m	Position of the projectile
z'	m	Position of the equivalent filiform current in the breech side armature
α		Ratio I_2/I_R ($\alpha=1-\lambda$)
γ		Ratio $F_{N,EM}/F_{EM}$
γ_{pr}	m/s^2	Acceleration of the projectile
Δe	m	Error on the distance between the optic fibers of the light barrier
Δt	s	Error on the passing time between the optic fibers of the light barrier
δ, ε	m	Position of the voltage loop
η		Efficiency
ζ		Fraction of the nominal contact area occupied by spots
λ		Theoretical ratio I_1/I_R (without i_{loop})
μ		Ratio I_{Am} / I_{Rm}
μ_0	H/m	Magnetic permeability in vacuum
μ_{fr}		Dynamic friction coefficient
μ_r		Magnetic relative permeability
ρ	Ω.m	Resistivity
ρ_a	Ω.m	Armature resistivity
τ_A	s	Time constant of the fitted current in outer rail
τ_R	s	Time constant of the fitted current in inner rail
Φ	Wb	Flux
Φ_{loop}	Wb	Flux in the loop for the voltage measurement in the loop
Φ_{pins}	Wb	Flux in the measurement loop for the voltage measurement between the pins

Résumé détaillé en français

Introduction

Un lanceur transforme une énergie potentielle en énergie cinétique et ceux qui sont les plus efficaces partent de l'énergie chimique. Ces canons ou lanceurs classiques ont atteint des performances remarquables. On peut citer le canon du char Leclerc qui développe une énergie de 11.7 MJ et lance un projectile de 7.3 kg avec une vitesse à la bouche de 1790 m/s. Pour un certain nombre d'applications, c'est la vitesse à la bouche qui doit être très élevée. Des solutions avec des gaz légers existent mais avec une constitution volumineuse. Les lanceurs électromagnétiques permettent d'atteindre ces vitesses élevées avec un rendement supérieur. De plus ils s'inscrivent dans les orientations AES (All Electric Ships) et AEV (All Electric Vehicles).

On distingue deux types de lanceur électromagnétique basés tous les deux sur la force de Lorentz, le lanceur à rails et le lanceur à bobines. Les réalisations sont encore au niveau des laboratoires. La source d'énergie utilise généralement des bancs de condensateurs bien que les machines tournantes aient une densité d'énergie plus élevée. Les travaux de recherche qui sont menés portent sur les six points suivants :

- le lanceur à rails
- le projectile et plus particulièrement les contacts entre parties fixe et mobile
- l'alimentation en énergie
- le diagnostic
- la modélisation et les codes de calcul
- les applications.

Les recherches dans ce domaine ont été développées dès 1984 aux Etats Unis, qui fondent de grands espoirs dans cette technique. La Chine est actuellement le deuxième pays par l'importance des chercheurs et des moyens affectés à ce domaine de recherche. En Europe, c'est l'ISL (Institut franco-allemand de Saint Louis) qui est le fer de lance de la recherche sur les lanceurs à rails dont les travaux ont débuté en 1987. Les autres laboratoires européens sont l'ERM (Ecole Royale Militaire) en Belgique sur le lanceur à rails augmenté, l'Université de Pise en Italie sur les champs magnétiques et l'Institute for Semiconductor Physics à Vilnius en Lithuanie.

Les chercheurs sur les lanceurs électromagnétiques se sont regroupés dans différentes sociétés savantes nationales ou internationales et des congrès sont régulièrement organisés comme EML (Electromagnetic Launch Symposium) dont les communications sont publiées dans IEEE Transactions on Magnetics, et depuis 2010 dans IEEE Transactions on Plasma Science.

Les travaux de recherche menés à l'ISL portent sur les lanceurs à rails, les contacts glissants et l'alimentation. L'ISL dispose de Pegasus, lanceur de 6 m de long avec une énergie de 10 MJ et d'un certain nombre de lanceurs de petites puissances. Il a en projet RAFIRA (RApid FIre RAilgun), lanceur rapide de 3 m de long autorisant des tirs multiples.

Les travaux sur le lanceur à rails augmenté (LARA) ont débuté avec la thèse de J. Gallant dans le cadre d'une coopération entre l'ISL et l'ERM. Les études théoriques et les simulations ont été menées à Bruxelles. Les essais et validations expérimentales ont été faits à l'ISL. Le champ extérieur permet à performances équivalentes, de réduire la densité de courant au niveau des contacts glissants et donc de rester à des contacts solides au lieu de générer un plasma qui a des effets destructeurs.

Les travaux menés dans le cadre de cette thèse sont également le fruit d'une collaboration entre les mêmes laboratoires dans les mêmes conditions. De nouvelles techniques de mesure devraient permettre d'étudier l'influence du champ extérieur sur la répartition des courants dans les ponts de courants. La non disponibilité de LARA durant une certaine période n'a pas permis de mener les investigations aussi loin que nous le souhaitions.

1. Lanceur électromagnétique à rails

Le principe des lanceurs électromagnétiques à rails est base sur la force de Lorentz que nous pouvons exprimer sous la forme :

$$\vec{F}_{EM} = \iiint_V \vec{J}_R \times \vec{B}_R \; dV$$

où $\vec{J_R}$ représente la densité de courant dans le projectile et $\vec{B_R}$ l'induction magnétique induite par ce courant.

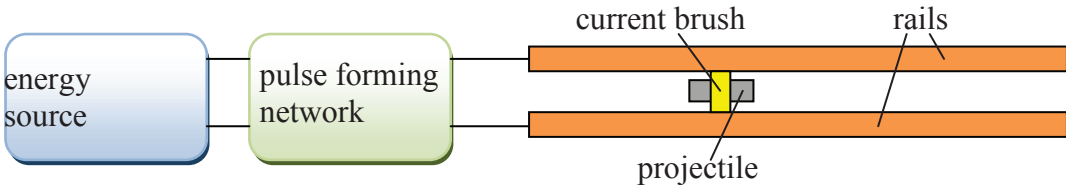

Fig.1.1 : Schéma de principe d'un lanceur à rails

La co-énergie magnétique de ce circuit est :

$$W_m = \frac{1}{2} L_R I_R^2 + \frac{1}{2} L_P I_R^2$$

où I_R est le courant dans les rails, L_R la self inductance des rails et L_P la self inductance de la partie mobile supportant le projectile. La force résultante F agissant sur le projectile, sachant que la self inductance L_P ne dépend pas de la position, est :

$$F = \frac{1}{2} \frac{\partial L_R}{\partial z} I_R^2 = \frac{1}{2} L'_R I_R^2$$

où z est la direction du tir et L'_R l'inductance incrémentale des rails.

La force qui s'exerce sur le projectile peut être augmentée en ajoutant un champ extérieur B_{ext} :

$$\vec{F}_{EM} = \iiint_V \vec{J}_R \times \left(\vec{B}_R + \vec{B}_{ext} \right) dV$$

Ceci est obtenu avec un deuxième système de rails avec son propre système d'alimentation (fig.1.2).

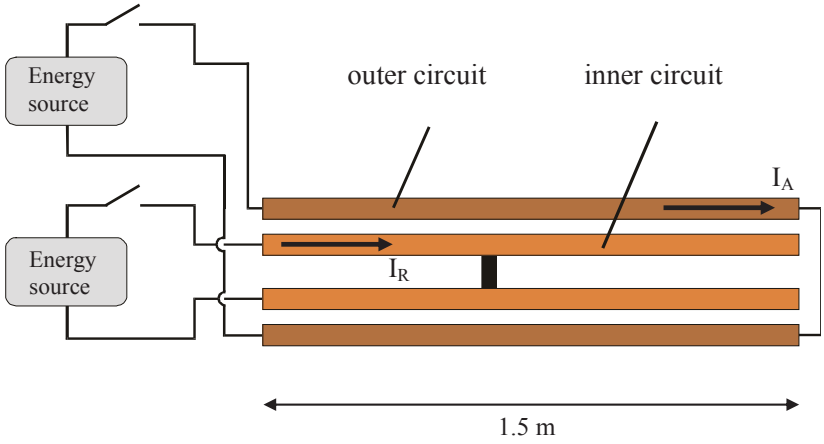

Fig.1.2 : Schéma d'un lanceur à rails augmenté

La force s'exprime dans ces conditions par :

$$F = \frac{1}{2} L'_R I_R^2 + M' I_A I_R$$

I_A est le courant dans le rail extérieur et M' la mutuelle incrémentale entre les deux rails. Dans ce cas de lanceur à rails dit augmenté, les deux sources sont indépendantes.

Les self et mutuelle inductances incrémentales ne sont pas constantes et dépendent de la position du projectile car la distribution de courant dans les rails évolue à cause de l'effet de peau qui est lié d'une part à la forme des courants injectés et d'autre part au déplacement du projectile.

Les courants I_A et I_R sont obtenus par la décharge de batteries de condensateurs. Le dispositif de mise en forme de l'impulsion de courant comprend une diode « crowbar » qui élimine les oscillations du courant.

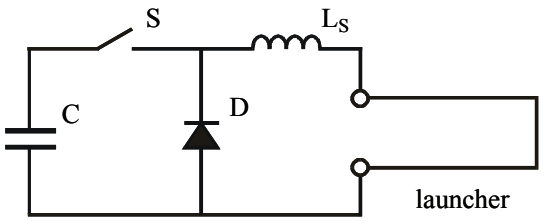

Fig.1.3 : Schéma de base du dispositif de mise en forme du courant

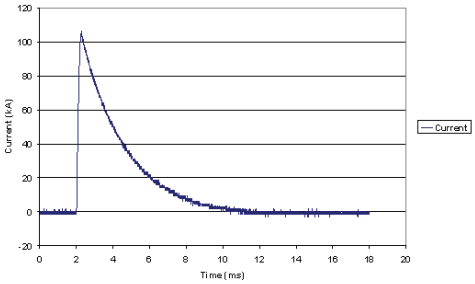

Fig.1.4 : Allure du courant

La partie mobile comporte souvent plusieurs ponts de courant pour diminuer la densité de courant et éviter la formation de plasma qui entraîne une détérioration des rails. L'ISL utilise des ponts de courant filamentaires. La charge thermique doit être limitée pour éviter la formation de plasma. Par ailleurs, les frottements sur les rails entraînent une érosion qui peut aller jusqu'à la suppression du contact pour un des ponts.

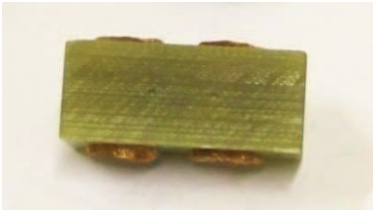

Fig.1.5 : Porte projectile utilisé à l'ISL

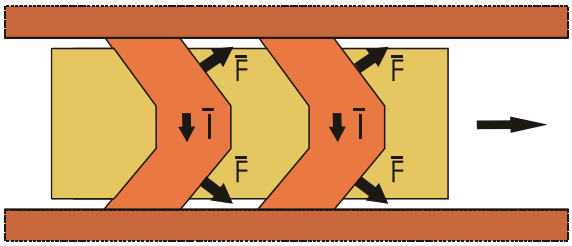

Fig.1.6 : Disposition des ponts de courant filamentaires

L'expression globale de la force n'est pas modifiée par le nombre de ponts de courant.

$$F_{pr} = F_P + F_Q = \frac{1}{2} L'_R \, I_R^2 + M' I_R I_A$$

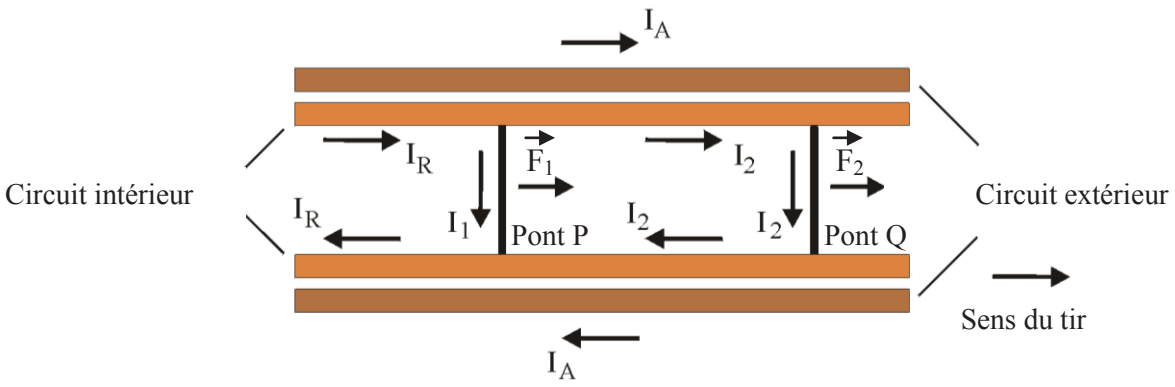

Fig.1.7 : Définition des différents courants

La répartition de courant entre les deux ponts n'est pas équilibrée et le courant I_1 côté culasse est toujours nettement supérieur au courant I_2 côté bouche du lanceur. Le lanceur à rail augmenté devrait permettre une meilleure répartition entre les deux ponts de courant et c'est un des objectifs de ce travail de thèse qui fait suite à celui mené par J. Gallant [GAL04].

L'objectif de cette thèse est de généraliser l'étude de la répartition de courants entre les deux ponts et de pouvoir valider les résultats au moyen d'essais sur le lanceur LARA (LAnceur à Rails Augmenté) de l'ISL. Deux techniques de simulation seront utilisées par la suite, une modélisation globale du circuit électrique utilisant PSpice et une modélisation locale au niveau du projectile utilisant ANSYS et mettant en œuvre une résolution par la méthode des éléments finis.

2. Modélisation globale du lanceur à rail

Le modèle comprend deux volets, une partie électrique et une partie mécanique couplées car les paramètres dépendent de la position, des courants, de l'échauffement de la vitesse et de l'effet de peau.

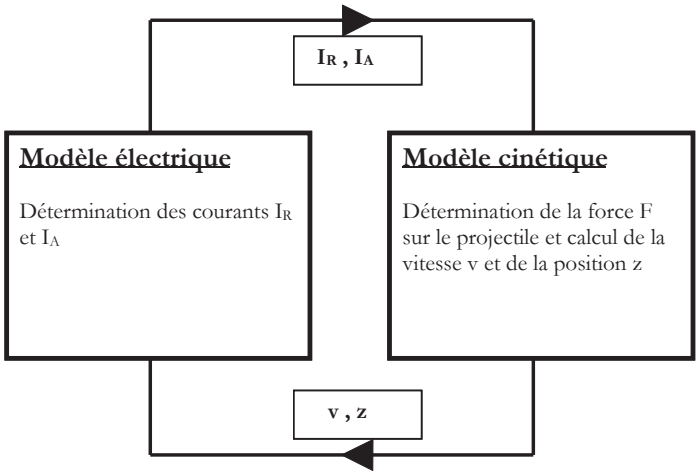

Fig.2.1 : Principe de couplage des deux modèles

2.1. Modèle électrique

2.1.1. Schémas de modélisation

L'alimentation et le système de mise en forme des courants sont modélisés suivant le schéma de la figure 2.2.

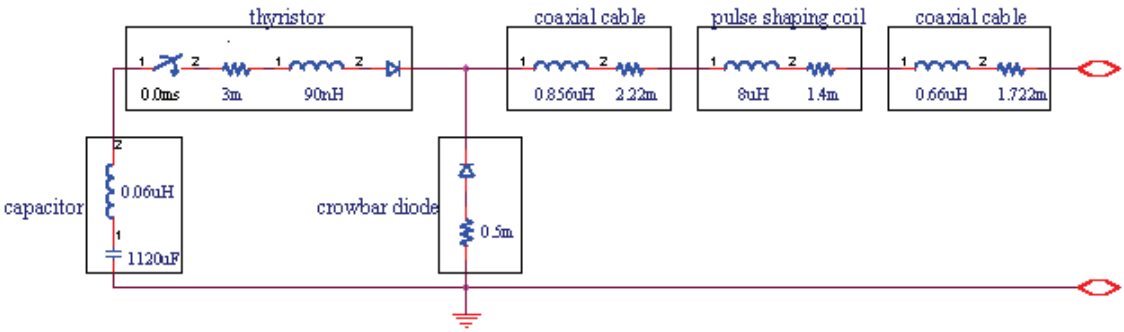

Fig.2.2 : Modélisation du circuit d'alimentation

Le schéma électrique est donné sur la figure dans le cas de deux ponts de courant. a est la distance entre ces deux ponts de courant.

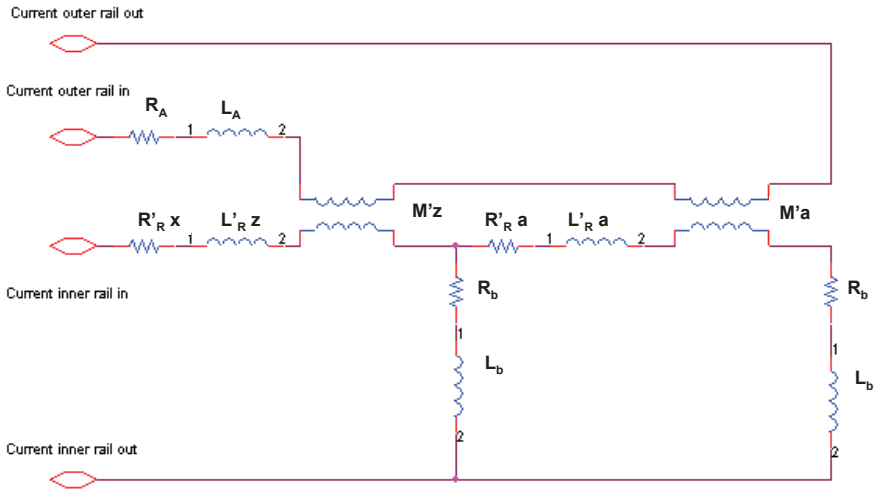

Fig.2.3 : Modélisation électrique du lanceur à rails augmenté

2.1.2. Paramètres

Les résistances varient en fonction du temps et en fonction de la température. Eu égard à la forme des courants, pour les connexions, une fréquence de 100 kHz convient. Pour les rails, le problème est plus complexe ; nous utilisons l'expression mise au point par [WEY97] pour les rails extérieurs :

$$R'(t) = R_0' \cdot \left[\sqrt{\frac{t_0}{t}} + \operatorname{erf}\left(\sqrt{\frac{t_0}{t}} \right) \right]$$

Par contre pour les rails intérieurs, la résistance doit être calculée par le produit de convolution

$$R(t) = \int_0^t R'(t-\tau).v(\tau)d\tau$$

Pour la résistance du projectile nous utilisons la relation approchée :

$$R_{pr}(t) = R_{pr,0} \frac{\sqrt{\frac{t_0}{t}} + \left(\frac{t}{t_0}\right)^{16}}{1 + \left(\frac{t}{t_0}\right)^{16}} \quad \text{avec } t_0 = 1\text{ms}$$

Les températures des rails ne varient pratiquement pendant un tir mais il faut tenir compte de l'échauffement du projectile par sa variation de résistivité.

$$\rho(T) = \rho_0 (0.453e-6T^2 + 4.241e-3T + 1)$$

Les inductances L'_R, L_A et M' ont été obtenues à partir de l'énergie magnétique calculées par la méthode des éléments finis. Comme nous le verrons plus loin ANSYS ne permet pas de prendre en compte le déplacement du projectile. Les calculs ont donc été faits pour trois fréquences, 10 Hz, 1 kHz et 100 kHz. Les inductances et mutuelle incrémentales ne sont pas constantes et nous les faisons évoluer comme indiqué par le tableau 2.1.

Tableau 2.1 : Variation des coefficients L'_R and M'

Temps	Coefficients	
	L'_R ($\mu H/m$)	M' ($\mu H/m$)
t ≤ 0.2 ms	0.440	0.270
0.2 ms < t < 1.5 ms	décroissance linéaire de 0.440 à 0.414	décroissance linéaire de 0.270 à 0.167
t ≥ 1.5 ms	0.414	0.167

L'inductance des ponts de courant est donnée par la relation suivante eu égard à leur forme cylindrique :

$$L_b = \frac{\mu_0 l}{2\pi}\left\{\ln\left(\frac{2l}{r}\right) - \frac{3}{4}\right\}$$

2.2. Modèle cinématique

Le modèle est basé sur la loi fondamentale de la mécanique. Le point délicat est d'apprécier les forces de frottement du système mobile, ponts de courant et projectile. Cette force dépend de la composante normale.

$F_{proj} = F_{EM} - F_f = (1 - \gamma\,\mu)\,F_{EM} - \mu\,F_{N,mech}$ avec $F_{N,EM} = \gamma\,F_{EM}$

Le coefficient de frottement est estimé à partir de la courbe $\mu(v)$

$$\mu(v) = 0.1 + 0.2\exp\left(-\frac{v}{100}\right)$$

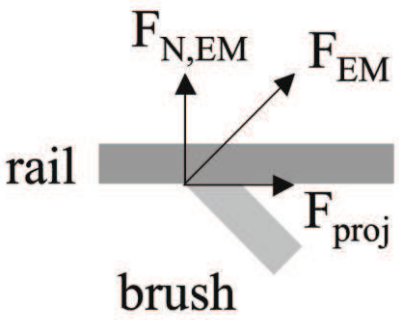

Fig.2.4 : Décomposition des forces

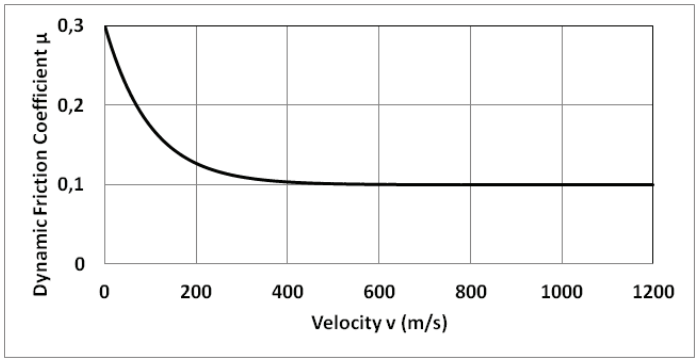

Fig.2.5 : Variation du coefficient de frottement en fonction de la vitesse

Connaissant l'accélération, on en déduit par intégration la vitesse et la position. Pour affiner le modèle mécanique, on peut tenir compte de la perte de masse du système mobile liée à l'usure des ponts de courant. Ceci intervient essentiellement pour des vitesses élevées. Ce ne sera pas le cas pour les essais que nous avons effectués.

Le modèle mécanique utilisé sous PSpice est donné sur la figure 2.6.

2.3. Validation du modèle

La validité du modèle complet a été testée sur des essais effectués par J. Gallant dans le cadre de sa thèse [GAL04]. Les courants dans les rails sont sous-estimés dans leur partie décroissante comme on peut le voir sur la figure 2.7. Néanmoins le comportement mécanique est très satisfaisant puisque les erreurs sur les vitesses à la bouche sont inférieures à 15% et en valeur moyenne à 2% ce qui est faible compte tenu des erreurs de mesure expérimentale.

Le modèle a été utilisé pour estimer les courants et les échauffements dans les ponts de courant. Les figures 2.8 et 2.9 ont été obtenues pour un lanceur à rails augmenté avec respectivement un déclenchement simultané des deux courants et un retard de 1.1ms pour le courant I_R. Les courants dans les deux brosses sont dus à un courant de circulation induit par le courant dans les rails externes, le projectile n'a pas bougé.

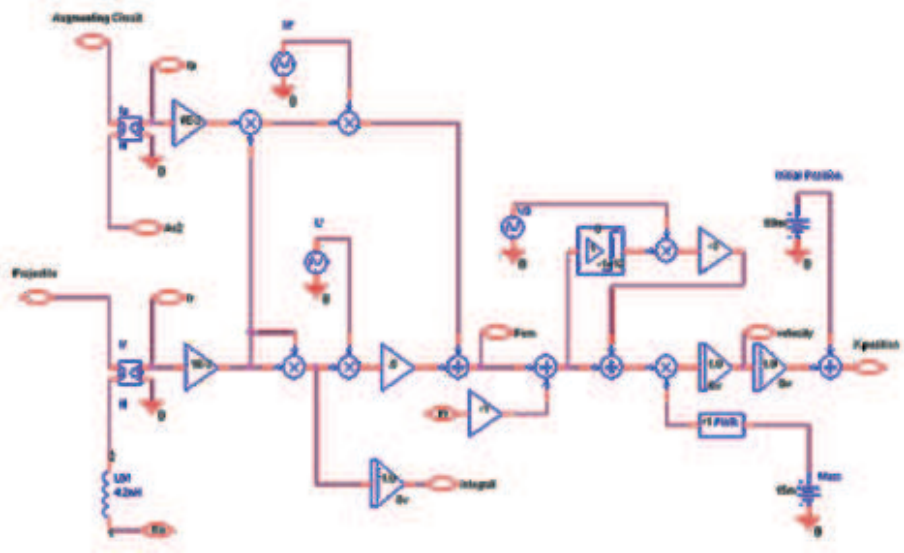

Fig.2.6 : Modèle mécanique du lanceur à rails

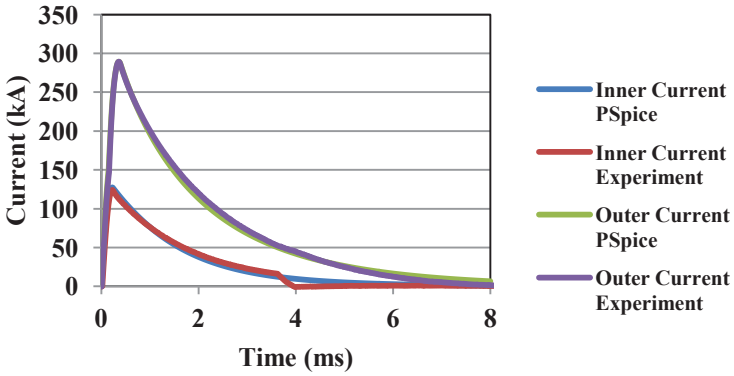

Fig.2.7**:** Variation des courants simulés par PSpice (PSp) et expérimentaux pour un lanceur à rails augmenté

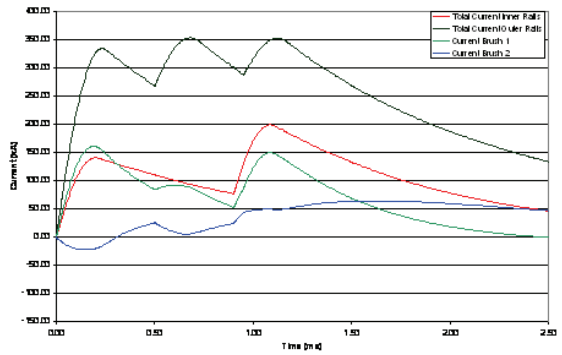

Fig.2.8 : Courants dans les rails et dans les deux ponts de courant pour un déclenchement simultané

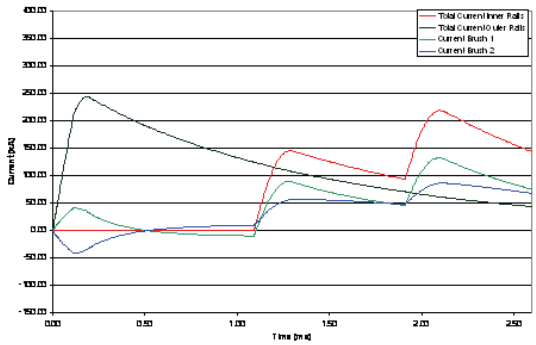

Fig.2.9 : Courants dans les rails et dans les deux ponts de courant pour un déclenchement retardé de I_R

Le tableau 2.2 donne les températures moyennes des ponts de courant suivant leur nombre dans les mêmes conditions de génération de courant. On note que le pont côté culasse présente toujours un échauffement marqué par rapport aux autres et que certaines configurations ne sont pas intéressantes.

Tableau 2.2 : Températures dans les ponts de courant

T (°C)	1brush	2 brushes	3 brushes	4 brushes
Pont 1	208	139	173	198
Pont 2		38	36	47
Pont 3			41	22
Pont 4				56

2.4. Conclusion

PSpice se révèle comme un moyen efficace et rapide pour étudier le comportement global d'un lanceur à rails. Les difficultés principales résident dans la détermination des paramètres tant électriques que mécaniques du modèle. Il faut faire une analyse fine des phénomènes physiques pour tenir compte des effets de peau tant liés à la forme impulsionnelle du courant qu'au mouvement du projectile. Les résultats sont très satisfaisants. Les grandeurs obtenues sont nécessairement globales ou moyennes comme pour les températures. Une analyse locale nécessite d'autres outils comme ANSYS. Les deux outils sont complémentaires.

3. Modélisation locale du lanceur à rails

3.1. Méthodologie

La simulation sous ANSYS résulte d'un couplage fort entre l'électromagnétisme et la thermique. Par contre on ne peut prendre en compte le déplacement du projectile. Un certain nombre de phénomènes sont donc occultés et en particulier l'effet de peau dans les rails lié au déplacement du projectile. L'effet de peau qui intervient est lié à la forme du courant. Il s'estompe par la suite du fait de la décroissance exponentielle du courant alors que pour le lanceur réel ce phénomène d'effet de peau apparaît toujours du fait qu'une nouvelle portion de rail est concernée comme le montre la figure 3.2 extraite de [MAR84].

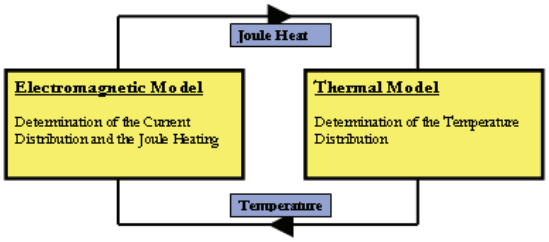

Fig.3.1 : Couplage entre les modèles électromagnétique et thermique

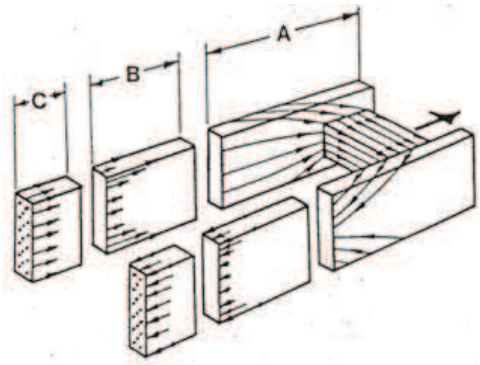

Fig.3.2 : Les différentes distributions de courant dans un lanceur à rails

Compte tenu de la dimension du lanceur, on ne peut le modéliser en entier. On admet en général qu'il faut quatre fois le calibre pour la partie entre la culasse et le projectile car 95 % de la force y est générée. Le calibre est de 15 mm. La longueur totale simulée est de 14 cm. Les ponts de courant sont des cylindres de rayon 3.5 mm.

Les conditions limites sur le plan électromagnétique sont précisées sur la figure 3.4. Le côté bouche est au potentiel zéro de même que les milieux des ponts de courant eu égard à la symétrie. Les courants injectés sur une surface équipotentielle côté culasse. $I_A(t)$ et $I_R(t)$ ont été obtenus soit par simulation sous PSpice soit expérimentalement.

Pour la modélisation thermique, on considère que les rails sont isothermes à la température ambiante et que les ponts de courant sont adiabatiques. Par ailleurs les brins en cuivre ont un sens de conduction thermique privilégié et on considère que les échanges thermiques sont inexistants dans le sens transverse.

Les ponts de courant sont formés de brins assemblés et a priori on ne connaît pas facilement la conductivité thermique équivalente. Nous avons introduit un coefficient k pour traduire ce coefficient de remplissage pour la conductivité thermique.

Par ailleurs, il faut tenir compte de la zone de contact balais-rails sous la forme d'une couche d'épaisseur d conduisant à une résistance de 2.5 μΩ. La résistivité des brins est celle des matériaux utilisés compte tenu du taux de remplissage.

$$\rho = (2.067e-8 + 8.765e-11T + 1.208e-14T^2)\Omega.m$$

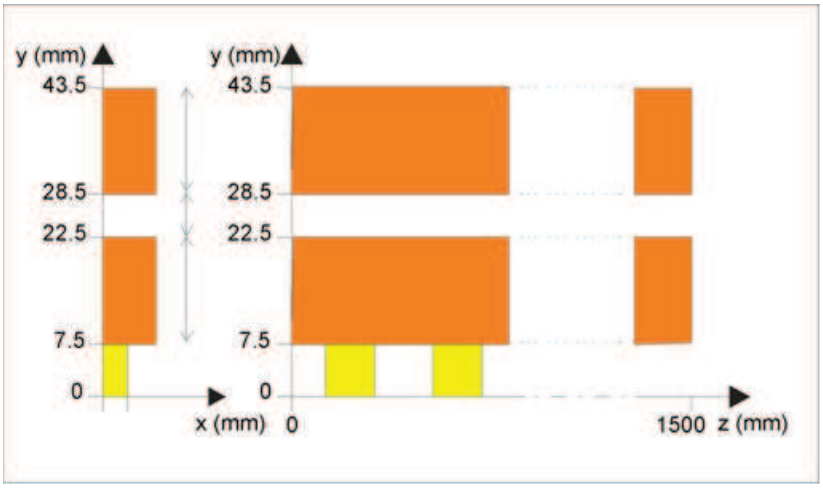

Fig.3.3 : Description géométrique de la portion du lanceur à rails modélisé

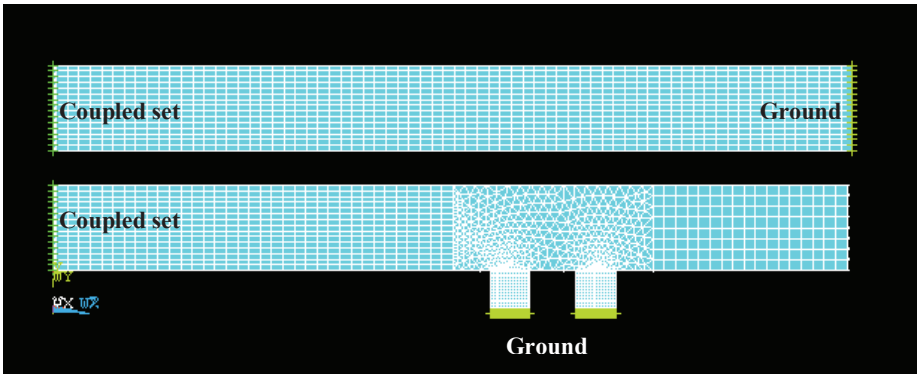

Fig.3.4 : Conditions aux limites électriques

3.2. Influence de la zone de contact et du rapport k des conductivités lié à la constitution des ponts de courant

Deux paramètres introduisent des incertitudes, d'une part l'influence du taux de remplissage en brins des ponts de courant et d'autre part l'épaisseur de la couche d'air sur le plan thermique sachant que sur le plan électrique, la résistance est connue.

On constate que l'incidence de l'épaisseur d est faible et nous avons retenu la valeur de d = 0.1 mm par la suite. L'incidence de k n'est pas non plus très significative sur les températures maximales obtenues tant que l'on reste dans un domaine de variation raisonnable.

Tableau 3.1 : Lanceur à rails conventionnel avec un seul pont de courant - Températures maximales et à la fin du tir pour différentes valeurs de l'épaisseur de la zone de contact et du rapport des conductivités thermiques k

	k	90%	95%	99%	100%
d = 0.1 mm	T_{max} (°C)	670	664	663	662
	T_{end} (°C)	487	483	480	477
d = 0.2 mm	T_{max} (°C)	663	655	649	647
	T_{end} (°C)	501	496	492	491
d = 0.5 mm	T_{max} (°C)	652	643	636	634
	T_{end} (°C)	508	499	493	492

Tableau 3.2 : Lanceur à rails augmenté avec 2 ponts de courants. Températures maximale et à la fin du tir, génération de chaleur par mm^3 et rapport des courants λ pour différentes valeurs du rapport k

	k	90%	95%	99%	100%
Pont de courant 1	T_{max} (°C)	567	564	561	560
	T_{end} (°C)	408	404	402	401
	$HGen_{max}$ (kW/mm^3)	34.5	34.5	34.5	34.6
Pont de courant 2	T_{max} (°C)	244	242	240	239
	T_{end} (°C)	237	234	233	232
	$HGen_{max}$ (kW/mm^3)	2.69	2.69	2.69	2.70
	λ	0.87	0.87	0.87	0.87

3.3. Simulations avec le code ANSYS

3.3.1. Détermination de L'$_R$ et de M'

Les self et mutuelle inductances incrémentales sont déterminées à partir de la force électromagnétique.

$$F_{EM} = \frac{1}{2} L'_R I_R^2 + M' I_R I_A \tag{3.1}$$

En raison de la forme impulsionnelle des courants, les simulations ont été menées pour des excitations sinusoïdales à deux fréquences, 1 kHz et 10 Hz pour des courants I_A égaux à 10 kA et à 100 kA, I_R étant égal à 100 kA. Le tableau 3.3 récapitule les valeurs obtenues.

Tableau 3.3: Valeurs des inductances incrémentales obtenues avec ANSYS à 10 Hz et 1 kHz

	L'$_R$	M'
10 Hz	0.414	0.167
1 kHz	0.440	0.270

La figure 3.5a montre que les valeurs retenues à fréquence élevée conviennent pour la montée en courant alors que celles à basse fréquence sont adaptées pour la queue de courant. En figure 3.5b, nous comparons les valeurs obtenues avec la variation donnée dans le tableau 2.1 et la force calculée par ANSYS.

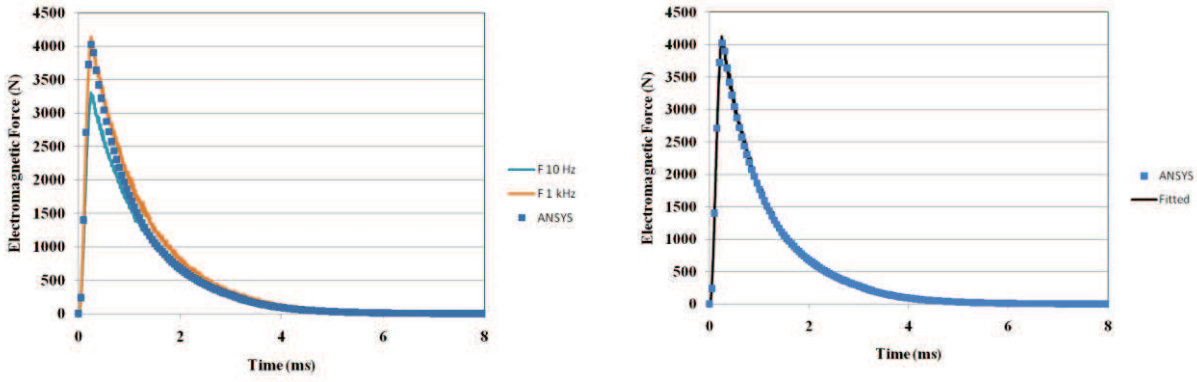

a) variation de F_{EM} pour les deux fréquences 10Hz et 1kHz et comparaison avec la force réelle

b) variation de F_{EM} pour les valeurs adoptées et comparaison avec la force réelle

Fig.3.5 : Calcul des forces électromagnétiques par ANSYS et par l'équation globale

3.3.2. Simulations pour deux ponts de courant

Nous nous intéressons essentiellement à la simulation des densités de courant et au comportement thermique. Nous privilégions dans ce résumé le cas d'un projectile avec deux brosses. Des études ont été menées dans le cas de 1 et de 4 ponts de courant.

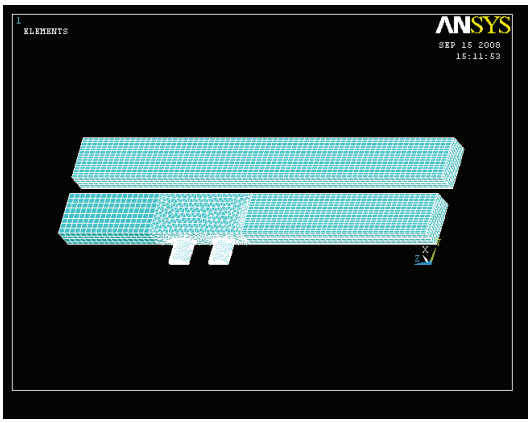

Fig.3.6 : Maillage de la zone utile

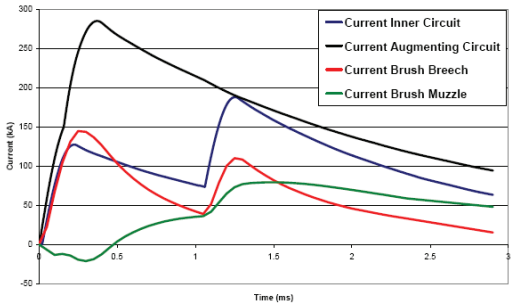

Fig.3.7 : Evolution des courants dans les rails et dans les ponts de courant

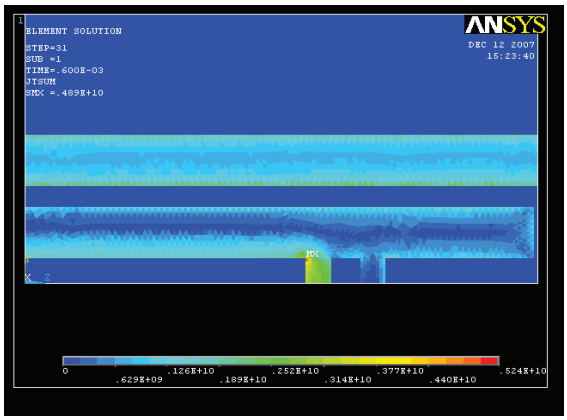

Fig. 3.8 : Densité de courant dans les rails à t = 0.2ms

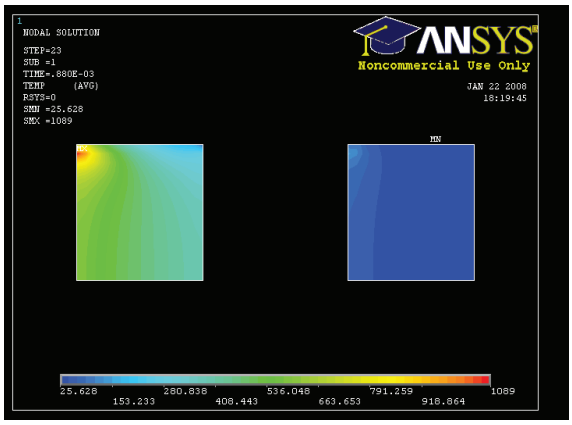

Fig. 3.9 : Température dans les ponts de courant à t = 0.880ms

On peut noter sur la fig. 3.7 que le courant de circulation augmente au départ le courant dans le pont de courant côté culasse. Le courant dans l'autre pont est d'abord négatif. Les deux courants décroissent ensuite comme les courants dans les rails. On peut noter sur la fig. 3.8 que l'effet de peau n'est plus très marqué du fait de la diffusion dans l'ensemble des rails. Il ne faut pas oublier que le projectile est fixe. Les températures à t = 0.880 ms données sur la fig. 3.9 montrent clairement que le pont de courant côté culasse s'échauffe beaucoup plus. Le courant qui y circule est important.

3.4. Comparaisons des deux méthodes de simulation

La figure 3.10 montre que les variations de courant simulées par les deux méthodes sont comparables. On n'observe pas de divergence particulière. Néanmoins les amplitudes ne sont pas les mêmes. ANSYS conduit à des valeurs plus élevées jusqu'à t = 1 ms environ. La répartition en fin de tir donnée par ANSYS est critiquable car I_1 devient quasi nul et tout le courant passerait par le pont de courant côté bouche. Comme dit plus haut, la diffusion de courant n'est pas représentative du fonctionnement réel lorsque le projectile est mobile.

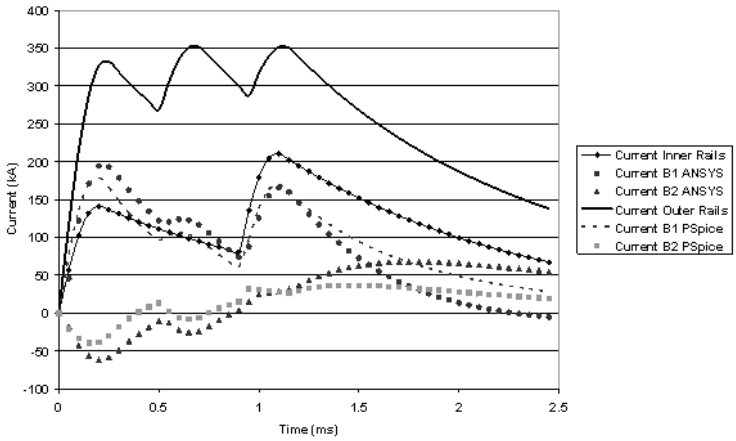

Fig. 3.10 : Comparaison des évolutions des courants simulés pas PSpice et par ANSYS

L'analyse des simulations thermiques conduit à faire les remarques suivantes :

- Les températures données par PSpice ne peuvent être que des valeurs moyennes dans les ponts de courant pour lesquels on considère qu'il n'y a pas d'échange de chaleur avec l'extérieur (domaine adiabatique). L'échauffement des rails n'est pas considéré. La température des ponts de courant est fixée par l'énergie qui est générée par la capacité calorifique des brosses.
- Sous ANSYS, on introduit une zone de contact dont la modélisation n'est pas évidente et on considère un matériau isotrope au niveau des brosses dont les paramètres sont à définir. Il n'y a pas d'échange de chaleur avec l'air ambiant mais avec les rails. Le projectile n'est pas mobile alors que dans le cas réel, le projectile rencontre toujours une nouvelle zone froide.

Malgré ces approximations, les deux méthodes donnent des résultats assez cohérents comme le montre le tableau 3.4 qui donne les températures moyennes dans les deux ponts de courant calculées avec les deux méthodes. Le paramètre est ici le rayon des brosses. PSpice a tendance à donner des températures plus élevées pour le pont de courant côté culasse. Les ordres de grandeur sont comparables. On a intérêt à utiliser des brosses de diamètre élevé et à rapprocher les armatures comme le montre le tableau 3.5.

Tableau 3.4 : Comparaison des températures moyennes dans les ponts de courant données par ANSYS et PSpice (a = 20mm et m = 20g)

	Température (°C)			
r (mm)	Th AN B1	Th AN B2	Th PS B1	Th PS B2
3	258	89	305	41
3.5	173	50	182	28
4	126	36	120	25
4.5	108	32	85	24

Tableau 3.5 : Comparaison des températures moyennes dans les ponts de courant données par ANSYS et PSpice (r = 4mm et m = 20g)

	Température (°C)			
a (mm)	Th AN B1	Th AN B2	Th PS B1	Th PS B2
15	109	35	98	27
20	126	36	120	25
25	142	37	127	28
30	158	38	139	28

3.5. Conclusion

ANSYS permet une modélisation locale du lanceur à rails. Ce logiciel présente deux défauts ; il ne prend pas en compte le mouvement du projectile et pour obtenir une précision acceptable, il faut modéliser assez finement ce qui limite la zone d'études qui doit être égale à au moins quatre fois le calibre du lanceur pour la partie avant le projectile. Les résultats sont corrects dans les premiers instants. Ils le deviennent de moins en moins lorsque l'effet de peau disparaît. ANSYS permet une étude thermique couplée. Les hypothèses que nous avons pu faire sur les paramètres physiques sont liées au fait qu'un tir a une durée courte et que seuls les échanges par conduction sont possibles. ANSYS permet une étude locale de la distribution de courant et de l'échauffement alors que PSpice ne peut donner que des valeurs globales ou moyennes lorsqu'il s'agit de température. Néanmoins on observe une cohérence satisfaisante entre les deux approches. Seuls les essais peuvent permettre de valider l'une et/ou l'autre des méthodes de simulation. Nous verrons que les contraintes et les incertitudes de mesures ne permettent pas de répondre clairement à la question.

4. Méthodes expérimentales

Nous décrivons dans ce chapitre les dispositifs expérimentaux qui ont été mis en œuvre à l'ISL. Le lanceur était déjà réalisé (cf. thèse J. Gallant). Les équipements de mesure ont été adaptés pour les manipulations réalisées et en particulier les mesures de tension pour approcher la répartition de courants entre les deux ponts de courant [SCH05].

4.1. Lanceurs LARC et LARA

La figure 4.1 regroupe les différents éléments constituant le banc de test. Nous avions à notre disposition 3 bancs de condensateurs et 2 bobines de mise en forme du courant. 2 bancs de condensateurs et une bobine servent pour l'alimentation du rail intérieur. Le dernier banc avec la bobine sont utilisés soit pour alimenter le rail extérieur dans le cas de LARA soit pour une deuxième injection de courant pour LARC. L'instant de déclenchement de cette alimentation est réglé séparément de l'autre alimentation. Nous reviendrons plus loin sur les autres équipements de mesure installés sur le banc.

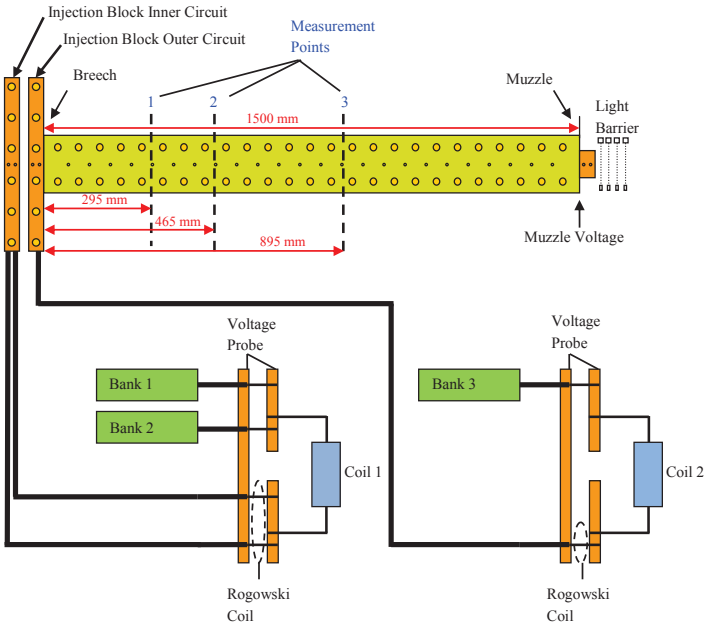

Fig. 4.1 : Schéma général du lanceur à rails avec les équipements de mesure

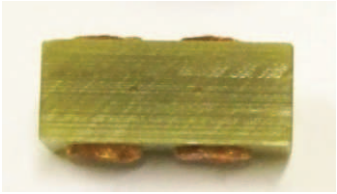

Fig. 4.2 : Vue du sabot du projectile avec les brins constituant les ponts de courant

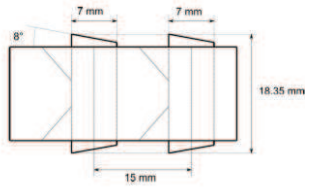

Fig. 4.3 : Coupe donnant les dimensions du sabot et montrant les évidements pour les brins

Le sabot qui porte le projectile est fabriqué en fibres de verre (fig. 4.2). Les contacts glissants sont assurés par des brins de cuivre logés dans des trous circulaires. Des évidements sont prévus pour que ces brins puissent légèrement se plier et assurer un meilleur contact avec le rail (fig. 4.3). Nous avons utilisé des brosses qui font un angle de 8° avec l'axe du sabot.

4.2. Equipements de mesure

Les courants délivrés par les alimentations sont mesurés au moyen de bobines de Rogowski. Le signal doit être intégré pour donner une image du courant. La tension mesurée à la bouche nous renseigne sur la qualité des contacts glissants. Elle est pratiquement égale à la chute ohmique aux bornes des ponts de courants. Les tensions des bancs de capacité sont mesurées pour connaître l'énergie apportée par les alimentations.

Des barrières lumineuses sont placées à la sortie du canon pour détecter la sortie du projectile et estimer sa vitesse. Sur les cinq diodes laser, seules deux donnent un signal utilisable. Des signaux lasers sont également utilisés pour détecter le passage du projectile en trois points P_1, P_2 et P_3 définis respectivement par les distances $z_1 = 0.295$m, $z_2 = 0.465$m et $z_3 = 0.895$m. Ces positions ont été choisies de manière que les signaux obtenus au passage du projectile ne soient pas perturbés par les fronts de montée des courants.

4.3. Mesure de la distribution de courant entre les ponts de courant

On ne peut mesurer directement la répartition de courant entre les deux ponts de courant pendant un tir. L'ISL a mis au point une nouvelle technique et l'a testé sur un lanceur à haute énergie donc à grande vitesse [SCH05]. Cette technique a également été mise en œuvre sur LARA. Elle comprend d'un côté du rail intérieur deux pointes espacées de 5mm et de l'autre côté une bobine. On mesure les tensions aux bornes soit respectivement V_{pins} et $V_{loop.}$ données par les deux relations suivantes. I_{AB} est le courant circulant entre les deux pointes donc dans le rail intérieur. Par différence on a une image de ce courant qui change au passage du projectile au point considéré.

$$V_{pins} = R_{AB} I_{AB} + L_{AB} \frac{dI_{AB}}{dt} + \frac{d\Phi}{dt} \;\; ; \;\; V_{loop} = \frac{d\Phi}{dt}$$

Cette méthode avait donné des résultats satisfaisants mais nous verrons qu'elle s'est trouvée inopérante dans notre cas car les hypothèses qui avaient été faites ne s'appliquent pas. Le courant I_R ne peut être considéré comme constant et la vitesse est trop faible.

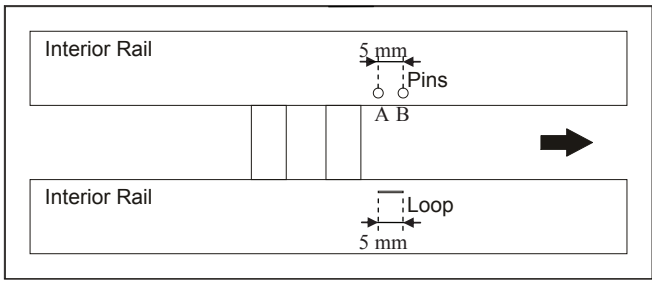

Fig. 4.4 : Emplacement des pointes et de la bobine de mesure

Fig 4.5 : Vue du dispositif permettant de mesurer la tension V_{pins}

Les figures 4.6 et 4.7 illustrent les mesures qui peuvent être faites, V_{pins}, V_{loop}, signal laser et courant I_R injecté. Les données sont numérisées et enregistrées. Elles doivent être filtrées en raison du bruit de mesure. Les courbes ont été obtenues au point P_1. L'action combinée du laser permet de positionner correctement le projectile.

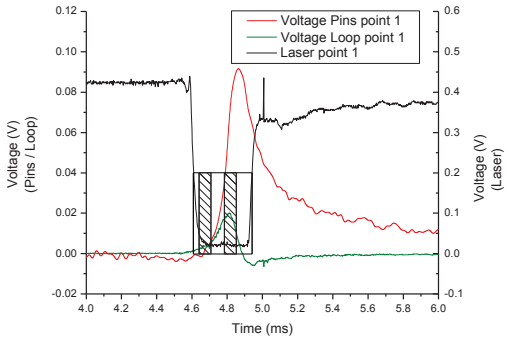

Fig. 4.6 : V_{pins}, V_{loop} et signal laser en fonction du temps en P_1

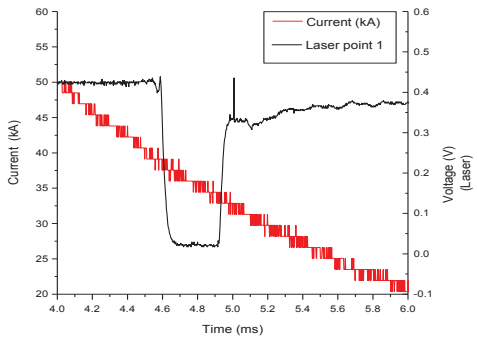

Fig. 4.7 : I_R et signal laser en fonction du temps en P_1

Le lanceur LARA (ou LARC si on n'alimente pas le rail extérieur) avec ses équipements sera utilisé pour 10 tirs en mode conventionnel et 2 en mode augmenté. Un défaut sur le thyristor de déclenchement d'une alimentation a limité cette deuxième série d'essais. Les résultats sont exploités dans le chapitre 5.

5. Analyse des résultats et estimation de la répartition des courants entre les deux ponts.

5.1. Les différents essais

Les essais ont été conduits à l'ISL sur le lanceur à rails augmenté. La non alimentation des rails extérieurs permet de traiter le cas du lanceur conventionnel. Nous disposons de trois bancs de condensateurs.

5.1.1. Lanceur à rails conventionnel – LARC

Les figures 5.1 et 5.2 montrent les connexions qui ont été réalisées respectivement avec deux et trois bancs de condensateurs. Le tableau 5.1 précise les tensions de charge des bancs de condensateurs et les instants de déclenchement pour les 10 tirs qui ont été effectués avec le même projectile pour les 5 premiers. Pour les 5 autres, il a été nécessaire de reprendre à chaque fois un nouveau projectile.

On peut noter que les différentes vitesses sont faibles, de l'ordre de 100 m/s et que tous les essais ne sont pas exploitables. Les vitesses à la bouche sont toujours plus faibles qu'en positions 2 et 3. Les courants sont faibles en fin de tir et les forces de frottement freinent le projectile. Les variations de masse sont négligeables.

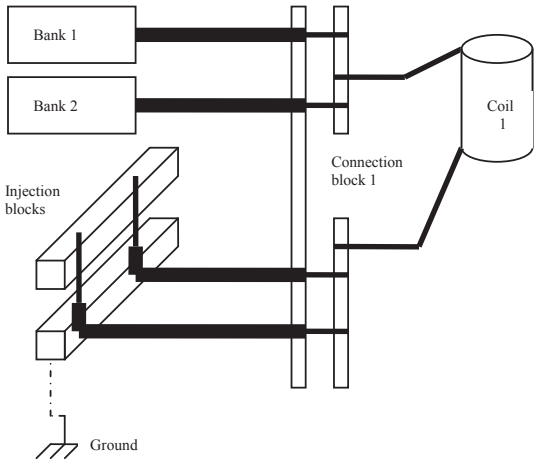

Fig.5.1 : Alimentation avec deux bancs de condensateurs

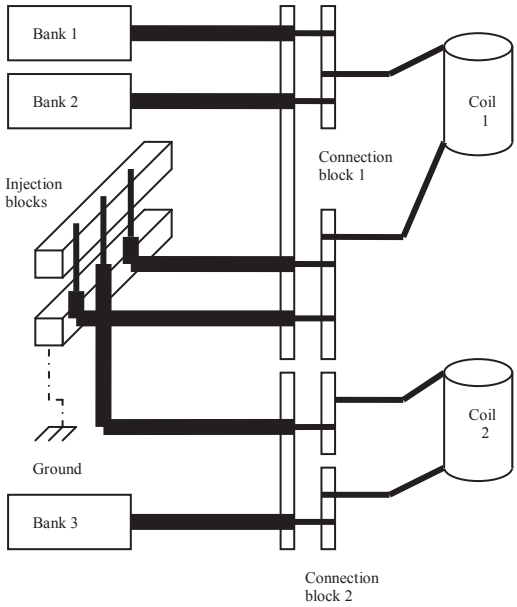

Fig.5.2 : Alimentation avec trois bancs de condensateurs

Tableau 5.1 : Conditions d'essais avec LARC

Tir	Banc 1 V_0 (kV)	Banc 1 t_0 (ms)	Banc 2 V_0 (kV)	Banc 2 t_0 (ms)	Banc 3 V_0 (kV)	Banc 3 t_0 (ms)	m_0 (g)	m_{after} (g)
1	8	0	8	0			19.86	19.86
2	7	0	7	0			19.86	19.85
3	8	0	8	0			19.85	19.81
4	7	0	7	0			19.81	19.77
5	8	0	8	0			19.77	19.52
6	7	0	7	0	7	0	19.97	-
7	7	0	7	0	7	3	19.96	19.92
8	7	0	7	0	7	2.5	20.03	20.00
9	7	0	7	0	7	1.5	19.86	19.83
10	8	0	8	0	8	1.5	19.79	19.71

Tableau 5.2 : Vitesses mesurées lors des différents tirs avec LARC

	z_1 = 0.295 m	z_2 = 0.465 m	z_3 = 0.895 m	z_{muzzle} = 1.5 m
	v_1 (m/s)	v_2 (m/s)	v_3 (m/s)	v_{muzzle} (m/s)
1	106.5	111.8	102.2	84.6
2	80.2	81.5	50.1	DNL*
3	108.9	118.4	100.8	85.8
4	91.3	95.1	70.4	48.3
5	115.5	126.1	108.3	101.6
6	142.2	159.1	157.1	153.2
7	-	121.6	110.8	100.0
8	-	-	120.5	117.7
9	138.2	158.9	160.4	154.1
10	-	-	213.0	214.4

* Le projectile n'a pas quitté le lanceur

5.1.2. Lanceur à rails augmenté - LARA

Pour le lanceur à rail augmenté, deux bancs de condensateur servent pour le rail intérieur. Le troisième alimente le rail extérieur comme indiqué sur la figure 5.3. Nous n'avons pu effectuer que deux tirs car au troisième, il s'est produit un défaut grave sur un des thyristors. Les résultats sont exploitables mais à nouveau les vitesses ne sont pas très élevées quoique supérieures à celles obtenues en moyenne avec le lanceur conventionnel.

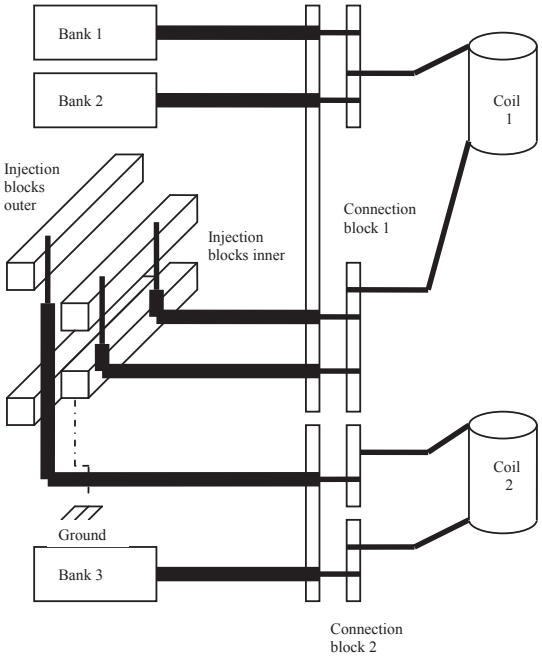

Fig.5.3 : Schéma d'alimentation du lanceur à rails augmenté

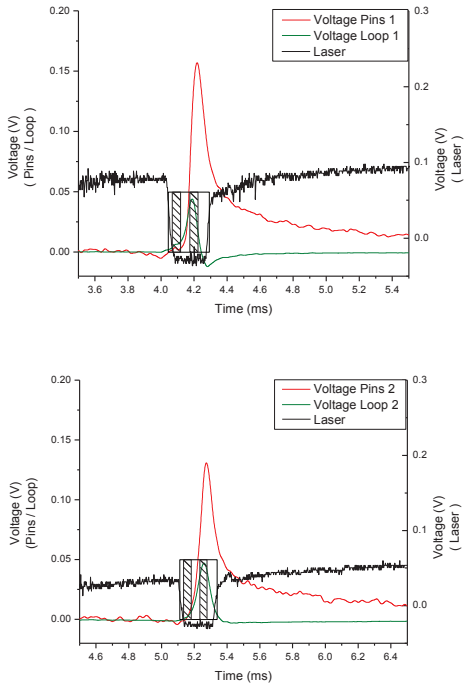

Fig.5.4 : Signal laser et tensions aux bornes des points de mesure et de la bobine aux points P_1 et P_2

Tableau 5.3 : LARA: Conditions de tirs

	Banc 1 V_0 (kV)	Banc 1 t_0 (ms)	Banc 2 V_0 (kV)	Banc 2 t_0 (ms)	Banc 2 V_0 (kV)	Banc 2 t_0 (ms)	m_0 (g)	m_{after} (g)
11	8	0	8	0	8	0	19.92	19.81
12	8	0	8	0	8	1	19.84	19.86*

* L'augmentation de masse est probablement due à un dépôt de matière lors du tir

Tableau 5.4 : LARA: Vitesses du projectile

	z_1 = 0.295 m	z_2 = 0.465 m	z_3 = 0.895 m	z_{muzzle} = 1.5 m
	v_1 (m/s)	v_2 (m/s)	v_3 (m/s)	v_{muzzle} (m/s)
11	145.8	166.6	171.6	164.3
12	140.7	158.6	160.4	151.2

Les deux enregistrements de la figure 5.4 donnent respectivement aux points P_1 et P_2 le signal laser permettant de repérer la position du projectile et les tensions mesurées aux bornes de la bobine de test et entre les deux points de mesure. Cette dernière courbe ne donne pas des renseignements intéressants pour déterminer la répartition de courant entre les deux ponts de courants, même si on fait la différence. De plus, ces deux courbes présentent un mauvais rapport bruit sur signal et il a été nécessaire de les filtrer (Filtrage FFT avec le logiciel Origin).

La méthode avait été mise au point par [SCH08] avec des vitesses de projectile très largement supérieures (de l'ordre de 1000 m/s) et permettant de considérer que les courants dans les rails étaient constants durant le passage du projectile entre les deux pointes de mesure. Ici ce n'est absolument pas le cas.

5.2. Calcul analytique de la tension aux bornes de la bobine de mesure

Nous avons essayé une autre technique pour estimer le rapport des courants dans les deux ponts de courant. Le signal aux bornes de la bobine semble le plus intéressant et nous pouvons donner une expression analytique moyennant un certain nombre d'approximations. Au voisinage des ponts de courant le courant circule dans une fine bande que nous pouvons approcher soit avec plusieurs conducteurs filiformes soit à la limite avec un seul. Le résultat n'est pas sensiblement modifié. Le flux à travers la bobine est calculé à partir de l'induction obtenue par la loi de Biot-Savart.

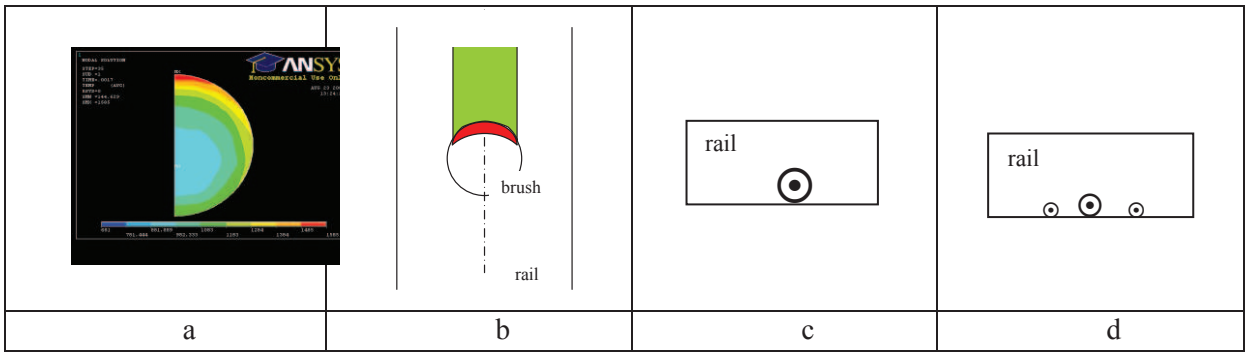

Fig. 5.5 : Modélisation de la distribution de courant au niveau des ponts de courant

Le flux dans la bobine est donné pour le lanceur à rails conventionnel, par l'expression ci-après qui fait intervenir les paramètres géométriques du lanceur, la position du projectile, la vitesse au point considéré et le rapport $\lambda = I_l/I_R$. On peut en déduire la tension du temps. La figure 5.6 montre l'influence de λ qui conditionne la forme de la courbe au niveau de la première bosse.

$$\Phi = \frac{\mu_0 s\delta}{4\pi} C(D, z', \lambda, v, t) \cdot I_R(t)$$

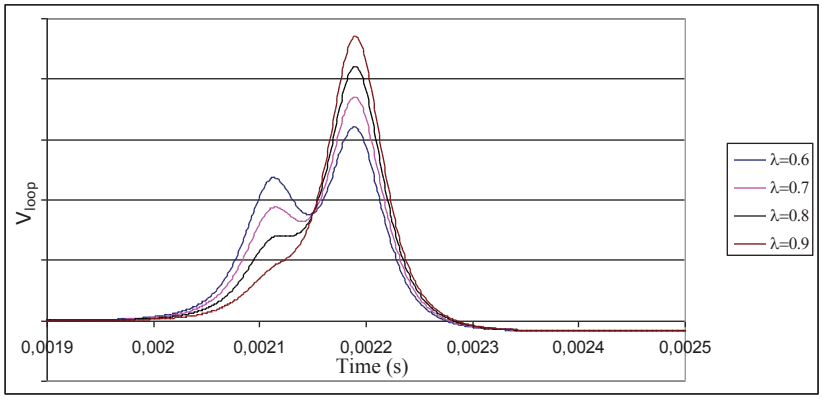

Fig.5.6 : Incidence de λ sur la tension induite dans la bobine

Dans le cas du lanceur à rails augmenté, il est indispensable de tenir compte du courant de circulation entre les deux ponts de courant. Le flux est donné par l'expression ci-après.

$$\Phi = \frac{\mu_0 s\delta}{4\pi} \left[C(D, z', \lambda, v, t) \cdot I_R(t) + C'(D) I_A(t) + C''(D, Z', v, t) i_{loop} \right]$$

Le courant de circulation prend deux valeurs différentes suivant que le courant I_A est en phase de croissance ou de décroissance. t_d représente le retard de déclenchement du courant dans le rail extérieur par rapport au rail intérieur. Le courant calculé avec deux expressions est cohérent avec celui obtenu par PSpice dans les conditions d'essai de la figure 2.7:

$$t_d \le t \le t_{0A} + t_d \qquad i_{loop} = D_1\left[-\cos\varphi_c \exp\left(-\frac{t-t_d}{\tau_c}\right) + \cos\left(\frac{\pi}{2}\frac{t-t_d}{t_{0A}} - \varphi_c\right)\right]$$

$$t_{0A} + t_d \le t$$

$$i_{loop} = \left[-D_1\cos\varphi_c \exp\left(-\frac{t_{0A}}{\tau_c}\right) + D_1\sin\varphi_c - D_2\right]\exp\left(-\frac{t-t_d-t_{0A}}{\tau_c}\right) + D_2\exp\left(-\frac{t-t_d-t_{0A}}{\tau_A}\right)$$

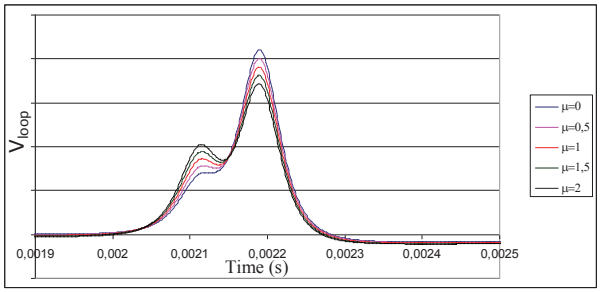

Fig.5.7 : Influence du rapport μ sur la première bosse pour λ = 0.8

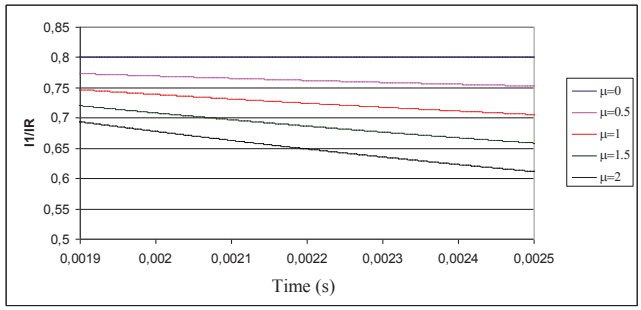

Fig.5.8 : Influence du rapport μ sur la répartition réelle des courants dans les ponts de courant (λ = 0.8)

La forme de la tension induite est fortement influencée par le ratio des amplitudes maximales des courants dans le rail extérieur et dans le rail intérieur $\mu = I_{Am}/I_{Rm}$ comme on peut le voir sur la figure 5.7. Par ailleurs les courants dans les ponts de courants sont donnés par :

$$I_1 = \lambda I_R - i_{loop} \text{ et } I_2 = (1-\lambda)I_R + i_{loop}.$$

Pour une valeur théorique de λ, μ a de nouveau une très grande importance sur la répartition des courants comme on peut le voir sur la figure 5.8. Pour équilibrer les courants dans les deux ponts, on a donc intérêt à travailler avec un courant dans le rail extérieur élevé.

5.3. Calcul avec ANSYS

Le calcul avec ANSYS à partir du courant réel, pose un certain nombre de problèmes. En effet, le projectile est fixe et peut être positionné soit en P_1 soit en P_2. Les courants injectés dans le lanceur sont connus mais si on les considère de manière brute avec injection au temps 0, les effets de peau ont quasi disparus lorsque le projectile est en P_1 et encore plus en P_2. En effet les effets de peau liés au déplacement du projectile ne sont pas pris en compte. Nous proposons de corriger la forme du courant injecté I_R pour recréer cet effet de peau comme indiqué sur la figure 5.9. La diffusion dans le rail extérieur n'est liée qu'à I_A et le courant à considérer est celui mesuré autour des points P_1 et P_2.

Une autre difficulté réside dans la valeur initiale de la température. Celle des rails est la température ambiante. Celle du projectile est estimée et nous avons pris la valeur obtenue avec le courant initial.

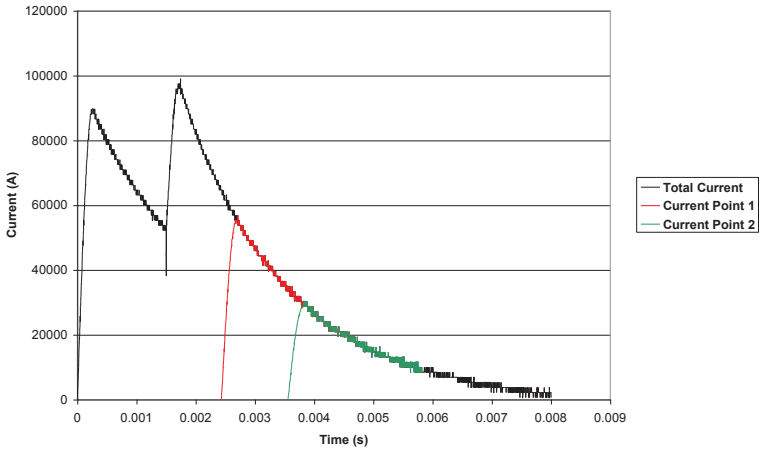

Fig.5.9 : Adaptation du courant I_R pour une simulation sous ANSYS

5.4. Comparaison des résultats

Nous avons analysé en détail deux tirs avec le lanceur conventionnel et les deux tirs disponibles avec le lanceur à rails augmenté. Les énergies mises en jeu sont réduites et les vitesses du projectile relativement faibles. Ceci a l'avantage de ménager le projectile mais rend la méthode proposée par [SCH05] inopérante comme le montre la figure 5.10 qui correspond au tir n°11 au point P_1. On n'observe aucune particularité au passage des deux ponts de courant au point choisi. Nous avons donc mis en œuvre la méthode analytique relative à la tension aux bornes de la bobine de mesure.

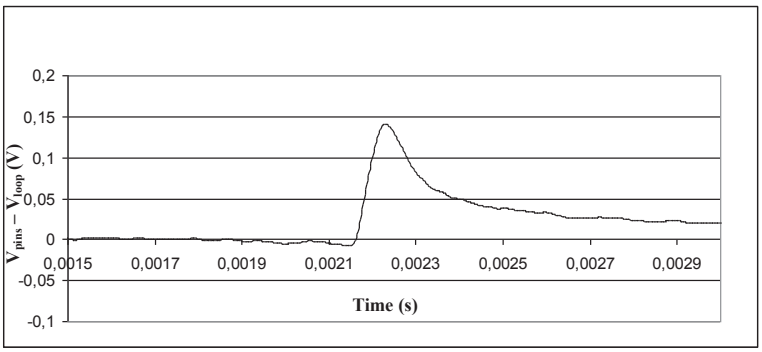

Fig. 5.10: Variation de la différence de tension $V_{pins} - V_{loop}$ lorsque les ponts de courants passent au point P_1

Tableau 5.5: Comparaison entre mesures et simulations pour le tir n°1

	Mesures		PSpice						ANSYS	Ana.
	temps (ms)	v (m/s)	t (ms)	v (m/s)	I_R (kA)	I_1 (kA)	I_2 (kA)	I_1/I_R	I_1/I_R	I_1/I_R
Point 1	2.76	106.5	2.82	112	27.9	21.3	6.6	0.763	0.692	≈0.75
Point 2	4.28	111.8	3.95	115	12.835	9.901	2.9	0.771	0.691	≈0.8
Point 3	8.13	102.2	6.73	111	1.6	1.2	0.4	0.772		
Bouche	19.12	84.6	13.80	101						

Nous donnons en tableau 5.5 la comparaison des trois méthodes mises en œuvre pour déterminer la répartition des courants dans les deux ponts de mesure dans le cas d'un lanceur à rails conventionnel (tir n°1). Les résultats sont comparables pour le tir n°9, deuxième cas analysé.

Les courbes des figures 5.11 et 5.12 sont relatives au tir n°11 en lanceur à rails augmenté.

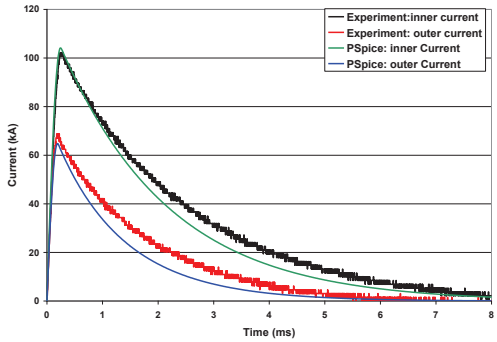

Fig. 5.11 : Comparaison des courants mesurés et simulés par PSpice pour le tir n° 11

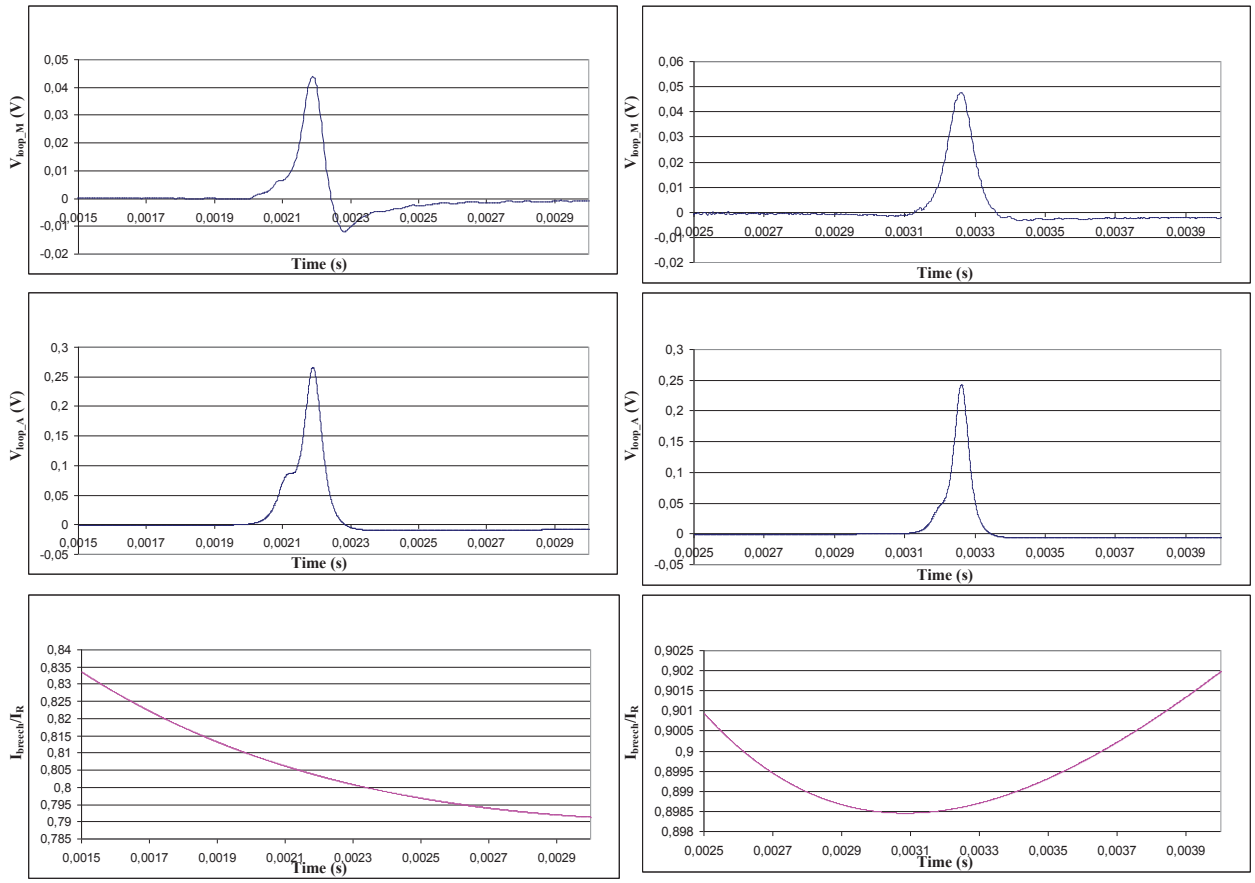

Point P_1; z_1 = 0.295m Point P_2; z_2 = 0.465m

Fig.5.12 : Comparaison entre mesures et approche analytique

L'analyse des courbes montre que la décroissance des courants est toujours plus rapide pour la simulation par rapport aux mesures. Cette remarque est vraie dans tous les cas de figure. On constate également que la méthode analytique est parfaitement applicable au point P_1 alors que c'est plus difficile pour le point P_2.

Tableau 5.6: Comparaison entre mesures et simulations pour le tir n°11

Tir 11	Essais		PSpice			ANSYS	Ana
x (m)	t (ms)	v (m/s)	t (ms)	v (m/s)	I_1/I_R	I_1/I_R	I_1/I_R
0.295	2.046	145.8	2.02	165	0.721	0.745	0.8
0.465	3.116	166.6	3.02	177	0.745	0.758	0.9
0.895	5.631	171.6	5.40	180	0.770		
1.500	12.81	164.3	8.79	176	0.784		

Quel que soit le cas de figure considéré, on peut tirer les conclusions suivantes :

- Les simulations par PSpice ont été faites avec des résistances variables continûment et des inductances constantes ou à variation linéaire entre les valeurs extrêmes ; le courant est néanmoins plus faible dans la phase décroissante.
- Pour tous les tirs, le pont de courant côté culasse fait passer environ les trois-quarts du courant I_R. Les résultats entre les trois méthodes de simulation sont à peu près cohérents sachant que chacune a ses défauts.
- Les remarques sont basées sur des tirs à faible énergie. Il est difficile d'extrapoler pour des énergies et donc des vitesses nettement supérieures.
- La méthode de mesure de la répartition de courants entre les ponts doit être améliorée pour que les simulations puissent être validées et être utilisées pour des développements futurs.

6. Analyses paramétriques pour des lanceurs à rails augmenté

Les lanceurs à rails augmentés devraient permettre d'obtenir des vitesses à la bouche supérieures à 2 km/s (projet RAFIRA) tout en garantissant un contact sans plasma entre le projectile et les rails. Nous nous proposons de faire un pré-design d'un tel lanceur avec les objectifs suivants :

- lancer une masse de 100 g à une vitesse de 2 km/s ou une masse de 200 g à une vitesse de 1 km/s ; ceci se traduit par une impulsion de 200 Ns
- limiter les forces linéiques qui s'exercent sur les rails à 8.10^6 N/m

La géométrie du rail interne étant donnée, quelle doit être la géométrie des rails pour obtenir la force maximale? Nous essayons de répondre à ces questions en utilisant ANSYS pour la détermination des paramètres électriques. Cette analyse paramétrique ne prend pas en compte les contraintes mécaniques et thermiques.

Dans une deuxième analyse paramétrique nous cherchons à optimiser la distance a entre les ponts de courant et le rayon r des ponts de courant pour un projectile pour LARA en utilisant PSpice.

La dernière partie est une analyse des différentes types d'alimentation en utilisant PSpice, effectué pour le lanceur LARA.

6.1. Optimisation du rail extérieur

Nous retenons un calibre de 25 x 25 mm ce qui fixe le rail intérieur et nous faisons varier la largeur w du rail extérieur, sa hauteur h et la distance g qui sépare le rail extérieur et le rail intérieur. Les courants sont choisis arbitrairement pour le moment et nous retenons trois couples tels que donnés dans le tableau 6.1. Nous supposons que nous disposons de 5 batteries de condensateurs (3 internes et 2 externes) et nous modifions les tensions aux bornes pour obtenir ces courants.

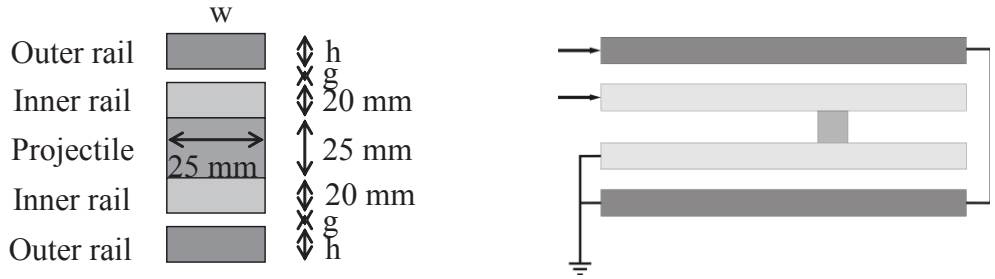

Fig.6.1 : Géométrie du lanceur à rails augmenté considérée

Tableau 6.1 : Couples de valeurs de courant dans les rails

I_R	400 kA	500 kA	600 kA
I_A	1267 kA	833 kA	511 kA

Les contraintes peuvent être obtenues en 2D transitoire. Les figures 6.2 et 6.3 donnent les variations des forces sur les rails par cette dernière méthode pour le couple de valeurs de courant (400 kA, 1267 kA) et deux géométries.

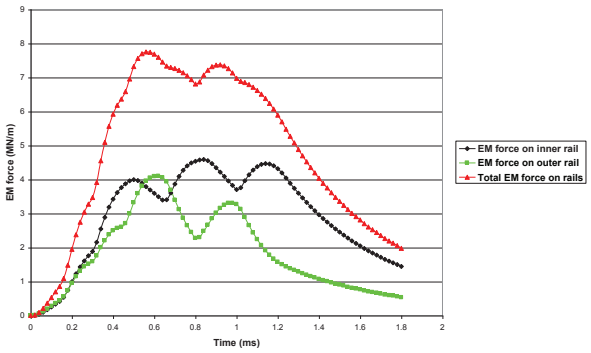

Fig.6.2 : Force électromagnétique sur les rails – rail externe large (24mm x 20 mm)

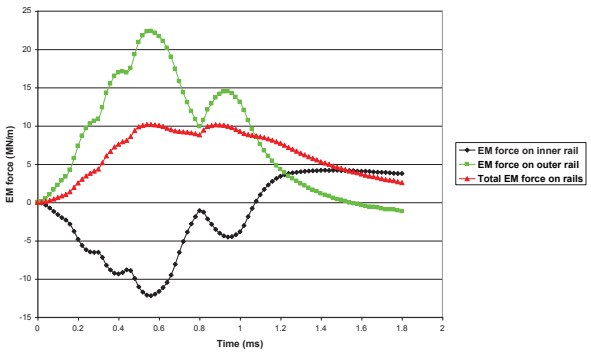

Fig.6.3 : Force électromagnétique sur les rails – rail externe étroit (2mm x 2 mm)

Même si la force sur le rail interne est négative pendant une longue période, les valeurs obtenues sont très élevées et cette disposition est à proscrire. Une analyse paramétrique conduit aux valeurs maximales des forces données sur le tableau 6.2.

Tableau 6.2 : Force maximale sur les rails

Force totale	Maximum	largeur w	hauteur h	distance g
I_R = 400 kA, I_A = 1267 kA	$10.4.10^6$ N/m	14 mm	2 mm	1 mm
I_R = 500 kA, I_A = 833 kA	$6.8.10^6$ N/m	12 mm	2 mm	1 mm
I_R = 600 kA, I_A = 511 kA	$4.8.10^6$ N/m	2 mm	2 mm	1 mm

6.2. Optimisation des forces sur le projectile

Cette optimisation nécessite de calculer les inductances L'_R et M' par ANSYS pour en déduire les forces électromagnétiques. Comme précédemment il faut décomposer en phénomènes lents et rapides aux premiers instants; pour cela nous considérons deux fréquences 10 Hz et 1 kHz car celle de 100 kHz n'est pas facilement accessible sous ANSYS. L'analyse paramétrique montre qu'à la fréquence de 10 Hz, h et w n'ont pas d'incidence sur L'_R et la variation de M' avec g est prévisible puisque cette valeur doit être minimale (valeur limitée par des considérations de mécanique). A la fréquence de 1 kHz, w n'a aucune incidence. Nous avons retenu les valeurs de L'_R et M'calculées à 1 kHz jusqu'à 0.3 ms et celles à 10 Hz au-delà de 1.97 ms avec une variation linéaire entre les deux. Ces valeurs conduisent à un bon compromis par rapport à une analyse transitoire complète.

Les valeurs maximales des forces sur le projectile sont données par le tableau 6.3. On note que les dimensions géométriques optimales sont indépendantes des couples de valeurs de courant.

Tableau 6.3 : Valeurs et dimensions pour une force électromagnétique maximale sur le projectile

Force électromagnétique	Maximum	w	h	g
I_R = 400 kA, I_A = 1267 kA	195 kN	8 mm	2 mm	2 mm
I_R = 500 kA, I_A = 833 kA	184 kN	8 mm	2 mm	2mm
I_R = 600 kA, I_A = 511 kA	173 kN	8 mm	2 mm	2 mm

6.3. Optimisation des courants

Nous retenons les valeurs suivantes w = 8 mm, h = 2 mm et g = 2 mm pour optimiser le rapport des courants. Les calculs conduisent aux valeurs du tableau 6.4 pour la force électromagnétique sur les rails. Le meilleur résultat est obtenu pour le couple (450 kA, 857 kA) car pour des courants I_R plus faibles, la partie négative sur le rail intérieur est trop importante.

Tableau 6.4 : Couples de courants pour obtenir une impulsion sur le projectile de 200 Ns

I_R (kA)	300	350	400	450	500	550	600
I_A (kA)	1518	1243	1030	857	713	589	480
F (10^6 N/m)	11.9	9.2	7.5	6.3	5.5	4.9	4.5

6.4. Optimisation du projectile

Nous cherchons à optimiser le couple (a, r) avec a distance entre les ponts de courant et r rayon des ponts de courant et nous recherchons les valeurs qui conduisent au courant le plus élevé et à l'échauffement le plus faible. Cette analyse est fait pour un projectile pour LARA en utilisant PSpice.

D'après la figure 6.4, on a intérêt à augmenter le rayon pour accroître le courant et diminuer en même temps la résistance. L'augmentation de a est surtout intéressante au début du tir où il y a des dI_A/dt importants.

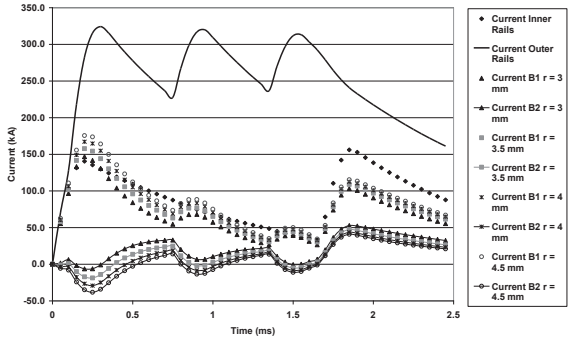

Fig.6.4 : Profil de courant dans les deux ponts de courant pour différentes valeurs de r (a = 15 mm)

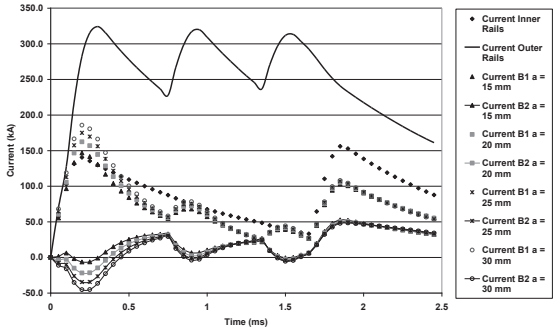

Fig.6.5 : Profil de courant dans les deux ponts de courant pour différentes valeurs de a (r = 3 mm)

6.5. Analyse de différentes alimentations

Cette étude est déconnectée par rapport à la précédente et nous souhaitons accélérer une masse de 15 à 25 g pour atteindre une vitesse de 1000 m/s à la bouche. Nous disposons de 2 bancs de condensateurs chargés à 7 kV pour le rail intérieur et de 4 bancs de condensateurs sous 10 kV pour le rail extérieur. Les temps de décharge peuvent varier. La géométrie étudiée est celle du lanceur LARA.

6.5.1. Alimentation dite parallèle

Une première étude consiste à étudier l'influence de la longueur des rails externes par rapport aux rails internes pour trois alimentations telles que décrites sur la figure 6.6. Les instants de décharge et l'efficacité énergétique sont donnés sur le tableau 6.5. Les rendements sont très faibles. La décharge type c est la plus efficace. Il peut y avoir intérêt à réduire la longueur des rails externes pour améliorer le rendement comme le montre le tableau 6.6.

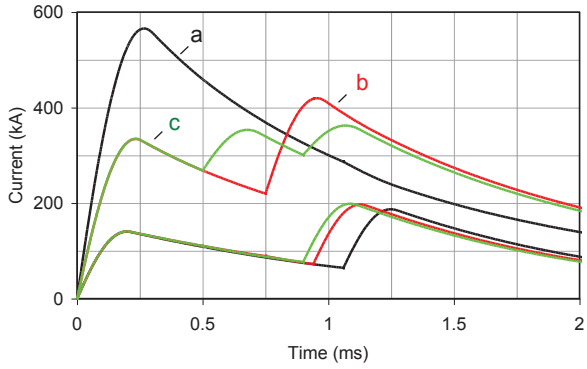

Cas a : les quatre bancs du circuit externe sont déclenchés en même temps à t = 0

Cas b : 2 bancs sont déclenchés à t = 0 et les deux autres en même temps que le deuxième banc pour le rail intérieur

Cas c : décharge calculée pour obtenir un courant pratiquement constant

Fig.6.6 : Evolution des courants

Tableau 6.5 : Vitesse à la bouche, rendement et instants de décharge t_1 du deuxième banc de condensateur du rail interne et t_2, t_3 et t_4 pour les $2^{ème}$, $3^{ème}$ et $4^{ème}$ bancs du circuit externe pour différentes masses du projectile

m (g)	t_1 (ms)	t_2 (ms)	t_3 (ms)	t_4 (ms)	Cas	v (m/s)	η (%)
15	1.80	0.00	0.00	0.00	a	999.7	2.15
15	1.70	0.00	1.65	1.65	b	999.7	3.32
15	1.67	0.10	0.75	1.35	c	1000.0	3.37
20	1.06	0.00	0.00	0.00	a	1001.0	2.88
20	0.94	0.00	0.75	0.75	b	999.3	4.03
20	0.90	0.00	0.50	0.90	c	1001.8	4.10
25	0.50	0.00	0.00	0.00	a	999.5	2.47
25	0.45	0.00	0.30	0.30	b	1000.7	4.36
25	0.21	0.00	0.45	0.90	c	1000.7	5.03

Tableau 6.6 : Vitesse à la bouche et rendement pour différents longueurs des rails externes

m (g)	Cas	Longueur (m)	v (m/s)	η (%)
15	a	1.5	999.7	2.15
20	a	1.2	1000.7	3.13
20	b	1.2	1000.0	4.39
20	c	1.2	999.7	4.44
25	a	0.9	999.9	4.44
25	b	0.9	1000.7	5.43
25	c	1.1	999.5	5.65

6.5.2. Alimentation dite segmentée et alimentation DES

Le principe de l'alimentation segmentée et de l'alimentation DES (Distributed Energy Storage) est décrit sur les figures 6.7 et 6.8.

Dans le premier cas la longueur du premier segment est telle que l'alimentation du deuxième segment intervient juste au moment où le projectile entre dans la zone (alimentation type b). Pour l'alimentation DES, les rails extérieurs sont en seul morceau mais on dispose d'un deuxième point d'injection. C'est également la position du projectile qui définit l'instant de déclenchement des deux derniers bancs de condensateurs. Les résultats sont regroupés dans le tableau 6.7. L'alimentation DES se caractérise par un meilleur rendement pour une efficacité équivalente.

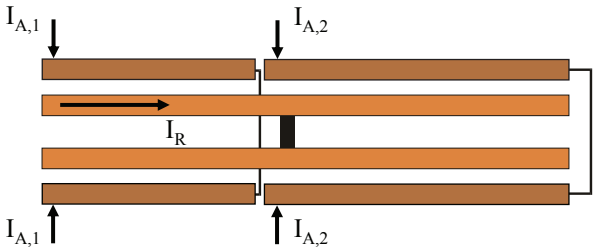

Fig.6.7 : Schéma de principe d'une alimentation dite segmentée

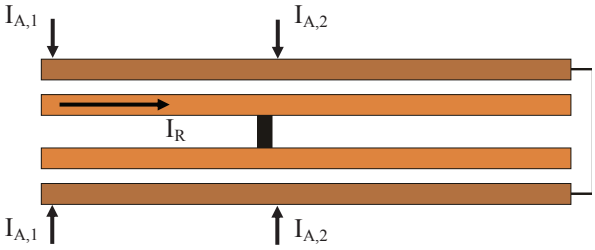

Fig.6.8 : Schéma de principe d'une alimentation dite DES

Table 6.7 : Vitesses et rendements pour les deux alimentations avec une longueur L_1 optimisée du point d'injection.

	m (g)	L_1 (m)	v_1 (m/s)	η_1 (%)	v_2 (m/s)	η_2 (%)
SEG	15	0.77	1088.9	3.29	1000.3	2.78
	20	0.19	882.2	4.53		
	20	0.25			940.8	3.29
DES	15	0.75	1051.5	4.37	999.7	4.00
	20	0.18	1043.5	4.53	1000.5	4.16

Le tableau 6.8 compare les 3 modes d'alimentation avec deux bancs de condensateurs pour les rails internes et externes. Les deuxièmes bancs de condensateur sont déclenchés au moment où le projectile atteint la position choisie. On note à nouveau la meilleure efficacité du système DES mais la construction est nettement plus délicate.

Table 6.8 : Vitesses à la bouche avec une injection de courant au moment où le projectile atteint la position x

Distance x	0.25 m	0.50 m	0.75 m	1.00 m
Normal	967 m/s	889 m/s	854 m/s	830 m/s
Segmenté	835 m/s	944 m/s	903 m/s	861 m/s
DES	996 m/s	923 m/s	878 m/s	845 m/s

6.6. Conclusion

Nous avons déterminé des dimensions optimales d'un lanceur à rails augmenté permettant de fournir une impulsion de 200 Ns avec des efforts sur les rails inférieurs à 8 MN/m. L'optimisation est basée sur une analyse paramétrique des dimensions en utilisant ANSYS soit directement soit par le biais du calcul des paramètres L'_R et M'. La distance entre les rails internes et externes doit être faible (g = 2 mm) et les rails ont une largeur w = 8 mm et une hauteur faibles devant le calibre (25 mm x 25 mm). Les courants injectés à partir de la décharge de 2 bancs de condensateurs pour les rails internes et 4 pour les rails externes nécessaires pour obtenir l'impulsion voulue tout en respectant les contraintes sont égaux à 450 kA et 857 kA soit un rapport I_A/I_R pratiquement égal à 2.

Dans une deuxième analyse paramétrique nous avons fait l'optimalisation pour la distance a entre les ponts de courant et le rayon r des ponts de courant pour un projectile pour LARA.

Dans une troisième analyse paramétrique, utilisant PSpice, nous avons comparé trois types d'alimentation avec optimisation des instants de déclenchement des bancs de condensateurs (2 pour I_R et 4 pour I_A). L'alimentation dite DES (Distributed Energy Storage) présente la meilleure efficacité énergétique comparée à l'alimentation normale ou segmentée. Dans tous les cas, le rendement énergétique est faible et ne dépasse pas 6 %.

Conclusions et perspectives

Le but initial de ce travail de thèse était d'étudier la répartition des courants entre les deux ponts de courant d'un lanceur à rails. A priori, le lanceur à rails augmenté par son champ extérieur nécessite un courant dans les ponts moins important pour une même vitesse à la bouche. On diminue ainsi les contraintes sur les brosses et on évite la formation de plasmas qui détériorent et le projectile et les rails.

Pour analyser cette répartition, nous avons mis en œuvre deux méthodes de simulation. La première utilise une approche circuit. Il s'agit de PSpice. Le modèle se décompose en deux parties, une partie électrique avec les bancs de condensateur qui fournissent l'énergie, les dispositifs de commande et les rails avec le projectile et une partie mécanique qui traduit la cinématique du projectile. La détermination des paramètres est délicate car il faut tenir compte de la forme impulsionnelle des courants, avec des fréquences élevées au début et basses pour la queue de l'impulsion. A l'effet de peau lié au courant, s'ajoute un effet de peau lié au mouvement du projectile. Les paramètres résistifs et inductifs doivent prendre en compte ces phénomènes. Les paramètres du modèle mécanique sont également délicats à définir en raison des frottements solide-solide.

La force électromagnétique dépend des courants et des selfs et mutuelles inductances incrémentales. Celles-ci ont été déterminées en utilisant ANSYS, logiciel utilisant les éléments finis. ANSYS permet une étude locale de la densité de courant et des échauffements. Ses défauts sont de ne pouvoir simuler l'ensemble du rail mais surtout de ne pas prendre en compte le mouvement du projectile. Les résultats sont donc rapidement faussés dès qu'il y a diffusion du courant dans le rail au voisinage du projectile. On observe néanmoins une bonne cohérence entre les deux méthodes. Pour étudier la répartition des courants entre les deux ponts de courants nous avons été amenés à modifier la montée en courant pour retrouver l'effet de peau.

Une méthode mise au point à l'ISL devait permettre de mesurer la répartition de courants entre les deux ponts. Elle s'est révélée impraticable en raison des vitesses faibles du projectile liées à une énergie disponible réduite. Nous avons pu effectuer dix tirs avec le lanceur à rails conventionnels mais que deux dans la configuration à rails augmenté suite à un défaut sur une alimentation. La disponibilité des moyens d'essais était également limitée.

Nous avons proposé une autre méthode pour utiliser les signaux fournis par une bobine de mesure. La méthode peut encore être améliorée. Il faut veiller tout particulièrement à la qualité des signaux pour diminuer le bruit et éviter le filtrage qui fait perdre des informations. La comparaison entre les deux méthodes de simulation et l'expérience est néanmoins intéressante et satisfaisante.

La dernière partie de ce travail consiste à faire une analyse paramétrique d'un lanceur à rails augmenté de grande vitesse à la bouche. Il doit fournir une impulsion de 200 Ns. Une étude paramétrique basée sur ANSYS pour les inductances incrémentales, permet de fournir un avant projet où la force sur le projectile répond au cahier des charges mais où les forces s'exerçant sur les rails sont également limitées à 8.10^8 N/m. Cette étude doit être complétée par une étude mécanique et thermique car les contraintes de courant sont très fortes. L'analyse paramétrique pour l'optimisation du projectile pour LARA en utilisant PSpice montre l'influence de la distance a entre les pont des courant et le rayon r des ponts de courant sur le profil de courant. Les études sur l'alimentation montrent que la solution DES (Distributed Energy Storage) conduit à une efficacité maximale ; néanmoins le rendement reste faible.

La solution du lanceur à rails augmenté mérite d'être approfondie. Deux pistes nous semblent intéressantes. D'une part réfléchir à une alimentation distribuée et commandable pour les rails intérieur et extérieur de telle manière que l'on apporte une énergie en phase ou en avance de phase par rapport à la position du projectile. Les énergies et les courants sont énormes, ce qui crée des difficultés de connectique. D'autre part pour définir ces lois de commande, il faut améliorer les moyens de simulation et en particulier la simulation locale qui devrait fournir plus d'éléments constructifs par rapport à PSpice. PSpice est un outil intéressant pour une étude rapide mais il faut également l'adapter pour une alimentation distribuée et synchrone avec la position du projectile.

Introduction

I.1. General Information on Electric Launchers

I.1.1. Motivation for the Development of Electric Launchers

A launcher is a device that transforms potential energy (of mechanical, chemical, or electromagnetic nature) into kinetic energy in order to launch an object. Mankind has searched since ages to increase the kinetic energy. The most powerful launchers nowadays are the chemical launchers. However, since these launchers have reached their limits, researchers now explore the physics and technology of electric launchers.

The most important limit of a pyrotechnical launcher (or powder gun) is the muzzle velocity. High muzzle velocities are important to defeat threats like anti-ship missiles and heavily armored tanks, and to increase the range of the projectile, allowing the gun to fire at a safe distance from the opponent forces. It also allows studying micro-meteor impact by testing armor for space-craft [MAR01] and by investigating material properties at high strain rates [SIA11]. The maximum muzzle velocity depends on the mass of the projectile and on the molecular mass of the combustion gasses [KLI92]. These gasses, generated in the gun chamber by the combustion of solid powder grains, accelerate the projectile during its travel in the barrel of the gun. The acceleration is directly related to the pressure at the base of the projectile. Therefore, the higher the pressure in the chamber is, the higher the base pressure and the acceleration will be. The chamber pressure, however, is limited for operational reasons. A high maximum pressure will lead to a thick and thus heavy launcher, limiting its efficiency on the battlefield. The gun of a modern main battle tank as the French tank Leclerc reaches one of the highest kinetic energies among the operational guns: 11,7 MJ (it launches a 7,3 kg-projectile with a muzzle velocity of 1790 m/s) [NEX11].

Higher muzzle velocities can be obtained with a light gas gun without increasing the maximum pressure. Indeed, since the molecular mass of a light gas, such as helium (4 g/mol), is much lower than that of the combustion products of a typical powder (28 g/mol), much less energy is lost in the acceleration of the molecules. However, light gas guns are voluminous and difficult to operate, and are therefore not suited for integration in mobile systems. They are typical laboratory instruments [KLI92].

Another major problem with chemical launchers is the low pyrotechnical safety. The explosion of munitions stored in ships, vehicles and factories has cost the life of many people, even recently as in Yemen, where more than 100 people died in a munitions factory explosion [IND11]. The US Navy lost 134 sailors after a series of chain-reaction explosions on the aircraft carrier USS Forrestal on 29 July 1967 when a rocket accidentally fired [STE04]. The use of electrical energy would reduce the explosion risk to zero and increase drastically the survivability of navy ships [MCF03]. Also, space agencies as NASA have lost satellites and astronauts due to a malfunction in the propulsion system, resulting in an explosion, as was the case with the Space Shuttle Challenger in 1986 [ROD86]. The feasibility to launch micro-satellites with railguns is being investigated by space agencies [MCN09, SCH11].

The use of electric energy for the launchers would also increase the energy efficiency of mobile platforms [LEH03], since the chemical energy contained in the solid powder can only be used for the acceleration of the projectile. Electric energy on the contrary is very versatile. Once it is generated, typically by the combustion of a fossil fuel, it finds a lot of applications, ranging from the propulsion

of the platform, over the energy supply of the sensors, to the guns. This fits very well in the concept of All Electric Ships (AES) and All Electric Vehicles (AEV) [GRO99].

I.1.2. Types of Electric Launchers

We distinguish two types of electric launchers: the electromagnetic launchers and the electrothermal launchers. The former include the railgun and the coilgun, the latter the electrothermal gun and the electrothermal-chemical gun. The railgun can be considered as a single-turn DC linear motor, consisting of a pair of rails, a projectile and a pulsed power supply. The coilgun on the other hand consists of a series of fixed coaxial coils, a projectile carrying a coil and a pulsed power supply. In both launchers the propulsive force acting on the projectile is the Lorentz force. Electrothermal launchers resemble much more the actual powder guns, since they consist of a chamber in which a pressure is generated, creating a force that accelerates the projectile. The barrel acts as a confined volume in which the potential energy is converted into kinetic energy. In pure electrothermal launchers only electrical energy is used to produce the working fluid, a high energy plasma. In an electrothermal-chemical launcher, the plasma is only used as an igniter for a chemical propellant, thus requiring much less electrical energy. The advantage of electrothermal launchers with respect to the powder guns is that they can use all kinds of working fluids or high-energy propellants to enhance performance, with reduced weight and volume [FAI01].

I.1.3. Power Supplies

A major problem for the integration of railgun systems in mobile platforms is the low energy density of the pulsed power supplies. An important part of the railgun is aimed at developing new technologies to reduce their volume. Diesel fuel has an energy density of 42 MJ/kg, TNT (a typical explosive) 4,4 MJ/kg, to be compared with the energy density of a high performance electrical pulsed power supply: 100 kJ/kg [MAR01]. Therefore, it will not come as a surprise when the first intended operational application of a railgun is on a ship.

Rotating machines have the highest energy density; in most laboratories however, capacitor banks are used as energy supply for railgun experiments. This is due to the fact the capacitors are very reliable, require very little maintenance, and that their volume is not a real issue in laboratories.

I.2. Actual Railgun Research

I.2.1. Research Topics

Railgun research can be divided into six major categories:

- the railgun itself,
- the projectile (especially the contacts between the rails and the conducting parts of the projectile),
- the power supply,
- diagnostics,
- simulation codes,
- and applications.

We will give some examples of current research in these categories for different countries in the following paragraphs.

I.2.2. United States of America

Railgun research became important in the United States in 1984 when Ronald Reagan created the Strategic Defense Initiative Organization (SDIO). Electric launchers were considered as one of the promising technologies to constitute a missile shield. Actually, the research focuses on typical military applications like long-range guns, especially at the US Navy [MCN07], but also on civilian applications like space launch systems [MCN09].

The main research institutes in the United States are the US Army Research Laboratory (ARL), the Institute for Advanced Technology (IAT) of the University of Texas and the Naval Surface Warfare Center (NSWC). A lot of effort has been invested in material research [FAI09], and in the development of diagnostic techniques and simulation tools such as the use of high-speed video as an in-bore diagnostic [WAT11] and the EMAP3D computer code (Electro-Mechanical Analysis Program in 3 Dimensions) [LIU09].

The institutes and organizations involved in electric gun research are member of the Electric Launcher Association (ELA), which assembles once a year.

I.2.3. China and Other Asian Countries

In railgun research, China is nowadays the second most important country (after the United States). Since a decade, the activity has strongly increased, such that at the last electromagnetic launch (EML) symposium in 2010 in Brussels, 151 of the 259 abstracts were introduced by Chinese scientists. A review of these abstracts shows that the Chinese laboratories are active in all fields of railgun research. The most important research groups are at the Harbin Institute of Technology, the Chinese Academy of Science, Beijing Institute of Special Electromechanical Technology, Northwest Institute of Mechanical & Electrical Engineering, the Huazhong University of Science and Technology and the China Academy of Engineering Physics. The Chinese research groups are organized in the National Electromagnetic Launch Society [EML10].

There is also a strong interest in theoretical research in Iran with a research group at the University of Tabriz [KES09], and researchers in Japan are exploring the use of pulsed power technology for fusion reactors [ASO09].

I.2.4. Europe

The leading center for railgun research in Europe is the French-German research institute of Saint-Louis (ISL), France. Several scientists work in a large experimental facility with different launchers. More details on the research activities at the ISL are given in par. 3. The ISL collaborates with smaller research groups in Europe: the Royal Military Academy (RMA) in Belgium on augmented railguns [GAL04, COF10], the University of Pisa in Italy on magnetic fields [BEC09, CIO09] and the Institute for Semiconductor Physics in Vilnius, Lithuania on sensors [SCH09a].

The research groups of the West-European countries involved in railgun research and related technologies (electrothermal-chemical, high power microwaves, power electronics) meet annually in the European Electromagnetic Launch Society (EEMLS).

In Russia, a small group at the Lavrentyev Institute of Hydrodynamics in Novosibirsk contributes to the railgun research [RUT09].

I.2.5. Electromagnetic Launch Symposium

In 1980, the ELA organized the first Electromagnetic Launch Symposium; the first European Electromagnetic Launch Symposium was organized by the EEMLS in 1987. Since 2000, both Symposia are combined with oversight and guidance provided by an International Permanent Committee. The IAT sponsors and supervises the publication of the papers. The Chinese National Electromagnetic Launch Society in Beijing will organize the 16th EML Symposium.

The symposia are attended by some 100 researchers, mostly from the United States and China. The papers are published by the IEEE, until 2008 in the IEEE Transactions on Magnetics, since 2010 in the IEEE Transactions on Plasma Science.

I.3. Railgun Research at the ISL

The ISL started railgun research in 1987. Since then, the ISL has been working on electromagnetic launcher technology (railgun and coilgun) and electrothermal-chemical guns. The railgun group at the ISL uses a medium caliber railgun (Pegasus) with a barrel length of 6 m for high energy shots (the energy supply has a capacity of 10 MJ) and several smaller railguns [LEH03a].

The railgun group is particularly interested in the electric sliding contacts in railguns [SCH03a, SCH05, REC09] and diagnostics [SCH03, SCH09, SCH09a]. The pulsed power group focuses on the development of technologies such as high power semiconductor based switches and power supplies [SPA05, SPA05a, DED08, ZOR09].

A recent development at the ISL is the RApid FIre RAilgun (RAFIRA) project. Its goal is to investigate the multishot capacity of the armature technology developed at the ISL. The launcher has a length of 3 m, a rectangular caliber of 15 mm x 30 mm and the muzzle velocity is below 2 km/s. These system parameters were chosen with respect to existing naval antimissile guns [SCH09b, SCH09c]. Indeed, it has been shown that these existing guns are not efficient against future supersonic ad hypersonic antiship missiles and that the railgun is a good candidate to replace them, thanks to the higher muzzle velocity and fire rate [GAL11].

Other remarkable projects are the design of a railgun as the first stage of a multistage earth orbit launcher for atmospheric research and space applications [SCH11], and the use of a railgun as an experimental tool to study impact phenomena for materials research [SIA11].

I.4. Previous Research on the Augmented Railgun at the ISL

The railgun used for this last project is the augmented railgun LARA (Lanceur A Rails Augmenté), developed in 2000 in order to study the influence of an exterior magnetic field applied to a railgun. Augmented railguns were developed to reduce the current in the projectile without reducing the electromagnetic force and thus reducing the heat load of the sliding contact [KOL76]. The concept, however, was not tested before at the ISL. This project was the PhD work of Johan Gallant. The theoretical study and the simulations were done at the RMA in Brussels; the experimental setup was constructed and tested at the ISL.

The results were very promising: it has been shown experimentally that the augmented rail launcher is capable of accelerating projectiles, without transformation of the solid sliding contact in a plasma contact, up to kinetic energy levels which are much higher than these obtained with a non-augmented launcher (an increase by a factor five or nine, for the one-brush and two-brush projectiles, respectively). During the same study, a model of the propulsive force on the projectile has been modeled and validated, and a model of the electric circuit of the launcher and its power supply was presented [GAL04, GAL05].

I.5. Continuation of the Research on the Augmented Railgun

The work of Johan Gallant focused on the validation of the concept of the augmented railgun and the study of the influence of the exterior magnetic field at a system level. The development of new sensors made it possible to study the influence of this field on the current distribution between the brushes of a projectile [SCH09]. This lead to a new collaboration between the ISL and the RMA. The results of this study are presented in this PhD thesis.

As it was the case with the previous collaboration between the ISL and the RMA, the experimental work was done at Saint-Louis, the rest of the study was done in Brussels. This set-up leads to some complications, since LARA, its power supply and its diagnostics were not exclusively available for the study: not all planned experiments could be executed.

Chapter 1

Electromagnetic Railgun

1.1. Introduction

In this first chapter an introduction to electromagnetic launch is given. The general concept of electromagnetic acceleration will be discussed. One of the most important features in a railgun is the electrical contact between the rails and the projectile; this will be addressed in § 1.3. Also the electromagnetic force acting on a multiple brush projectile will be treated. First we start with an historic overview.

The construction of the first electromagnetic gun is attributed to the Norwegian scientist Kristian Birkeland. At the beginning of the twentieth century, he obtained a patent for a coilgun (Fig. 1.1). He succeeded in accelerating a mass of 10 kg to a velocity of 100 m/s. A failure of his coilgun during a demonstration to raise funds put an end to his research on electromagnetic launchers [GER99],[EGE89].

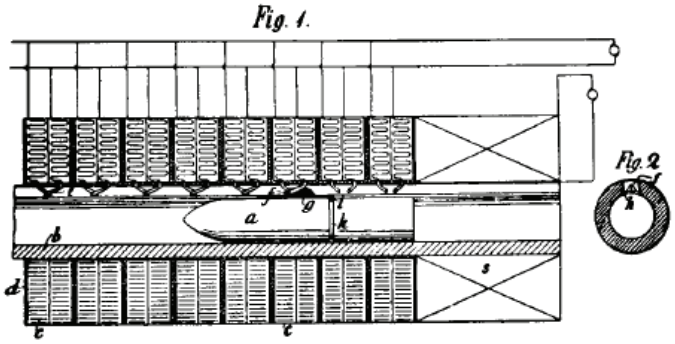

Fig. 1.1: Schematic of the first electromagnetic gun conceived by Birkeland [EGE89]

During the First World War, Fauchon-Villeplée started studies on railguns. The launcher and the projectiles he used are presented in Fig. 1.2. The projectile used had copper fins. These copper fins provided the electric contact between the two rails. He used batteries as an energy source. The launcher was 2 m long and accelerated projectiles of 50 g up to a velocity of 200 m/s. The main problem for his project was to find a suitable energy source [MCN99].

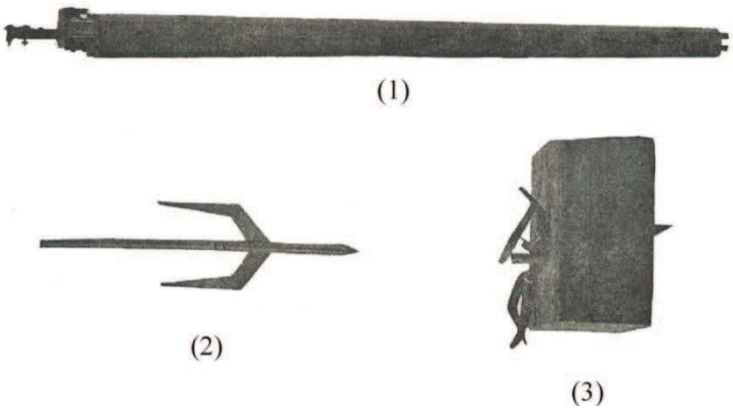

Fig. 1.2: Launcher of Fauchon-Villeplée (1) and the projectile before (2) and after (3) the shot [MCN99]

The next attempts were made by the German Hänsler during the Second World War. He first started to work on coilguns, using capacitors, batteries and AC-machines as power supplies. But after six months he switched to the railgun approach. He constructed a 2 m long railgun and accelerated projectiles with a mass of 10.3 g up to a velocity of 1200 m/s. Confronted with the same energy source problems as Fauchon-Villeplée, he also started research on power supplies. The end of his research coincides with the end of the Second World War. In 1946 an American Committee, The Armour federation, reviewed and evaluated his research. They concluded that the anti-aircraft railgun was technically feasible [MCN99].

A big step forward in railgun research was made by Richard Marshall and the Australian National University in Canberra in 1977. He constructed a 5 m long railgun and obtained a velocity of 5.9 km/s for projectiles with a mass of 3 g. He used a homopolar generator with an energy of 550 MJ for the power supply [MEI07].

The railgun used in this thesis is the LARA (Lanceur A Rails Augmenté) railgun of the French-German research institute of Saint-Louis (ISL) in France. This augmented railgun can be easily converted into a non-augmented railgun by opening the exterior circuit that generates the augmenting magnetic field. Shots made in this mode are registered as shots with the LARC (Lanceur A Rails Conventionnel) railgun.

The activities of electromagnetic launch at ISL started in 1987. During the years ISL has developed its own technology. I would like to mention especially the development of projectiles with current brushes as armature. These projectiles will be discussed later in this chapter.

1.2. Railgun: A General Overview

1.2.1. Principle

The fundamental principle of all electromagnetic launchers is based on the basic observation that an electric charge q moving at a velocity $\vec{v}$ in a magnetic field $\vec{B}$ experiences a force called the Lorentz force:

$$\vec{F} = q(\vec{v}x\vec{B}) \tag{1.1}$$

An electromagnetic railgun consists of an energy source, a pulse forming network and two parallel conductors, the rails, connected by a movable conductor, the armature (Fig. 1.3).

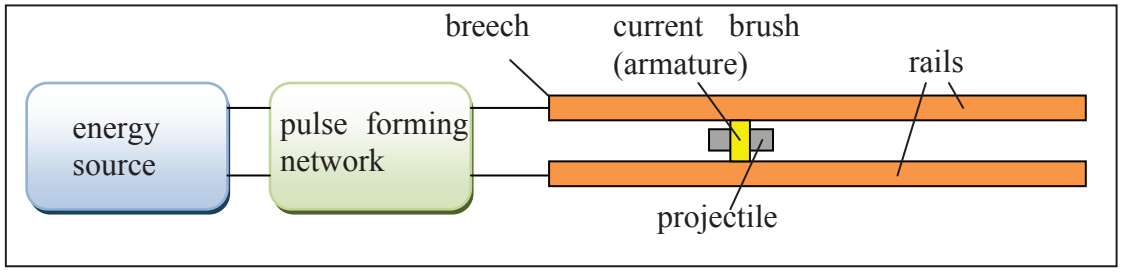

Fig. 1.3: Schematic of an electromagnetic railgun

The current, provided by the energy source and shaped by the pulse forming network, is injected at the breech, passes through the upper rail until it reaches the armature and then runs through the armature to the lower rail and back to the breech (Fig. 1.4). The magnetic field induced by the current running through the rails interacts with the current in the armature, resulting in an electromagnetic force accelerating the armature:

$$\overrightarrow{F_{EM}} = \iiint_V \overrightarrow{J_R} x \overrightarrow{B_R} dV \tag{1.2}$$

Here $\overrightarrow{J_R}$ represents the current distribution in the projectile and $\overrightarrow{B_R}$ is the magnetic field induced by this current.

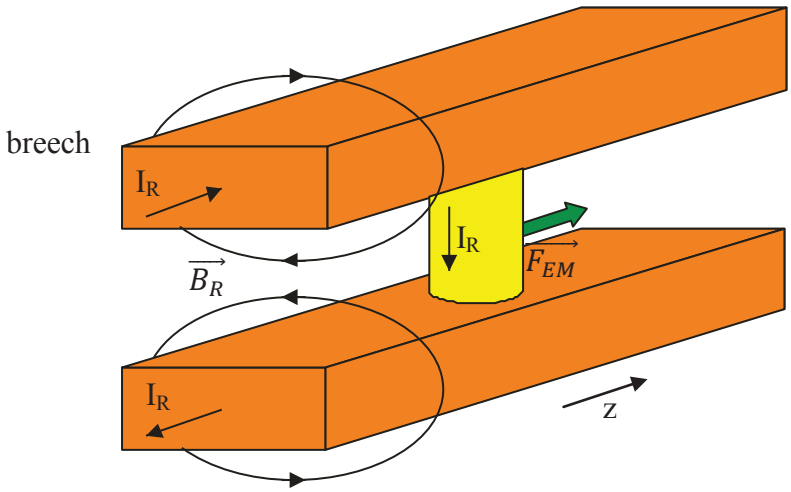

Fig. 1.4: General principle of an electromagnetic railgun

The projectile and the rails form an electric circuit. The magnetic coenergy W_m of this circuit can be described as [MAR04]:

$$W_m = \frac{1}{2} L_R I_R^2 + \frac{1}{2} L_{pr} I_R^2 \tag{1.3}$$

I_R represents the current in the rails, L_R is the self inductance of the rails and L_{pr} is the self inductance of the armature of the projectile. The resulting force F acting on the projectile is:

$$F = \frac{\partial W_m}{\partial z} = \frac{1}{2} \frac{\partial L_R}{\partial z} I_R^2 + \frac{1}{2} \frac{\partial L_{pr}}{\partial z} I_R^2 \tag{1.4}$$

with z the direction of the shot.
The self inductance of the armature L_{pr} is independent of the position of the armature and thus eq. 1.4 becomes:

$$F = \frac{1}{2} \frac{\partial L_R}{\partial z} I_R^2 \tag{1.5}$$

Equation 1.5 is the railgun force equation.

In the railgun community, most often the force equation is written as:

$$F = \frac{1}{2} L'_R I_R^2$$

with $L'_R = \partial L_R / \partial z$, the inductance gradient.

1.2.2. Pulse Forming Network and Current Impulse

The energy source of a railgun has to provide a high current to the rails and the energy has to be delivered in a few milliseconds. Thus a high energy and power density are required. At ISL capacitor banks are used as an energy source [GAL04], [CHA91], [SPA92]. The principle is presented in Fig. 1.5. When the switch S is closed the capacitor C is discharged in the pulse forming network and the rails. When the current reaches its maximum the capacitor has to be short-circuited to prevent oscillations. Therefore a "crowbar" diode D is used in parallel with the capacitor. Current flowing back to the capacitor would not only mean an energy loss but can also cause serious damage to the capacitor.

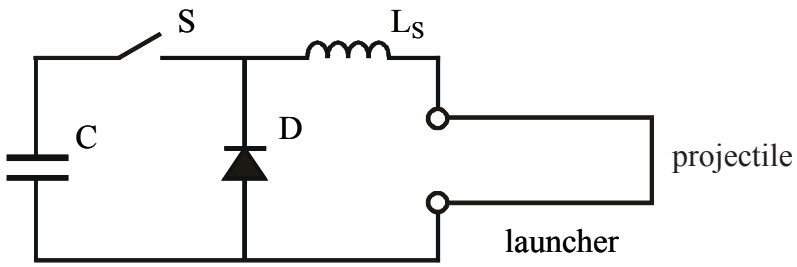

Fig. 1.5: Schematic of a capacitor bank and pulse forming network

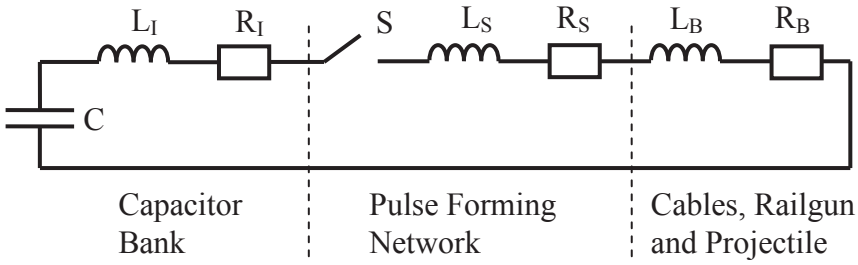

Fig. 1.6: Schematic without crowbar diode

Fig. 1.6 represents the circuit for charging the pulse forming coil without crowbar diode. This results in the following equation for the current *I*, under the hypothesis of filiform conductors, [DAR86], [GAL04]:

$$\frac{\partial^2 I}{\partial t^2} + \frac{1}{(L_I+L_B+L_S)}\frac{\partial((R_I+R_B+R_S)I)}{\partial t} + \frac{I}{(L_I+L_B+L_S)C} = 0 \tag{1.6}$$

R_B and L_B represent the resistance and inductance of the conductors and L_I and R_I the inner inductance and resistance of the capacitor bank. The inductances are considered constant. If L_T is the total inductance and R_T the total resistance of this circuit and if we consider the resistance to be constant, eq. 1.6 becomes:

$$\frac{\partial^2 I}{\partial t^2} + \frac{R_T}{L_T}\frac{\partial I}{\partial t} + \frac{I}{L_T C} = 0 \tag{1.7}$$

with the initial conditions:

$$I_{(t=0)} = 0 \tag{1.8}$$

$$\left(\frac{\partial I}{\partial t}\right)_{t=0} = \frac{U_0}{L_T} \tag{1.9}$$

For the solution of eq. 1.7 we have to consider two cases:

- $\frac{4L_T}{R_T^2 C} > 1$: undercritically damped
  The current will oscillate.

- $\frac{4L_T}{R_T^2 C} < 1$: overdamped
  The current will be aperiodically damped.

Only the first solution is interesting because in the second case a large part of the electric energy will be dissipated in the resistances due to the Joule heating.

The solution for the capacitor bank with a thyristor as a switch, which is presented in Chapter 2, with U_0 = 8 kV is presented in Fig. 1.7. We take into consideration the values of the inductances, resistances and capacitance of the electrical model of the pulse forming network used in the PSpice model, discussed in Chapter 2 and represented in Fig. 2.4 but without crowbar diode. We consider the railgun to be short circuited.

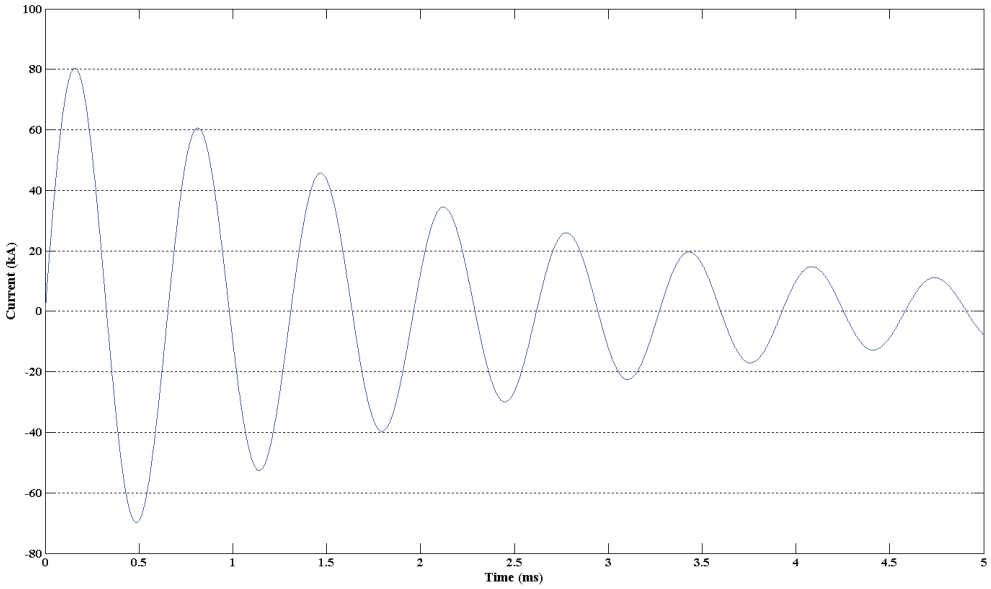

Fig. 1.7: Oscillating current profile for the capacitor bank with a thyristor as switch and without crowbar diode for U_0 = 8 kV

To limit the joule losses, $\frac{4L_T}{R_T^2 C}$ should be as high as possible. For $\frac{4L_T}{R_T^2 C} \gg 1$ the solution of eq. 1.7 becomes:

$$I(t) = \frac{U_0}{L_T b} e^{-a_0 t} \sin(b_0 t) \tag{1.10}$$

with:

$$a_0 = \frac{R_T}{2L_T} \tag{1.11}$$

$$b_0 = \sqrt{\frac{1}{L_T C} - \frac{R^2}{4L_T^2}} \tag{1.12}$$

If we consider the case of weak damping:

$$a_0 \approx 0 \tag{1.13}$$

$$b_0 \approx \sqrt{\frac{1}{L_T C}} \tag{1.14}$$

Then the expression for the current becomes:

$$I(t) \approx \frac{U_0}{\sqrt{L_T/C}} \sin\left(\sqrt{\frac{1}{L_T C}}\, t\right) \tag{1.15}$$

and thus the current reaches its maximum $I_0 \approx \frac{U_0}{\sqrt{L_T/C}}$ at the moment $t \approx \frac{\pi}{2}\sqrt{L_T C}$

The pulse shaping coil L_S acts as energy storage and maintains the current after the maximum. A typical current shape is presented in Fig. 1.8. A description of the capacitor banks used during the experiments is given in Chapter 4.

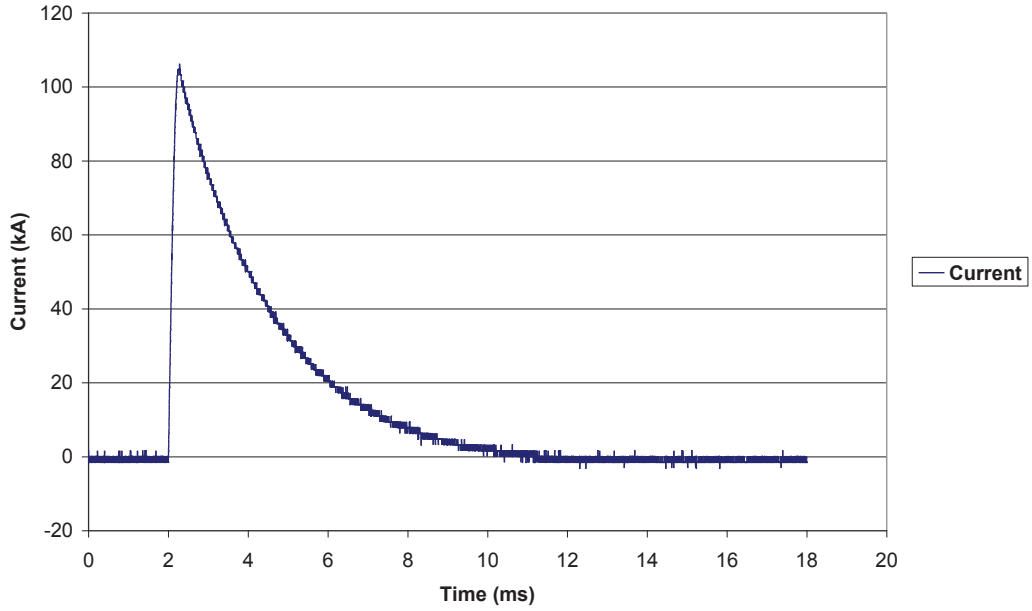

Fig. 1.8: Current measured during shot 3

1.2.3. Augmented Railgun

In an augmented railgun, a second pair of rails is used to obtain an additional external magnetic field. The additional pair of rails can be connected in series with the inner rails or have a separate energy source. When the rails are connected in series, the current first flows through the inner rails and the projectile and then is injected in the outer rails. The total resistance is high in this case which results in high Joule losses. The LARA railgun discussed in this thesis is a parallel augmented railgun with a separate inner and outer circuit (Fig. 1.9).

Augmented railguns have multiple advantages. The presence of an external magnetic field augments the force on the projectile (eq. 1.16).

$$\vec{F}_{EM} = \iiint_V \vec{J}_R \times \left(\vec{B}_R + \vec{B}_{ext} \right) dV \tag{1.16}$$

The current I_A in the outer circuit induces the external magnetic field B_{ext} that reinforces the magnetic field $\overrightarrow{B_R}$ (Fig. 1.10). Because we have two separate circuits only the current I_R of the inner circuit runs through the projectile. This means that we can augment the force on the projectile through this external field without raising the current in the inner circuit and thus without raising the current I_R through the projectile.

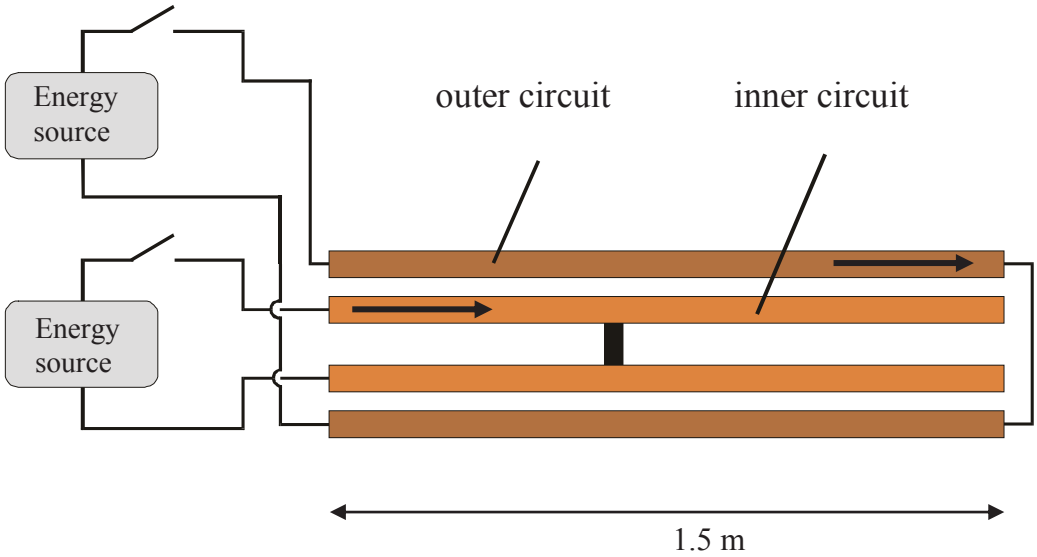

Fig. 1.9: Schematic of an augmented railgun

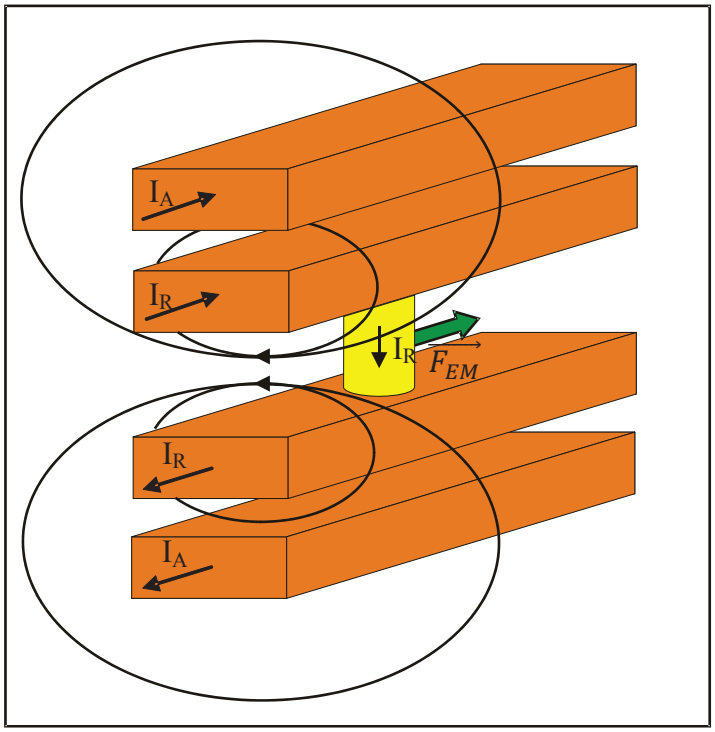

Fig. 1.10: Principle of an augmented railgun

This is an important advantage of an augmented railgun. In a conventional railgun the current through the projectile is limited because of the heating of the sliding contacts between the projectile and the rails. The heating of these contacts is due to the Joule-effect and the friction and can cause the contacts to melt. Melting of these contacts can result in contact transition which leads to an increase of

the armature resistance and the deterioration of the rails. Different types of contacts between the rails and the projectiles can be used. In this thesis we use projectiles with a solid contact and we try to avoid contact transition. Another approach is the use of plasma contacts or a combination of both, the hybrid contacts. This will be discussed in § 1.3. Having to separate circuits also allows the optimization of the external current.

The railgun force equation for an augmented railgun is:

$$F = \frac{1}{2} L'_R I_R^2 + M' I_R I_A \tag{1.17}$$

with L_R' the self inductance gradient of the inner rails and M' the mutual inductance gradient of the inner and outer rails and I_A the current in the augmenting circuit.

However, experimental results show that eq. 1.17 overestimates the electromagnetic force on the armature. Keefer et al. [KEE93] compared the forces calculated with eq. 1.17, with the results of a 3D MEGA simulation of the electromagnetic force. They also conclude that eq. 1.17 gives an overestimation. For an augmented railgun, there is a larger difference because a larger portion of the force is exerted in the rail, since the augmenting current has had time to diffuse into the rail prior to the passing of the projectile. Another conclusion of their simulations is that for a conventional railgun L'_R increases in time as the fields diffuse in the conducting structure of the railgun.

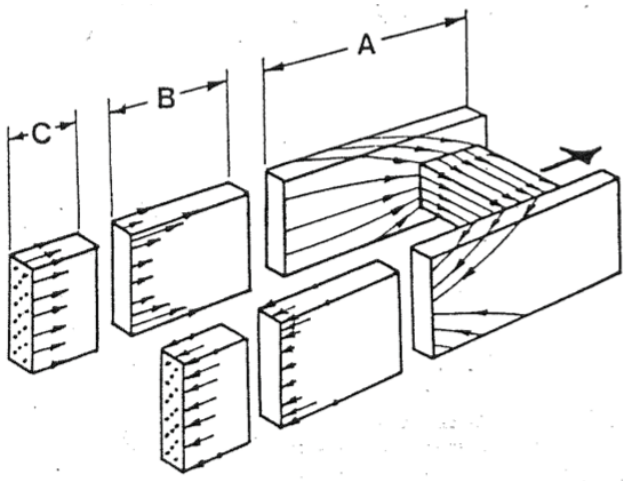

Fig.1.11: The three different current regions [MAR84]

In [MAR84] it is stated that $F = \frac{1}{2} L'_R I_R^2$ has to be used with caution because I is not uniformly distributed and it is better to use eq. 1.2. In this article three different current flow regions are discussed (Fig. 1.11). In the first short region A directly behind the armature there is no field inside the rails and the current flow is influenced by the presence of the armature. The effective L'_R of region A could be derived if the value of the electromagnetic force is known.

In region C the current has fully penetrated the rails and the current density is uniform. And region B is the region in between where the current is flowing in the surface of the rails but the effect of the armature is not yet noticeable.

1.3. Electrical Contacts

A good electrical contact between the rails and the projectile is an important factor for railgun efficiency. A low contact resistance results in less Joule losses and thus less heating of the contact. In

general four types of armatures are used: plasma armatures, solid armatures, transitioning armatures and hybrid armatures.

In a plasma armature the current is carried in a high temperature and high pressure arc. This arc is typically several centimeters long. The plasma can be generated by exploding a metal foil behind the projectile or by directing a plasma discharge against the base of the projectile. If a high-pressure gas is used to pre-accelerate the projectile, the arc can be generated by initiating a discharge in the gas behind the projectile [LEH91], [THO89].

In a solid armature a solid contact is maintained between the rails and the projectile. Those armatures can consist of solid plates or current brushes of conducting material. Joule losses during acceleration can cause the heating of the contact and can result in contact transition. A solid armature that transitions into a plasma armature is called a transition armature.

A hybrid armature consists of a solid conductor with plasma brushes in the small gap between the solid conductor and the rails.

All four types of armatures have their advantages and disadvantages. For a plasma armature one of the disadvantages is ablation drag or the loss in acceleration arising from the ablation of bore materials and their entrainment into the plasma armature. Ablation can cause serious damage to the rails. Another problem is the appearance of secondary arcs behind the projectile for velocities higher than 3 km/s. The ablated bore material joins the plasma which is losing material on the same time. Under certain conditions this can cause the creation of a secondary arc. This secondary arc also carries current but doesn't contribute to the electromagnetic force on the projectile and thus the total force on the projectile is reduced [THO89], [BAR91]. A plasma contact has a higher electrical resistance but assures a good electrical contact at high velocities.

A solid armature has a lower resistance compared with a plasma armature. Joule heating can cause the solid contact to melt, the parasitic mass necessary to prevent this melting can be high. Also the armature has to withstand high stress levels to assure its structural integrity. A solid-solid contact is limited to ±3 km/s [THO89]. A solid armature has no ablation drag. However gouging can cause erosion of the rails. The surface of the rails is never perfect. Gouging is caused by an intermittent contact between the rails and the projectile which results in a plastic deformation of the rails and, for high velocities, in high contact pressure and high temperatures. The result is a tear-shaped groove [FAI01].

Hybrid armatures have a lower resistance than plasma armatures. The appearance of a secondary arc is less likely but can't be ruled out [LEH91]. A transitioning armature combines the advantages and disadvantages of both plasma and solid armatures.

For the experiments discussed in Chapter 4 and 5, we use a projectile developed at ISL. It is made of metal brush armatures incorporated in sabots made of insulating low-density material. Fig.1.12 shows a projectile used in the experiments. It has two fiber brush armatures in CuCd and a glass fiber reinforced resin is used for the sabot. It is a solid armature and we try to avoid contact transition.

Fig. 1.12: Projectile with two fiber brush armatures used in the experiments at ISL

For a solid armature, there are two main conditions to keep a good contact between the rails and the projectile [SCH03]:

- The normal force pushing the contact against the rails has to be sufficient. Otherwise electric arcs can occur which can result in contact transition.
- The thermal charge has to be limited because heating and melting of the contact can also result in contact transition.

First we discuss the normal force on the current bridge. The most common solid armature is the C-shape armature, Fig. 1.13, still used by American researchers. A schematic of the projectile used for the experiments at ISL is presented in Fig. 1.14. Also here a "C-shape" is present. The brushes are bent backwards. As shown in Fig. 1.14.b this results in a current flowing in the direction of the bent brush and a corresponding electromagnetic force $\overline{F_{EM}}$ with a component $\overline{F_z}$ in the shot direction and a component $\overline{F_x}$ pushing the current brush against the rails.

Fig. 1.13: C-shape solid armature with two current bridges [GAL04]

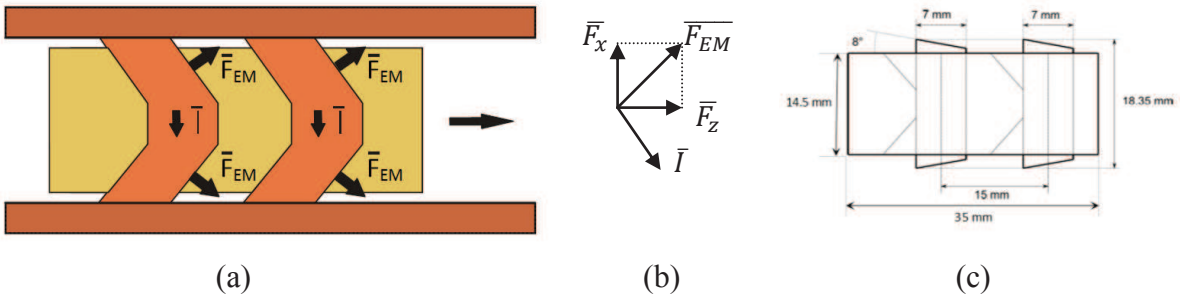

Fig. 1.14: Schematic of the projectile used in the experiments (a), forces acting on the bent part of the current brush (b), and dimensions of the projectile (c)

Marshall [MAR04] set forth the "gram per amp" rule which means that at least 9.8 N of force must be exerted to compress the rail-armature interface for each kiloampere of current that flows across it. The electromagnetic force rises with the square of the current which means that an initial mechanical force must be present to ensure the contact until the current is high enough [BAR03]. The length of the fiber brushes is initially greater than the caliber, pushing them backwards in a reservoir. This results in a mechanical force pushing the brushes against the rails. The design of the projectile ensures that this mechanical force is sufficient enough to maintain the contact between the brushes and the rails at the beginning of the shot.

Second we discuss the thermal charge on the projectile. The heating of the contact is due to the joule heating in the projectile and, in a lesser extent, due to mechanical friction between the projectiles and the rails. The thermal charge (TC) due to the joule effect can be expressed through the action integral [SCH03]:

$$TC = \int_0^t I^2(t)\,dt \tag{1.18}$$

The projectile has two current brushes. To know the TC on each current brush, we should know the current flowing through each brush separately and evaluate the action integral for each current brush.

Different mechanisms for contact transition have been proposed. The most important theoretical approaches are the current-wave model based on the velocity skin effect (VSE) and the contact-spot model.

The diffusion of the current in the rails depends on different effects. First there is the proximity effect. When two current carrying conductors are placed in proximity of each other, the currents will influence each other. The currents will concentrate in the areas where the magnetic field is maximal, which means between the rails of the railgun. The skin effect refers to the tendency of an alternating electric current to flow at the skin of the conductor. For a railgun, with transient currents, this means that the current will flow first at the surface of the rails and diffuses into the rails over time. Due to the combination of these effects the current will flow mainly in a layer at the inner surface of the rails (Fig. 1.15).

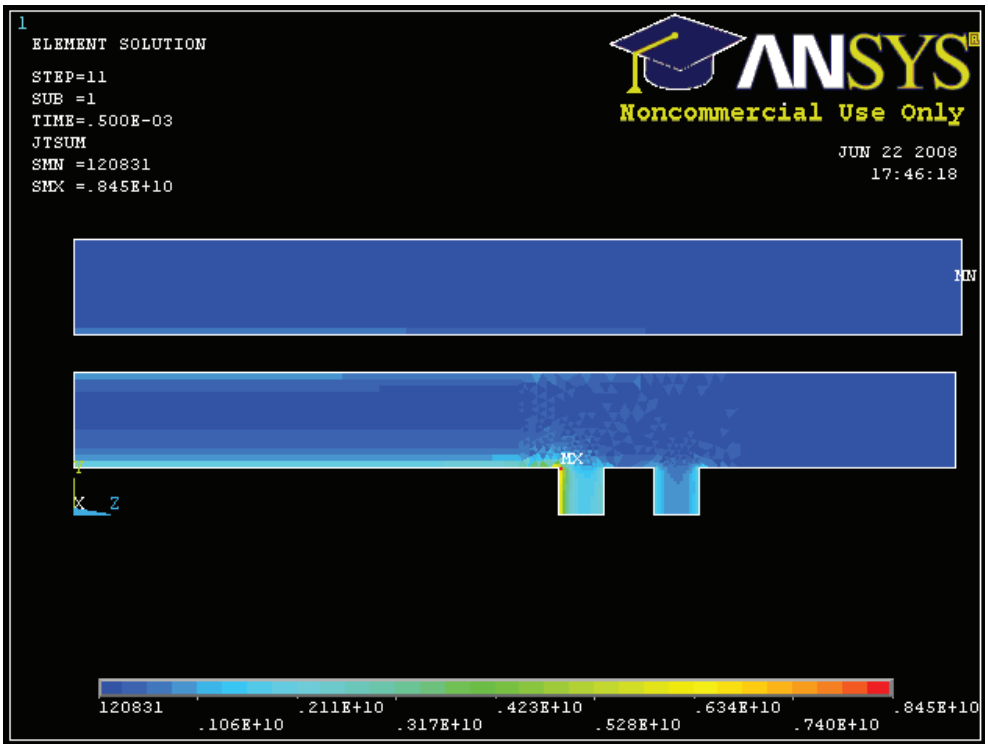

Fig. 1.15: Example of a current distribution simulated with a transient analysis with ANSYS at t = 0.5 ms

The velocity skin effect is a combination of effects caused by the finite diffusion rate of current into the rails. In [BAR93] the armature is thought of as a moving current source which injects current into the rails. As the armature moves, it “sees” a fresh, cold part of the rails where the current diffusion into the rails has not started yet. The limited diffusion rate in the rails results in a current being dragged to the trailing edge of the armature. This current density concentration increases with velocity.

The current melt-wave model, [WOO97], [PAR90], [BAR93] and [BAR95] states that the current concentration at the rear corners of a solid armature due to the VSE, causes these corners to melt due to Ohmic heating. The melted material is entrained on the rails. The resulting gap has a higher resistivity than the solid phase and the current will flow forward into the cold, solid region which is then heated and melts. As a result a “melt wave” will travel from the back to the front of the armature. This melt wave leaves a high-resistance plasma gap between the armature and the rails. If the melt wave reaches the front of the contact and the gap is large enough transition will occur. Generally, the

melt wave will need to traverse the contact several times to create a gap large enough to cause transition due to the normal pressure between the surfaces [WOO97].

For the current melt-wave model, in [WOO97] as well as [PAR90], the main assumptions are:

1) A perfect electrical contact ahead of the melt wave;
2) The rapid removal of the liquid metal by entrainment on the rail.

The first assumption is not realistic, certainly not with the use of fiber brushes. In [BAR95], a comparison between the experimental data and the predictions based on the current melt-wave theory with an ideal contact between the rail and the armature leads to the conclusion that the predictions of the transition velocity were too low. The contact between two solid metals is never ideal. Spots of intimate contact, or so-called A-spots, are randomly distributed throughout the nominal contact area. The current flow across the contact is concentrated within the A-spots which occupy only a fraction of the nominal contact area. This results in an additional voltage drop across the contact. The higher current concentration in these contact spots also results in a higher dissipation. When the characteristic size of the A-spots is small the voltage drop can be described by a contact resistance per unit area R_c , which characterizes the contact between the armature and the rails [BAR95] under the assumption that all A-spots are about the same size:

$$R_c = \rho_a \frac{a_{spot}}{\zeta} \tag{1.19}$$

Here a_{spot} represents the A-spot size, ρ_a the armature resistivity and ζ the fraction of the nominal contact area occupied by spots. This contact resistance increases the magnetic diffusion into the contact zone and decreases the current concentration due to the VSE. The contact resistance slows down the melt wave and delays transition.

The material loss for the brush armatures caused by Joule heating is due to the melting of material at the contact spots. In [SCH03a] a linear dependence between the mass loss and the joule heating in the contact zone is reported. A possible simple model for the transition mechanism in brush armatures is presented in Fig. 1.16. A brush has initially a greater length than the distance between the rails. This mass reservoir is used to cover for mass loss during launch. When the brush is shortened during the shot by erosion and wear it finally loses direct contact.

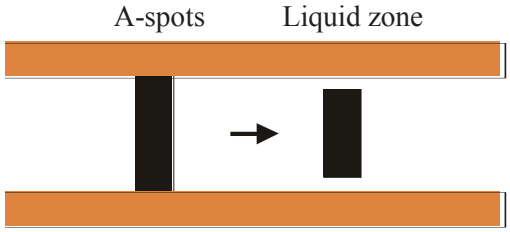

Fig. 1.16: Schematic drawing of mass loss in a fiber armature

1.4. Electromagnetic Force on Multiple Brush Projectiles

1.4.1. Projectile with One Brush

The electromagnetic force acting on a projectile with one current brush is equal to:

$$F_{proj} = \frac{1}{2} L'_R I_R^2 + M' I_R I_A$$

with I_A the current in the augmenting circuit and M' the mutual inductance gradient.

1.4.2. Projectile with Two Brushes

In a projectile with two current brushes, the current will be distributed between the two brushes as presented in Fig. 1.17. Under the assumption of filiform conductors and constant currents, the forces F_1 and F_2 acting on the current brush P towards the breech and the current brush Q towards the muzzle can be expressed as [GAL04]:

$$F_1 = \frac{1}{2} L'_R \, I_1^2 + L'_R \, I_1 \, I_2 + M' \, I_1 \, I_A \tag{1.20}$$

$$F_2 = \frac{1}{2} L'_R I_2^2 + M' I_2 I_A \tag{1.21}$$

with I_1 and I_2 represent respectively the current in the brush P and in the brush Q.

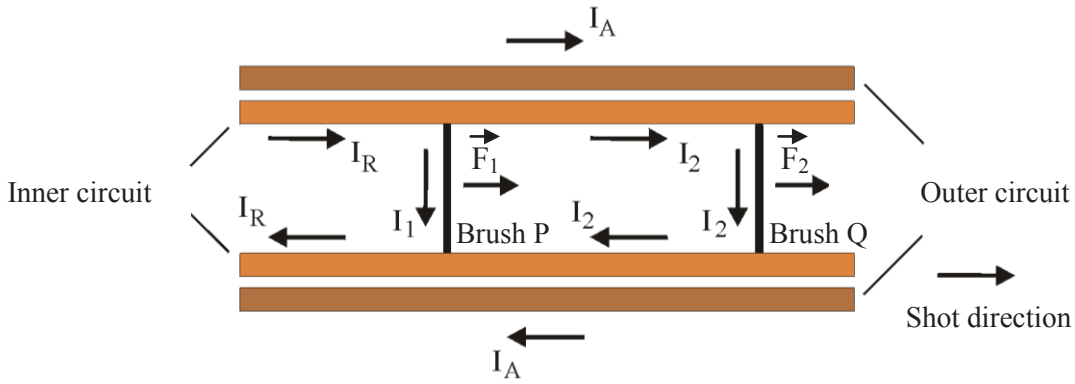

Fig. 1.17: Electromagnetic force acting on a projectile with two brushes in an augmented railgun [GAL04]

The resulting total force on the projectile is:

$$F_{proj} = F_1 + F_2 = \frac{1}{2} L'_R \, I_R^2 + M' I_R I_A \tag{1.22}$$

In projectiles with multiple brushes launched with a conventional railgun the force on the brushes is very poorly distributed and can cause very high stress levels in the projectile [PFL03].

With eq. 1.20 and 1.21 we can prove that an augmenting circuit contributes to a better equilibrium of the forces acting on the projectile. We consider the case of a projectile with two brushes and an augmented launcher with following values for the inductance gradients based on LARA:

$$L'_R = 0.4 \ \mu H/m$$

$$M' = 0.2 \ \mu H/m$$

For a conventional railgun, with a current I_R = 200 kA the total force on the projectile is 8 kN (eq. 1.5). Then we can calculate with eq. 1.22 for the case of an augmented railgun, which current I_R we need in the inner circuit in function of the current I_A in the augmenting circuit to obtain the same total force. The result is presented in Fig. 1.18. This figure shows that if you raise the current in the augmenting circuit you can obtain the same force on the projectile with a lower current in the inner, resulting in a lower thermal charge on the current brushes.

The current distribution between the brushes can be expressed with the parameter $\lambda = \frac{I_1}{I_2}$:

$$I_1 = \lambda \, I_R \tag{1.23}$$

$$I_2 = (1 - \lambda) I_R \tag{1.24}$$

Experiments and finite elements calculations have been carried out by Wey et al., [WEY99]. They determined the current distribution for a projectile with two current brushes. For current brushes in CuCd with a diameter of 5 mm and a distance of 10 mm between the centre of the brushes, they found $\lambda = 0.62$. The measurement and the calculations are in perfect agreement from the moment of current injection until the current reaches its maximum.

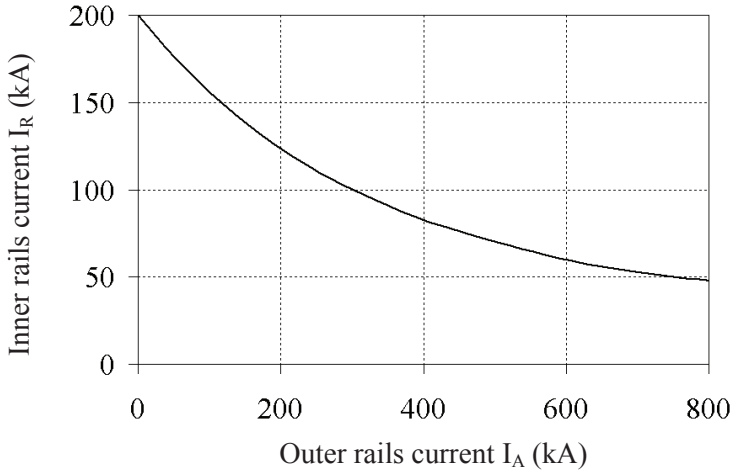

Fig. 1.18: Current in the inner circuit in function of the current in the outer circuit to obtain a constant force of 8 kN [GAL04]

With the expressions for the currents (eq. 1.23 and 1.24), the forces F_1 and F_2 on the bridges P and Q (eq. 1.20 and 1.21) become:

$$F_1 = \frac{1}{2} L'_R \lambda^2 I_R^2 + L'_R \lambda (1-\lambda) I_R^2 + M' \lambda I_R I_A \tag{1.25}$$

$$F_2 = \frac{1}{2} L'_R (1-\lambda)^2 I_R^2 + M'(1-\lambda) I_R I_A \tag{1.26}$$

This result is only valid under the condition of constant currents. The effects of current induction were not taken into account and they can influence the current distribution. A changing current in the outer rails I_A will, for example, induce a current in the loop formed by the current brushes and the inner rails. Fig. 1.19 shows the forces on the brushes, expressed in percentages of the total force on the projectile in function of I_A. The currents I_R and I_A used are the currents presented in Fig. 1.18 to obtain a force of 8 kN on the projectile.

For a conventional railgun, 88 % of the force on the projectile acts on the current brush towards the breech P [WEY99] (point a in Fig. 1.19 with $I_A = 0$). In an augmented railgun, a better distribution of the forces on the brushes is found. The repartition between the brushes P and Q tends to $\lambda/(1-\lambda)$ for a high current I_A compared to I_R. When $I_A >> I_R$, $M'\lambda I_R I_A$ and $M'(1-\lambda) I_R I_A$ become the prevailing terms in eq. 1.25 and 1.26 and the forces on the brushes are:

$$F_1 \approx M' \lambda I_R I_A$$
$$F_2 \approx M' (1-\lambda) I_R I_A$$

The augmenting field contributes to a better force distribution between the current brushes, resulting in less stress in the projectile.

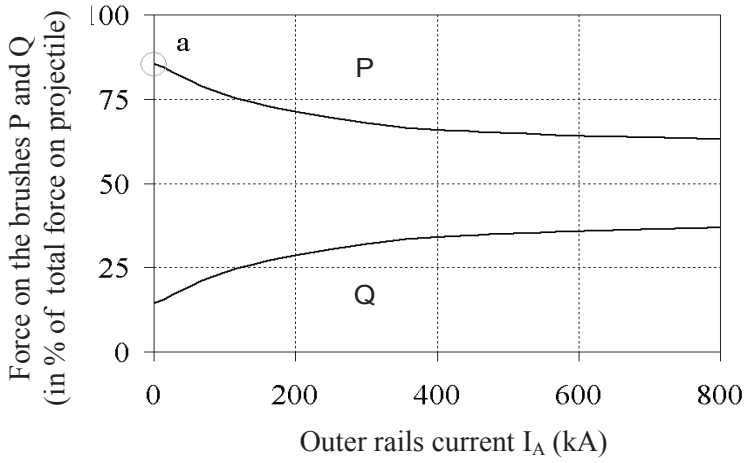

Fig. 1.19: Force distribution between the brushes of the projectile with $\lambda = 0.62$ [WEY99]. Corresponding inner rails current in Fig. 1.18.

1.5. Conclusion

Even if the concept of a railgun is quite simple, the velocity of the projectile and the thermal charge of the brushes due to the current in the railgun, are such that it is very difficult to maintain a good solid contact between the brushes in the projectile and the rails. Experiments have been made with other types of contacts, such as plasma contacts and hybrid contacts, but the plasma always leads to a reduced lifetime of the rails. A way to reduce the thermal charge is to equip the projectiles with multiple brushes.

Ideally, the current in a multiple brush projectile is equally distributed over the different brushes such that every brush has the same thermal charge. However, due to the velocity skin effect and the impedance of the rails segments between the brushes, the current is not equally distributed. It is concentrated in the rear brushes, until the thermal charge leads to a meltdown of the solid contact between the brush and the rails. The resulting high-resistance plasma gap leads to a new current distribution: more current is now running through the front brushes. This phenomenon continues until the solid contacts of all brushes are lost and the projectile than transitions.

A method to attain an equal current distribution, despite the velocity skin effect, is to select a different resistivity for each brush. A.G. Schmitt has studied the feasibility of this concept extensively during her PhD work [SCH98]. She demonstrated that it is theoretically possible to define the required electrical properties of the metals used for the different brushes. However, the thermal and mechanical properties of the available metals were not suited for the brushes of a railgun projectile, except for some Cu alloys, leading to problems other than the current distribution.

The experiments with LARA by J. Gallant at ISL have shown that the maximum kinetic energy at the muzzle – without the transition of the solid contact between the rails and the brush to a plasma contact – can be significantly increased in an augmented railgun. The maximum kinetic energy has increased by a factor of 5 for one-brush projectiles and by a factor of 9 for two-brush projectiles [GAL05]. A part of the success can be explained by the reduced thermal load without loss of electromagnetic force thanks to the exterior magnetic field. There was also an assumption that the augmenting field had a positive effect on the current distribution between the brushes, but the experimental setup at that time did not allow measuring the current distribution.

Since then, new experimental techniques have been developed, and nowadays it is possible at ISL to measure the current distribution between the different brushes of an accelerating projectile [SCH05a]. This method will be used in this work. The muzzle velocities obtained during our experiments are within the range of 85 to 213 m/s and we avoid contact transition.

Chapter 2

Global Modeling of the Railgun

2.1. Introduction and Philosophy of the Modeling

The global model of the railgun, described in this chapter, combines an electrical model of the pulse forming network, the rails and the projectile with a model of the kinematics of the projectile. It is a first step for the modeling of a railgun, but it cannot be decoupled of the second one which is more local due to diffusion and heating effects.

We use the PSpice code which allows the simulation of the global railgun with equivalent electric networks. The electrical and kinematic models are coupled as presented in Fig. 2.1. The electrical model is used for the calculation of the global currents in the rails and the current distribution between the current brushes. The current found with the electrical model is used in the kinematic model to calculate the electromagnetic force on the projectile. Together with a model for the friction force it allows an estimation of the velocity and position of the projectile. The position of the projectile is needed for the determination of the resistance and inductance of the inner rails. The parameters of the electrical model are time-dependent due to the variation of the skin depth caused by the current pulse and the velocity of the projectile. The skin effect and the velocity skin effect are therefore simulated.

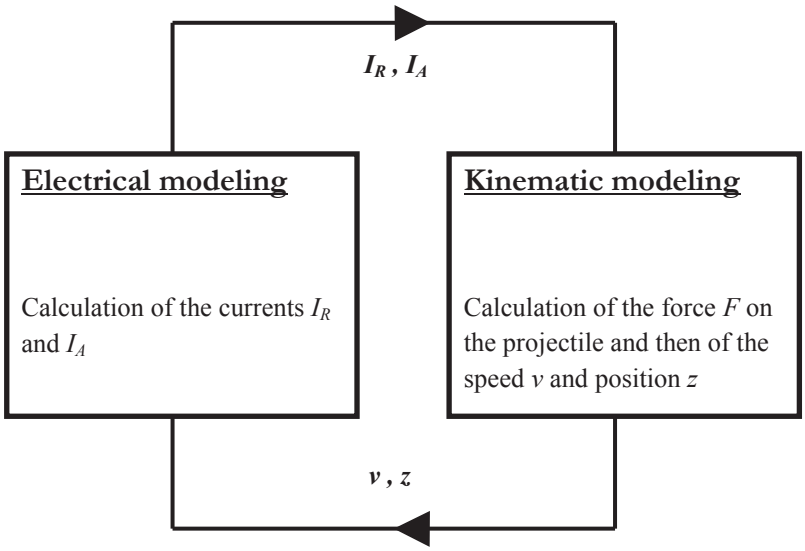

Fig. 2.1: Global synopsis of modeling

There is also a coupling between the electrical model and the thermal model for the projectile. Only the heating of the projectile is taken into account and not the heating of the rails. The current in the brushes and their resistance is used to calculate the joule losses in the brushes and an average temperature for each current brush is determined. This temperature is then used in the temperature-dependent resistance model of the current brushes. We will have to make some assumptions and use empirical expressions obtained in previous works to define the needed parameters.

Considering the assumptions and the empirical expressions for the parameters, it is necessary to appreciate the accuracy of the used model. Comparison is made in different conditions with experiments for a non-augmented and an augmented railgun. We will use the results obtained on the railguns LARC and LARA given in [GAL04]. The global model will be used to estimate performance.

2.2. Railgun Feeding and Electrical Modeling

2.2.1. Description of the PSpice Model

The PSpice model combines an electrical model of the Pulse Forming Network (PFN), the rails and the projectile with a model of the kinematics of the projectile. The PSpice code uses the Kirchoff laws to calculate the electric potential and the current at each node of the circuit.

The first step in the simulation process is the design of the electric circuits. PSpice has a large database with realistic electric components and allows taking various characteristics into account. This is an important feature for the modeling of complex components, such as diodes and thyristors.

In the second step the analysis type is specified. A finite difference method is used to solve the differential equations. The time step used for the calculations is variable and automatically adapted to the variation in time of the current and the electric potential. For the analysis the transient time domain is used and the maximum time step is set to 10 μs.

2.2.2. Pulse Forming Network

The PFN is a combination of a fast discharge capacitor with a high-voltage semiconductor switch, a crowbar diode and a pulse shaping inductance. The capacitor discharges into the pulse shaping coil and, after the passing of the coaxial cables, connection and injection blocks, into the rails and the projectile. When the voltage across the capacitor passes through zero, the current passes through the crowbar diode. The capacitor is then short-circuited. The high voltage capacitor delivers its energy in a short time and therefore a pulse shaping coil is used as an intermediate energy store. Each capacitor bank has its own system for charge and discharge. The switches are synchronized.

Two different types of energy supply modules are simulated. Both are capacitor banks but the modules used for the experiments described in [GAL04] use a spark gap diode as semiconductor switch, while for our experiments a thyristor is used. Both models are represented respectively in Fig. 2.3 and 2.4. The number of capacitor banks (energy supply module) in parallel varies from 1 to 5 (Fig. 2.2) in the experiments described in [GAL04]. In our experiments a total of three capacitor banks were used.

The PFN is connected to the railgun through coaxial cables, connection and injection blocks. The resistance and inductance in function of the frequency of a 5 meter long coaxial cable was determined with an LCR meter [SIA]. The results are listed in Table 2.1. Experience shows that a frequency of 100 kHz is a good compromise especially in the first instants of the current impulse. If the variation of inductance is weak for high frequency, it is not the same for the resistance.

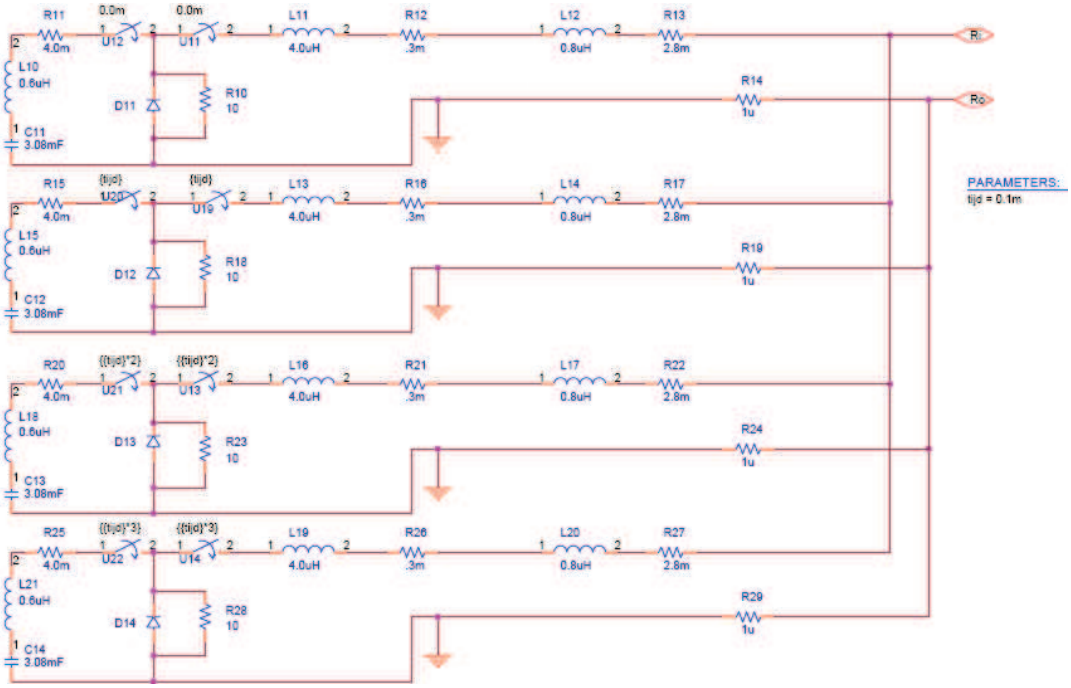

Fig. 2.2: Modeling of the capacitor banks and their systems

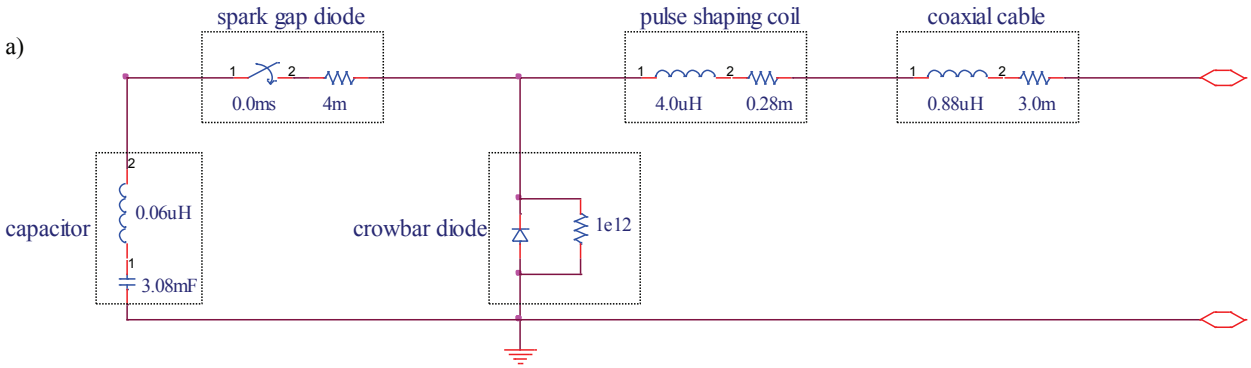

Fig. 2.3: Scheme of the Pulse Forming Network using a spark gap diode

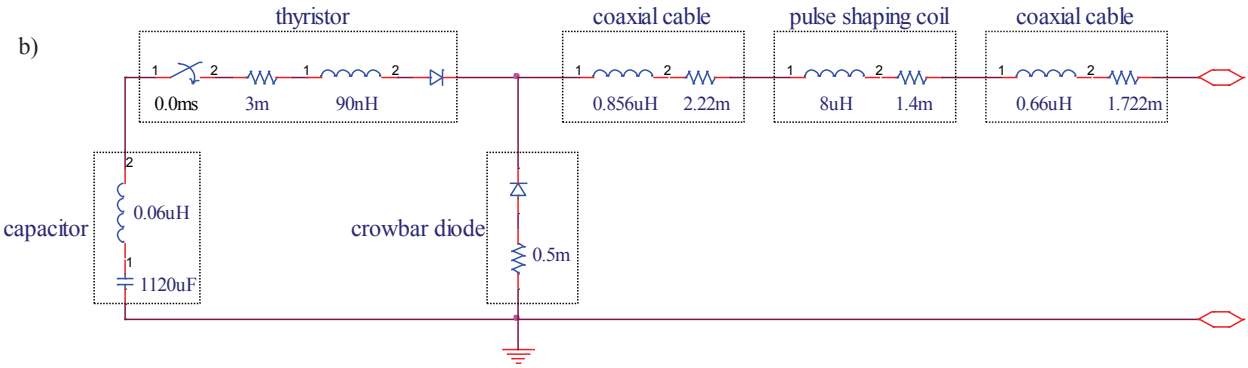

Fig. 2.4: Scheme of the Pulse Forming Network using a thyristor

Table 2.1: Frequency dependent parameters of a 5 m long coaxial cable [SIA]

f (Hz)	R (ohm)	L (μH)
100	0.004	2
200	0.004	1.82
400	0.004	1.48
600	0.004	1.4
1000	0.004	1.4
2000	0.005	1.4
3000	0.005	1.3
5000	0.006	1.3
8000	0.007	1.3
13000	0.0086	1.3
20000	0.0115	1.26
30000	0.016	1.24
40000	0.0208	1.23
60000	0.0315	1.21
80000	0.0432	1.2
100000	0.0556	1.19
120000	0.0681	1.18
180000	0.089	1.16

The influence of the pulse shaping coil on the current profile for the configuration with a thyristor for two energy supply modules with an initial charge of 8 kV is shown in Fig. 2.5.

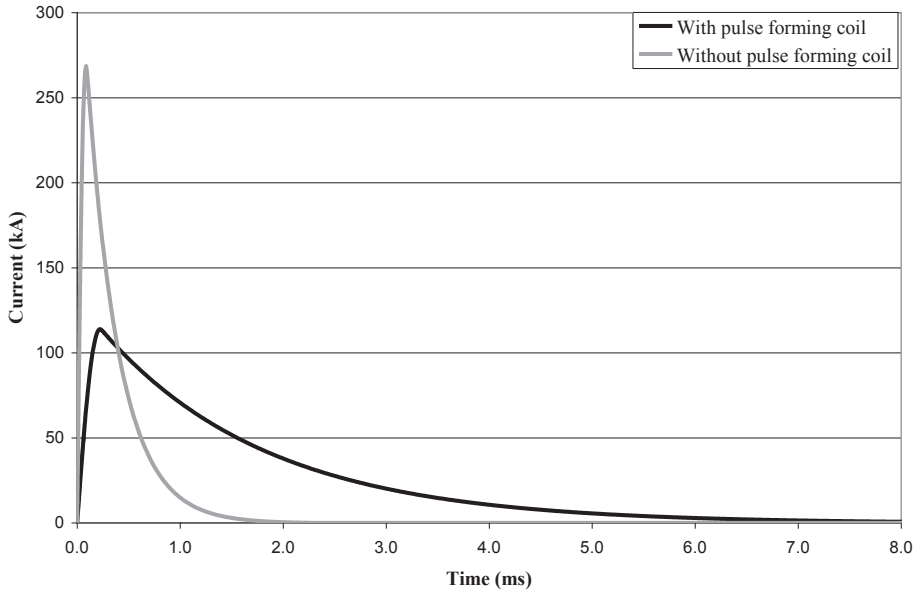

Fig. 2.5: Influence of pulse forming coil

2.2.3. Rails

2.2.3.1. General Model

As seen in Chapter 1, the force F on the projectile depends on the incremental value of the inductance L'_R and mutual inductance M' in case of an augmented railgun. We can also define a time-dependent incremental value $R'(t)$ for the resistance. The velocity skin effect will modify its value. For a non-augmented railgun only the resistance $R'_R(t).z$ and self inductance $L'_R.z$ (z is the position of the projectile) of the inner rails, both depending on the position of the projectile, have to be modeled. The velocity skin effect is taken into account but the heating of the rails is not simulated. The duration of a shot is very short and the dimensions of the rails are important so we may consider that the rails are isothermal. On the other hand, the projectile temperature will be considered.

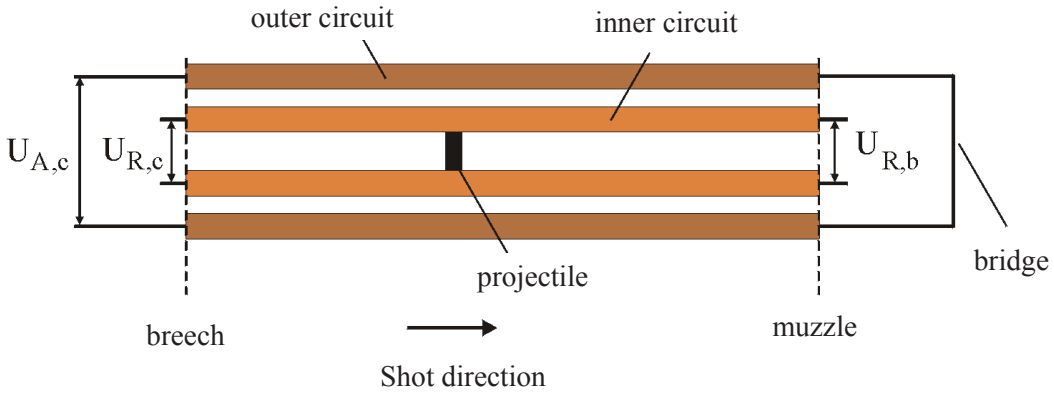

Fig. 2.6: Schematic of an augmented railgun

For an augmented railgun, the interaction between the inner and outer rails results in an additional term due to the mutual inductance gradient M'. The self inductance L_A and resistance $R_A(t)$ of the outer rail are constant; the term due to the mutual inductance depends on the position of the projectile. Fig. 2.6 represents the schematic of an augmented railgun. The voltage at the breech of the inner rails $U_{R,c}$ and of the outer rails $U_{A,c}$ can be expressed as:

$$\begin{aligned} U_{R,c} &= R'_R\, z\, I_R + R_{pr}\, I_R + L_{pr}\frac{dI_R}{dt} + L'_R\, v\, I_R + L'_R\, z\frac{dI_R}{dt} + M'\, v\, I_A + M'\, z\frac{dI_A}{dt} \\ U_{A,c} &= R_A\, I_A + L_A\frac{dI_A}{dt} + M'\, v\, I_R + M'\, z\frac{dI_R}{dt} \end{aligned} \tag{2.1}$$

with R_{pr} the resistance and L_{pr} the inductance of the projectile.

The model must also take into account the number of brushes for the projectile. The case is easy if there is only one brush. For 2, 3 or more, the auxiliary circuits created by the brushes have to be considered. They induce mesh currents. Fig. 2.7 shows the general model for an augmented railgun with two brushes. It translates the voltage equation (eq. 2.2) for this mesh.

$$0 = R'_R\, aI_2 + L'_R\, a\frac{dI_2}{dt} + M'a\frac{dI_A}{dt} + R_b I_2 + L_b\frac{dI_2}{dt} - R_b I_1 - L_b\frac{dI_1}{dt} \tag{2.2}$$

with R_b the resistance and L_b the inductance of a current brush and a the distance between the brushes.

The numerical values have been determined for the LARC and LARA railgun based on a series of experiments allowing the validation of the model [GAL04].

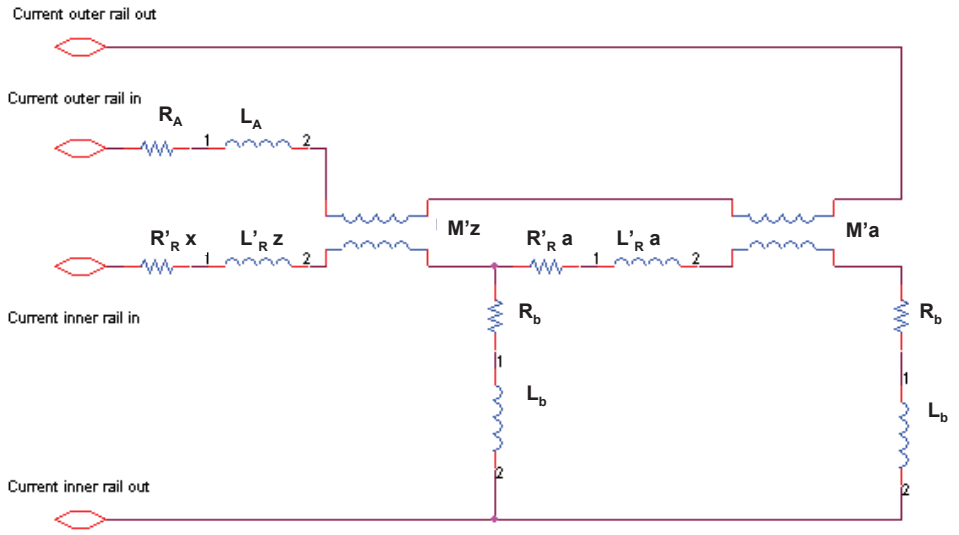

Fig. 2.7: General model for an augmented railgun with a projectile with two current brushes

2.2.3.2. Resistance Model

The resistance depends on many parameters. The temperature influences the resistivity and the resistance is time-dependent because of the variation of the skin depth due to the shape of the current and the projectile velocity. It is possible to define three parts of the rails based on the current diffusion (Fig. 2.8). For the first part behind the starting position of the projectile only the skin effect is taken into account (cf. eq. 2.3.). For the second part between the starting position and the actual position of the projectile and for the third part between the current brushes the movement of the projectile must be considered and the velocity skin effect must be modeled (cf. eq. 2.5).

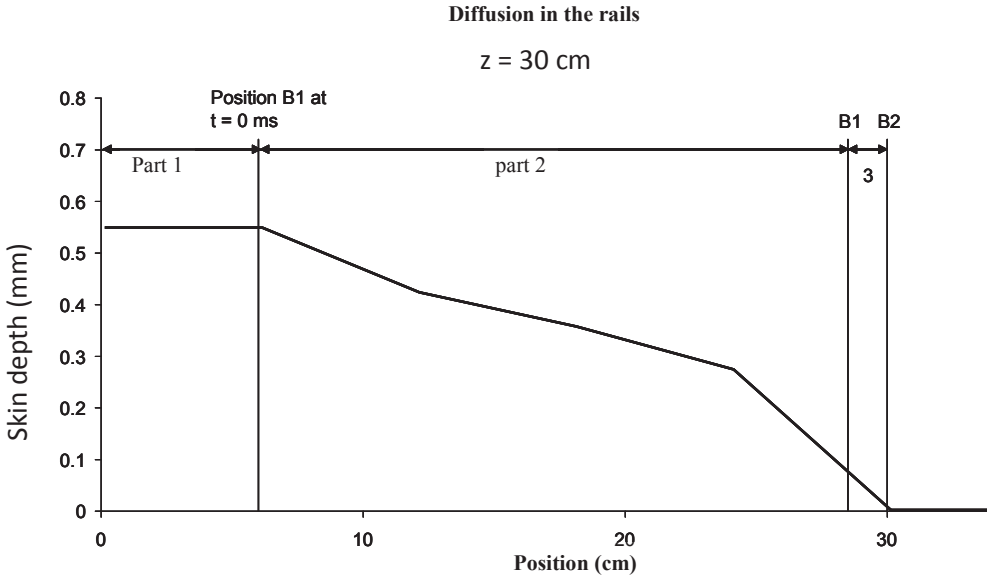

Fig 2.8: Skin depth evolution in function of projectile position

For the resistance of the rails we use the model described in [WEY 97]. For the outer rails, the normal skin effect resistance *R'(t)* is described by:

$$R'(t) = R_0'.\left[\sqrt{\frac{t_0}{t}} + erf\left(\sqrt{\frac{t_0}{t}}\right)\right] \tag{2.3}$$

For R_0' the value for the resistance per meter for a fully diffused current for copper cadmium is used; this is the material used for the rails. But for the inner rails, the velocity skin effect has to be taken into account. While the projectile moves along the rails during the shot, it "sees" always a new part of the rails. The diffusion in the rails starts with the passing of the projectile. The resistance dR of a rail with length dz at position z can be written as

$$dR = R'(t-\tau).v(\tau).d\tau. \tag{2.4}$$

with $R'(t)$ expressed by eq. 2.3. Integration leads to the convolution between R' and v:

$$R(t) = \int_0^t R'(t-\tau).v(\tau)d\tau \tag{2.5}$$

and the Laplace transform is then $R(s) = R'(s).v(s)$. We can then obtain $R(t)$ by modeling $R'(s)$ as a transfer function and by transforming $v(t)$. The Laplace transform of eq. 2.3 yields to:

$$R'(s) = R'_0.\left[\sqrt{\frac{\pi.s}{t_0} + \frac{1}{s}}.\exp\left(-2.\sqrt{t_0.s}\right)\right] \tag{2.6}$$

So we can simulate the resistance of the part of the inner rails behind the brush on the breech side and the starting position of the projectile by using a Laplace filter. Fig. 2.9 illustrates an example of a variation of the resistance vs. time. The curve depends on the position and the velocity profile of the projectile.

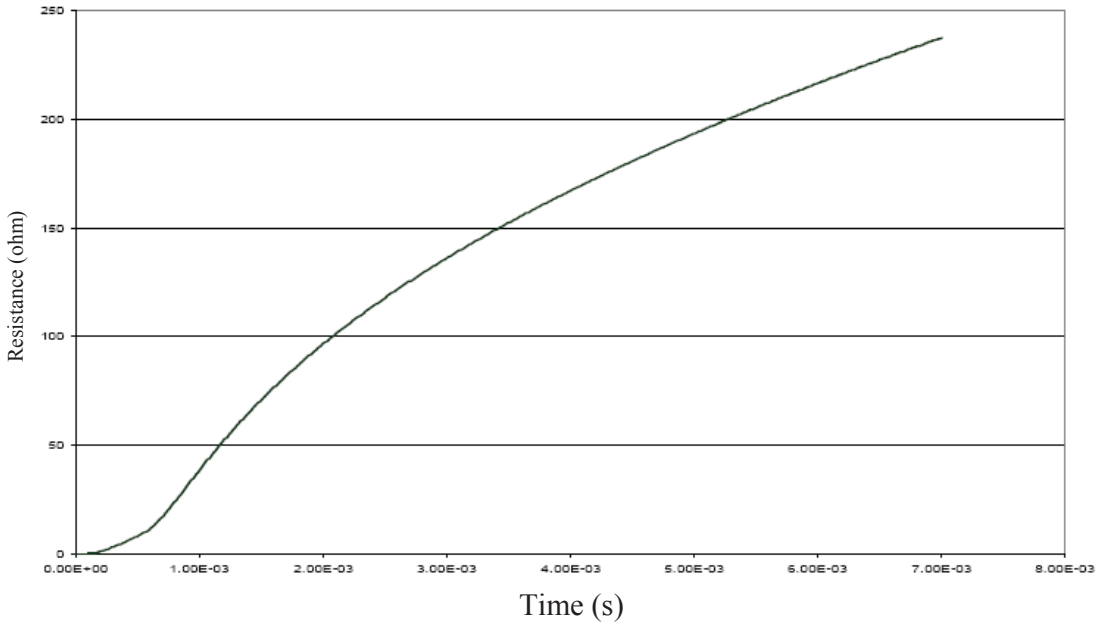

Fig.2.9: Resistance variation vs. time (example)

2.2.3.3. Inductance Model

The inductance gradients *L'* and *M'* of the rails are calculated based on the magnetic energy E_m of the railgun as described in [TAY93],[FIK84][FUL91],[SCH93] and [GAL04]. For an augmented railgun the magnetic energy E_m is equal to:

$$E_m = \frac{1}{2} L_R I_R^2 + M I_R I_A + \frac{1}{2} L_A I_A^2 \tag{2.7}$$

The magnetic energy is calculated with the finite element code ANSYS. A 2-dimensional harmonic analysis was used and the frequency is set again to 100 kHz to simulate the skin effect. E_m depends only on the geometry of the rails for given amplitude of the current. The calculations were made for the non-augmented and the augmented railgun. For the non-augmented railgun one calculation was made for I_R = 100 kA. For the augmented railgun the amplitude of the inner current was fixed at 100 kA, the amplitude of the current in the outer rails was set to 100 kA, 200 kA and 300 kA. ANSYS calculates the RMS value of the energy. The energy in the rails is negligible compared to the energy in the air. The results for the magnetic energy per meter E_m' are listed in Table 2.2.

Table 2.2: Magnetic energy per meter E_m'

	I_R (kA)	I_A (kA)	E_m' (J/m)
Non-augmented railgun	100	-	1128.8
Augmented railgun	100	100	4253.6
	100	200	10742.4
	100	300	20558.4

The inductance gradients can then be calculated with eq. 2.7. The results are listed in Table 2.3 and compared with results of the calculation with another software MEGA by J. Gallant [GAL04]. The calculations in MEGA were carried out for a 3D model that presents a 1 mm thick slice of the rails. The values calculated with ANSYS are slightly lower than those calculated with MEGA. The very small deviation is probably in relation with a 2D modeling for ANSYS and 3D for MEGA but with a thin slice.

Table 2.3: Values for L'_R, M' and L'_A

		L'_R (µH/m)	M' (µH/m)	L'_A (µH/m)
Non-augmented railgun	ANSYS	0.452	-	-
	MEGA	0.453	-	-
Augmented railgun	ANSYS	0.437	0.300	0.665
	MEGA	0.439	0.302	0.668

As discussed in Chapter 1, experimental results show that $F = \frac{1}{2} L'_R I_R^2 + M I_R I_A$ overestimates the electromagnetic force on the armature [KEE93],[MAR84].

In the case of an augmented railgun, as explained by J. Gallant in [GAL04], constant values are not adequate for the whole duration of a shot due to variation of the skin depth. He proposed on the

LARA railgun a variation of these parameters in relation with the frequency of the AC current imposed in the FEM simulation. These values are inserted in the model through sources depending on time. The same approach was used for the determination of L_R' and M' used in the kinematic model discussed in § 2.2.5 and is explained in more detail in § 3.4.1.

Table 2.4: Values for L'$_R$, M' for different frequencies

Simulation method	**Conventional Railgun**	
	L_R' (μH/m)	***M' (μH/m)***
Rails, 100 kHz	0.452	-
Rails and armature, 1 kHz	0.416	-
Rails and armature, constant current	0.397	-
	Augmented Railgun	
Rails, 100 kHz	0.437	0.300
Rails and armature, 1 kHz	0.440	0.270
Rails and armature at low frequency (10Hz)	0.414	0.167

Table 2.5: Variation of the coefficients L'$_R$ and M' for LARA

Time	**Coefficients**	
	L'_R (μH/m)	***M' (μH/m)***
$t \leq 0.2$ ms	0.440	0.270
0.2 ms < t < 1.5 ms	linear decrease from 0.440 to 0.414	linear decrease from 0.270 to 0.167
$t \geq 1.5$ ms	0.414	0.167

2.2.4. Projectile

2.2.4.1. General Model

The general model for a projectile with two current brushes is represented in Fig. 2.7. The resistance R_b of the current brushes is time-dependent and temperature dependent through the heating of the brushes. The self inductance L_b of the brushes is considered constant.

For a projectile with one current brush we can then simulate the total resistance of the inner rails in two parts. The first part is the resistance of the inner rails behind the starting position. The second part, between the starting position and the brush towards the breech, is modeled by using a Laplace filter. For a projectile with two current brushes the resistance of the inner rails is simulated in three parts. The third part is the resistance of the inner rails between the brushes of the projectile. Here the discussion of the current distribution between the two brushes starts. If there is a current in the brush

towards the muzzle, the diffusion in the rails starts after the passing of this current brush. Otherwise the diffusion starts after the passing of the current brush towards the breech.

The resistance of the second part between the current brushes is delayed for a passing time equal to *a/v(t)* with *v(t)* the instantaneous velocity of the projectile and the distance *a* between the current brushes. The velocity is considered constant between the passing of the two brushes. The calculated passing time and eq. 2.6 allow to estimate the resistance between the current brushes for each velocity, with a correction at the beginning of each shot when v = 0 m/s. The resistance is calculated in function of *v* and inserted as a table in PSpice. Fig. 2.10 represents the PSpice model of a current brush which combines the resistance, inductance and thermal models discussed in the next paragraphs.

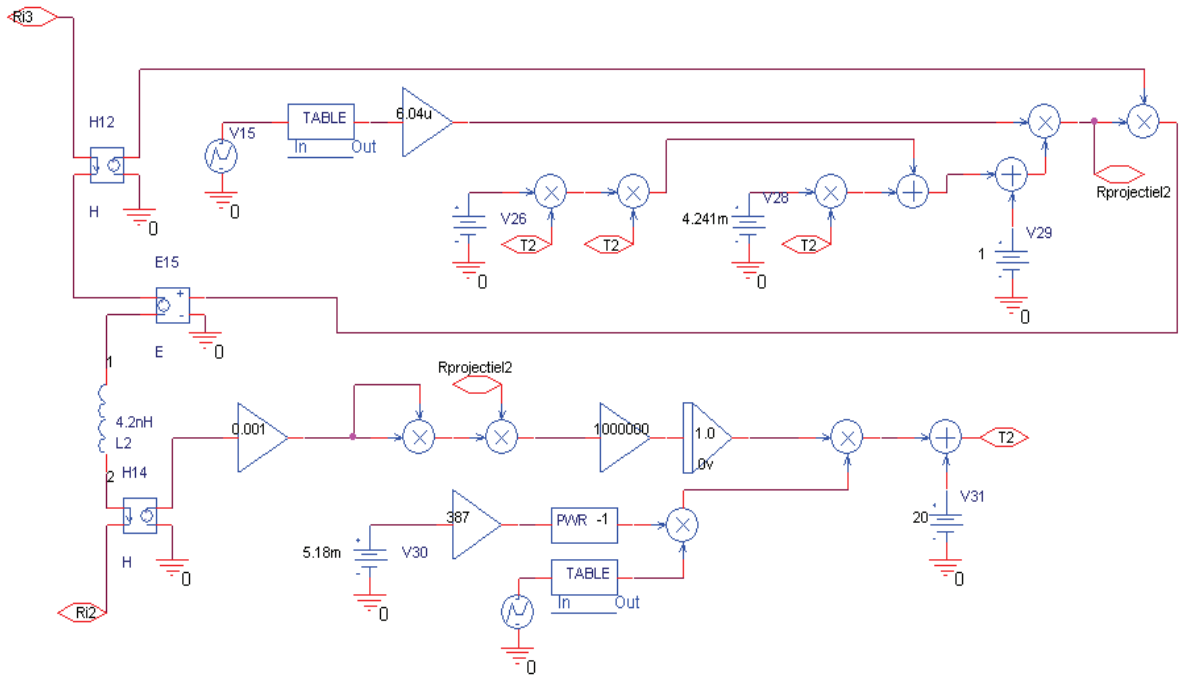

Fig.2.10: PSpice model for a current brush

2.2.4.2. Resistance Model

For the resistance of the current brushes R_b an empirical expression was used as defined by [WEY97]:

$$R_b(t) = R_{b,0}\frac{\sqrt{\frac{t_0}{t}} + \left(\frac{t}{t_0}\right)^{16}}{1 + \left(\frac{t}{t_0}\right)^{16}} \tag{2.8}$$

with t_0 = 1 ms and $R_{b,0}$ a temperature-dependent value.

2.2.4.3. Inductance Model

For the self inductance L_b of the brushes we use eq. 2.9 which is an approximation based on the assumption that the current brush is a cylinder with length l and radius r [PET95]:

$$L_b = \frac{\mu_0 l}{2\pi}\left\{\ln\left(\frac{2l}{r}\right) - \frac{3}{4}\right\} \tag{2.9}$$

with a radius r = 3.5 mm and a length l of 15 mm, this results in L_b = 4.2 nH. The inductance L_b is the contribution of the current brushes to the total inductance of the loop formed by the rails, the current brushes and the feeding bridge at the breech.

2.2.4.4. Temperature Model

The heating of the current brushes is simulated. The resistivity ρ is dependent on the temperature. The values for pure copper are used [SCH98]:

$$\rho(T) = \rho_0(0.453\exp(-6T^2) + 4.241\exp(-3T) + 1) \tag{2.10}$$

with ρ_0 = 15.5 nΩ and T expressed in °C. This expression is used to calculate $R_{b,0}$ in eq. (2.8). The temperature is calculated through the joule heating. Eq. (2.8) takes into account the diffusion in the brushes. The current flows only through a part of the cross-section of the brush. This surface can be calculated with eq. (2.8) and multiplied with the length of the current brush. This results in a volume in which the current flows. This volume is used to calculate the temperature. We make the hypothesis that the energy of the Joule heating is dissipated in this volume and we calculate a homogeneous temperature for this volume. The mass density of the current brush is 6720 kg/m^3 and the specific heat is 387 J/(kg.K).

2.2.5. Kinematic Model

The kinematic model is based on the classical equation

$$\mathrm{m}\frac{\mathrm{d}^2\mathrm{z}}{\mathrm{dt}^2} = \sum \mathrm{Forces} = \mathrm{F}_{\mathrm{proj}} \tag{2.11}$$

but about all the terms are depending on time including the mass of the projectile. We will examine successively the different terms.

2.2.5.1. The Forces on the Projectile

The total force on the projectile F_{proj} is given by

$$F_{proj} = F_{EM} - F_f \tag{2.12}$$

where F_{EM} is the electromagnetic force on the projectile and F_f the mechanical friction force, on the assumption that all other forces are negligible. This is particularly the case for eddy current losses which can be expressed as a resistant force. This force is difficult to estimate. A correction is made by using the time-dependent values for the inductance gradients.

The mechanical friction force is a function of the normal force exerted by the brush on the rails F_N and the friction coefficient μ_{fr}:

$$F_f = \mu_{fr} F_N \tag{2.13}$$

The normal force has two components, mechanical ($F_{N,mech}$) and electromagnetic ($F_{N,EM}$):

$$F_N = F_{N,mech} + F_{N,EM} \tag{2.14}$$

The normal mechanical component is due to the flexion of the brush filaments in contact with the rails. This flexion intervenes also for the normal component of the electromagnetic force which is not oriented in the shot axis as can be seen on Fig. 2.11 [SCH03]. The electromagnetic normal force ($F_{N,EM}$) is proportional to the electromagnetic force (F_{EM}):

$$F_{N,EM} = \gamma F_{EM} \tag{2.15}$$

γ depends on the geometry of the current bridge. For the brushes used in the experiments the value of $\gamma = 0.44$ [GAL04].
The axial and normal components of the electromagnetic force are depicted in Fig. 2.11 [SCH03].

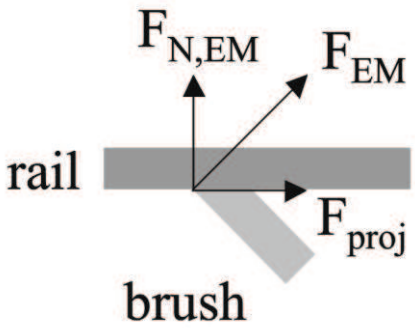

Fig. 2.11: The axial and normal component of the electromagnetic force at the brush-rail interface

By combination of eq. (2.11) to (2.14) we find an expression for the force on the projectile.

$$F_{proj} = F_{EM} - F_f = (1 - \gamma \mu_{fr}) F_{EM} - \mu_{fr} F_{N,mech} \tag{2.16}$$

2.2.5.2. The Electromagnetic Force

The expression of the electromagnetic force as discussed in Chapter 1, is

$$F_{EM} = \frac{1}{2} L'_R I_R^2 + M' I_R I_A \tag{2.17}$$

where I_R is the current in the inner circuit, I_A the current in the outer circuit, L_R' the inductance gradient and M' the mutual inductance gradient. Their values are given in § 2.2.3.3.

2.2.5.3. The Friction Force

The friction force is highly dependent on the dynamic friction coefficient μ_{fr} which varies in a large proportion with the velocity. The friction coefficient μ_{fr} has not been determined yet for sliding brushes at the high velocities that are typical for railguns. Therefore, assumptions will have to be made. A typical value of the sliding friction coefficient $\mu_{fr} = 0.3$ for sliding Cu-brushes on flat Cu-surfaces, but only for low velocities, normal forces and current densities. As soon as a projectile gains velocity, the friction mechanism changes and μ_{fr} decreases sharply [SCH03]. Values of μ_{fr} at high velocities are not available in the literature, but are certainly very low and are estimated at 0.1.

Taking these observations into account, we use an exponential function for μ_{fr} shown in Fig. 2.12 and expressed by [GAL04]:

$$\mu_{fr}(v) = 0.1 + 0.2 \exp\left(-\frac{v}{100}\right) \tag{2.18}$$

This function provides a good agreement between the measured and the simulated kinematics of the projectiles, but experimental work will be necessary to obtain more information on the friction coefficient at high velocities.

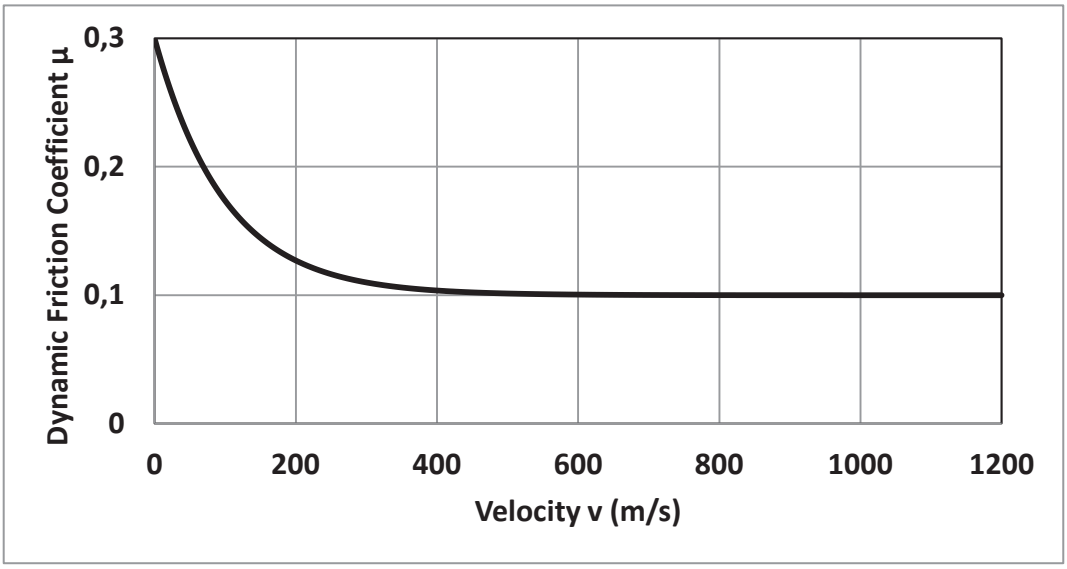

Fig. 2.12: The dynamic friction coefficient as a function of the velocity

To estimate the friction force F_f at rest, the normal mechanical force $F_{N,mech}$ has been obtained by use of a force measuring probe. This Kistler probe was used to measure the force required to initiate the movement of the projectile. The mean value for $F_{N,mech} = 100$ N per brush. This value will be used in the model.

2.2.5.4. Case of a Multiple Brush Projectile

It is easy to demonstrate that the expression of the electromagnetic force is not modified in case of a multiple brush system. The friction force must be adapted. It is increased proportionality to the number of brushes.

2.2.5.5. Mass Loss

To ameliorate the calculation of the position and the velocity of the projectile a correction for the mass loss is made after the experiment. The mass of the projectile is measured before and after the shot and an exponential decay between these values is assumed. This mass loss is expressed by [GAL04]:

$$\Delta m(t) = \left(m_{pr,0} - m_{pr,b}\right)\left(\frac{\exp\left(t / t_b\right) - 1}{e - 1}\right) \tag{2.19}$$

with $\Delta m(t)$: mass loss vs. time
$m_{pr,0}$: projectile mass before the shot
$m_{pr,b}$: projectile mass after the shot
t_b : time necessary for the projectile to go out of the muzzle

The mass during the acceleration is given by:

$$m_{pr}(t) = m_{pr,0} - \Delta m(t) \tag{2.20}$$

2.2.5.6. Velocity, Position and Global Scheme

The kinematic model used in PSpice for the mechanical behavior of the projectile is based on the force on the projectile. The acceleration of the projectile γ_{pr} is equal to:

$$\gamma_{pr}(t) = \frac{F_{proj}(t)}{m_{pr}(t)} \tag{2.21}$$

and the speed at position z and time t is given by :

$$v(t) - v(0) = \int_0^t \gamma_{pr}(\tau)\, d\tau \tag{2.22}$$

The position z can be obtained using:

$$z(t) - z(0) = \int_0^t v(\tau) d\tau \tag{2.23}$$

2.3. Comparison with Previous Results

2.3.1. Voltage and Current

For the experimental validation of the model we compared the results of the simulations with the results of the experimental study on LARA for a one brush armature. The comparison was made for LARA and for projectiles with masses of 16.0-17.7 g.

An example of the currents in the inner and outer circuit calculated with PSpice compared with the experimental results for a projectile of 17.7 g with one bank for the inner and two for the outer circuit is represented in Fig. 2.13. The current curves calculated with PSpice show a faster decrease of the current suggesting an underestimation of the inductances for the PSpice model. The current drop

in the curve for the experimental measured inner current corresponds with the moment t_b when the projectile leaves the railgun. In the PSpice simulations the inner circuit is not opened at t_b to avoid instabilities.

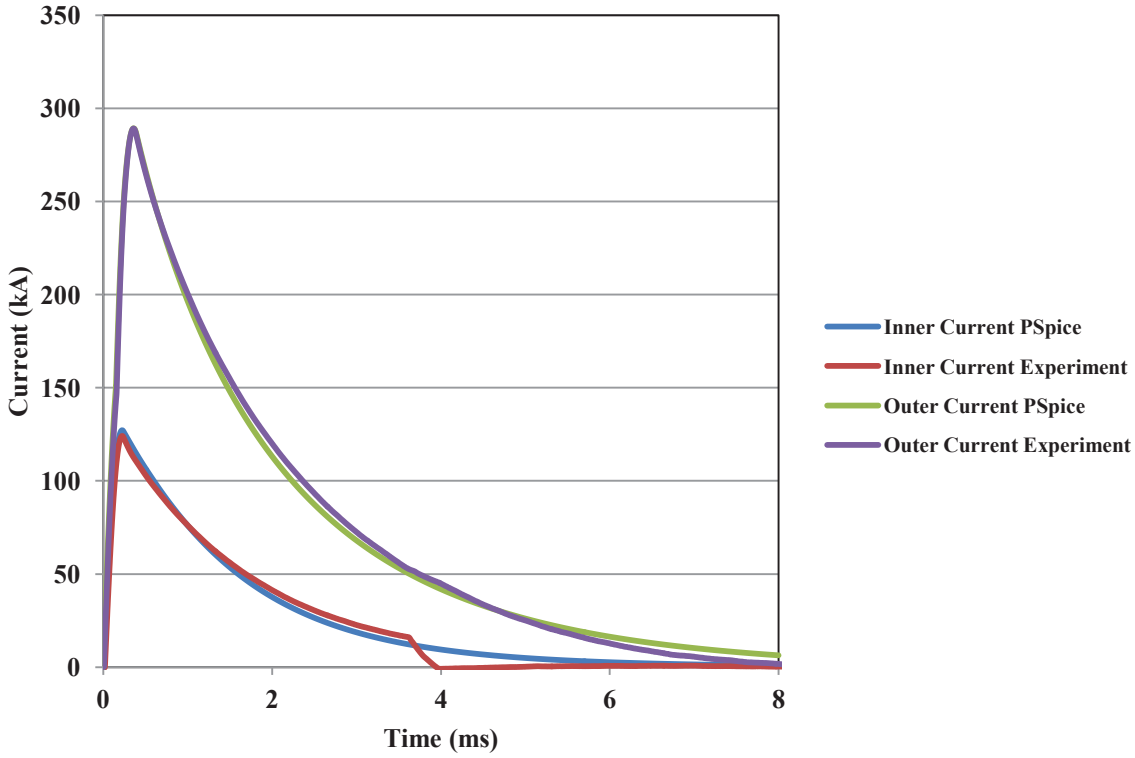

Fig. 2.13: Current curves from an experiment and calculated with PSpice for a projectile of 17.7 g with one bank for the inner and two for the outer circuit. Corresponding position and velocity are shown in Fig. 2.15.

2.3.2. Position and Velocity

If it is difficult to compare the simulated position of the projectile with experiments, it is easier to compare the speed at the muzzle. It integrates all the parameters, currents, electromagnetic force and friction. 14 shots are at our disposal. Table 2.6 gives experimental and simulated speeds.

Table 2.6: Experimental and calculated muzzle velocities for different shots with LARA and the initial masses m_0 of the projectile. The experimental data is obtained from the experiments described in [GAL04]

Shot n°	m_0 (g)	v(exp) (m/s)	v(PSp) (m/s)
11	17.4	470	494
12	17.5	520	551
13	17.4	744	745
14	17.4	767	785
15	17.5	548	555
24	17.5	560	517
25	17.5	646	579

Shot n°	m_0 (g)	v(exp) (m/s)	v(PSp) (m/s)
26	17.7	520	515
27	17.6	557	528
30	17.4	534	524
31	17.6	593	557
49	16.0	575	561
51	16.0	919	850
54	16.0	809	701

The difference between the muzzle velocities calculated with PSpice *v(PSp)* and obtained in the experiments *v(exp)* are within 15% but the mean error value is about equal to 2% with a standard deviation of 6% (Fig. 2.14). This is acceptable when we take the measurement uncertainty into account as well as the errors on the knowledge of the parameters of the model. Also the initial circumstances, like the condition of the rails and the tolerance on the caliber, differ for each shot.

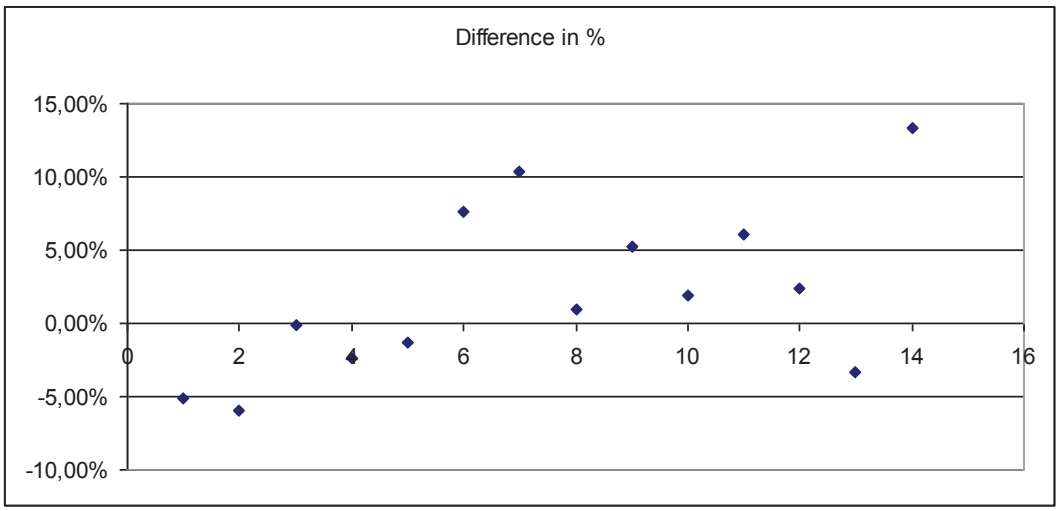

Fig. 2.14: Relative error on muzzle velocity for different shots.

2.3.3. Conclusions on the Validity of the PSpice Model

The PSpice model predicts correctly the behavior of the conventional and the augmented railgun. The currents are underestimated for the part where they decrease. Some assumptions have been made to obtain the different parameters like the self and mutual inductance gradients, the resistance with taking into account the skin effect, the contact resistance, … The parameters of the kinematic model also depend on different phenomena. In spite of all these uncertainties the speed at the muzzle is obtained with a satisfying accuracy.

Fig. 2.15 shows an example of the position and the velocity of a projectile calculated with PSpice and the experimental determined muzzle velocity for a projectile of 17.7 g with one bank for the inner and two for the outer circuit.

In the next paragraph we will examine the current distribution between the different brushes in a multiple brush projectile

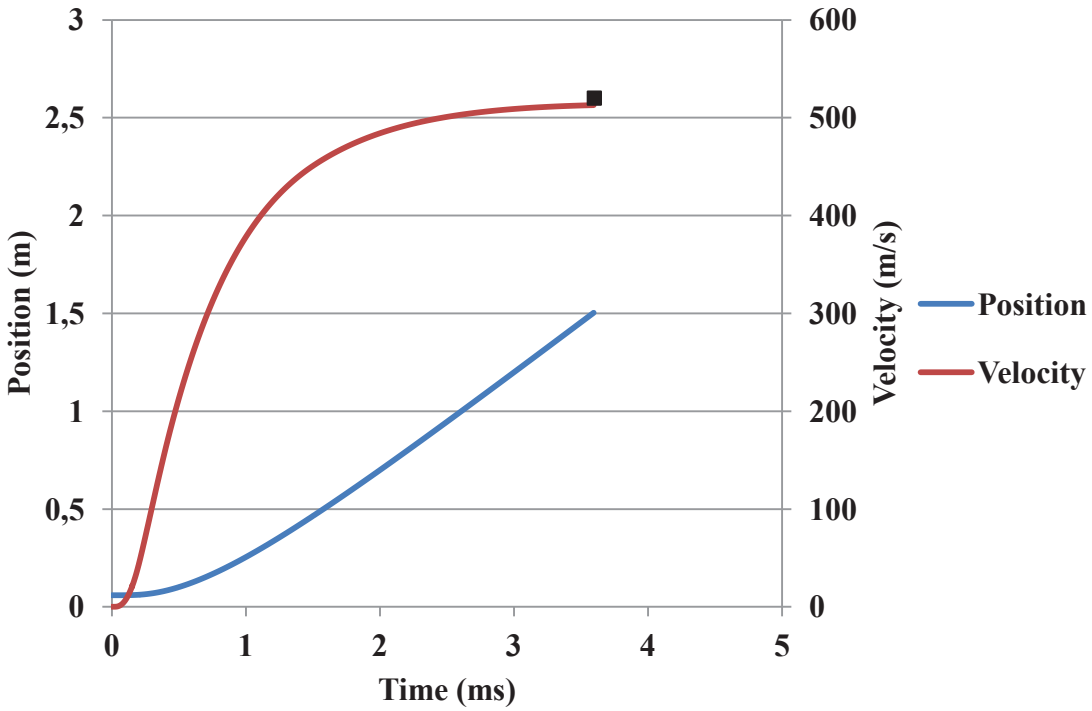

Fig.2.15: Experimentally determined muzzle velocity and the position and velocity calculated with PSpice for a projectile of 17.7 g with one bank for the inner and two for the outer circuit for LARA (1.5 m)

2.4. Current Distribution between the Brushes and Overheating

The model will be used to obtain the evolution of the current in the brushes during a shot. We will use as example the case where two capacitor banks are used for the inner circuit and three for the outer one. The two currents I_R and I_A are visualized in Fig. 2.16.

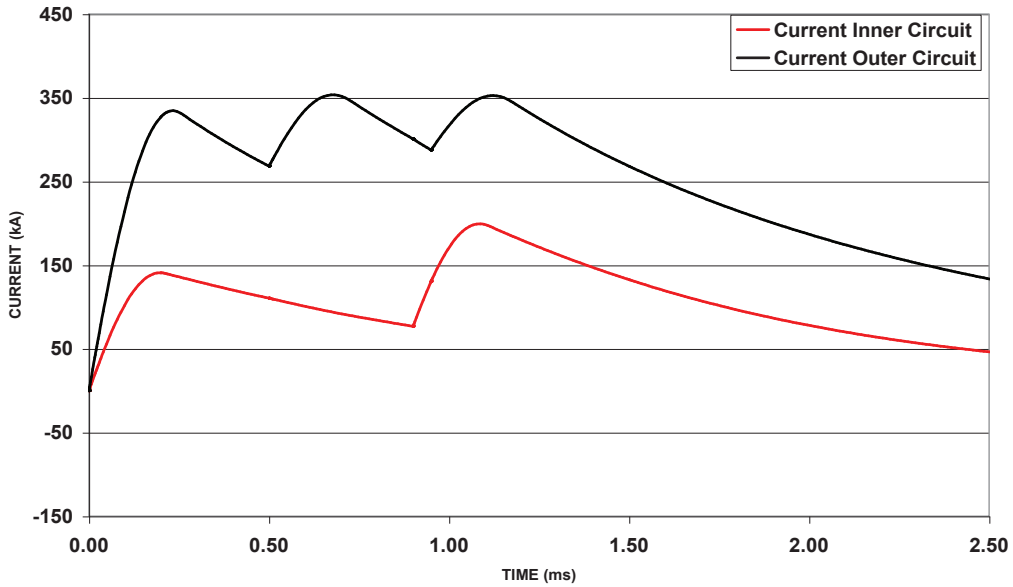

Fig. 2.16: Current simulated with 2 capacitor banks for the inner circuit and 3 for the outer circuit.

Fig. 2.17 gives the current evolution in the case of two brushes. It can be observed that for a long time, the current in brush 2 (muzzle side) is negative and the current in brush 1 (breech side) is higher

than the current which is furnished by the inner feeding. This is due to the current induced by the augmenting field of the outer circuit in the mesh constituted by the two brushes and the included part of the rails. Although the current in brush 1 is higher than the total inner current at the beginning of the shot, the mean temperature at the end of the shot in brush 1 is lower than the mean temperature of a projectile with one brush.

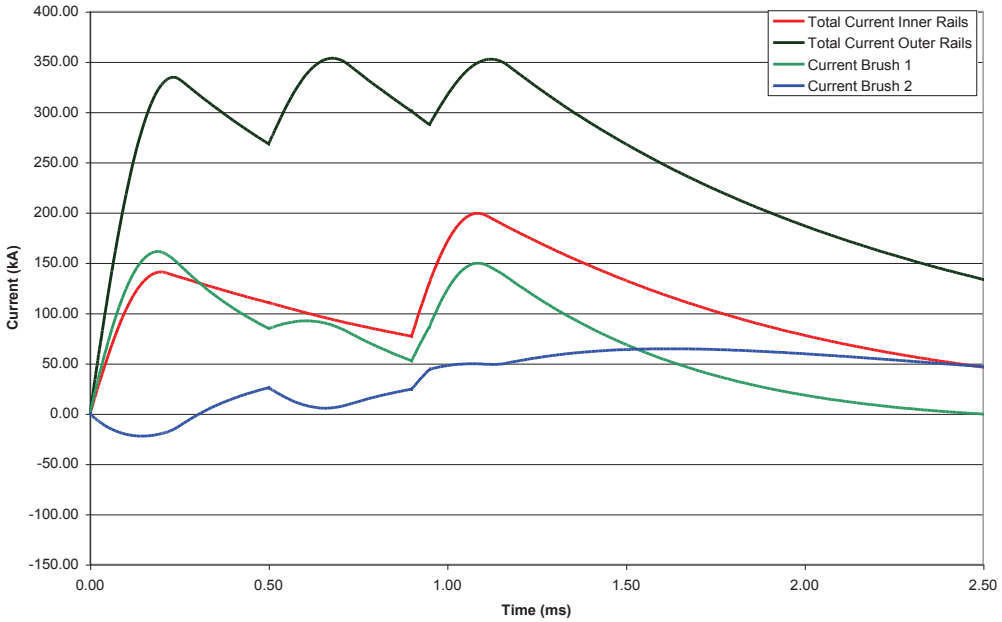

Fig. 2.17: Current distribution for a projectile with two brushes

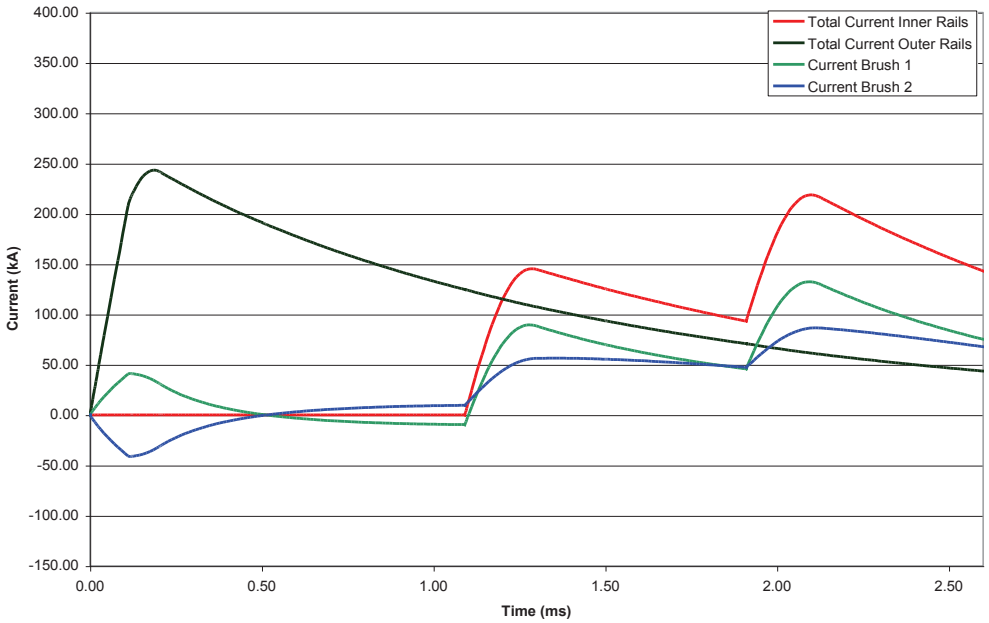

Fig. 2.18: Current distribution in the brushes for a delayed inner rail feeding

We may observe the same phenomenon on Fig. 2.18 where the capacitor bank of the outer circuit is discharged at t = 0 ms and the inner current is delayed by 1.1 ms. A current can be observed in the current brushes before the discharging of the capacitor banks in the inner circuit. The sum of the

current in the two brushes is zero, which confirms that it is a loop current. In this test, there is only one capacitor bank simulated for the outer circuit.

Fig. 2.19 and 2.20 show the current distributions for projectiles with respectively three and four brushes. Adding additional brushes also means adding additional loops and loop currents. For the projectiles with three and four brushes the currents in the brush on the muzzle side, respectively I_3 and I_4, are negative during a long time due to the mesh currents induced by the augmenting field of the outer circuit. This results in a higher current I_1 in the brush on the breech side at the beginning of the shot. For the projectile with four brushes, the current I_1 is higher than the total current in the inner circuit until the discharging of the second capacitor bank in the inner circuit. The current in brush 3 is also negative at the beginning of the shot and stays low for the whole duration of the shot. We can conclude that, due to the current loops, adding current brushes in an augmented railgun does not automatically lead to a better current distribution between the brushes.

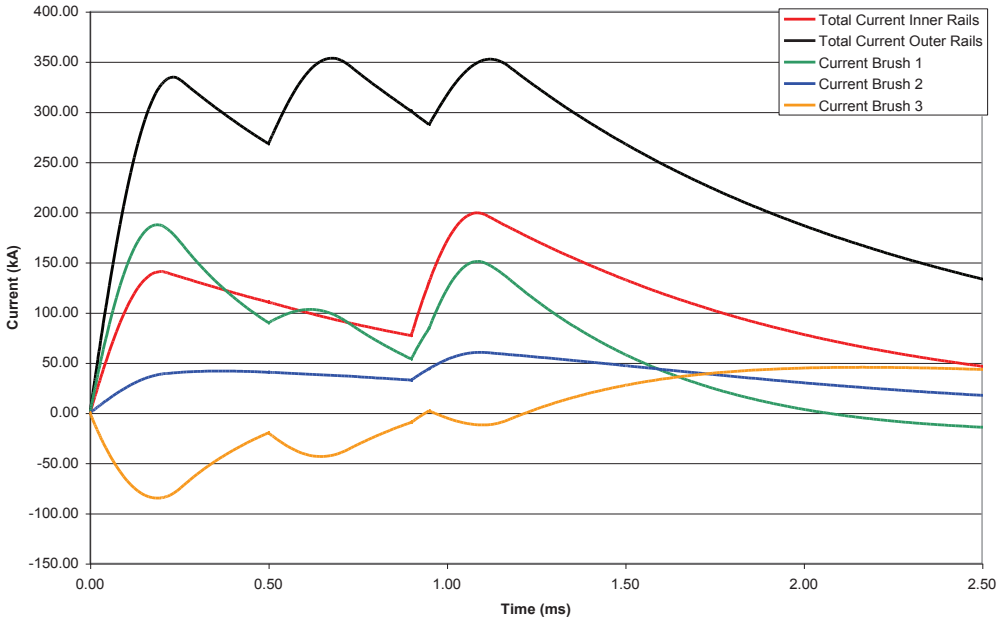

Fig. 2.19: Current distribution in the case of three brushes

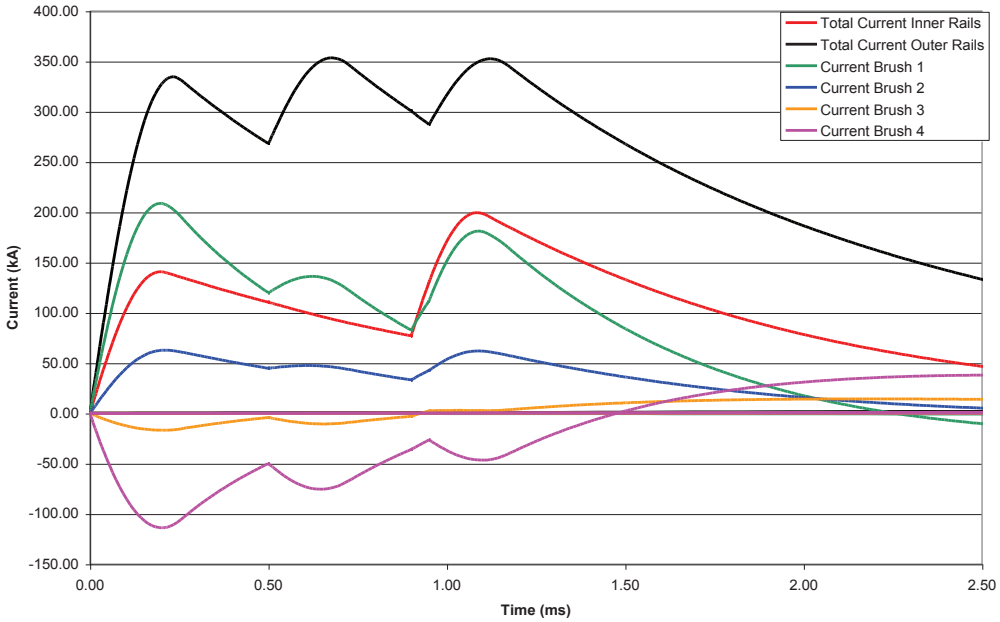

Fig. 2.20: Current distribution in the case of four brushes

Knowing the currents, it is easy to calculate the Joule losses and the reached temperature in the brushes of the projectile. Table 2.7 gives the temperature of the brushes obtained with PSpice. It is a mean value and not a spot temperature. The temperature distribution and maximum temperature in the current brushes will be obtained in next chapter by a local modeling using the finite-element code ANSYS. It can be observed that the temperature reached by brush 1 on the breech side is always high in comparison with the others. If we compare the temperature in the brush on the breech side for the different projectiles, we can conclude that increasing the number of brushes is not always an advantage due to the additional loop currents. But the results are better than for a projectile with one current brush.

Table 2.7: Mean temperature in the brushes

T_h (°C)	1brush	2 brushes	3 brushes	4 brushes
Brush 1	208	139	173	198
Brush 2		38	36	47
Brush 3			41	22
Brush 4				56

2.5. Conclusion

PSpice turns out to be an efficient and fast medium to study and evaluate the global behavior of an electromagnetic railgun, especially for the determination of the global currents in the rails and the current distribution between the brushes. The principal difficulties are the determination of the different parameters of the electrical, thermal and kinematic model. The modeling of the skin effect and velocity skin effect requires special attention. As well the shape of the current pulse, as the velocity of the projectile for the velocity skin effect have to be considered. The determination of the normal mechanical force and the dynamic friction coefficient for the friction force of the kinematic model are also not straightforward. The determination of the coefficients L'_R and M' for the

electromagnetic force equation based on simulations with the FEM ANSYS will be discussed in the next chapter. The thermal model for the projectile allows only the determination of the mean temperature of each current brush. PSpice provides only global results. For the determination of the local current and temperature distribution we will need another means like the FEM ANSYS. Both methods are complementary.

Chapter 3

Local Modeling of the Railgun

3.1. Introduction

The PSpice code described in Chapter 2 represents a global model of the railgun. This program calculates the total current and the electromagnetic force on the projectile. It also allows an estimation of the position and the velocity of the projectile and of the temperature of the current brushes. To study the distribution of the current in the rails and in the brushes or the temperature distribution in the brushes, we need a local model of the railgun. Therefore we use the finite element code ANSYS.

The simulations in ANSYS are a combination of a thermal and an electromagnetic analysis. It is a coupled-field analysis with a two-way coupling. The Joule heat loads calculated in the EM analysis are used in the thermal analysis to calculate the temperature distribution. The temperature distribution is then used to determine the temperature dependent resistivity of the projectile in the EM analysis (Fig. 3.1). A fixed timestep is used and an end time is defined.

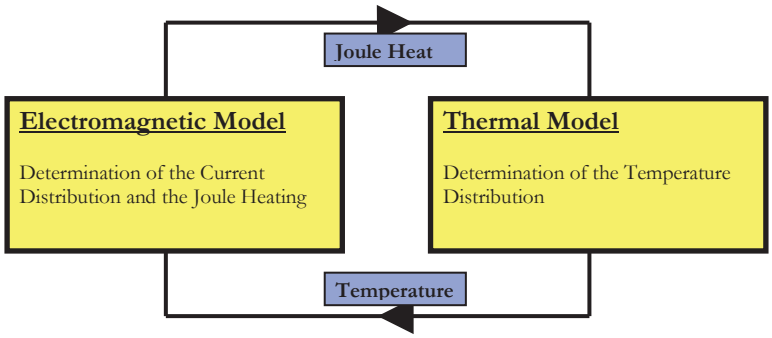

Fig. 3.1: Principle of the coupling between the electromagnetic and thermal analysis in ANSYS.

The objectives are to forecast the behavior of the railgun and the projectile. We want to determine on one side the force applied on the projectile, and on the other side the constraints applied to the railgun. The constraints are important for the mechanical design. The overheating influences on one side the efficiency of the railgun and on the other side imposes the kind of material used.

ANSYS would be an interesting tool for the design but it is not able to take into account all the parameters and all the phenomena. Its main drawback is that the position of the projectile is fixed. The movement is not considered so some effects like the velocity skin effect are neglected and it modifies notably the current distribution in the rails.

Nevertheless ANSYS brings a lot of results which may be validated by experimental ones even when, as we will see in Chapter 4 and 5, these experimental results have not a sufficient accuracy. So we will study the behavior, by a Finite Element Method of a part of the railgun using the geometrical symmetry. The results will allow estimating the global parameters necessary for the PSpice modeling, i.e. the self and mutual inductance gradients. The current distribution between and in the current brushes can be determined as well as the forces on the rails and the projectile for a given input defined by the current in both rails. The heating of the brushes can be studied based upon the temperature

distribution which allows the determination of the mean temperature for each current brush as well as the maximum temperature at the contact layer. The results will be compared with those deduced from the global model with PSpice in the same conditions. So we are able to appreciate the interest of a local model in comparison with a global model which has a lot of advantages in particular for the computing time.

3.2. Description of the Finite Element Model

3.2.1. Hypothesis

The position of the projectile is fixed in this simulation and thus the velocity skin effect is not taken into account so it is only valid at low speed.

Because a moving projectile continually sees a "fresh" part of the rails, only the temperature-dependent resistance and the heating of the projectile were modeled. With ANSYS we can determine the maximum temperature T_m in the current brush as well as the average temperature T_h.

3.2.2. Material Models

For the electromagnetic model, four different material models are defined. The air around the model is non-conductive and has a relative magnetic permeability $\mu_r = 1$. The rails, the current brushes and the contact layer are conductive. They all have a relative magnetic permeability equal to 1. For the conductivity of the rails, the constant value of 50 MS, corresponding with CuCd, is used. The resistivity of the current brushes is temperature-dependent. Here the values for pure copper in the solid phase are used. The filling ratio of the fiber current brushes of 75 % has been taken into account and the resistivity of the fiber brushes becomes:

$$\rho = (2.067e-8 + 8.765e-11T + 1.208e-14T^2)\Omega.m \tag{3.1}$$

with T expressed in °C. The model for the contact layer is discussed in paragraph 3.3.

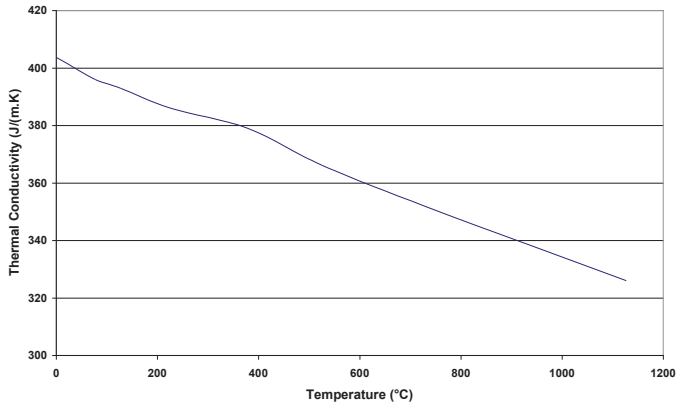

Fig. 3.2: Temperature-dependent thermal conductivity *k* of pure copper in the solid phase

The thermal analysis calculates the temperature distribution in the current brushes and in the rails. The air is not simulated in this analysis and again only a quarter of the model is simulated. The specific heat used for the rails and the current brushes is 387 $J.kg^{-1}.K^{-1}$. The density is 8960 $kg.m^{-3}$ for the rails and 6720 $kg.m^{-3}$ for the current brush with a filling ratio of 75%. The temperature-dependent thermal conductivity K_{Cu} of pure copper is used for the rails (Fig. 3.2) [SCH98]. The thermal conductivity in a fiber current brush is anisotropic because the conductivity is much better in the

direction of the fibers and is low on the surface due to bad contacts and a possible oxidation. A sensitivity analysis for the thermal conductivity was carried out and is discussed in § 3.3.3.

3.2.3. Mesh and Boundary Conditions

The non-augmented and augmented railgun have both a square caliber of 15 mm x 15 mm. The distance between the inner and outer rails for the augmented railgun is 6 mm and the rails have a square cross-section of 15 mm x 15 mm. The length of the rails is 1.5 m. Only a quarter of the railgun is modeled (Fig. 3.3) for symmetry reasons. The length of the model in ANSYS is only 14 cm because the numbers of elements that can be used in a simulation is limited due to memory reasons. The electromagnetic model for the augmented railgun with two current brushes counts 122962 elements and 37379 nodes. The center of the brush towards the breech is simulated at 8 cm from the surface were the current is injected and thus the four caliber rule is respected. This empirical rule states that 99% of the driving-field "seen by the armature is produced by the current in just the four calibers of rail lengths behind the rear surface of the armature [MAR04]. The distance between the centers of the brushes is 15 mm. The radius *r* of the current brushes is 3.5 mm.

For the electromagnetic model, a cylinder of air with a radius of 14 cm is simulated around the rails and the current brushes. The transversal and longitudinal cross-section plane, the outer surface of the cylinder of air and the two planes perpendicular to the rails which define the beginning and end of the simulated part of the rails define the outer limits of the model. The magnetic boundary condition used for the longitudinal cross-section is flux normal, for the other outer surfaces of the model the magnetic boundary condition is flux parallel.

Because the number of elements is limited, the size of the elements is adapted for the different regions of the model. The finest mesh is used for the contact layer and the current brushes, next in line are the rails. The element size of the air elements is coarser near to the outer surface of the cylinder then around the rails and the current brushes (Fig. 3.4).

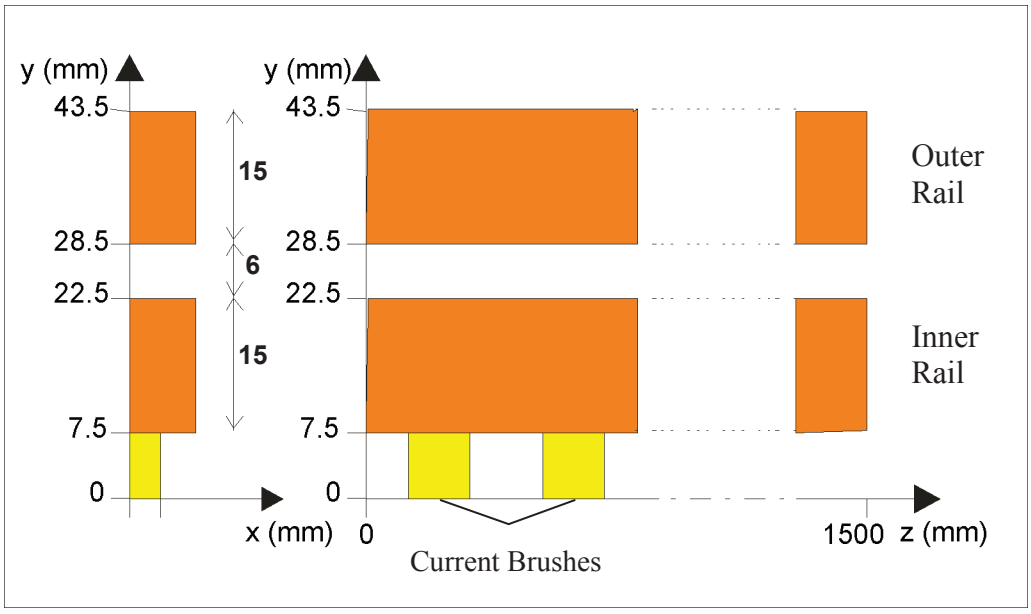

Fig. 3.3: Quarter of the geometry of the studied parallel augmented railgun. Figure on the left: transversal cross-section. Figure on the right: longitudinal cross-section

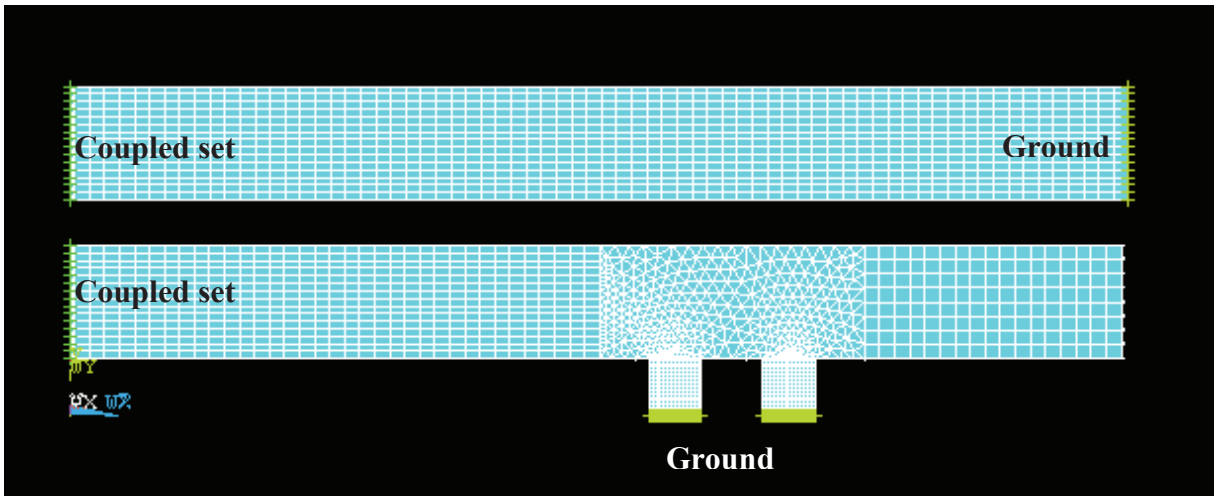

Fig. 3.4: Meshing in the symmetry plane with the coupled sets at the beginning of the rails and the ground nodes defined at the end of the outer rail and the current brushes. Only a quarter of the geometry is modeled.

3.3. Electromagnetic-Thermal Model

3.3.1. Electromagnetic Model

ANSYS provides three formulations for a 3D transient low frequency (between 10 and 1 kHz) electromagnetic analysis. The electromagnetic field analysis is based on Maxwell's equations for all three formulations. The primary unknowns, the degrees of freedom (DOF), are the magnetic and electric potentials. The other magnetic field quantities are derived from these degrees of freedom. The Magnetic Scalar Potential (MSP) and Magnetic Vector Potential (MVP) formulations are both nodal-based, while the third formulation is an edge-based formulation based on the edge-flux. According to the ANSYS release documentation, the edge-based formulation is the most accurate one, but for models that contain no iron regions they advise to use the nodal-based methods.

We use the MVP formulation because it allows to use more DOF's then the MSP method. Besides the magnetic vector DOF's in the x, y and z directions, A_X, A_Y and A_Z, it also allows to use of up to three additional DOF's: the electric potential or VOLT DOF, the current or CURR DOF and the electromotive force drop or EMF DOF.

We use the the additional VOLT DOF to apply a current to the model of the rails and the projectile. First we select the surfaces that define the cross-sections of the current brushes at the horizontal symmetry plane and the outer surface that defines the cross-section the outer rails at the end of the model. We select all the nodes attached to these surfaces and set their VOLT degree of freedom to zero. The selected nodes act as the ground nodes of the model (Fig. 3.4). Then we select the outer surface that defines the cross-section of the inner rails at the beginning of the model and select the nodes attached to this surface. We define a coupled set by coupling these nodes in the VOLT degree of freedom. In the same way we define a second coupled set for the nodes attached to the surface that defines the cross-section of the outer rails at the beginning of the model. Finally the currents I_R and I_A respectively in the inner and outer rails are applied as a force load on one node for each coupled set.

3.3.2. Thermal Model

For the thermal model only the rails and the brushes are simulated. The adiabatic boundary condition is used for all outer surfaces of the model. The initial temperature is chosen T = 20 °C. The thermal analysis in ANSYS is based on a heat balance equation based on the conservation of energy. We consider only as heating source, the Joule losses in the brushes and in the contact layer.

Only the heat transfer through thermal conduction in the brushes, the rail and the contact layer is taken into account for the simulations described in this chapter. The finite element solution calculates the nodal temperatures. These temperatures are then used to calculate other thermal quantities.

The thermal analysis with ANSYS is used to calculate the temperature distribution in the current brushes. It allows us to determine the maximum temperature and the average temperature in the current brushes and the contact layer.

3.3.3. Contact Model

To simulate the heating of the electric contact between the rails and the current brushes, a contact resistance was modeled [BAR95]. This contact resistance plays a key role in the electromagnetic analysis. Therefore the resistivity in a contact layer, (Fig. 3.5) between the current brush and the rails was adapted to obtain an additional contact resistance of 2.5 μΩ per contact [GAL04]. The simulations were made for layers with different thickness *d* as discussed in § 3.4. A thickness of 0.1 mm was chosen for the further calculations. For a thickness of d = 0.1 mm for the contact layer the resistivity ρ becomes:

$$\rho = 9.823e-7 + 8.765e-11T + 1.208e-14T^2$$

For the thermal model of the contact layer the values for the current brushes are used.

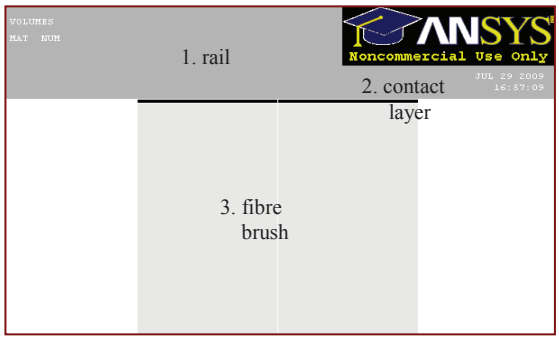

Fig. 3.5: Geometry of the contact layer

For the thermal analysis, the thermal conductivity for the brushes and the contact layer plays a main role. For the rails the values for pure copper are used. For the fiber brushes the value for the thermal conductivity $K_{fiber} = k.K_{Cu}$ is uncertain. Therefore the influence of this parameter on the maximum temperature, the heat generation and the current distribution between the brushes was studied [COF09a] . The values for *k* in the current brushes were altered between k = 0.9 - 1.0.

The first simulations are made for a shot with a non-augmented railgun. Two capacitor banks (with sparkgapdiode) with an initial charge of 7 kV are discharged with a delay of 0.21 ms. The simulated projectile has only one current brush. For these simulations the influence of the thickness of the contact layer *d* and the thermal conductivity ratio *k* on the temperature distribution was studied and the results are presented in Table 3.1. When the thickness of the contact layer is smaller, the volume in which the Joule heating due to the additional resistance resides, is smaller. This would lead to a higher temperature. But this results in a higher ΔT with the surrounding elements and then the influence of *k* plays a key role.

T_{max} represents the overall maximum temperature in the contact layer; T_{end} represents the maximum temperature found in the contact layer at the end of the shot. For the results found for k = 0.9-1.0, T_{max} is increasing with decreasing thickness of the contact layer, while T_{end} is decreasing. For the calculations for k = 0.5-0.75, the highest T_{max} is found for d = 0.2 mm.

Table 3.1: Non-augmented railgun, projectile with one current brush (Temperatures are calculated for different values for the contact layer thickness d and the thermal conductivity ratio k)

	k	90%	95%	99%	100%
d = 0.1 mm	T_{max} (°C)	670	664	663	662
	T_{end} (°C)	487	483	480	477
d = 0.2 mm	T_{max} (°C)	663	655	649	647
	T_{end} (°C)	501	496	492	491
d = 0.5 mm	T_{max} (°C)	652	643	636	634
	T_{end} (°C)	508	499	493	492

Fig. 3.6 represents the maximum nodal temperatures found in the contact layer between the rails and the current brush for each load step for k = 99%. At the beginning of the shot the highest temperatures are found for d = 0.1 mm. After 1.85 ms the highest temperatures are found for d = 0. 5 mm.

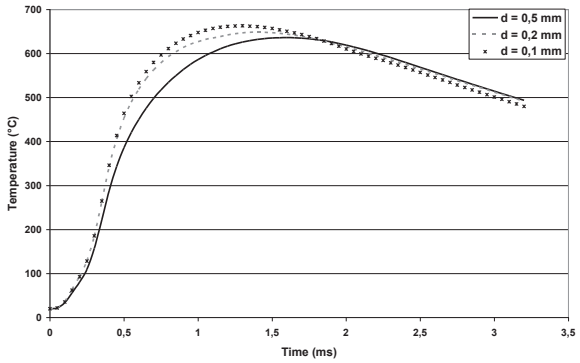

Fig. 3.6: Maximum temperature in the contact layer for each load step for different values of d and for k = 99%.

The second set of simulations is done for an augmented railgun. Two capacitor banks (with spark gap diode) with an initial charge of 7 kV are discharged with a delay of 1 ms in the inner circuit. Two capacitor banks with an initial charge of 10 kV are discharged with a delay of 0.15 ms in the augmenting circuit. The simulated projectile has two current brushes. For these simulations the influence of the thermal conductivity ratio *k* on the temperature distribution, the heat generation and the current distribution between the current brushes is studied.

The influence on the overall maximum temperature T_{max} and the maximum temperature in the contact layer at the end of the shot T_{end}, on the maximum heat generation rate ($HGen_{max}$) and on the current distribution is presented in Table 3.2. The current I_1 is the current in the brush (1) towards the breech, I_2 in the brush (2) towards the muzzle.

For the augmented and non-augmented cases the highest temperatures are found for the lowest value of the thermal conductivity. As expected a higher thermal conductivity results in a better thermal diffusion and lower maximum temperatures. The influence of the thermal conductivity on the maximum heat generation is limited. The maximum heat generation rate is about 13 times higher in brush 1 towards the breech. The influence of the thermal conductivity on the current ratio I_1/I_2 is not significant; the ratio $\lambda=I_1/I_R$ is equal to 0.87. The current flows mainly in the brush towards the breech. This explains that the heat generation, which is proportional to I^2 , and the temperature are also higher in brush 1.

Table 3.2: Augmented railgun, projectile with two current brushes. Temperatures, heat generation per mm^3 and current ratio calculated for different values for the thermal conductivity ratio *k*

	k	90%	95%	99%	100%
Brush 1	T_{max} (°C)	567	564	561	560
	T_{end} (°C)	408	404	402	401
	$HGen_{max}$ (kW/mm^3)	34.5	34.5	34.5	34.6
Brush 2	T_{max} (°C)	244	242	240	239
	T_{end} (°C)	237	234	233	232
	$HGen_{max}$ (kW/mm^3)	2.69	2.69	2.69	2.70
	λ	0.87	0.87	0.87	0.87

The simulations for the non-augmented railgun show a significant influence of the thickness of the contact layer on the maximum temperatures in the contact layer. At the end of the shot the highest temperature is found in the layer with the highest thickness. This effect is more pronounced for lower values of *k*. The overall maximum temperature is the highest in the thinnest layer for k = 0.9-1.0. The lowest influence of the thermal conductivity on T_{max} is found for d = 0.1 mm. This value is used for the further calculations.

The simulations for the augmented railgun show a significant influence of the thermal conductivity on the calculated temperatures. Differences up to 14 % are found. The influence on the heat generation rate is limited to 2%. For the current ratio I_1/I_2 no significant influence was found.

3.4. Simulations with the Finite Element Model

3.4.1. Determination of L'$_R$ and M'

The inductance gradients L'_R and M' used in the kinematic model of the PSpice model discussed in Chapter 2 are determined with the finite element code ANSYS. Here we use the method presented in [GAL04]. He found that constant values for L'_R and M' for the whole duration of a shot were inadequate to calculate the electromagnetic force on the projectile for an augmented railgun. He proposed time-dependent values for L'_R and M' varying from the values determined with an AC-analysis at 1 kHz at the beginning of the shot till the values determined with a DC-analysis at the end of the shot. The same approach was used for the determination of these coefficients for the PSpice model discussed in this thesis.

A 3D finite element model of the rails and the projectile was used for our simulations. A total of four harmonic, electromagnetic analyses were carried out, two at 1 kHz and two at 10 Hz. The amplitude of the current I_R was 100 kA for all simulations. The amplitude if the current I_A was 10 kA for the first analysis at each frequency and 100 kA for the second analysis. For each simulation the electromagnetic force on the projectile was determined. This allows us to calculate L'_R and M' based on the railgun force equation:

$$F_{EM} = \frac{1}{2} L'_R I_R^2 + M' I_R I_A \tag{3.2}$$

The results of these simulations are presented in Table 3.3. Fig. 3.7 shows the current distributions and electromagnetic forces calculated with ANSYS for the simulations with I_A = 100 kA. For the simulation at 1 kHz, the current is more concentrated at the corners of the rails and at the back of the current brush while at 10 Hz the current is well diffused into the rails and in the current brush.

Table 3.3: Values for the inductance gradients simulated with ANSYS at 10 Hz and 1 kHz

	L'_R	M'
10 Hz	0.414	0.167
1 kHz	0.440	0.270

Then an electromagnetic 3D transient analysis was carried out with the same model and the electromagnetic force was simulated. The currents used in the transient analysis are also used to calculate the electromagnetic force based on the railgun force equation and the values for the inductance gradients simulated with the harmonic analyses at 10 Hz and 1 kHz. The results are presented in Fig. 3.8. A good correspondence is found with the values for 1 kHz at the beginning of the shot until 0.2 ms. At the end of the shot the values of the transient analysis coincide with the calculations for 10 Hz. The projectile is fixed in the FEM simulations. This means that the velocity skin effect is not taken into account. This explains why the transient analysis corresponds with the harmonic analysis at 10 Hz at the end of the shot where we found a well-diffused current.

For the calculation of the electromagnetic force in PSpice time-dependent values for L'_R and M' are used. The values for the inductance gradients for 1 kHz until 0.2 ms and for 10 Hz after 1.5 ms are used because a good correspondence is found between the electromagnetic force obtained with the transient analysis and calculated based on the railgun force equation. Between 0.2 ms and 1.5 ms the values for L'_R and M' are linearly adapted between the the values for 1 kHz en 10 Hz. Fig. 3.9 shows the comparison between the electromagnetic force determined with a transient analysis in ANSYS and calculated based on the time-dependent inductance gradients for LARA. A good correspondence is found. The time-dependent values for L'_R and M' are given in Table 3.4.

The same analysis was made for the non-augmented railgun LARC. The results for the time-dependent values for the inductance gradients are listed in Table 3.5.

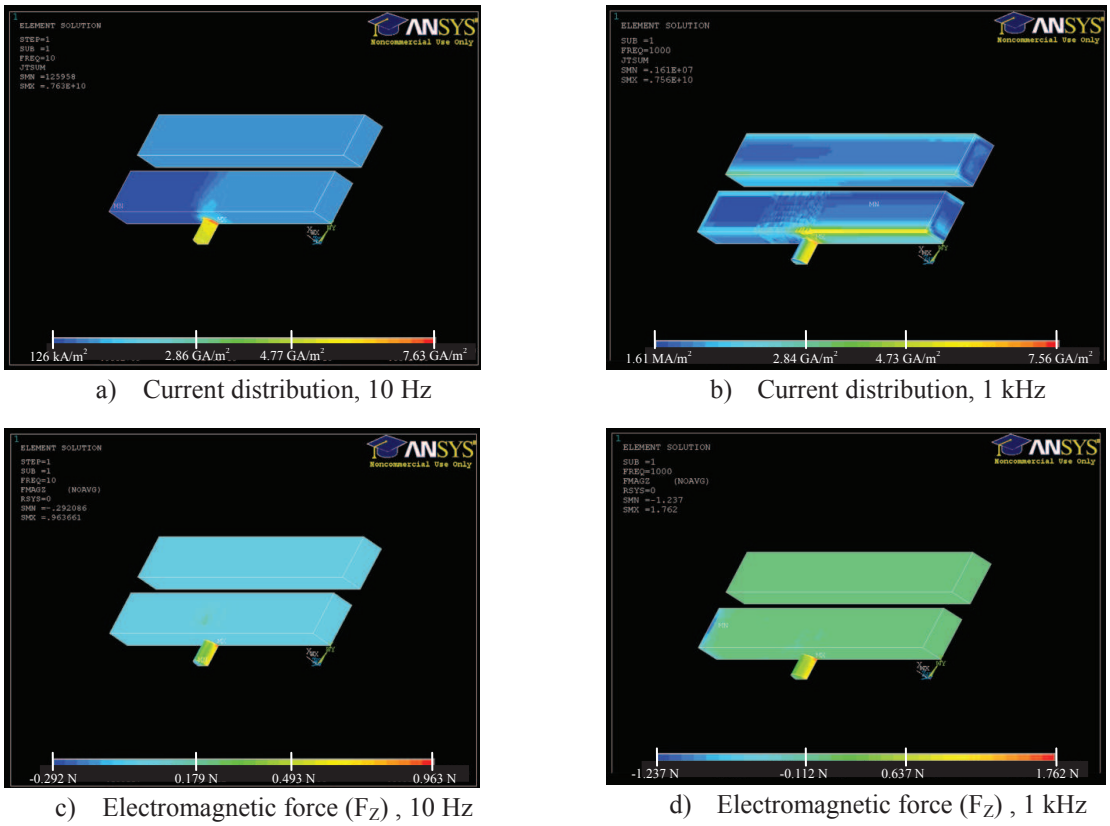

a) Current distribution, 10 Hz

b) Current distribution, 1 kHz

c) Electromagnetic force (F_Z) , 10 Hz

d) Electromagnetic force (F_Z) , 1 kHz

Fig. 3.7: Simulations of the current distribution and the electromagnetic force with ANSYS at 10 Hz and 1 kHz with I_R = 100 kA and I_A = 100 kA

Table 3.4: Values for the time-dependent inductance gradients used in the PSpice model for LARA

Time	Coefficients	
	L'_R (μH/m)	M' (μH/m)
t ≤ 0.2 ms	0.440	0.270
0.2 ms < t < 1.5 ms	linear decrease from 0.440 to 0.414	linear decrease from 0.270 to 0.167
t ≥ 1.5 ms	0.414	0.167

Table 3.5: Values for the time-dependent inductance gradient used in the PSpice model for LARC

Time	L'_R (μH/m)
t ≤ 0.2 ms	0.416
0.2 ms < t < 1.5 ms	linear decrease from 0.416 to 0.397
t ≥ 1.5 ms	0.397

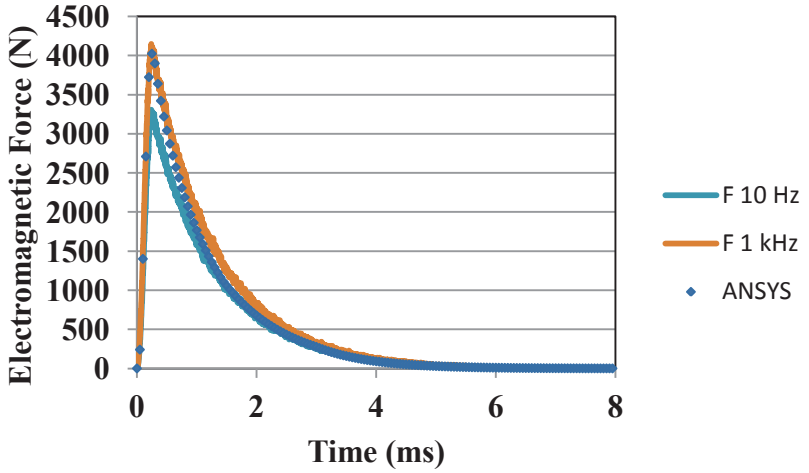

Fig. 3.8: Comparison between the electromagnetic force determined with a transient analysis in ANSYS and calculated based on the railgun force equation with the values for the inductance gradients at 10 Hz and 1 kHz

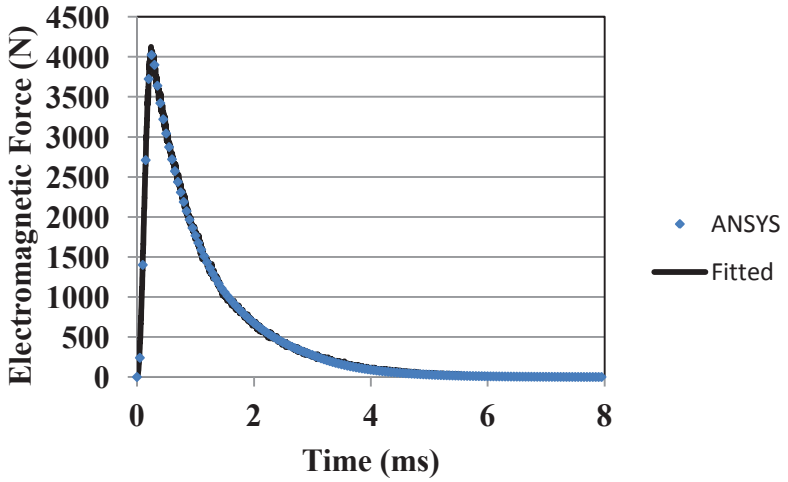

Fig. 3.9: Comparison between the electromagnetic force determined with a transient analysis in ANSYS and calculated based on the time-dependent inductance gradients for LARA

3.4.2. *One Brush Projectile*

In this paragraph we use the FEM ANSYS to study the temperature and current distribution in a one brush projectile for a non-augmented railgun [COF09]. The experimentally obtained currents used for the simulations are the currents obtained with the non-augmented railgun LARC [GAL05]. The inner circuit was connected to two capacitor banks with 7 kV each. The discharging time of the first bank corresponds with t = 0 ms. The discharging time t_c of the second bank is represented in Table 3.6 together with the measured velocity v_{muzzle} ($\Delta v/v < 5\%$) and the muzzle time t_b and the experimentally obtained plasma time t_P. The calculated action integral IA_P at the plasma point and the action integral IA_b at the muzzle are decreasing with increasing time between the discharges (Table 3.6).

The thermal conductivity in a fiber current brush is anisotropic. Therefore the calculations are made twice for an upper and a lower limit. Once with a thermal conductivity for the current brush that is the same as for the rails k_1, which serves as upper limit. And once with a thermal conductivity k_2 of 1e-12 $W.m^{-1}.K^{-1}$ (ANSYS does not allow k = 0 $W.m^{-1}.K^{-1}$), which is the lower limit. The melting energy was not simulated in the ANSYS model.

When we compare the maximum temperatures at the contact surface at t_P for both methods (k1 and k_2), we can conclude that the T_P calculated with the thermal conductivity of copper k_1 is only 23 to 41 % of the T_P calculated with k_2. The values for T_P calculated with k_2 are all higher than the melting temperature of copper, the T_P calculated with k_1 are lower. Thus, although a shot lasts only a few milliseconds, the influence of the thermal conductivity is not negligible. Fig. 3.10 represents the current distribution a) and the temperature distributions b) and c). The left side of a) en c) and the top of b) corresponds with the side towards the breech. The heating of the current brush takes mainly place at the contact surface and towards the breech. But the highest current density at that time is found towards the muzzle. We keep in mind that the velocity skin effect is not taken into account, neither is the heat caused by the friction. These phenomena would lead to an increase of the maximum temperature. The melting temperature of copper is 1083 °C. In Fig. 3.10.b) it is shown (calculations for k_2 = 1e-12 $W.m^{-1}.K^{-1}$) that for the first shot with t_c = 0.21 ms almost 40 % of the contact surface has reached the melting temperature at t_P, what was the highest value for all shots.

Table 3.6: Calculation results for different shots in a non-augmented railgun

t_C [ms]	t_P [ms]	IA_P [$C^2.s^{-1}$]	t_b [ms]	IA_b [$C^2.s^{-1}$]	V_{muzzle} [$m.s^{-1}$]	T_P [°C] k_1	T_P [°C] k_2
0.21	1.71	52.6	2.95	59.5	694	648	1585
1.00	2.98	51.2	3.96	54	580	501	1500
1.50	3.26	45.3	4.41	48.3	539	447	1326
1.75	3.64	44.5	4.62	46.8	520	416	1303
2.00	-	-	5.38	40.4	391	268	1175

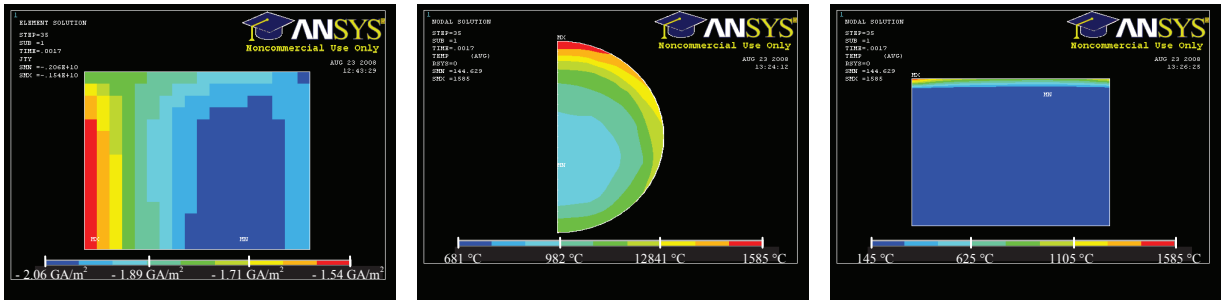

a) b) c)

Fig.3.10: Current density distribution in the brushes calculated for the shot with t_c = 0.21 ms at t_P : a) current density at the longitudinal cross-section, b) temperature distribution at the contact surface, c) temperature distribution at the longitudinal cross-section.

3.4.3. Two Brush Projectile

Now we consider the simulations for a two brush projectile and the augmented railgun LARA (Fig. 3.11). The global currents in the rails that are used as input for the ANSYS simulations are defined with PSpice (Fig.3.12). The evolution of the current in the two brushes was then determined with ANSYS. It must be noticed that I_A is important in comparison with I_R. The current I_2 in the muzzle side brush is first negative. This is due to the mesh current between the two brushes. It becomes higher than I_1 on breech side at the end of the shot but this result must be taken with caution. The velocity skin effect is not considered in the simulations; as a result we find a well-diffused current at the end of the shot. When the projectile reaches a high velocity at the end of the shot we expect the velocity skin effect to be distinct.

Fig. 3.13 gives the current distribution at t = 0.6 ms. Both currents are positive and I_2 is about equal to $I_1/4$. It can be observed that the skin effect is reduced in both rails. The temperature distribution is given in Fig. 3.14 at t = 0.88 ms. The temperature of the brush on the breech side is much higher than for the brush on the muzzle side. This is coherent with the current distribution.

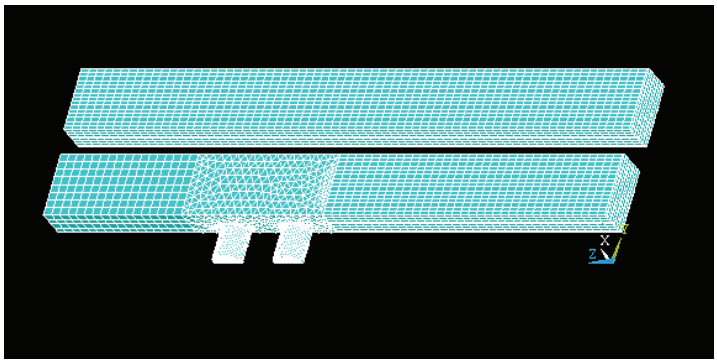

Fig. 3.11: Mesh for the augmented railgun LARA and a two brush projectile

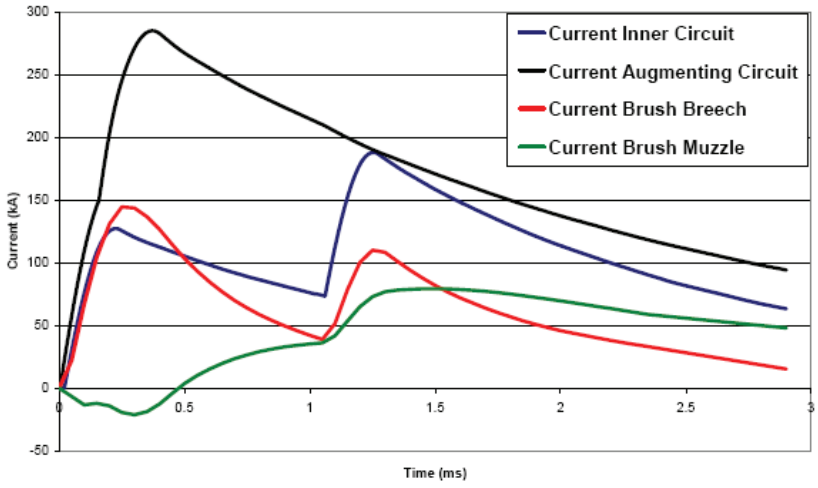

Fig. 3.12: Evolution of the different currents

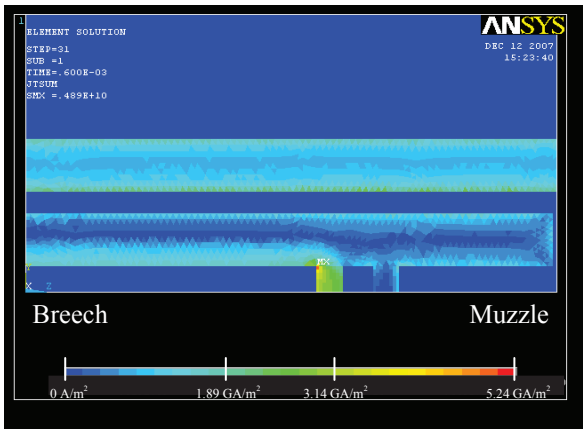

Fig. 3.13: Current density in the rails

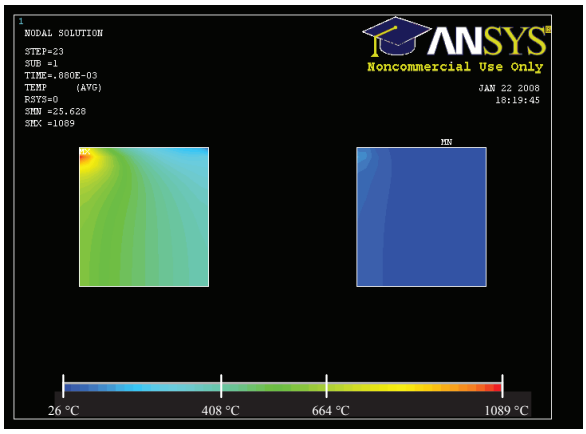

Fig. 3.14: Temperature in the brushes

3.4.4. Current Distribution for a Four Brush Projectile

The results are confirmed in the case of a four brush projectile. The skin effect is pronounced in the simulation at t = 0.2 ms in both rails as it can be seen in Fig. 3.16 on the left. The phenomenon is reduced at t = 0.72 ms. The current evolution in the brushes is difficult to forecast if we examine the results given in Fig 3.17. It can be seen in Fig. 3.18 that the circulating current created by I_A is important and is distributed between the brushes so that there is almost no current in brush 3. The current in the first brush is higher than the total current in the inner rails at the beginning of the shot. So this solution is not very interesting if we want a balanced current distribution.

Fig. 3.19 gives the temperature distribution at t = 0.72 ms. The highest temperature is found in the brush on the breech side, the temperature in the second and fourth brush stays low while the third brush shows almost no heating. This corresponds with the results for the current distribution.

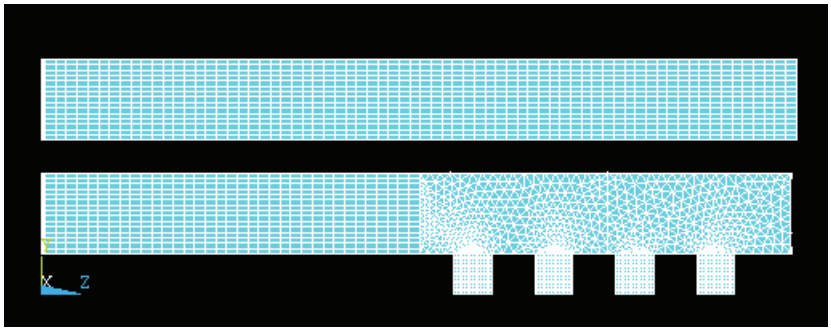

Fig 3.15: Four brushes modeling with ANSYS

t = 0.2ms

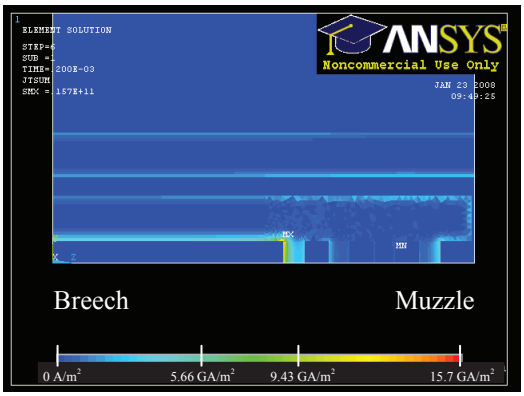

t = 0.72ms

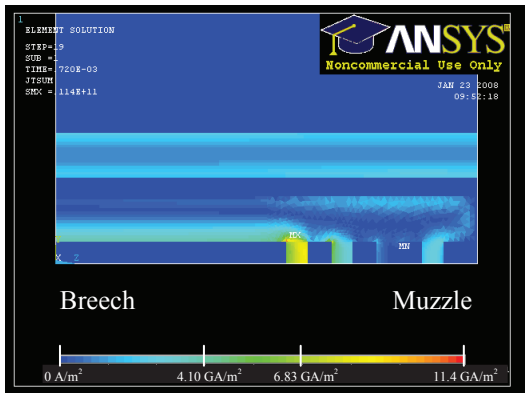

Fig. 3.16: Current density in the rails at t = 0.2 ms and at t = 0.72 ms

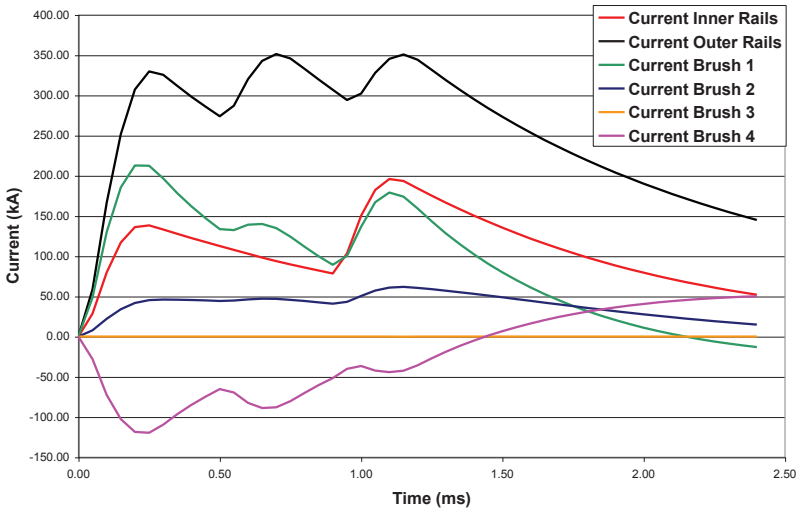

Fig 3.17: Calculated evolution for the current in the brushes

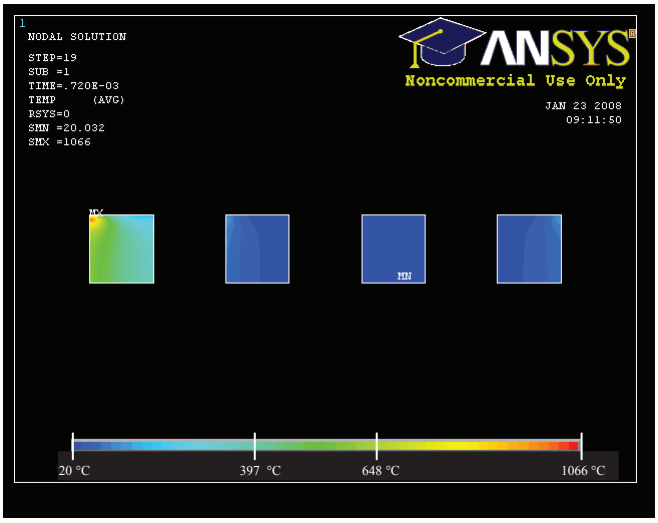

Fig. 3.18: Temperature in the brushes at t = 0.72 ms

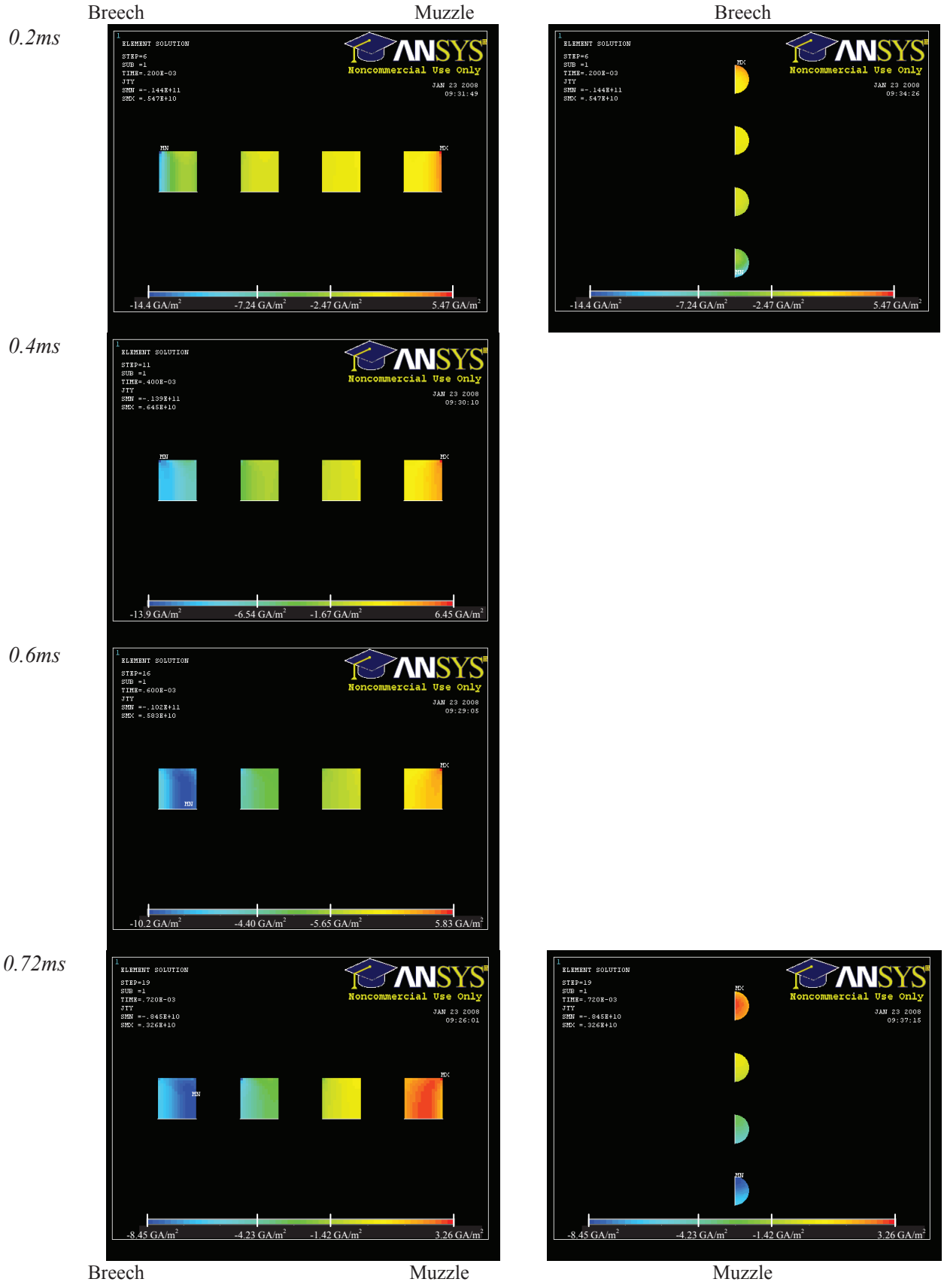

Fig. 3.19: Current density in the brushes at different times

3.5. *Comparison with the PSpice Simulation*

3.5.1. *Electromagnetic Force*

The first comparison concerns the electromagnetic force for the conventional and augmented railguns. There is in both cases a good concordance as seen in Fig. 3.20 and 3.21. This was predictable because L'_R and M' used in PSpice are determined through ANSYS simulation.

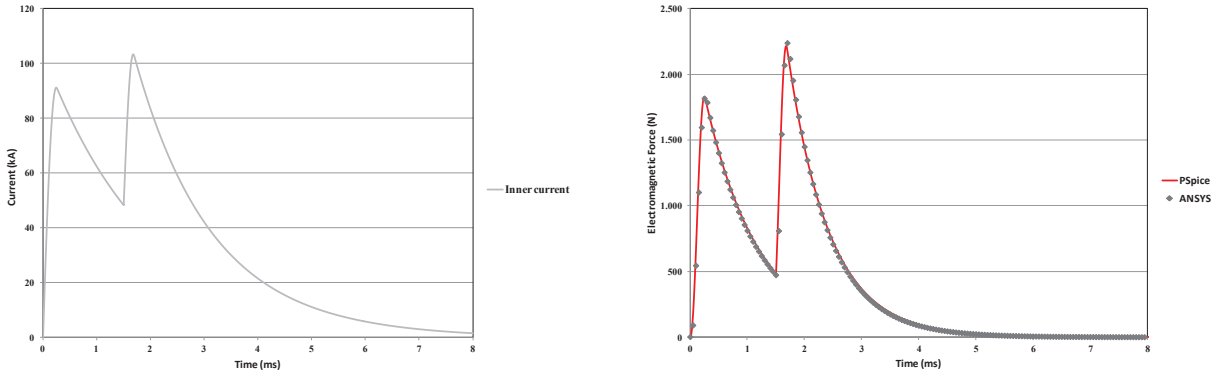

Current Electromagnetic force

Fig. 3.20: Comparison of the electromagnetic force simulated by PSpice and ANSYS for a conventional railgun
Shot 9, m_{pr} = 19.86 g, v_{muzzle} = 154 m/s

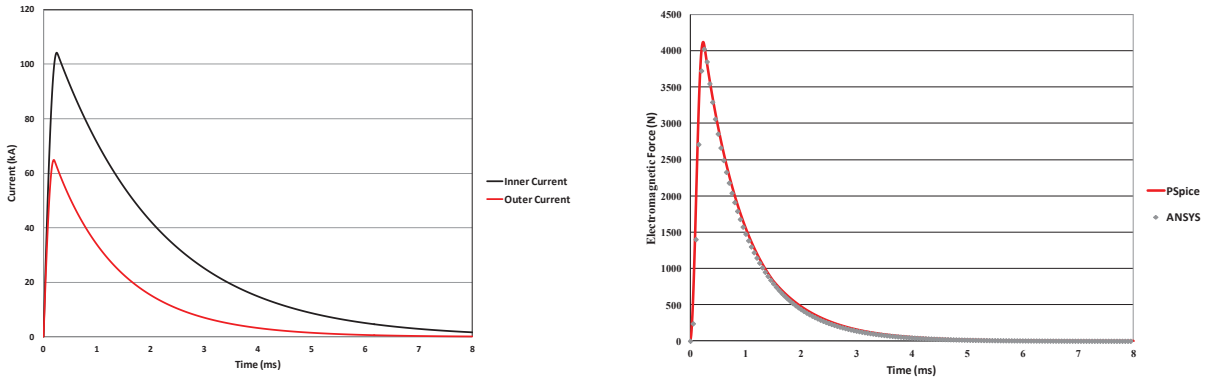

Currents Electromagnetic force

Fig. 3.21: Comparison of the electromagnetic force simulated by PSpice and ANSYS for an augmented railgun
Shot 11, m_{pr} = 19.92 g, v_{muzzle} = 164 m/s

3.5.2. *Thermal Model*

We will compare the two types of modeling, PSpice and ANSYS in the case of a two brush projectile. Currents and temperatures are simulated. If we consider the evolution of the currents we can see on Fig. 3.22 that the absolute values given by ANSYS are higher than those obtained by PSpice up to t = 1 ms. The differences are small and the variation is similar. So we can say that there is coherence between the two approaches.

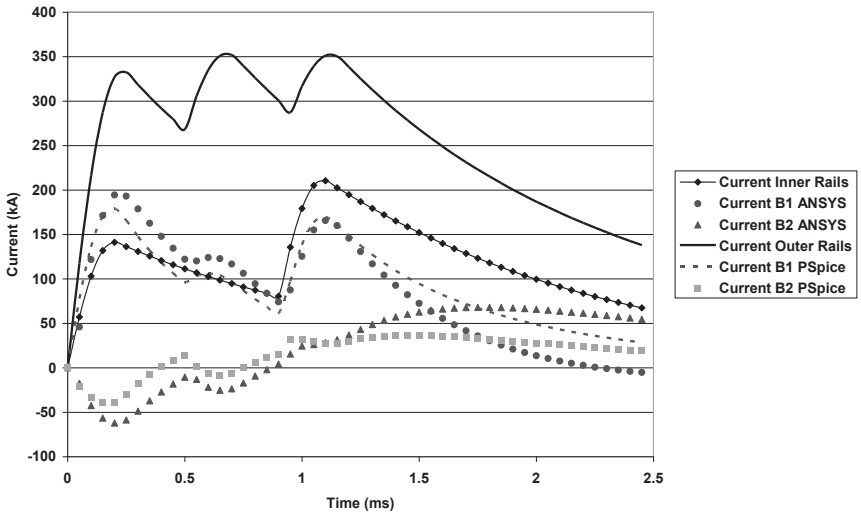

Fig. 3.22: Evolution of the currents simulated by ANSYS and PSpice

Table 3.7 gives the mean value of the temperature for each brush calculated by the two methods. The parameter is the radius of the brushes *r*. It can be seen that the values given by PSpice are higher in the brush on the breech side for the two first lines. The temperature in the other brush is always lower by PSpice than by ANSYS. Increasing the diameter of the brushes is favorable. But as shown in Table 3.8, it is better to reduce the distance between the brushes *a*.

Table 3.7: Mean temperature T_h computed by ANSYS and PSpice (a = 20 mm, m_{pr} = 20 g)

	Temperature (°C)			
r (mm)	T_h AN B1	T_h AN B2	T_h PS B1	T_h PS B2
3	258	89	305	41
3.5	173	50	182	28
4	126	36	120	25
4.5	108	32	85	24

Table 3.8: Mean temperature T_h computed by ANSYS and PSpice (r = 4 mm, m_{pr} = 20 g)

	Temperature (°C)			
a (mm)	T_h AN B1	T_h AN B2	T_h PS B1	T_h PS B2
15	109	35	98	27
20	126	36	120	25
25	142	37	127	28
30	158	38	139	28

There are no great differences in the results obtained by PSpice and ANSYS. There are assumptions for both. As we said before projectile movement is not taking into account in ANSYS. On the thermal point on view, the brushes are modeled as isotropic and there is no heat exchange with the ambient air but only with the rails. It is also difficult to correctly represent the contact layer.

On the other side, PSpice is a global modeling and only a mean value of the brush temperatures can be obtained. It is considered that there is no heat exchange for the brushes (adiabatic) and the environment. The temperatures depend on the heat capacity of the brushes which are made of copper wires.

Each method has its advantages and its drawbacks. Nevertheless the results are relatively similar. From our point of view, the major difficulty for ANSYS is that the projectile is immobile. The current

diffusion intervenes rapidly and the physical conditions are changed due to the reducing of the skin effect in the interesting part of the railgun.

3.6. Conclusion

ANSYS is a powerful software for studying the local behavior of a railgun. It has the advantage to allow a strong coupling between electromagnetic and thermal analysis in electrical dynamic evolution. But it has a major drawback; the movement of the projectile is not taken into account. This means that the velocity skin effect due to the displacement of the projectile is neglected. So the results obtained by ANSYS are only valid in the first instants. Later, the diffusion phenomenon modifies the current distribution and therefore the current distribution in the armatures does not correspond to the real distribution. We will propose in Chapter 5 a method to recreate the skin effect in the armatures at any initial instant.

The modeling domain is necessarily limited by the performance of the computer and in our case we had to limit the length to 14 cm. It introduces errors in the electromagnetic analysis. However, for the electromagnetic force the error is very limited because the length of the model is large enough in comparison with the gun caliber.

The simulation results have to be confirmed by experiments. In the next chapter we will discuss in detail the test bench and the measurement equipment. We will see in Chapter 5 that the experiment results are not accurate enough to valid completely the simulation methods for the current distribution between the two brushes of the armature.

Chapter 4

Experimental Set-Up

4.1. Introduction

In the previous chapters we discussed global and local simulations of the electromagnetic railguns LARC and LARA. The next step is the experimental validation. The experimental set-up for the LARA railgun with two capacitor banks for the inner circuit and one for the outer circuit is presented in Fig. 4.1. Two Rogowski coils were at our disposal for the measurement of the current in the inner circuit I_R and in the augmenting circuit I_A. Two high voltage probes were placed at the connection block to give an estimate of the voltage at the capacitor banks. The muzzle voltage between the inner rails at the muzzle is also measured. This voltage gives an indication about the quality of the contact and will be discussed in § 4.2.2.2. The passing of the projectile is detected in several points along the railgun. First there are the laser detections at the measurement points at $z_1 = 295$ mm, $z_2 = 465$ mm and $z_3 = 895$ mm. At the muzzle of the railgun a light barrier is installed with four detection points. This allows an estimation of the muzzle velocity. As discussed in § 4.2.3.2, the shape of the laser signal also allows to estimate the velocity of the projectile at the measurement points.

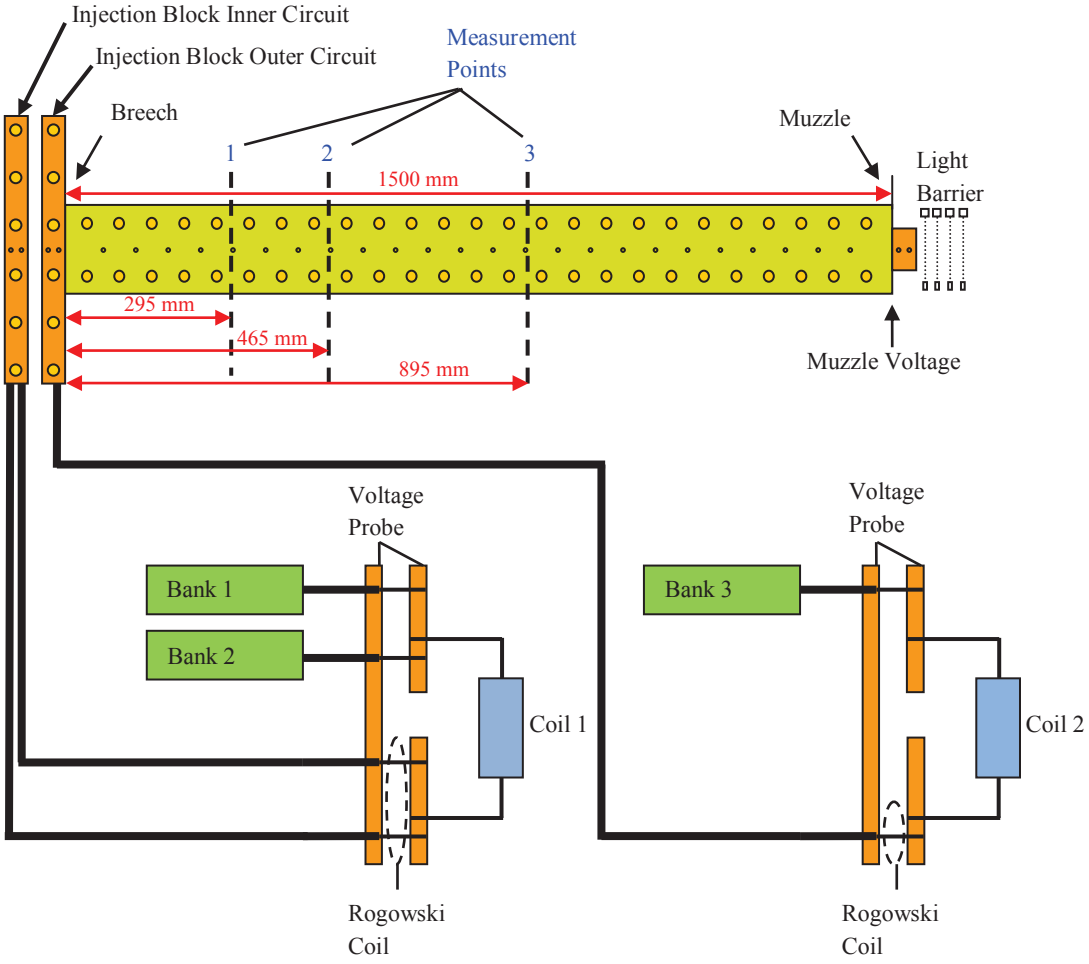

Fig. 4.1: Schematic overview of the experimental set-up

The most important measurement of this set-up is the measurement of the current distribution in the projectile discussed in § 4.5. This distribution is important for the further development of projectiles and different methods have been developed to study it.

The first method we want to discus is the use of B-dots as described in [GAU94]. B-dots are small coils and the voltage they generate is proportional to flux variation through the surface of the windings of the coils. As a result the B-dot will measure the magnetic field in the direction of the axis of the B-dot. The B-dots for the measurement of the current distribution in the projectile are positioned with the axis in the shot direction. They have 40 windings on a 5 mm square, epoxy core. During the experiments fixed projectiles were used. The projectiles were made of Cu or Ti and the thickness of the plates used as current bridge were 0.1 mm, 10 mm and 60 mm. The general conclusion of the experiments was that this method allows only making a qualitative observation of the quality and the length of the contact.

The second method is based on the use of a B-Scalar sensor based on the Colossal Magnetoresistance (CMR) effect [ZUR11], [LIE09], [LIE11], [SCH09a]. These sensors are based on a thin (< 1 μm) manganite film, which exhibits the CMR effect. The sensor's operation is based on an electrical conductivity change of thin polycrystalline La-Sr-MnO3 films due to external magnetic fields. Experiments have shown that the response of a CMR-based sensor to a magnetic field pulse does not depend on its orientation in the magnetic field and allows measuring the absolute value of the magnetic field [LIE09]. Experiments with a static projectile set-up were carried out [LIE11]. Holes were drilled in the projectile and the magnetic field was measured at six points. Due to the small dimensions of the sensors, they can be placed in drill holes very close to the brushes. The current distribution observed during the first experiments showed a qualitatively typical behavior for multiple brush armatures during launch conditions. During the experiments it was shown that, for the case of two brushes being separated in shot direction, the formation of an appropriate contact interface is difficult for the front brush during about 500 μs and ends with the formation of a stable contact zone.

A third method to measure the current distribution in a projectile is discussed in [WEY99]. In these experiments with a two brush projectile, miniature Rogowski coils are placed around the brushes. The signal from the coil is transferred via thin twisted copper wires located in front of the projectile. These wires are pushed during the shot and can only withstand the large acceleration for a certain amount of time. The Rogowski coils consist of a double layer winding and are designed to reject the effect of nearby currents in the rails and the other brush. They measure the current distribution during the first 500 μs in a moving armature with two brushes.

The method we will use in this thesis was presented in [SCH05a] and [SCH09]. It is a combination of three measurements: the voltage measured between two pins in the rails, the voltage in a loop placed partially in the rails and the laser detection of the projectile. This method will be discussed in § 4.5. It allows measuring the current distribution in different points along the rails during a shot for a moving projectile.

During our experiments we try to avoid contact transition and therefore we work with, for railgun standards, "low" currents and energy. The muzzle velocities obtained in our experiments vary between 48 and 214 m/s.

4.2. Test Bench

The electromagnetic launcher LARC/LARA was used for the experiments (Fig. 4.2). This railgun is 1500 mm long and has a square caliber of 15 mm. The square cross-section of the rails, interior and augmenting, is 15 mm x 15 mm.

Fig. 4.2: The electromagnetic launcher LARC/LARA at ISL

Fig. 4.3 shows a transversal cross-section of the electromagnetic launcher LARA. The support structure (1) has an upper and a lower part, which hold each an interior (2) and exterior (3) rail. To assure a distance of 15 mm between the interior rails, the caliber, cylindrical supports (4) are put around the threaded rods (5) in steel that keep everything in place. A 6 mm thick isolating plate (6) is placed between the interior and exterior rails. The rails are attached to the support structure with bolts (7) that pass vertically through the support structure, the exterior rails and the isolating plate into the interior rails. The bolts are isolated from the exterior rails. To ensure the direction of the projectile and the contact between the brushes and the rails, two plates (8) are placed along the lower interior rail to guide the projectile.

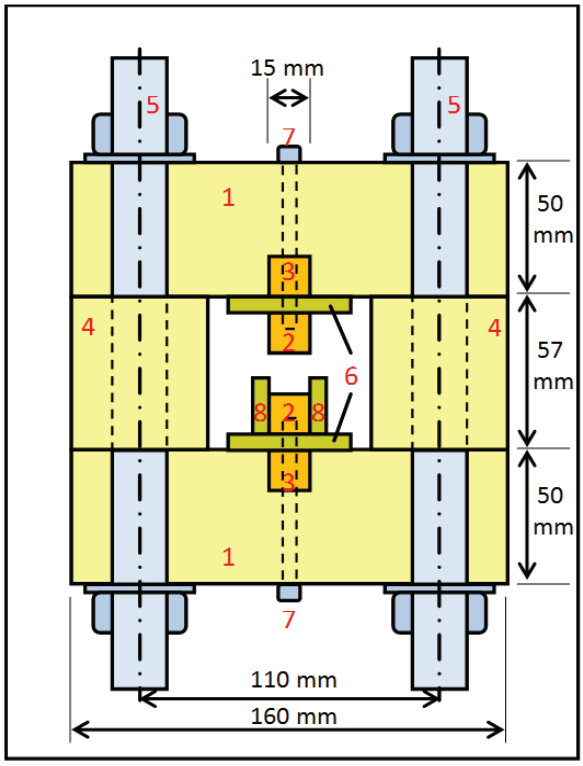

Fig. 4.3: Transversal cross-section of the electromagnetic launcher LARA: (1) support structure, (2) inner rails, (3) outer rails, (4) cylindrical support, (5) threaded rods, (6) 6 mm thick isolating plate, (7) bolts, (8) guides

The connection between the inner rails is assured by the current brushes of the projectile. The augmenting rails are connected with a bridge at the muzzle of the railgun.

Capacitor banks are used as current source for the railgun. A total of three capacitor banks were at our disposal. For the experiments we used the non-augmented set-up LARC and the augmented set-up LARA. During the experiments with the non-augmented railgun, the augmenting rails were connected with each other through the bridge at the muzzle and the lower augmenting rail was connected to ground. The initial charges of the capacitor banks are varied between 7 and 8 kV which correspond with energy between 27-36 kJ per bank. The electric circuit of the capacitor bank is discussed in Chapter 2.

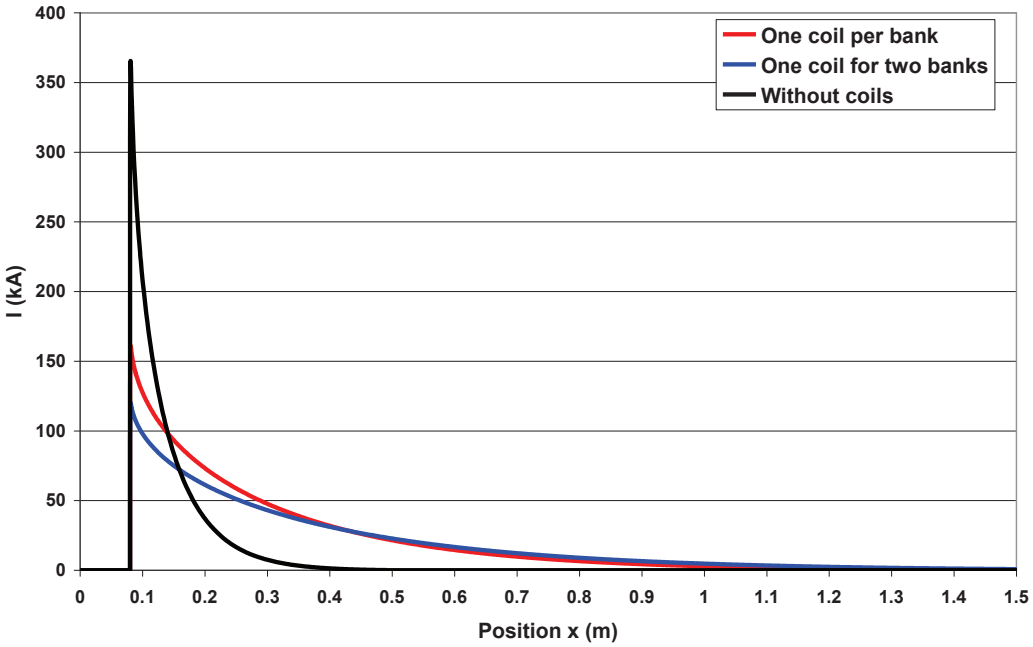

Fig. 4.4: Current profiles in function of the position of the projectile for a non-augmented railgun for three different configurations of the pulse forming network: one coil per bank, one coil for two banks and without coils

The first experiments with LARC were with two capacitor banks. The goal of the experiments was to measure the current distribution between the current brushes in the projectile. The measurement devices are placed along the rails in the fixed points. The positioning of these measurement devices is limited by the current profile. If the current is too low at the moment the projectile passes a measurement point, we do not acquire a signal.

Fig. 4.4 represents the simulation with PSpice for the total current in function of the position, for three different configurations for a non-augmented railgun with two capacitor banks. The highest maximum current is found for the simulation without pulse forming coils. However after 40 cm the current is almost zero. Therefore we used pulse forming coils (Fig. 4.5) to shape the current. Two coils with an inductance of 8 µH were available. The simulations were made for two configurations. In the first configuration the current of both banks was injected in the same coil while in the second configuration each bank was connected to another coil. The configuration with two coils has a higher current until approximately 43 cm. Because we had only two coils at our disposal, we chose the configuration with one coil. For the augmented railgun configuration, one pulse forming coil was used for the inner circuit with two capacitor banks and one for the augmenting circuit. In this way the configuration for the inner circuit was the same for the augmented and the non-augmented railgun. In

the configuration for the non-augmented railgun with three capacitor banks, the second coil was used for the third bank.

Another way to obtain a current at the moment the projectile passes the measurements points would be to delay the discharging of the second capacitor bank. However as shown with the second shot, discussed in Chapter 5, with two capacitor banks discharged at t = 0 ms in the inner circuit of the non-augmented railgun, the projectile did not leave the railgun. For the configuration with two capacitor banks for the inner circuit, non-augmented and augmented, these banks were discharged simultaneously. For the third bank, for the inner circuit or the augmenting circuit, the discharge times were varied. The discharging of a capacitor bank disturbs the measured signals, thus it is recommended not to discharge a capacitor bank just before the passing of the projectile at a measurement point.

Fig. 4.5: Pulse forming coil (L = 8 µH, R = 1.4 mΩ)

4.3. Projectiles

An example of a projectile used in the experiments is presented in Fig. 4.6. The sabot of the projectile is made of glass-fiber reinforced plastic and is 35 mm long, 15 mm wide and 14.5 mm high. Two boreholes are drilled with a diameter of 7 mm, the diameter of the brushes. The centre of the brushes is in the middle of the projectile at 7 mm and 22 mm from the front of the sabot. Two dense copper brushes are pulled through the boreholes. On both sides there is a reserve volume in the sabot which allows the brushes to bend during the loading. The arrow in the figure indicates the shot direction.

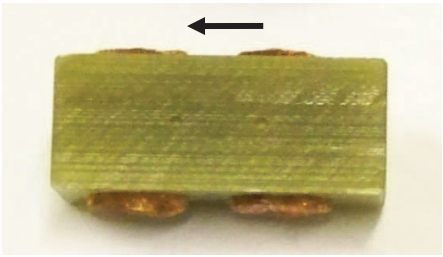

Fig. 4.6: Example of a projectile with a sabot in GRP and two current brushes used in the experiments

Fig. 4.7 shows two schemas for projectiles with different current brushes. The brushes have a different length and thus a different mass reservoir. The mass reservoir is the additional length of the brushes to cover for mass loss during launch. A higher mass reservoir is better to avoid contact transition but a higher length of the brushes also causes a higher normal mechanical force $F_{mech,N}$ due to the bending of the brushes and thus a higher friction force (as discussed in § 2.2.5.). Projectiles of type b were used during the first tests, without current distribution measurement, and we established that the friction force was too high for our experiments. Therefore the length of the brushes was adapted, based on an existing one brush projectile [SIA], and projectiles of type a were used during the experiments discussed in Chapter 5. The brushes are cut at an angle of 8° with the sabot in order to obtain a good contact between the rails and the bend brushes. The mass of the projectiles used in the experiments is approximately 20 g.

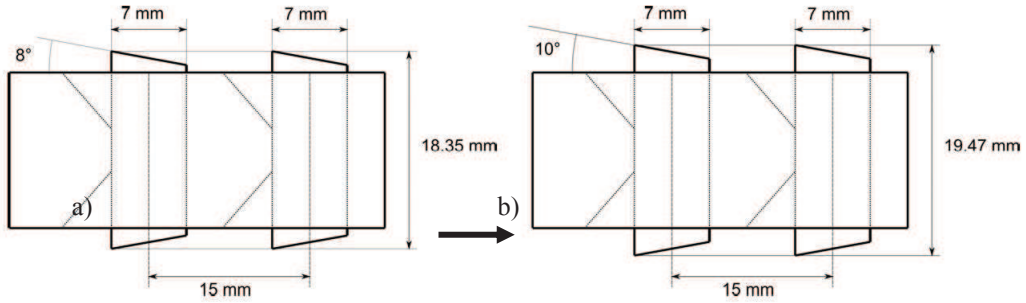

Fig. 4.7: Schemas of the projectile

4.4. Measurement Devices

4.4.1. Current Measurement

For the measurement of the currents in the inner and outer rails, two Rogowski coils with active integrators are used. The coil is wound around a flexible non-magnetic tube with circular cross-section to become a helical coil. The wire returns through the centre of the coil so that both ends of the wire are at the same side of the coil. This coil is then looped around the current conductor. The voltage measured with a Rogowski coil is proportional to the rate of change of the current enclosed by the coil (dI/dt) and also to the number of windings and the surface of these windings. In order to become a voltage that is proportional to the current, an active integrator is used (Fig. 4.8) [CWT02].

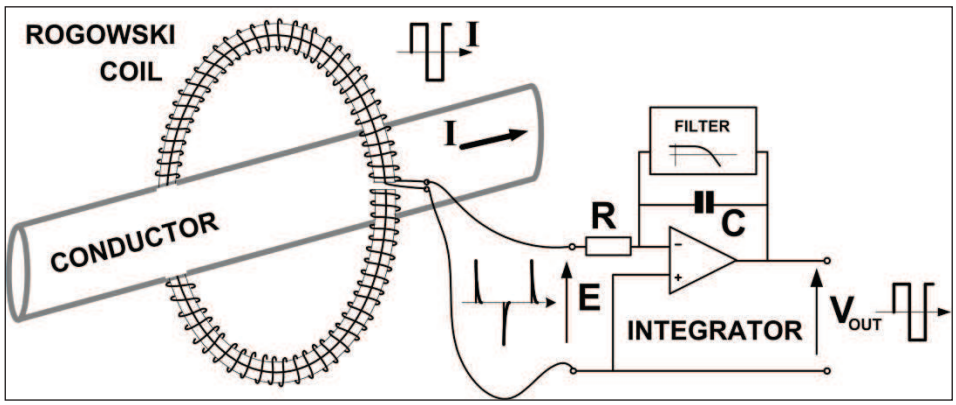

Fig. 4.8: Schematic of a Rogowski coil with an active integrator [CWT02]

The sensitivity of the Rogowski current transducer used in the experiments is 0.02 mV/A. The peak current is 300 kA and the peak *dI/dt* is 40.0 kA/µs. The Rogowski coil transducer, to measure the total current in the inner rails, is put around the inner parts of the coaxial cables at the connection blocks. Figure 4.9 represents the setup for LARC with two capacitor banks. For the configuration with three capacitor banks for LARC a second Rogowski coil was used for the measurement of the current for the third capacitor bank, placed at the second connection block after the second pulse forming coil. For the augmented railgun LARA the second Rogowski coil was used for the measurement of the augmenting current at the second connection block.

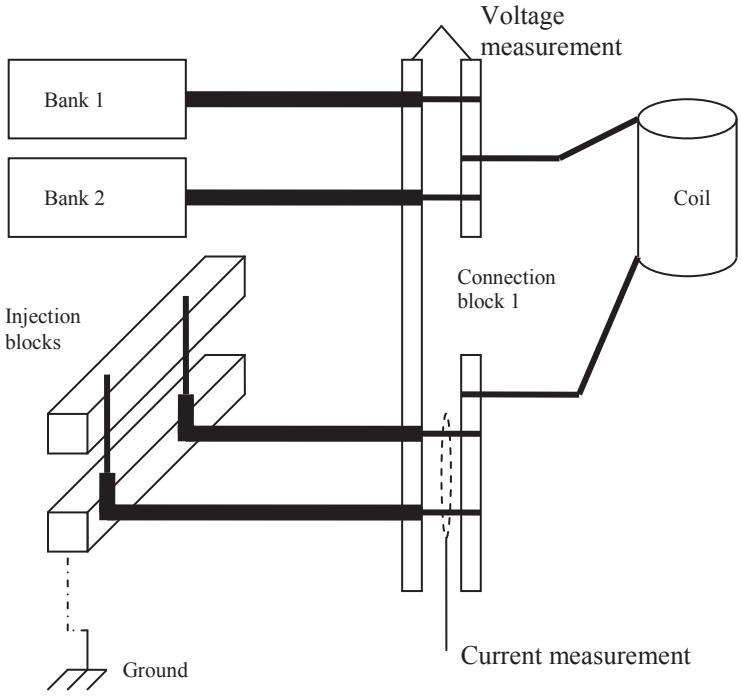

Fig. 4.9: Schema of the setup of the current and voltage measurement
for LARC with two capacitor banks

4.4.2. Voltage Measurements

4.4.2.1. Voltage at the Capacitor Banks

High voltage probes are used to measure the voltage at the capacitor banks. The voltage probe is placed at the connection block before the pulse forming coil (Fig. 4.10) for LARC in the configuration with two capacitor banks. A second probe is placed at the corresponding position when the third capacitor bank is used for LARC and LARA. The probe tip is connected to the inner conductor and the ground lead to the outer conductor of the coaxial cables (Fig. 4.10). The probe has a 1000 x attenuator so the output can be connected to an oscilloscope.

4.4.2.2. Muzzle Voltage

A voltage change at the muzzle of a railgun can be an indication for the transition from a “low voltage” metal-to-metal contact to a “high voltage” arcing contact. Therefore muzzle voltage is an important diagnostic tool for railguns. The definition of what is a low or a high muzzle voltage depends on the size of the railgun, the materials and the design of the armature [REC09], [BAR03].

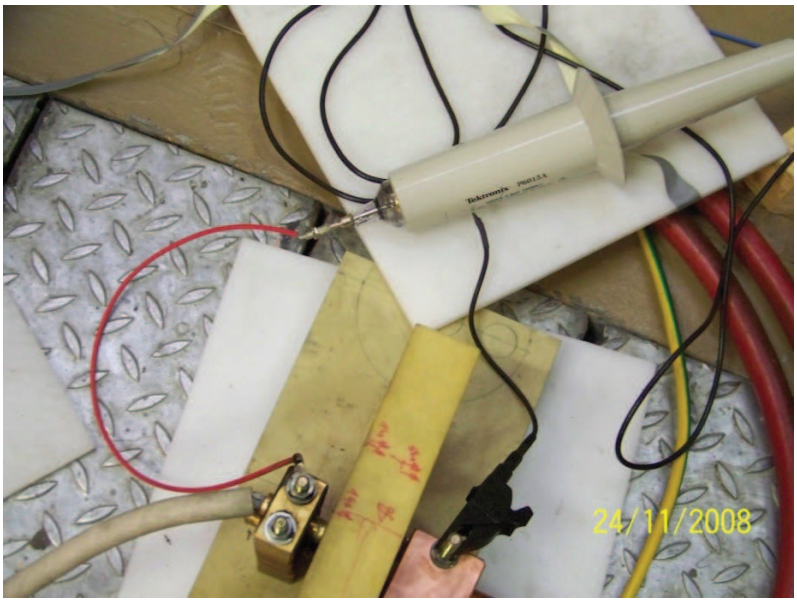

Fig. 4.10: High voltage probe

In the experiments discussed in this thesis, we work, for railgun standards, with low currents (order of magnitude 100 kA) and velocities (v_{muzzle} between 48 and 214 m/s) and we try to avoid contact transition. The muzzle voltage V_m is measured between the inner rails at the muzzle. A voltage divider is used and the connection with the oscilloscope is through optic coupling. An overview of the contributions for the low voltage parts is discussed in [DRE95]. The muzzle voltage obtained with the measurements is the line integral of electric field over a contour C shortly connecting the muzzle ends of the rails (Fig. 4.11). The Faraday induction equation states that any other contour C_1 connecting M_1 and M_2 can be used but then an induction term $d\Phi/dt$ must be added with Φ the magnetic flux through the closed contour formed by C and $-C_1$. The contour is chosen along the surface of the rails and the armature, ([DRE95]) in a reference system with the armature fixed and the rails moving with velocity v. If we consider only the armature part of C_1, then the line integral of electric field over a contour C_1 would correspond with the resistive contribution of the armature.

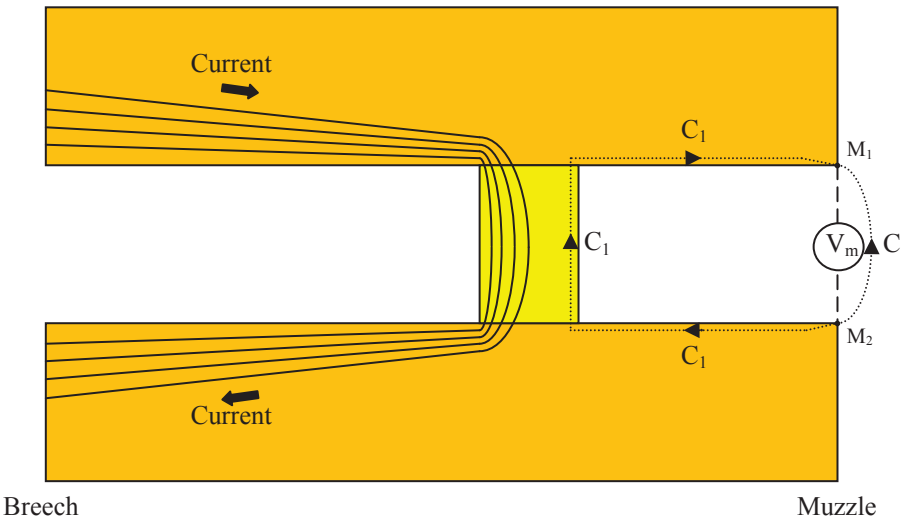

Fig. 4.11: Schematic Muzzle Voltage V_m

The experimentally measured muzzle voltages, are significantly higher than expected based on the armature resistive contribution and the induction term. A possible explanation is the contact resistance between the armature and the rails. In [DRE95] is stated that this is adequate for low velocities and small contact zones. For high velocities the current is concentrated at the rear end (breech side) of the armature due to the velocity skin effect. Contour C_1 as chosen in Fig. 4.11 does not pass through the high current density area of the contact zone. The conclusion was that changes in the contact properties will not significantly contribute to the muzzle voltage until the current concentration zone reaches the muzzle end of the contact.

Another contribution to the muzzle voltage arises from the current flowing in the rails ahead of the armature ([DRE95], [PAR99]). The armature current produces a magnetic field ahead of the armature. A transient magnetic field generated parallel to a conducting surface results in a surface current. The surface current creates an electrical field in the rails ahead of the armature. This electrical field will contribute to muzzle voltage. Fig. 4.12 represents the muzzle voltage measured during the first shot with LARC in the configuration with two capacitor banks. Both capacitor banks were discharged simultaneously, corresponding with t = 2 ms in Fig. 4.12. The delay of 2 ms is due to the optic coupling of the signal. The first part of the signal (t < 2 ms) is used for the scaling of the measurement. The signal is disturbed by the discharge of the capacitor banks (peak at 2 ms) and is noisy. The measured muzzle voltage is lower than 5 V which corresponds with a “low voltage” metal-to-metal contact. No loss of contact was found during the experiments. As discussed in Chapter 5, the measurements of the current distribution in the projectile suggest the existence of a current in front of the projectile.

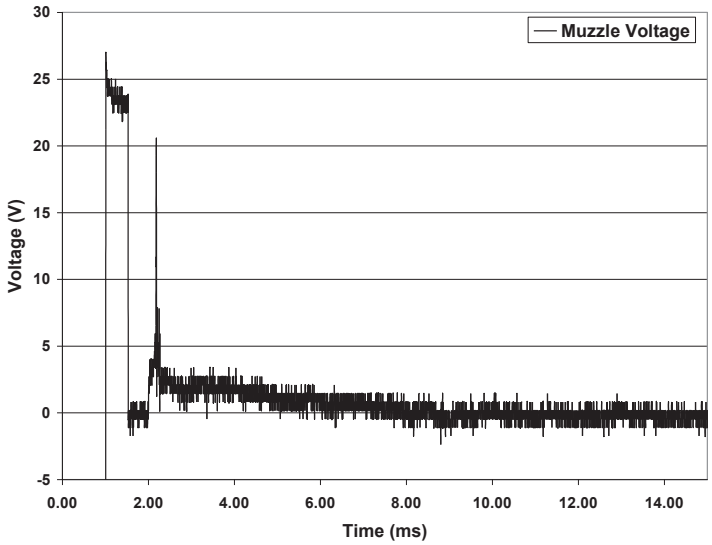

Fig. 4.12: Muzzle voltage measured during a shot

4.4.3. Position and Velocity Measurements

4.4.3.1. Light Barrier

During the experiments, there is no continuous measurement of the position and the velocity of the projectile. The position and velocity is only measured at discrete points. The muzzle velocity is measured with a light barrier. The principle is presented in Fig. 4.13.

The four optic fibers are placed at one side, equally spaced at a distance of 5 cm from each other. At the other side the four sensors that receive the signal from the optic fibers are placed at the same distance just in front of the fibers. When the projectile passes in front of a sensor, the signal is

interrupted. So we know at which times the projectile passes each fiber-sensor couple. We assume the velocity of the projectile to be constant while it passes the light barrier. Knowing the distance between the measurements points we estimate the velocity of the projectile at the muzzle of the railgun.

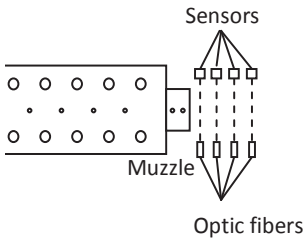

Fig. 4.13: Schematic of the light barrier for the measurement of the muzzle velocity

Fig. 4.14 presents the signals measured during a shot with LARC in the configuration with two capacitor banks. During the measurements, we established that the signals from the first and second fiber-sensor couple grow weak during the experiments. Therefore we decided to use only the last two signals for the estimation of the muzzle velocity. The relative error on the measured velocity $\Delta v/v$ can be calculated based on [GAL04],[SIA11]:

$$\frac{\Delta v}{v} = \frac{\Delta e}{e} + \frac{v}{e}\Delta t \tag{4.1}$$

With e the distance between the optic fibers, Δe the error on the distance between the optic fibers and Δt the error on the passing time between the optic fibers. The measurement error on the distance between optic fibers is estimated at 1 mm. The diameter of the optic fibers is 1 mm and Δe is estimated at 2 mm. Δt corresponds with the sampling duration of the oscilloscope which is 1 µs. The maximum muzzle velocity measured during the experiments is 214 m/s and thus the relative error on the velocity measurement is less than 4.4 %.

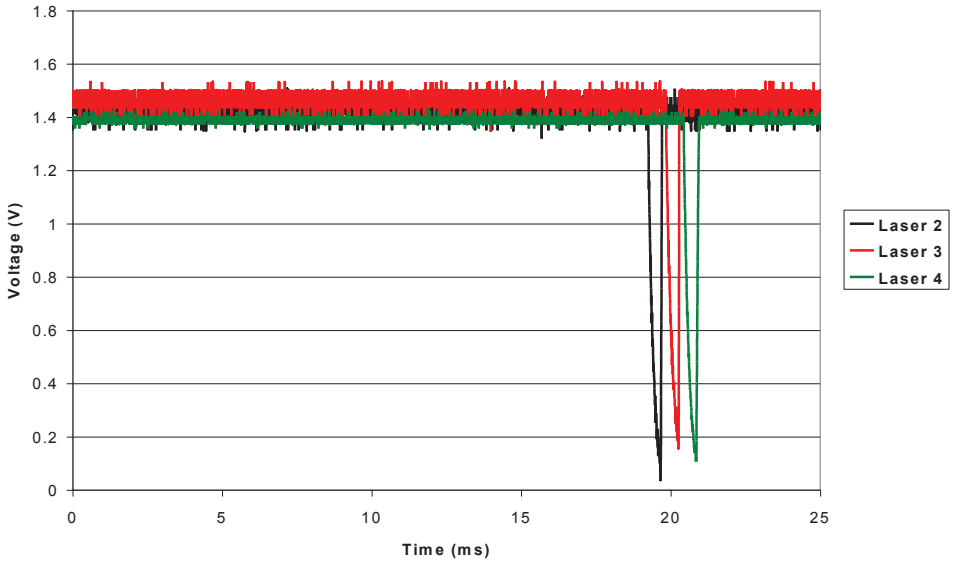

Fig. 4.14: Signals measured with the light barrier during a shot with LARC in the configuration with two capacitor banks.

4.4.3.2. Laser Detection at the Measurement Points

Besides the velocity measurement and position detection at the muzzle, the passing of the projectile is also detected at the passing of a measurement point. For this purpose, a laser-sensor combination is used. Fig. 4.15 shows a typical laser signal measured at the first measurement point (z_1 = 29.5 cm) . In most cases the edges of the signal are sharp enough to allow velocity estimation. We assume that the velocity is constant during the passing of the projectile. The average maximum before and after the voltage drop and the average minimum during the passing of the projectile is calculated. Two straight lines are fitted at the edges (10 % - 90 %). The time difference between the moments where the signals reaches 50 % is determined. This allows estimating the velocity at the moment the projectile passes the measurement point.

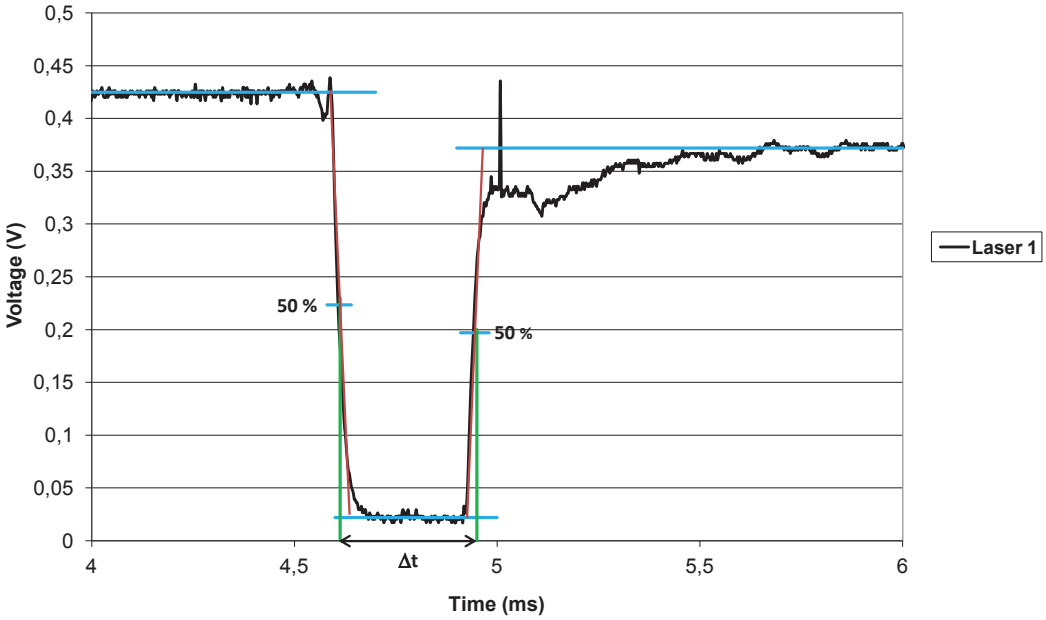

Fig. 4.15: Typical laser signal at a measurement point for the detection of the passing of the projectile

4.5. Measurement of the Current Distribution between the Brushes

For the measurement of the current distribution between the brushes of the projectile, the method described in [SCH05a] and [SCH09] was used. This method includes three measurements.

The first one is the voltage measurement between two points along the rails. Therefore the voltage V_{pins} is measured between two pins placed in the upper inner rail. The distance between the pins is 5 mm. The voltage measured between the pins is:

$$V_{pins} = R_{AB} I_{AB} + L_{AB} \frac{dI_{AB}}{dt} + \frac{d\Phi_{pins}}{dt} \tag{4.2}$$

The current I_{AB} is the current in the section AB of the rails (Fig. 4.16) and R_{AB} and L_{AB} are the ohmic and inductive impedances of this section. The term $d\Phi_{pins}/dt$ is the flux change induced in the measurement loop.

a

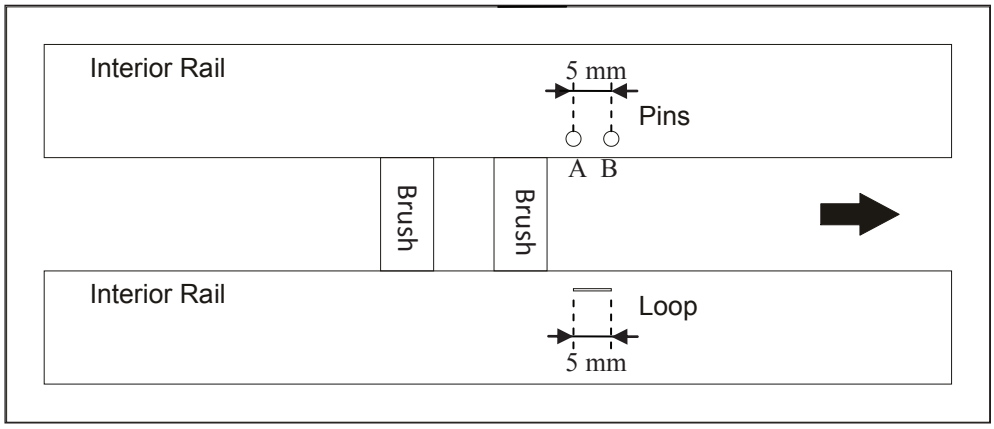

b

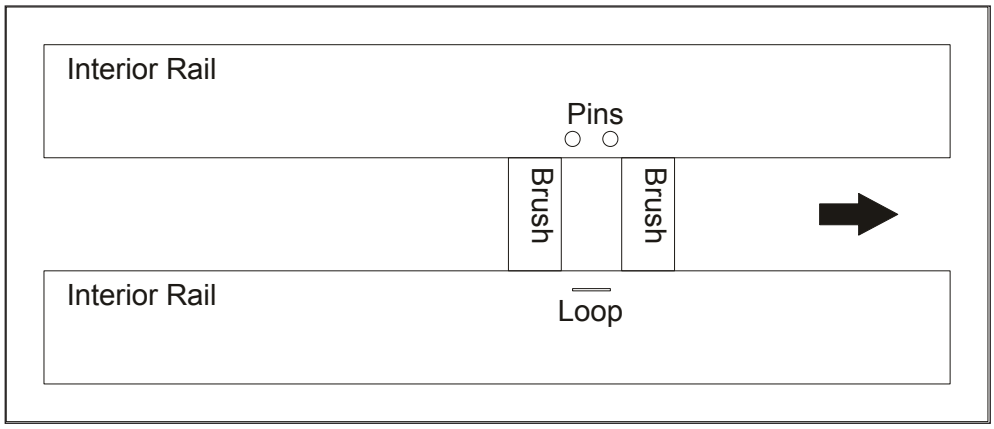

c

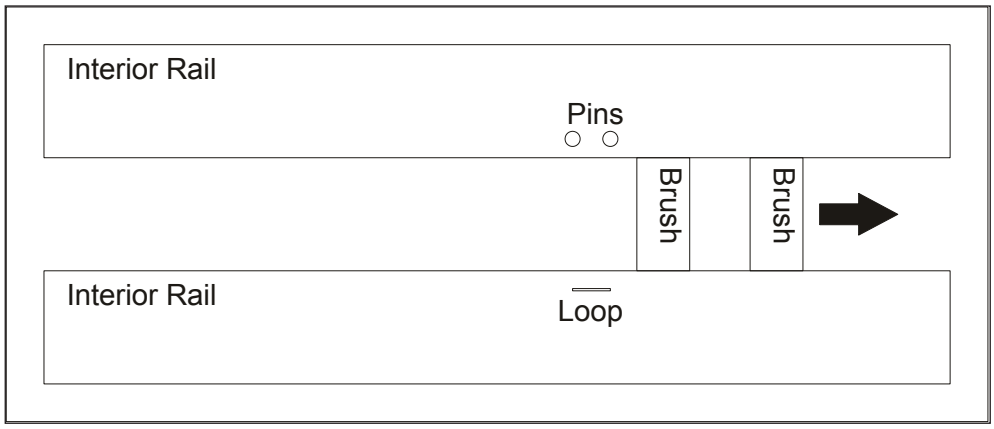

Fig. 4.16: Representation for the measurement of the current distribution for different positions of the projectile: a) the projectile has not reached the measurement point, b) only the current brush towards the muzzle has passed the measurement point, c) both current brushes have passed the measurement point

For the second measurement a loop is placed in the lower inner rail at the same distance as the pins in the upper inner rail. This loop is isolated from the rail and placed in a slot in the rail. This measurement is used as a compensation measurement for the term $d\Phi_{loop}/dt$. The voltage V_{loop} is:

$$V_{loop} = \frac{d\Phi_{loop}}{dt} \tag{4.3}$$

The third measurement is the detection of the projectile with a laser barrier as discussed in § 4.4.3.2. Fig. 4.17 is a picture of the measurement device used during the experiments. The importance of the position of the projectile is explained in Fig. 4.16. In situation a, the projectile has not reached the measurement position yet. If the projectile is far from the measurement point, no current flows in the rails. When the projectile approaches the measurement point, the eddy currents in front of the projectile have to be taken into account. In situation 4.16 b, the current in the rail section between the pins is the current flowing in the brush towards the muzzle. In situation 4.16 c, the current in the rail section between the pins is the total current.

The distance between the pins is 5 mm, while the diameter of the brushes is 7 mm and the distance between the centers of the brushes is 15 mm (Fig. 4.18). When the position of the projectile is known we can determine the current flowing in the brush towards the muzzle.

The three measurements points located at z_1 = 29.5 cm, z_2 = 46.5 cm and z_3 = 89.5 cm measured from the breech side of the railgun, were chosen based on different considerations. The starting position of the projectile is z = 8 cm. The position of the first measurement point can't be too close to the starting position of the projectile. The discharging of the capacitor banks disturbs the signal and the velocity is still low. For the configurations for LARC and LARA with two capacitor banks the current in the inner circuit drops very fast (Fig. 4.4). So if we choose the measurement points too close to the muzzle, the measured signal is too weak. Furthermore, the measurement device has to be placed between the bolts of the support structure.

Fig. 4.17: Measurement device for the determination of the current distribution between the current brushes.

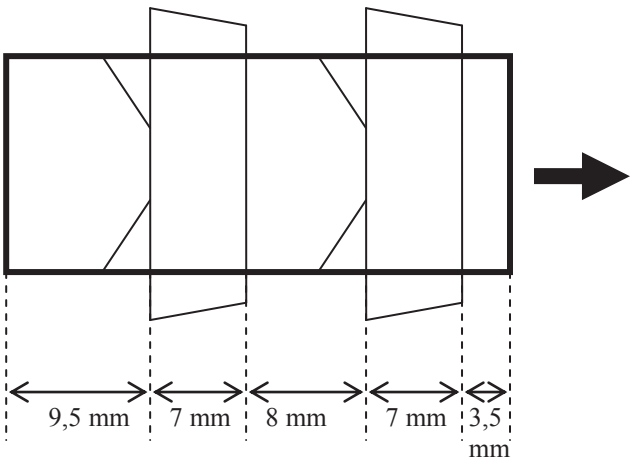

Fig. 4.18: Schema of the projectile used in the experiments

An example of a measurement is given in Fig. 4.19. The red curve represents the voltage measurement between the pins; the green curve is the corresponding voltage measurement in the loop. The laser signal allows to determine the position of the current brushes. The front and tail of the projectile are indicated. In [SCH09b] the voltage measurement in the loop is used to correct the term $d\Phi_{pins}/dt$ in the voltage measurement between the pins. Under the assumption that there is no current in front of the projectile, the voltage measured between the pins before the passing of the first current brush is only due to the term $d\Phi_{pins}/dt$. This part of the signals is used to fit the voltage measurement in the loop to the voltage measurement between the pins. The fitted signal in the loop can then be subtracted from the voltage measurement between the pins. During the experiments discussed in this thesis, in almost every measurement of the current distribution, the voltage measurement between the pins is negative before the passing of the first current brush indicating a current in front of the projectile. As a result we cannot fit the signals. Therefore another method for the determination of the current distribution between the current brushes based on the voltage measurement in the loop is used. This method is discussed in § 5.3.

Figure 4.20 shows the current during the passing of the projectile for the first measurement point for the first shot discussed in Chapter 5. The current variation cannot be neglected in our experiments. The velocity of the projectile is considered constant during the passing of the projectile at the measurement points.

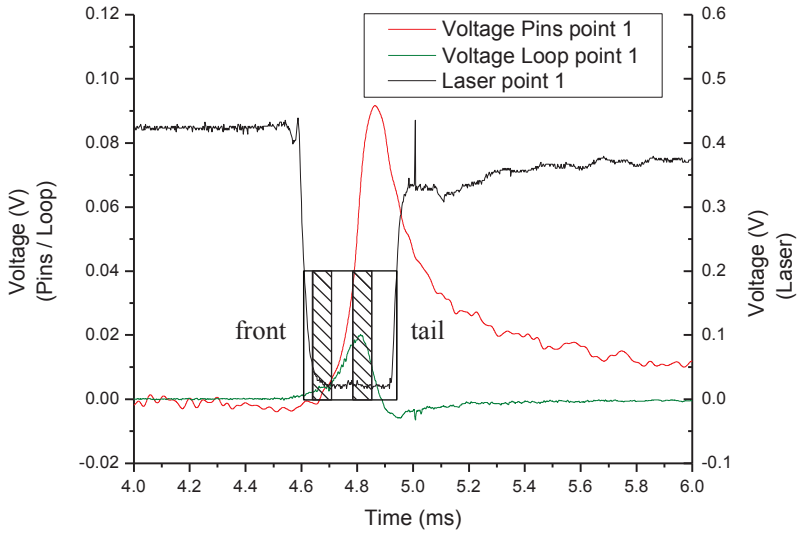

Fig. 4.19: Measurement of the current distribution: Voltage between the pins and in the loop measured during the first shot at the first measurement point, $z_1 = 0.295$ m.

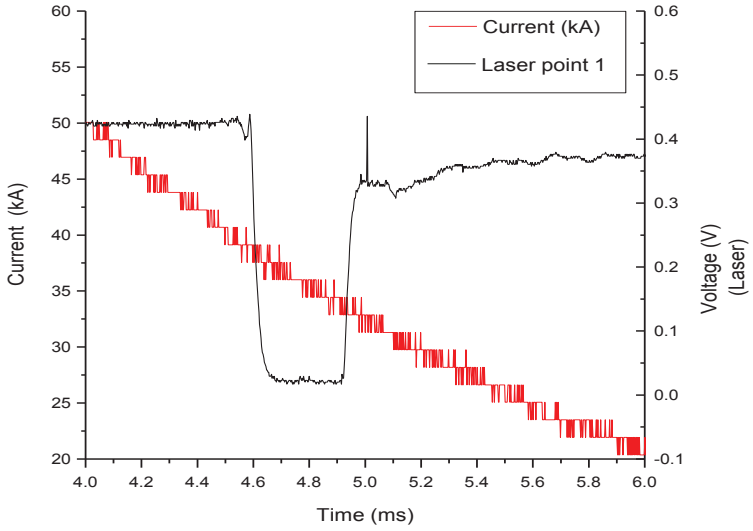

Fig. 4.20: Measurement of the current distribution: Current measured during the first shot while the projectile passes the first measurement point, $z_1 = 0.295$ m.

4.6. Conclusion

The experimental set-up with LARC/LARA allows determining the total current in the inner and outer rails, the voltage at the capacitor banks and the muzzle voltage. The detection of the projectile in the measurement points and at the muzzle provides information of the position of the projectile and allows estimating the velocity in these points. The results of the current distribution measurements will be discussed in the next chapter and a comparison between the experimental data and the simulations will be made.

Chapter 5

Analysis of the Results and Estimation of the Current Repartition between the Two Brushes

5.1. Introduction

In Chapter 2 we have developed a model with PSpice able to simulate the behavior of an augmented railgun and to forecast the speed at the muzzle, the current in the rails for a given voltage of the capacitor banks and the current distribution in the brushes and therefore their overheating. The current distribution and the temperatures in the armature may also be determined by using ANSYS software knowing the current in the rails. Both softwares have their advantages and drawbacks and they are complementary. It is hence interesting to validate these models through experiments.

In Chapter 4 we discussed the measurement techniques used for the experiments on the test bench. The augmented railgun can also be used as a conventional one. The number of capacitor banks is limited so the speed at the muzzle is also limited to about 100 m/s for projectiles with a mass of about 20 g. To obtain the current distribution in the armatures, a technique with measurement of the voltage between two pins and proposed by [SCH05a] has been used. We will see that this method which gives acceptable results for a high speed experiment has some drawbacks for low speed and does not introduce sufficient information to determine the current distribution between the two armatures which equip the projectile.

The voltage induced in the loop which is necessary to use this method may give also some indication on the current distribution and we propose to use it. Thanks to some assumptions, it is possible to estimate the ratio between the two currents even though the results are not always conclusive. The other results concerning the speed at the different measuring points allow validating the PSpice model.

5.2. Example of a Shot

5.2.1. Laser Signal and Velocity

A velocity profile of the projectile is not experimentally determined. The detection of the passing of the projectile at the measurement point is done with a laser as described in § 4.4. In Fig. 5.1 we see an example of a laser signal. The signal is disturbed by the discharge of the capacitor banks at 2 ms. The voltage drop between 4.5 and 5 ms corresponds with the passing of the projectile. In most experiments the profile of the laser measurement allows an estimation of the average velocity of the projectile while passing the measurement point. For the calculation of the flux variation we had to introduce a correction factor for the velocity based on a linearity approximation to obtain the correct position at the right time.

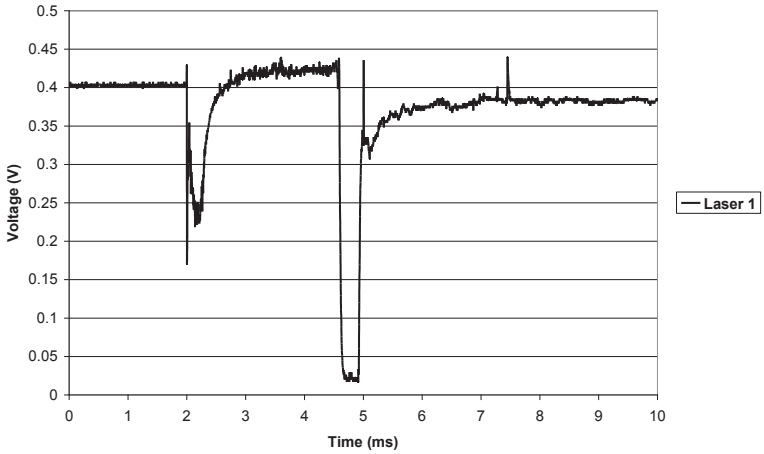

Fig. 5.1: Laser signal at measurement point 1 (z = 0.295 m) for the detection of the passing of the projectile

5.2.2. Non-Augmented Railgun

5.2.2.1 Shots with Two Capacitor Banks

Five shots are carried out with the railgun LARC for the configuration with two capacitor banks (Fig. 5.2) and one pulse forming coil. The discharge time t_0 and initial voltage U_0 for each bank and the mass of the projectile before $m_{pr,0}$ and after $m_{pr,b}$ the shot are listed in Table 5.1. The same projectile was used for all shots. The brushes showed no visible wear even though progressive mass loss was established. Both capacitor banks are discharged simultaneously.

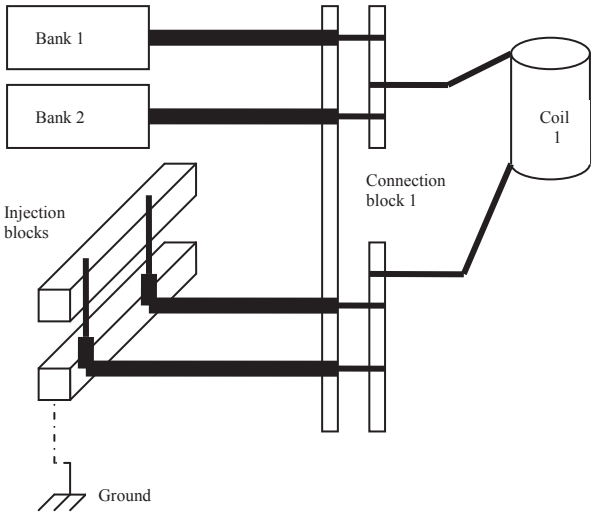

Fig. 5.2: LARC: Configuration with two capacitor banks

Table 5.1: LARC: Discharge time t_0 and initial voltage U_0 for the configuration with two capacitor banks

	Bank 1 U_0 (kV)	Bank 1 t_0 (ms)	Bank 2 U_0 (kV)	Bank 2 t_0 (ms)	$m_{pr,0}$ (g)	$m_{pr,b}$ (g)
1	8	0	8	0	19.86	19.86
2	7	0	7	0	19.86	19.85
3	8	0	8	0	19.85	19.81
4	7	0	7	0	19.81	19.77
5	8	0	8	0	19.77	19.52

Table 5.2: LARC: Measured velocities for the configuration with two capacitor banks

	z_1 = 0.295 m	z_2 = 0.465 m	z_3 = 0.895 m	z_{muzzle} = 1.5 m
	v_1 (m/s)	v_2 (m/s)	v_3 (m/s)	v_{muzzle} (m/s)
1	106.5	111.8	102.2	84.6
2	80.2	81.5	50.1	DNL*
3	108.9	118.4	100.8	85.8
4	91.3	95.1	70.4	48.3
5	115.5	126.1	108.3	101.6

* DNL: Did not leave

The measurement of the current distribution was carried out in two points along the rails, z_1 = 29.5 cm and z_2 = 46.5 cm. The passing of the projectile in these points and in z_3 = 89.5 cm, was detected with lasers and photodiodes. The measured signal allows an estimation of the corresponding velocities v_1, v_2 and v_3. These velocities and the velocity at the muzzle v_{muzzle} are listed in Table 5.2. The velocity at the muzzle was measured with a light barrier. During the second shot, the projectile did not leave the railgun.

The experimental results for the measurement of the current distribution for the first shot are presented in Fig. 5.3 and Fig. 5.4. The voltage between the pins is negative for the passing of the first brush. This negative signal is due to the eddy currents in front of the projectile. Therefore the method presented in [SCH09] and discussed in Chapter 4 cannot be used. It is not possible to match both signals before the passing of the first brush. The measured signals have a bad signal-to-noise ratio (SNR). The signals presented in Fig. 5.3 and 5.4 are smoothed with a Fast Fourier Transform (FFT) filter from the data analysis software Origin.

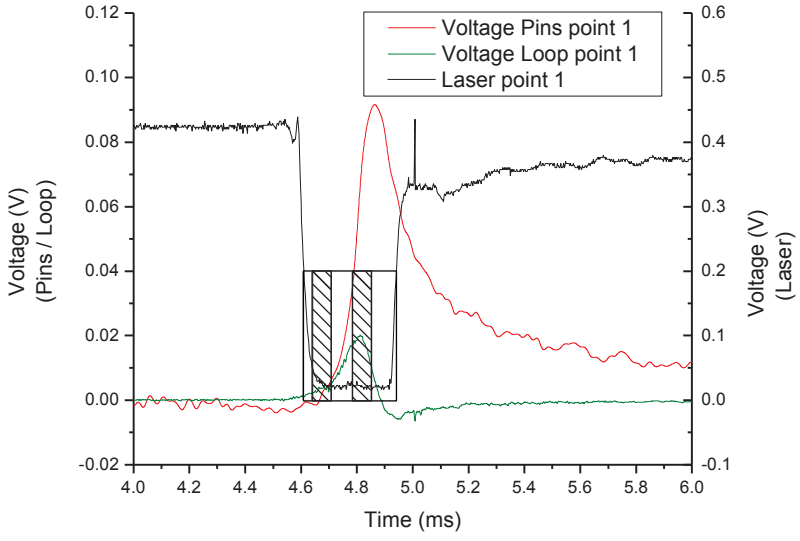

Fig. 5.3: Measurement of the current distribution: Voltage between the pins and in the loop measured during the first shot at the first measurement point, z_1 = 0.295 m.

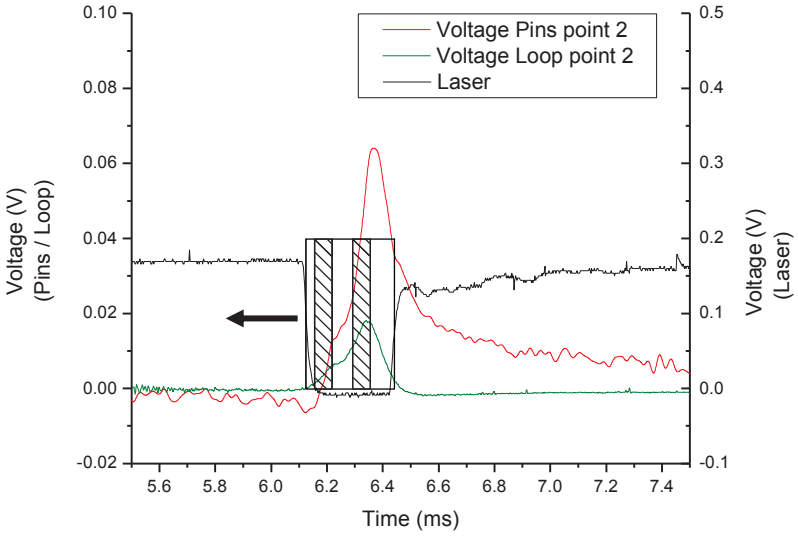

Fig. 5.4: Measurement of the current distribution: Voltage between the pins and in the loop measured during the first shot at the second measurement point, $z_2 = 0.465$ m.

5.2.2.2 Shots with Three Capacitor Banks

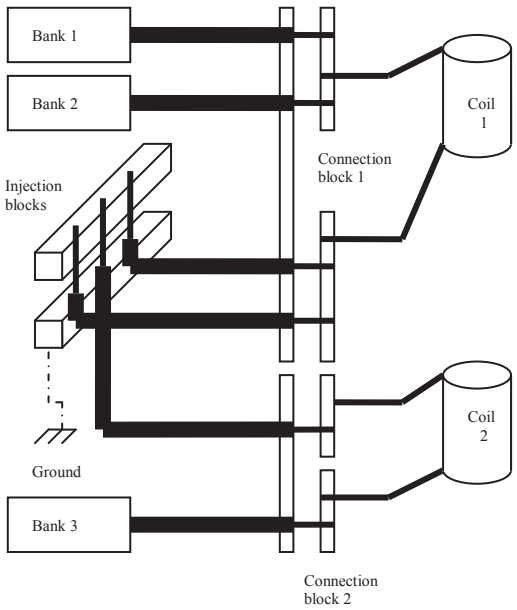

Fig. 5.5: LARC: Configuration with three capacitor banks

The configuration with three capacitor banks is presented in Fig. 5.5. Bank 1 and 2 are connected with the same pulse forming coil. A second pulse forming coil is used for bank 3. The first and second capacitor banks are discharged simultaneously. The discharging time t_0 of the third bank is varied. Five shots are carried out; the discharge time t_0 and initial voltage U_0 for each bank and the mass of the projectile before $m_{pr,0}$ and after $m_{pr,b}$ the shot are listed in Table 5.3. The projectile used in the 6th shot was not recovered. The brushes of the projectiles showed wear after the shots. A new projectile for each shot was used.

The measured velocities are listed in Table 5.4. The discharging of the capacitor banks disturbs the laser signal and for several points the velocity could not be determined (Fig. 5.6.).

Table 5.3: LARC: Discharge time t_0 and initial voltage U_0 for the configuration with three capacitor banks

	Bank 1 U_0 (kV)	Bank 1 t_0 (ms)	Bank 2 U_0 (kV)	Bank 2 t_0 (ms)	Bank 3 U_0 (kV)	Bank 3 t_0 (ms)	$m_{pr,0}$ (g)	$m_{pr,b}$ (g)
6	7	0	7	0	7	0	19.97	-
7	7	0	7	0	7	3	19.96	19.92
8	7	0	7	0	7	2.5	20.03	20.00
9	7	0	7	0	7	1.5	19.86	19.83
10	8	0	8	0	8	1.5	19.79	19.71

Table 5.4: LARC: Measured velocities for the configuration with three capacitor banks
(- = measurement unavailable due to data acquisition problem)

	z_1 = 0.295 m	z_2 = 0.465 m	z_3 = 0.895 m	z_{muzzle} = 1.5 m
	v_1 (m/s)	v_2 (m/s)	v_3 (m/s)	v_{muzzle} (m/s)
6	142.2	159.1	157.1	153.2
7	-	121.6	110.8	100.0
8	-	-	120.5	117.7
9	138.2	158.9	160.4	154.1
10	-	-	213.0	214.4

The experimental results are presented in Fig 5.6 and 5.7. Again the voltage measured between the pins becomes negative due to the eddy currents in front of the projectile. The voltage measured with the loop represents the flux variation. This signal becomes negative after the passing of the brush towards the breech, as expected. This effect is less pronounced in the second measurement point because the current is decreasing slower at that point.

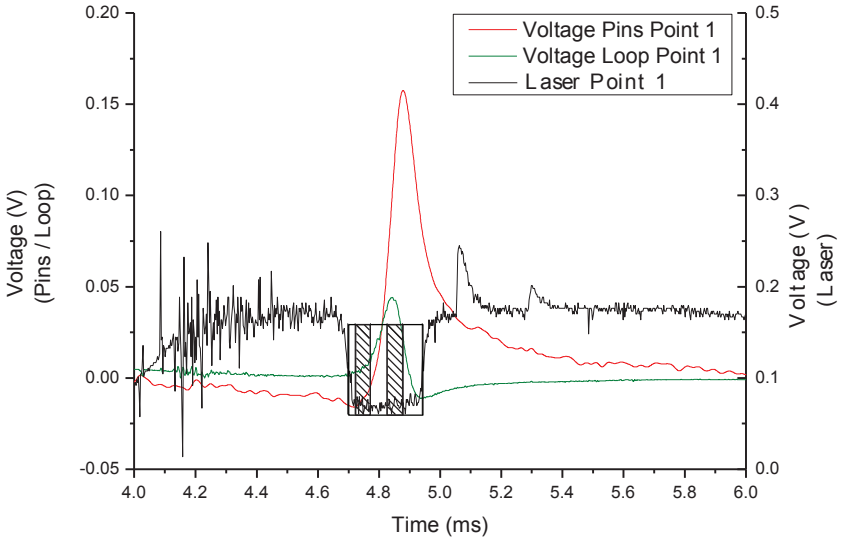

Fig. 5.6: Measurement of the current distribution: Voltage between the pins and in the loop measured during the shot 9 at the first measurement point, z_1 = 0.295 m.

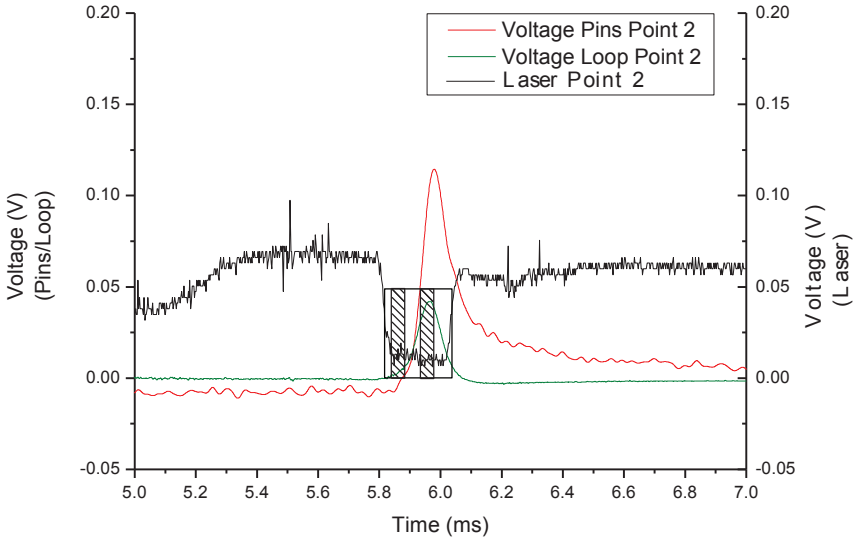

Fig. 5.7: Measurement of the current distribution: Voltage between the pins and in the loop measured during the first shot at the second measurement point, $z_2 = 0.465$ m.

5.2.3. *Augmented Railgun*

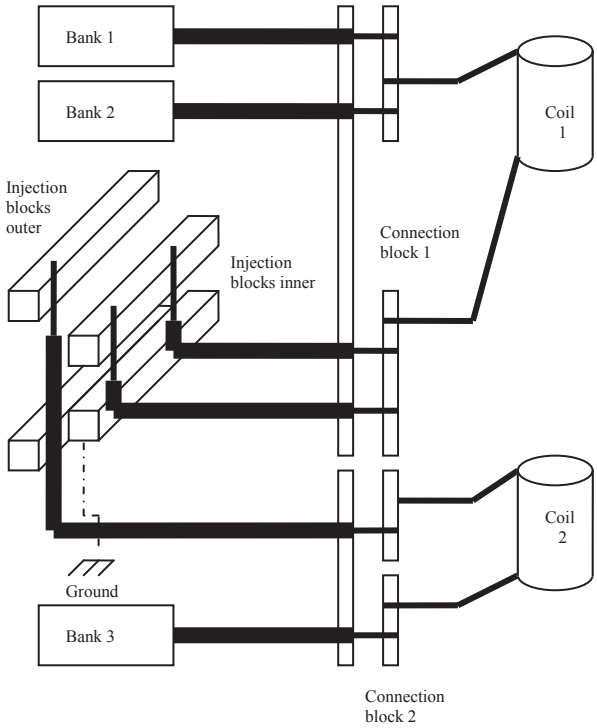

Fig. 5.8: LARA: Configuration with three capacitor banks

Only two shots were carried out with the augmented railgun LARA with three capacitor banks. The configuration in presented in Fig. 5.8. The discharge time t_0 and initial voltage U_0 for each bank and the mass of the projectile before $m_{pr,0}$ and after $m_{pr,b}$ the shot are listed in Table 5.5. Again for each shot a new projectile was used because of the wear of the brushes. Two capacitor banks (1 and 2) are used for the inner circuit and one for the augmenting circuit. Otherwise the projectile would not leave

the railgun. During the third shot, the gate of the thyristor of third capacitor bank burned out. The measured velocities are listed in Table 5.6.

Table 5.5: LARA: Discharge time t_0 and initial voltage U_0 for the three capacitor banks

	Bank 1 U_0 (kV)	Bank 1 t_0 (ms)	Bank 2 U_0 (kV)	Bank 2 t_0 (ms)	Bank 2 U_0 (kV)	Bank 2 t_0 (ms)	$m_{pr,0}$ (g)	$m_{pr,b}$ (g)
11	8	0	8	0	8	0	19.92	19.81
12	8	0	8	0	8	1	19.84	19.86*

* The mass increase may be due to a material deposit during the shot

Table 5.6: LARA: Measured velocities for the configuration with three capacitor banks

	z_1 = 0.295 m	z_2 = 0.465 m	z_3 = 0.895 m	z_{muzzle} = 1.5 m
	v_1 (m/s)	v_2 (m/s)	v_3 (m/s)	v_{muzzle} (m/s)
11	145.8	166.6	171.6	164.3
12	140.7	158.6	160.4	151.2

The experimental results for the measurement of the current distribution for shot 11 are represented in Fig. 5.9 and 5.10. The voltage measured with the loop shows the presence of a current in the brush towards the muzzle in the first measurement points. In the case of the first shot with the non-augmented railgun with two capacitor banks, the presence of this current is more pronounced in the second measurement point. This suggests that the current distribution between the current brushes improves towards the end of the shot. The voltages measured with the loop in an augmented railgun suggests a better current distribution at the first point. This corresponds with the expected influence of the augmenting current.

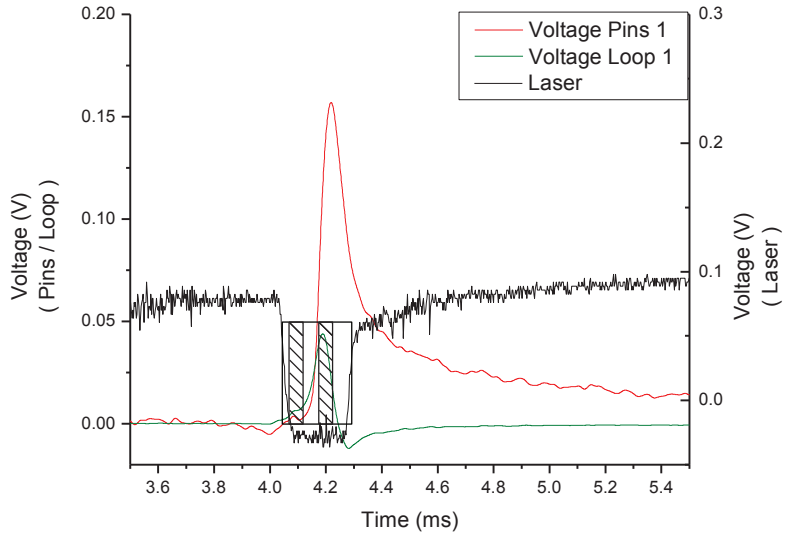

Fig. 5.9: Measurement of the current distribution: Voltage between the pins and in the loop measured during shot 11 at the first measurement point, z_1 = 0.295 m.

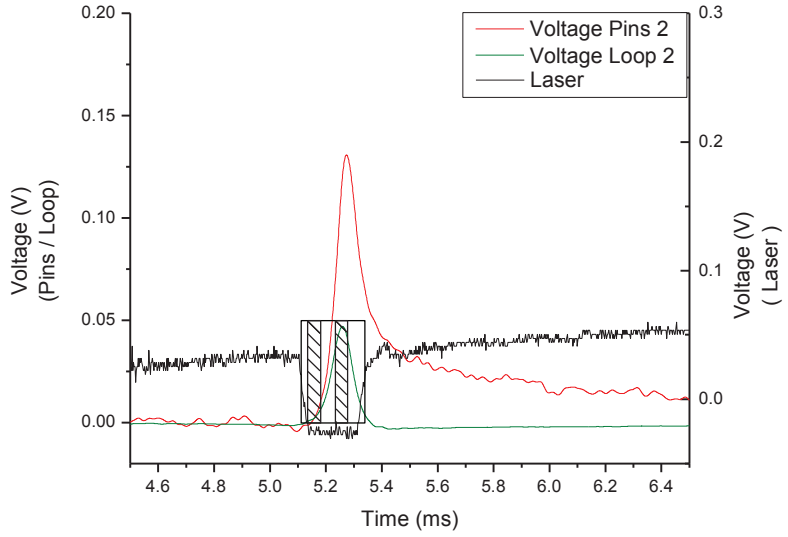

Fig. 5.10: Measurement of the current distribution: Voltage between the pins and in the loop measured during shot 11 at the second measurement point, $z_2 = 0.465$ m.

5.2.4. Conclusion

If we take a closer look at the voltage measured in the loop at the first measurement point (Fig. 5.9), the signal indicates the presence of a current in the current brush towards the muzzle. An analytic method discussed in § 5.3. is developed to estimate the current ratio.

5.3. Analytic Calculation of the Voltage in the Loop [COF10]

5.3.1. Principle

The measurement of the current distribution between the armatures of the projectile is discussed in § 4.5. At two fixed points along the rails the voltage between two pins in the rails and in a loop, Fig. 4.16, are measured. In this paragraph an analytic method to estimate the voltage in the loop is discussed. The voltage in the loop corresponds with the flux variation through the surface defined by the loop:

$$V_{loop} = n\frac{d\Phi}{dt} \tag{5.1}$$

with n the number of windings, in this case n = 1. In order to calculate this flux variation three hypotheses are made. First the current profile in the rails is not taken into account; we represent the rails with a thread line conductor. This hypothesis is realistic if we consider the current density distribution in a brush given in for example Fig. 3.7 and repeated here in Fig. 5.11a. It means that the current in the rail is also located in a small strip as shown on Fig. 5.11b. The simplest modeling consists of a long straight wire but the solution proposed in Fig. 5.11d is also possible with a current distribution of 70% in the middle and 15% for the two other conductors. The final result is not modified. A second assumption is that the surface of the loop is considered small compared with the other dimensions and thirdly the magnetic induction **B** is considered constant. B is calculated by using the BIOT-SAVART law. The development is given in the Annex.

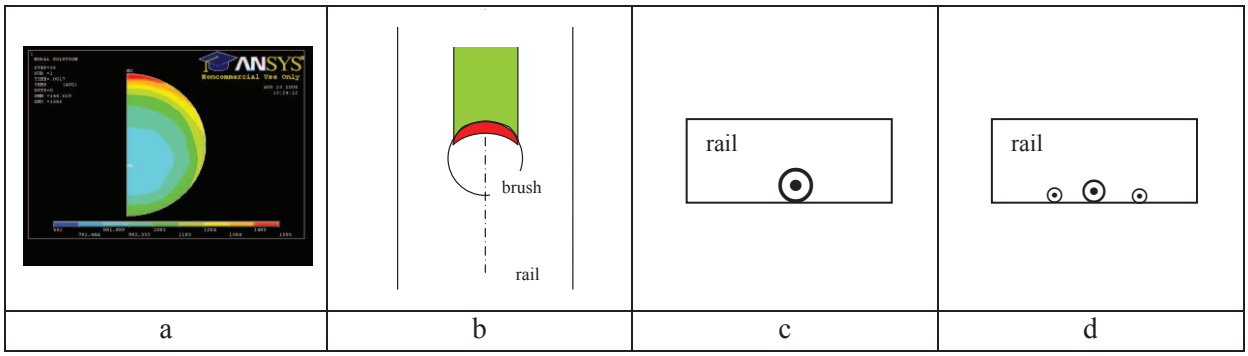

Fig. 5.11: Modeling of a current brush by a strip (a,b), a wire (c) or a combination of wires (d).

5.3.2. *Non-Augmented Railgun*

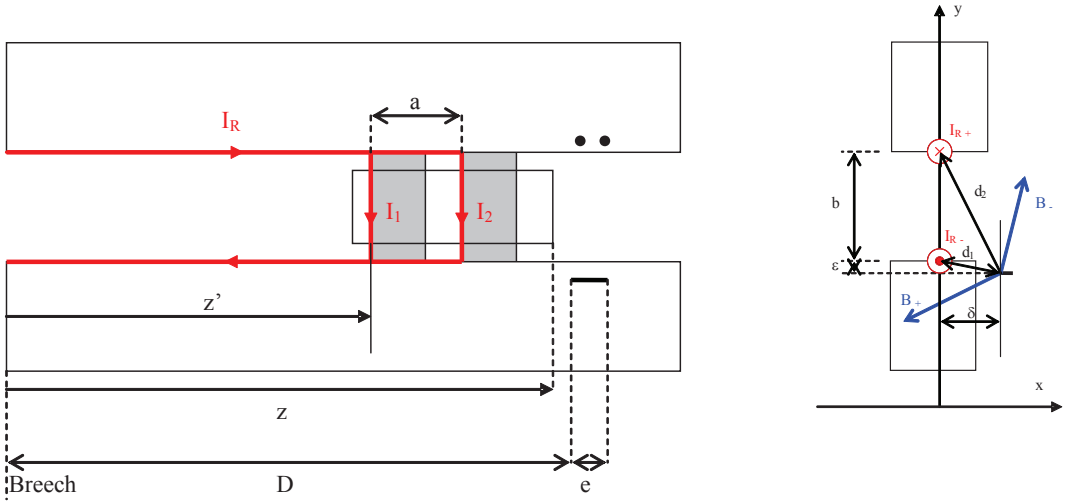

Fig. 5.12: Geometry of the measurement of the current distribution between the brushes of the projectile.

The axis of the loop is parallel with the *y*-axis of the figure which corresponds with the axes of the current brushes. Therefore there is only a contribution of the horizontal current in the rails and not from the current on the current brushes.

$$\Phi = \frac{\mu_0 s \delta}{4\pi} C(D, z', \lambda, v, t) \cdot I_R(t) \tag{5.2}$$

C is depending on the geometry of the railgun, on the position of the loop, on the projectile position through *z'* but also on its velocity and on the ratio $\lambda = I_1/I_R$. δ represents the distance between the centre of the loop and the y-axis and *s* is the section of the loop.

Fig. 5.13 shows the influence of λ at point P_1; the scale is arbitrarily chosen for the amplitude. The geometric parameters are given in Table 5.7. The velocity *v* is considered constant and equal to v = 100 m/s. The current at this point is fitted as an exponential with a time constant equal to τ_R:

$$I_R(t) = I_{Rm} \exp\left(\frac{-t}{\tau_R}\right) \tag{5.3}$$

Table 5.7: Geometrical dimensions for the voltage loop

a	0.015 m	ε	0.0025 m
b	0.015 m	D	0.270 m
δ	0.0075 m	τ_R	2 ms

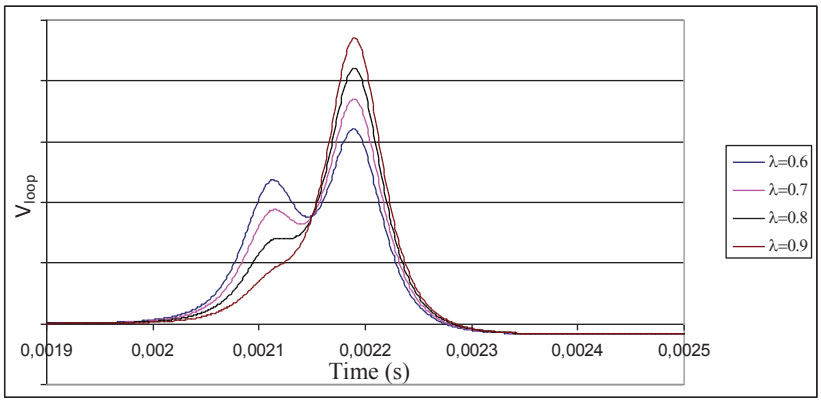

Fig. 5.13: Example of evolution of loop voltage vs time at z = 0.295 m.

5.3.3. Augmented Railgun

The principle is the same. Due to an invariant geometry, the induced voltage caused by the augmenting field depends only on the variation of the current I_A. To the previous expression, we have to add a second term proportional to I_A.

$$\Phi = \frac{\mu_0 s\delta}{4\pi}\left[C(D,z',\lambda,v,t)\cdot I_R(t) + C'(D)I_A(t)\right] \tag{5.4}$$

The current in the outer rail is also fitted with an exponential with a time constant τ_A :

$$I_A(t) = I_{Am}\exp\left(\frac{-t}{\tau_A}\right) \tag{5.5}$$

In these conditions, the loop voltage is given by

$$V_{loop} = \frac{n\mu_0 s\delta}{4\pi} I_{Rm}\left[\frac{d}{dt}C(D,z',\lambda,v,t)\cdot\exp\left(\frac{-t}{\tau_R}\right) - \frac{I_{Am}}{I_{Rm}}\frac{C'(D)}{\tau_A}\exp\left(\frac{-t}{\tau_A}\right)\right] \tag{5.6}$$

with n the number of turns of the test coil. The geometry is presented in Fig. 5.14.

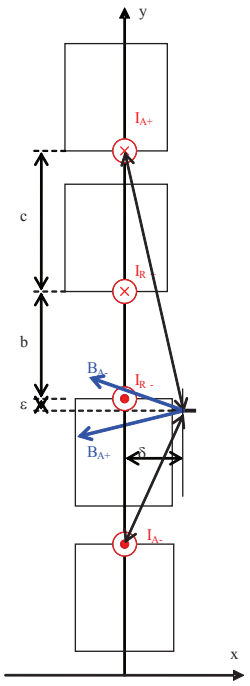

Fig. 5.14: Geometry for an augmented railgun, cross-section of the rails.

Fig. 5.15 shows the influence of the outer rail for the same geometry as before with I_{Am}/I_{Rm}= 2.00, λ = 0.80, τ_A = 2.5 ms, L_A = 1.5 m and c = 0.021 m. The difference is very small and decreases with I_{Am}.

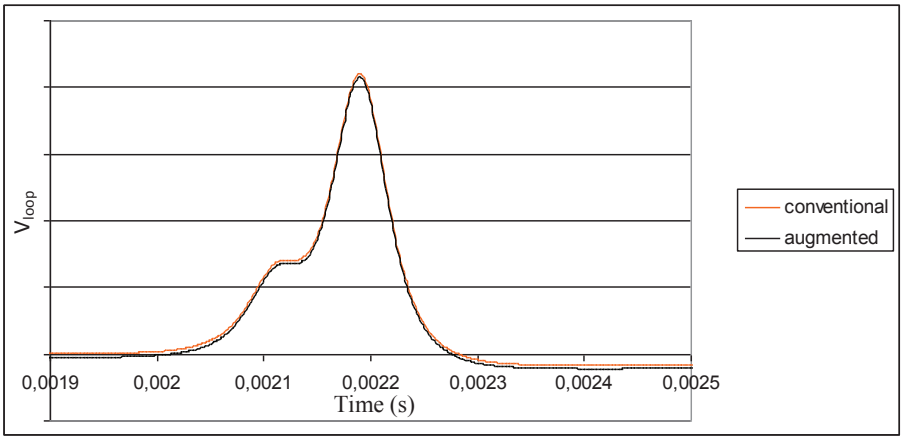

Fig. 5.15: Comparison of loop voltage between augmented and non augmented railgun at z = 0.295 m

5.3.4. *Influence of Current in the Loop between the Two Brushes*

The variation vs. time of the current in the augmented rail creates a current i_{loop} in the loop formed by the two brushes and parts of the inner rails. The movement of the projectile does not influence the mutual inductance between the two circuits. If we consider that the current in the augmenting rail may be delayed by a time t_d than I_A is given by:

$$t_d \le t \le t_{0A} + t_d \qquad I_A = I_{Am} \sin\left(\frac{\pi}{2}\frac{t - t_d}{t_{0A}}\right) \tag{5.7}$$

$$t_{0A} + t_d \le t \qquad I_A = I_{Am} \exp\left(-\frac{t - t_d - t_{0A}}{\tau_A}\right) \tag{5.8}$$

In these conditions (cf. Annex) the current in the loop is given by:

$$t_d \le t \le t_{0A} + t_d \qquad i_{loop} = D_1\left[-\cos\varphi_c \exp\left(-\frac{t - t_d}{\tau_c}\right) + \cos\left(\frac{\pi}{2}\frac{t - t_d}{t_{0A}} - \varphi_c\right)\right] \tag{5.9}$$

$$t_{0A} + t_d \le t$$

$$i_{loop} = \left[-D_1\cos\varphi_c \exp\left(-\frac{t_{0A}}{\tau_c}\right) + D_1\sin\varphi_c - D_2\right]\exp\left(-\frac{t - t_d - t_{0A}}{\tau_c}\right) + D_2\exp\left(-\frac{t - t_d - t_{0A}}{\tau_A}\right) \tag{5.10}$$

The flux in the test probe is therefore given by

$$\Phi = \frac{\mu_0 s\delta}{4\pi}\left[C(D,z',\lambda,v,t)\cdot I_R(t) + C'(D)I_A(t) + C''(D,z',v,t)i_{loop}\right] \tag{5.11}$$

and the voltage induced in the loop is given by eq. 5.1.
If $t_{0A} << t - t_d$ the flux in the loop is given by

$$\Phi = \frac{\mu_0 s\lambda}{4\pi}\left[C(D,z',\lambda,v,t)\cdot I_R(t) + C'(D)I_A(t) + C''(D,z',v,t)\cdot K_A I_A(t)\right] \tag{5.12}$$

and

$$V_{loop} = \frac{\mu_0 s \lambda}{4\pi} I_{Rm} \left[\frac{d}{dt} C(D,z',\lambda,v,t) \cdot \exp(\frac{-t}{\tau_R}) - \frac{I_{Am}}{I_{Rm}} \frac{C'(D)}{\tau_A} \exp(\frac{-t}{\tau_A}) + K_A \frac{I_{Am}}{I_{Rm}} \frac{d}{dt} C''(D,z',v,t) \exp(\frac{-t}{\tau_A}) \right] \quad (5.13)$$

It must be noticed that the real current in the brushes are respectively $I_1 = \lambda I_R - i_{loop}$ and $I_2 = (1-\lambda) I_R + i_{loop}$. Their ratio can be estimated at each point.

5.3.5. *Conclusion*

The different expressions are based on thread line conductors and the current in the loop is calculated by using constant parameters. This is not true due to skin effect evaluating during a shot. In spite of some assumptions, this analytic development allows to give an idea about the ratio λ. The variation of the velocity will be fitted with a linear approximation, because we know the velocity only at the points P_1 and P_2. The velocity at the muzzle cannot be used, because the velocity is decreasing due to friction forces associated to an electromagnetic force decreasing.

Fig. 5.6. shows the influence of i_{loop} on V_{loop} for an augmented railgun. The curves in Fig. 5.17 show the influence of the ratio $\mu = I_{Am}/I_{Rm}$ on voltage in the loop when taken into account i_{loop}. They have been obtained for $\lambda = 0.8$ at point P_1. It is clear that the current in the armature loop has a great influence on the current in the brushes.

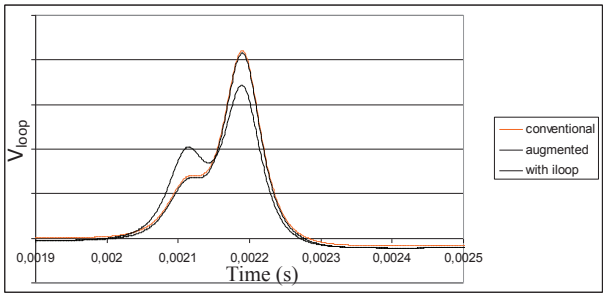

Fig. 5.16: Comparison of V_{loop} when i_{loop} is taken into account

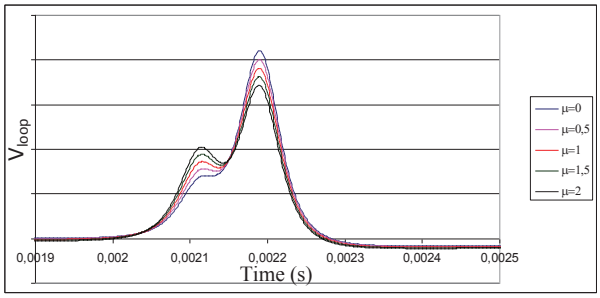

Fig.5.17: Influence on V_{loop} of the ratio μ

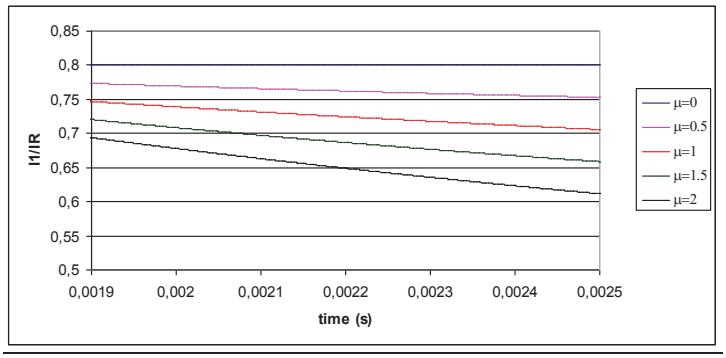

Fig. 5.18: Influence of the ratio μ on I_1 / I_R

The Fig. 5.18 represents the evolution of the ratio I_1 / I_R vs. time for different values of μ. It shows clearly that this ratio depends considerably on the circulating current i_{loop}. This figure demonstrates the favourable influence of the augmenting current I_A on the current repartition in the armatures. The Fig. 5.18 has been obtained for an initial value $\lambda = 0.8$ which corresponds to a conventional railgun.

5.4. Calculations with the Finite Element Code ANSYS

As described in Chapter 3, we simulate in ANSYS a fixed projectile. This means that the velocity skin effect is not taken into account. In a first simulation we used the total current and injected it in the rails, which corresponds with the realistic situation when the capacitor banks are discharged in a railgun with a fixed projectile. In the experiments the projectile moves during the shot. The diffusion in the rails starts with the passing of the projectile. In the ANSYS simulations the diffusion in the rails after the projectile starts when the capacitor banks are discharged. So the diffusion in the rails in the simulations for the method with the total currents will be further evolved at the moment corresponding with the passing of the projectile. To reduce the diffusion in the rails, the method described below was used. Instead of starting the current injection of the rails at the beginning of the shot, we adapted the currents as presented in Fig. 5.19.

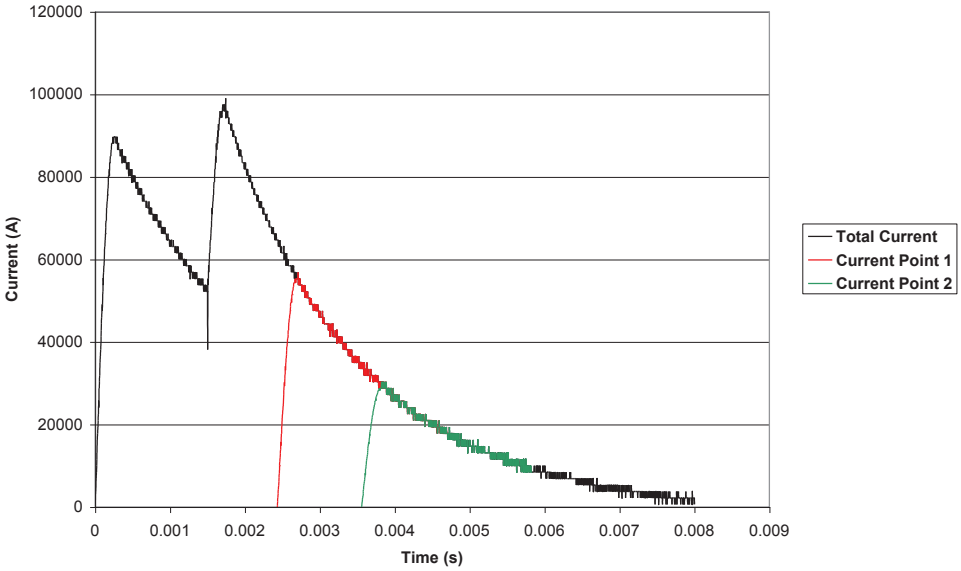

Fig. 5.19: Total and adapted currents I_R for the ANSYS simulations for shot 9

The red and green curves in Fig. 5.19 represent the currents used in the ANSYS simulations for the first and second measurement point.We used the original current profile (black curve in Fig. 5.19) from the moment the projectile passes the measurement point until 2 ms later. To simulate the rising part, we used the first part of the original current profile [0-0.26 ms] until the first maximum is reached. The rise time (t_r = 0.26 ms) was respected and the amplitude was adapted to fit the original current profile for the passing of the measurement point. In this case the diffusion in the rails starts later and will be limited.

However several remarks have to be made. The diffusion in the rails starts at the moment the projectile passes but the diffusion in the current brushes starts at the beginning of the shot. The diffusion in the current brushes will be incorrect. The temperature of the current brushes is also a point of concern. We have to define a starting temperature for the simulation because the total current runs to the projectile and not the current we use for the simulations. We make an estimation of this temperature based upon the first simulations with the total current.

The use of the adapted currents limits the diffusion in the rails but still does not simulate the velocity skin effect. The diffusion in the rails start at the injection of the current for each point of the rails and will already start during the rise time, t_r = 0.26 ms. The movement of the projectile is not accounted for. The rise time is the same for each calculation. So although the projectiles have different velocities while they pass the measurement points, the diffusion is the same.

For the augmented railgun, the discussion becomes more complex. The diffusion in the inner rails starts at the moment the projectile passes, for the outer rails the diffusion over the total length of the rails starts at the beginning of the shot. A first possibility is to adapt the current in the outer rails as we did with the current in the inner rails. In this case the diffusion in the outer rails is incorrect. The augmenting current will also influence the current in the inner rails. The armatures of the projectile and the rails form a loop. The augmenting field will induce a current in this loop proportional to dI_A/dt. During the rise time of the augmenting current in the simulations, the augmenting current in the experiments shows an exponential decay. So the influence of the augmenting circuit will be different. A second possibility is to start the diffusion in the outer rails first so the diffusion is already in place and the augmenting current shows an exponential decay at the moment the current in the inner rail is injected. But still the augmenting field will induce a current in the loop even before current in the inner rails is injected. The starting temperature for this simulation has to be defined before the injection of the augmenting current and will be influenced. Both methods were explored. The influence of the augmenting current during the rise time in the first method with adapted currents could not be neglected. The results of the second method with adapted currents are presented in § 5.6.

5.5. Calculations with the PSpice Code

The PSpice code, discussed in Chapter 2, represents a global model of the railgun. It allows the calculation of the total currents, the position and the velocity of the projectile. The velocity skin effect is modeled. The calculated velocities, currents and the current distribution between the brushes will be discussed and compared with the experimental results.

5.6. Comparison of the Results

In this paragraph we compare the results obtained with the global and local simulations and the analytical calculations with the obtained experimental results. Two shots with the non-augmented railgun and the two shots with the augmented railgun will be discussed in detail.

5.6.1. Non-Augmented Railgun LARC

5.6.1.1. Shot 1

For the first shot two capacitor banks (thyristor) with an initial voltage of 8 kV are discharged simultaneously. Fig. 5.20 compares the experimentally obtained current with the PSpice calculations. A good correspondence is found for the maximum. The current obtained with the PSpice calculations decays faster than the experimental current.

Table 5.8 compares the experimental velocities with the PSpcice results. The calculated velocities show an overestimation of the velocity. For the muzzle velocity we find an overestimation of 18.8%. PSpice underestimates the current. This suggests an overestimation of the inductances used for the electromagnetic force model or an underestimation of the friction force. The muzzle voltage is presented in Fig. 5.21. The muzzle voltage represents the voltage over the current brushes and can be used to detect transition. We didn't find loss of contact between the brushes and the rails in any of the experiments discussed in this chapter. This was expected because we worked with, for railgun standards, low velocities.

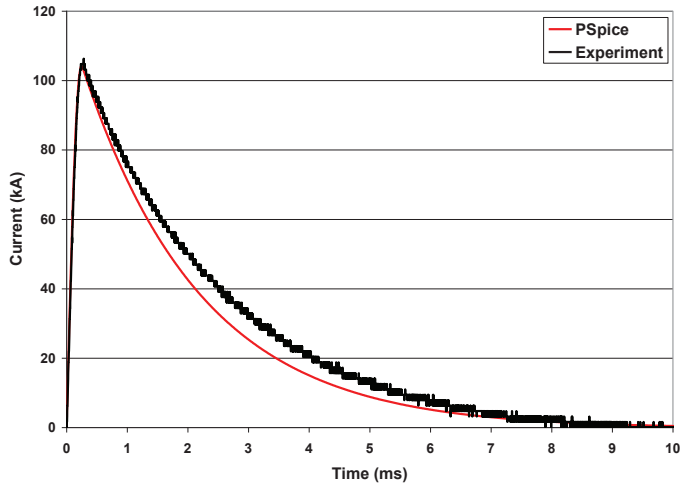

Fig. 5.20: Comparison between experimental and simulated current I_R

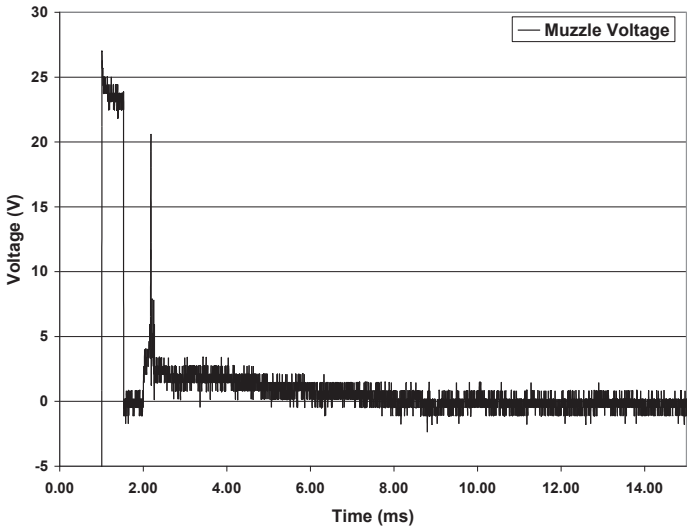

Fig. 5.21: Voltage at the muzzle

For an estimation of the current distribution between the brushes we use the analytical method discussed in § 5.3. For the current, we used an exponential fit of the experimental current for the period of the passing of the projectile. The velocities used for the calculations are listed in Table 5.8 and the parameters of the exponential fit for both measurements points are represented in Table 5.9. The exact surface of the loop is not known and the results presented in Fig. 5.22 and 5.23 are scaled to fit the maximum of the experimental signal. This method allows a crude estimation of the current based in the rising part of the signal. In the first measurement point about 25 % of the current flows through the brush towards the muzzle, for the second point about 20 % is found. Table 5.9 presents the current ratios calculated with the PSpice model. The values for the first and second measurement point are not far apart: 23.7 -22.9 %. The best current ratio is found in the first measurement point.

With the finite element code two simulations are used, the simulation with the method for the total currents in which the non-adapted current is injected from the beginning and the method with adapted currents in which the inner current is injected just before the projectile arrives at the measurement point. In the first method, 52 % of the current flows through the brush towards the muzzle, with the adapted method 31 % of the current. PSpice takes into account the velocity skin effect. We expect to find the highest current ratio I_I/I_R for the highest velocity. The heating of the brushes has also an influence on the current distribution. The current brush towards the breech will have a higher

temperature and thus a higher resistance. This effect increases in time. Still we find with PSpice the lowest current ratio at the first measurement point.

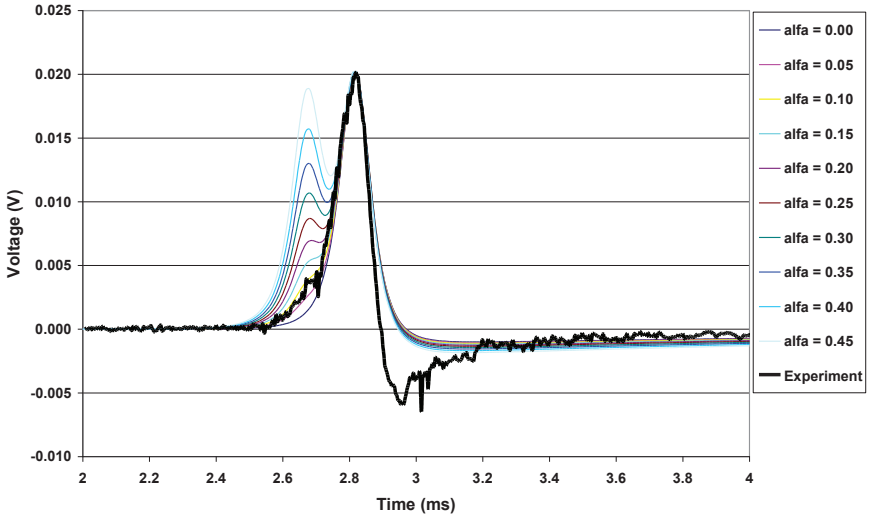

Fig. 5.22: Estimation of $\alpha=1-\lambda$ at point P_1 ($z = 0.295$ m)

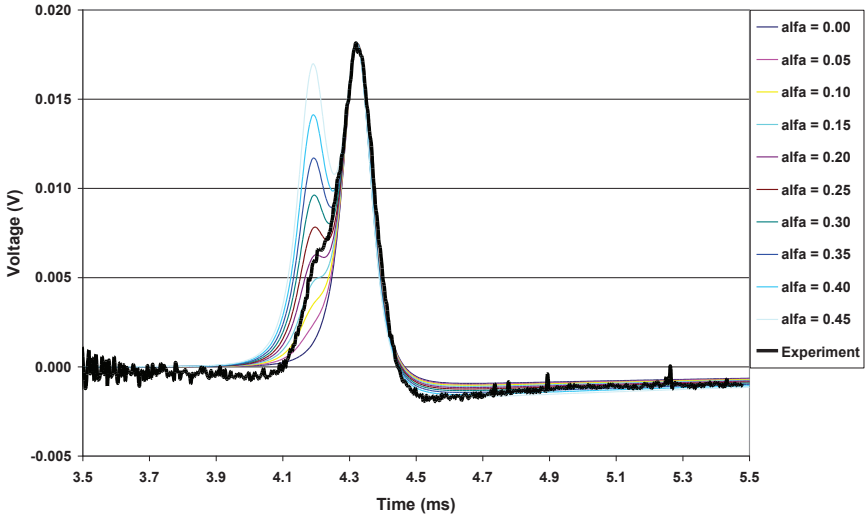

Fig. 5.23: Estimation of $\alpha=1-\lambda$ at point P_2 ($z = 0.465$ m)

Table 5.8: Comparison between experiments and simulations for shot 1

	Measurements		PSpice						ANSYS	Ana.
	time (ms)	v (m/s)	t (ms)	v (m/s)	I_R (kA)	I_1 (kA)	I_2 (kA)	I_1/I_R	I_1/I_R	I_1/I_R
Point 1	2.76	106.5	2.82	112	27.9	21.3	6.6	0.763	0.692	≈0.75
Point 2	4.28	111.8	3.95	115	12.835	9.901	2.9	0.771	0.691	≈0.8
Point 3	8.13	102.2	6.73	111	1.6	1.2	0.4	0.772		
Muzzle	19.12	84.6	13.80	101						

Table 5.9: Approximation of the measured current

	I_{Rm} (kA)	τ_R (ms)
Point 1	121.9	2.26
Point 2	145.3	2.05

5.6.1.2. Shot 9

For the ninth shot with LARC, three capacitor banks with an initial voltage of 7 kV were used. The first two capacitor banks were discharged simultaneously, the third capacitor bank was delayed by Δt = 1.5 ms. In Fig. 5.24 a comparison between the experimental current and the current simulated with PSpice is presented. Again the current calculated with PSpice decreases faster. The muzzle voltage measured during shot 9 is presented in Fig. 5.25. The signal is disturbed by the discharges of the capacitor banks. The experimentally determined and calculated values for the current ratio I_I/I_R are listed in Table 5.10.

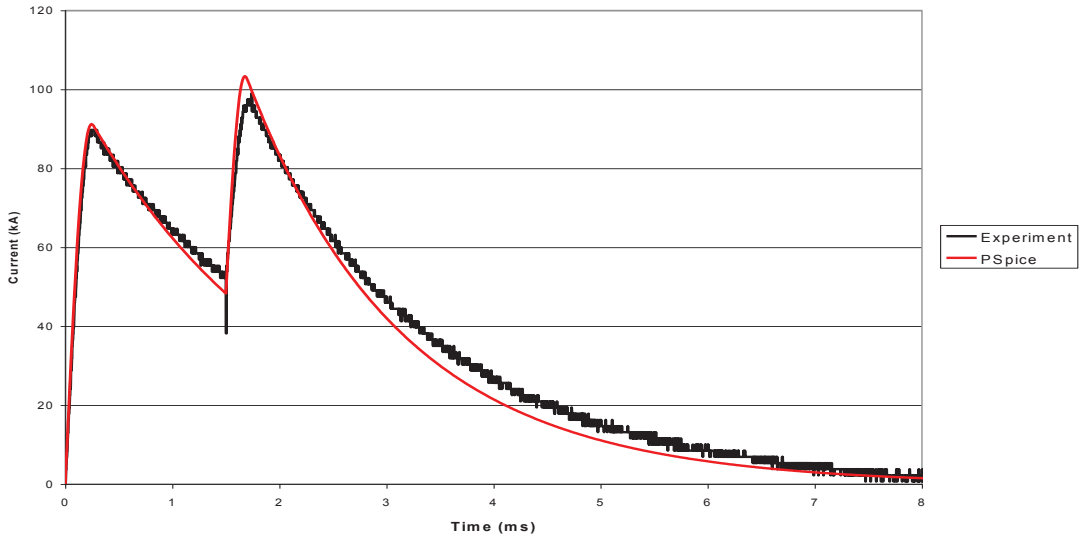

Fig. 5.24 Comparison between the experimentally measured current and the simulated current with PSpice for shot 9

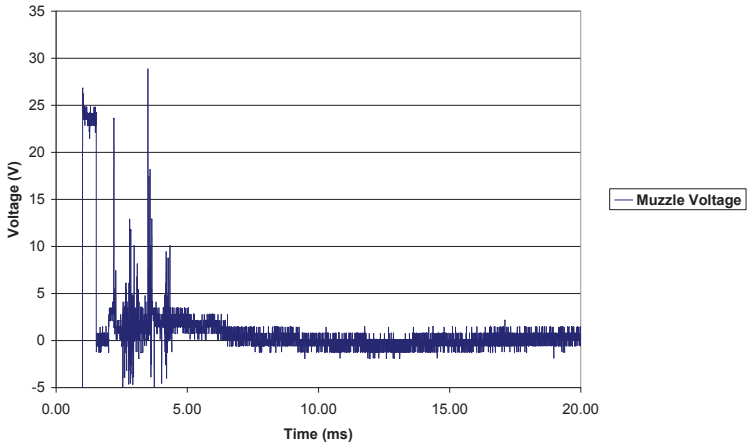

Fig.5.25: Experimentally measured muzzle voltage for shot 9

Table 5.10: Comparison between experiments and simulations for shot 9

	Measurements		PSpice			ANSYS	Ana.
	time (ms)	v (m/s)	t (ms)	v (m/s)	I_I/I_R	I_I/I_R	I_I/I_R
Point 1	2.78	138.2	2.85	144	0.772	0.683	≈0.85
Point 2	4.28	158.9	3.98	156	0.787	0.689	≈0.90
Point 3	8.13	160.4	6.73	155	0.790		
Muzzle	14.03	154.1	10.70	149			

5.6.1.3. Comparison between Measurements and Simulation

The comparison for the current shows clearly that the decrease is overestimated by PSpice. The increase of the current seems to correspond much better. This is due to difficulties to estimate the parameters of the circuit. On one side, L'_R has been approximated by a constant value obtained at 1 kHz till 0.2 ms to reach, after a linear variation, a constant value at 10 Hz after 1.5 ms. On the other side, the resistance varies continuously due to the skin effect (current variation and velocity effect). Nevertheless the errors are limited and especially for shot 9 where three capacitor banks are used with a delay for the third.

If we compare the velocities of the measurements and the simulations we can observe that the error is small but the duration of the shot estimated by PSpice is about 20% less than in reality. This means that the friction losses are not well appreciated. Probably the coefficients also depend on the temperature which is increases during the shot. The armatures may also come under stress and deformations may occur.

The comparison of the ratio I_l/I_R is not conclusive. The approximations in using ANSYS have been explained in § 5.4. PSpice leads to reasonable values but the analytical values give only an order of magnitude.

5.6.2. Augmented Railgun LARA

The parameters for the two shots are given in Table 5.5 and we will first give the different results before comparing measurement and simulation.

5.6.2.1 Shot 11

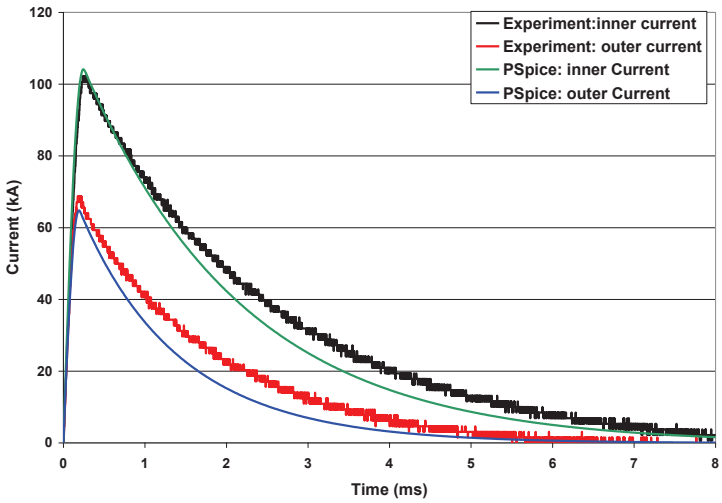

Fig. 5.26: Comparison between the experimentally measured current and the simulated current with PSpice for shot 11

In shot 11 the two capacitor banks for the inner circuit and the capacitor bank for the outer circuit are discharged simultaneously. The experimental and simulated currents are compared in Fig. 5.26. Fig. 5.27 shows the experimentally measured muzzle voltage for shot 11. The signal is coupled optically and the measurement starts 2 seconds before the discharging of the capacitor banks in the inner circuit. The measured muzzle voltage is negative during the positive slope of the augmenting

current I_A. The parameters for the current fitting necessary for the analytical values at points P_1 and P_2 are given in Table 5.11.

Table 5.11: parameters of the fitted currents

Point	I_{Rm} (kA)	τ_R (ms)	I_{Am} (kA)	τ_A (ms)
P_1	113.1	2.35	77.7	1.64
P_2	116.6	2.29	101.2	1.43

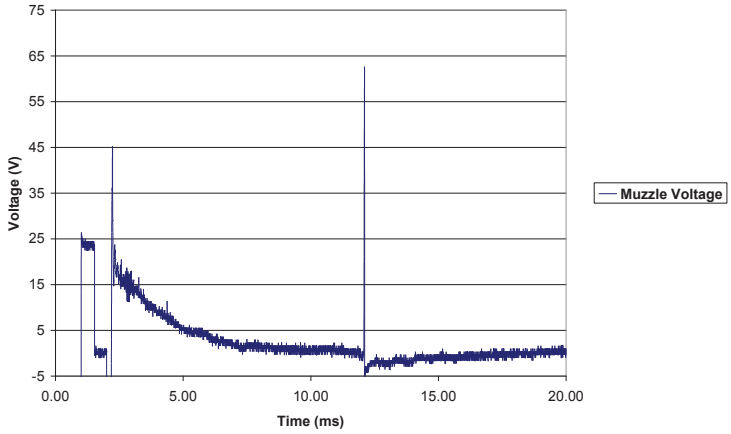

Fig. 5.27: Experimentally measured muzzle voltage for shot 11

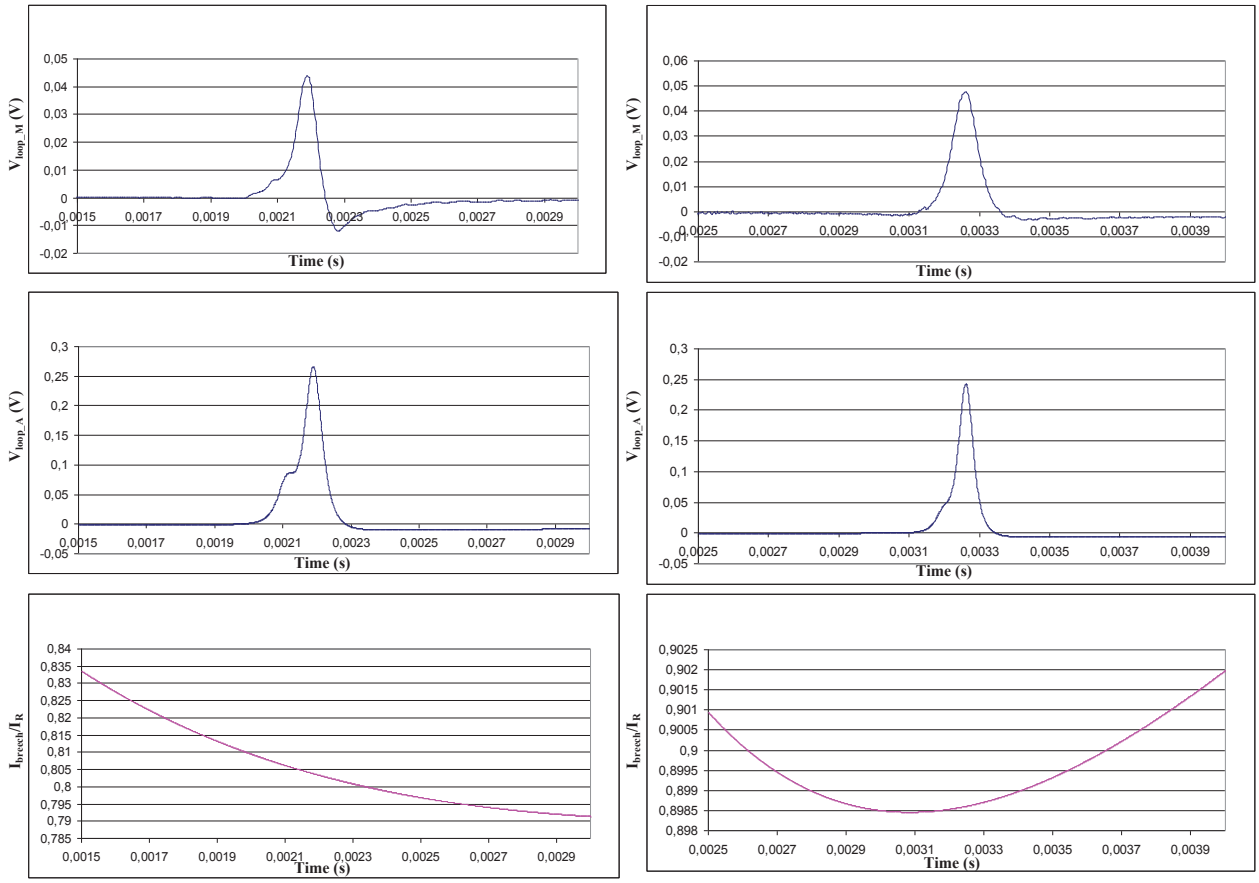

Point P_1; z_1 = 0.295m

Point P_2; z_2 = 0.465m

Fig.5.28: Comparison between measurements and analytical approach

The curves V_{loop_M} in Fig. 5.28 have been obtained during the tests but as said before, the signals are very noisy, so they have been filtered. This may result in loss of information. The curves V_{loop_A} have been obtained knowing the currents and the velocity at the different points. An exponential form has been used to fit the experimental currents and it can be observed that they decrease slower than expected by the PSpice simulations. At point P_1 a similarity can be observed between the two curves representing the voltage in the loop. It must be noticed that the maxima are obtained for the same time instant which is an indication of coherence of the proposed method. The amplitudes are not in a constant ratio. The results are not so clear at point P_2. It is difficult to explain why. Probably it is linked with measurement difficulties. The current repartition between the two brushes can be estimated and the decrease of the outer current leads to a non constant ratio. The different results are summarized in Table 5.11 for the shot 11.

Table 5.11: Comparison of the results for the current distribution in the measurements points for shot 11

Shot 11	Experiments		PSpice			ANSYS	Ana
x (m)	t (ms)	v (m/s)	t (ms)	v (m/s)	I_1/I_R	I_1/I_R	I_1/I_R
0.295	2.046	145.8	2.02	165	0.721	0.745	0.8
0.465	3.116	166.6	3.02	177	0.745	0.758	0.9
0.895	5.631	171.6	5.40	180	0.770		
1.500	12.81	164.3	8.79	176	0.784		

5.6.2.2 Shot 12

The same method was also applied for the shot 12. The remarks formulated for shot 11 also hold for shot 12. During this shot the capacitor bank for the outer circuit was delayed by $\Delta t = 1$ ms. The experimental and simulated currents are presented in Fig. 5.29.

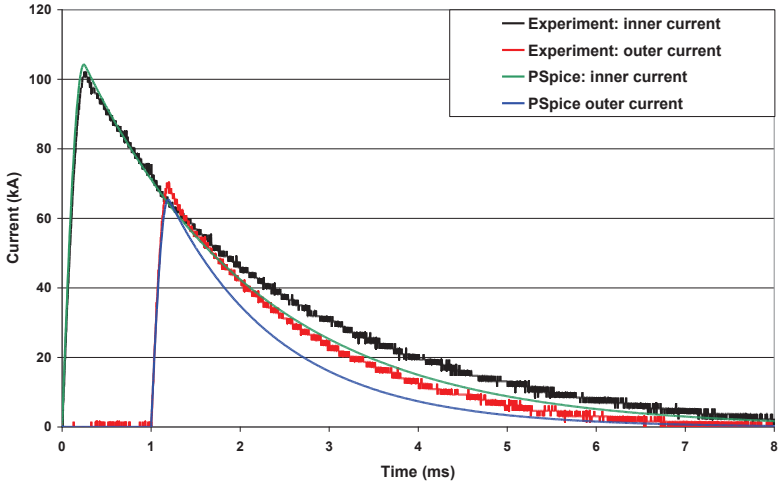

Fig. 5.29 Comparison between the experimentally measured current and the simulated current with PSpice for shot 12

Table 5.12: Parameters of the fitted currents

Point	I_{Rm} (kA)	τ_R (ms)	I_{Am} (kA)	τ_A (ms)
P_1	105.9	2.41	133	1.73
P_2	109.2	2.35	150.9	1.61

Figure 5.30 shows the experimentally measured muzzle voltage for shot 12. As in Fig. 5.27, the time t = 2 ms in the figure corresponds with the discharging time of the capacitor banks in the inner circuit. The measured muzzle voltage is again negative during the positive slope of the augmenting

current I_A. The curves in the center plot in Fig. 5.31 are calculated based on the parameters deduced from the experiments.

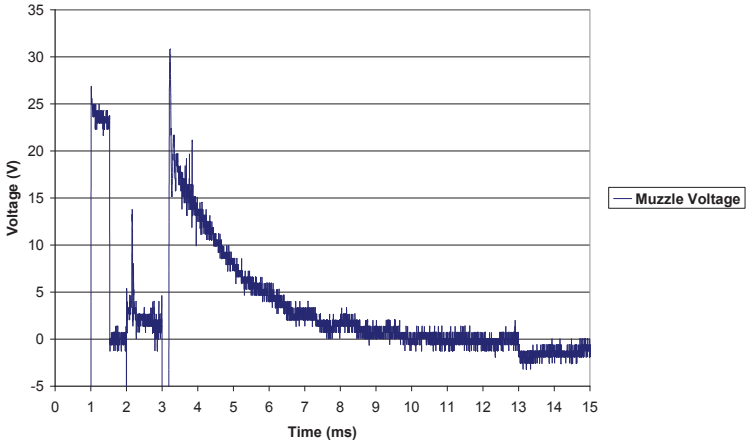

Fig. 5.30: Experimentally measured muzzle voltage for shot 12

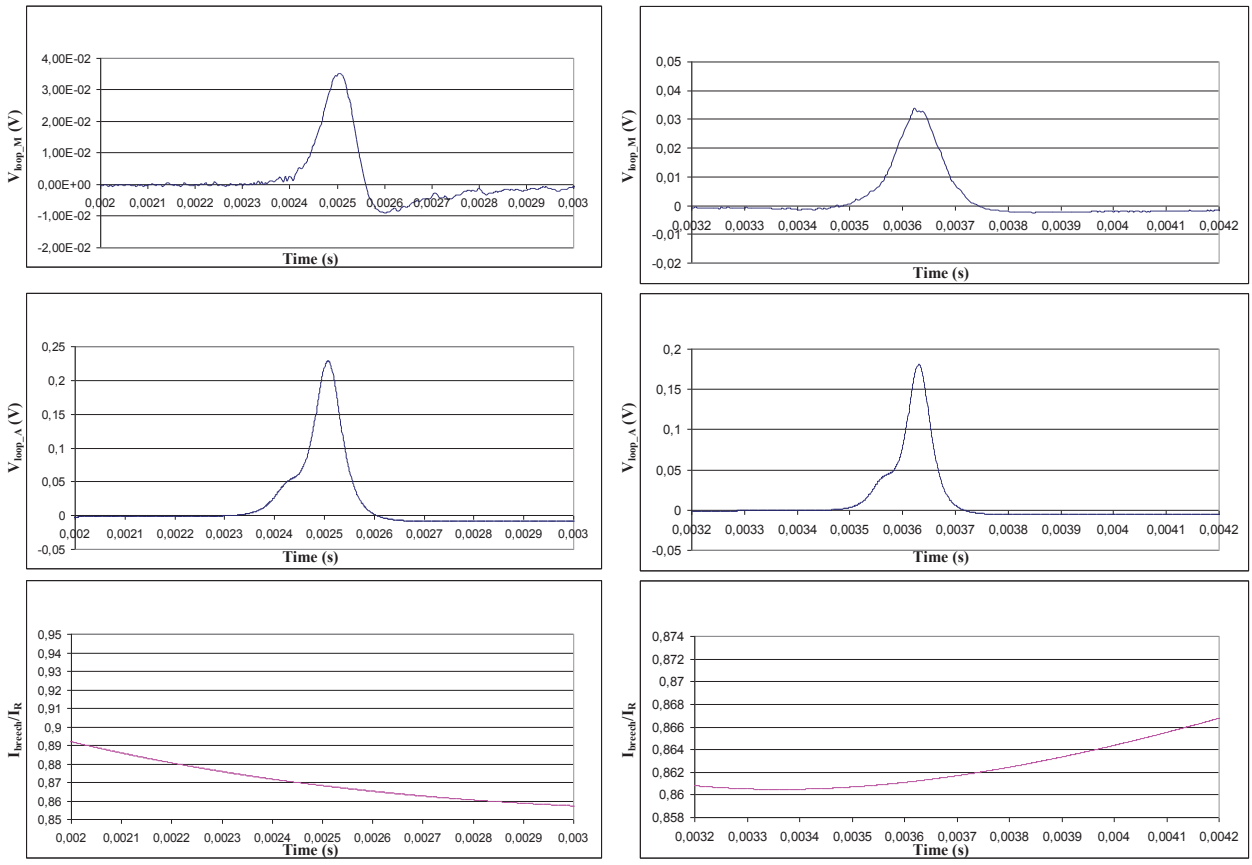

Point P_1; $z_1 = 0.295$m

Point P_2; $z_2 = 0.465$m

Fig.5.31: Comparison between measurements and analytical approach

Table 5.13: Comparison of the results for the current distribution in the measurements points for shot 12

Shot 12	Experiment		PSpice			ANSYS	Ana.
x (m)	t (ms)	v (m/s)	t (ms)	v (m/s)	I_1/I_R	I_1/I_R	I_1/I_R
0.295	2.358	140.7	2.55	138	0.693	0.711	0.87
0.465	3.478	158.6	3.74	147	0.698	0.724	0.86
0.895	6.159	160.4	6.66	146	0.740		
1.500	13.78	151.2	10.89	140	0.791		

5.6.2.3 Analysis of the Results

The number of shots is severly limited for the augmented railgun. Some coherence in the results can be observed even though the shot conditions were not the same.

- The simulations with PSpice tend to overestimate the decrease of the currents in the inner and the outer rails. The parameters of the circuit are variable but this is not sufficient to take into account all the phenomena.
- The energy used in the experiments was low and the velocities are not very high, about 100 to 160 m/s. The conditions to maintain solid contacts are respected as it can be verified with the measured muzzle voltage.
- The method proposed by [SCH09] is not applicable. As an example the curve in Fig. 5.32 represents the difference between the voltage at the pins and the voltage in the loop at point P_1. There is no information available to estimate the ratio of the current in the two brushes.
- Using the voltage in the loop offers more information. The accuracy is nevertheless not very high.
- The values given by the ANSYS simulations are erroneous because the moving of the projectile cannot be considered
- The comparison with the two other methods shows that the armature on the breech side supports about three quarters of the global inner current. This is about the same for the non-augmented railgun.
- The measurement techniques are complex but they have to be improved if we want to estimate the current distribution in the armature correctly.

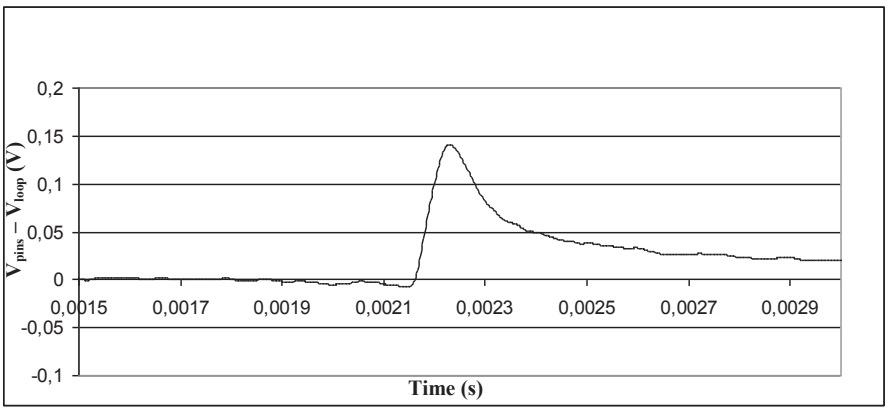

Fig. 5.32: Evolution of $V_{pins} - V_{loop}$ when the brushes passes across the point P_1

5.7 Conclusion

The final result is not what has been expected when we started this work. We were confident in the possibility to obtain an accurate current ratio between the two brushes and to demonstrate that the augmented railgun can have a positive influence on the current distribution in the armature. The techniques are not well adapted for low velocities and we could not explore any modifications of the proposed method due to a fault on a thyristor.

We have estimated the errors made by using PSpice and FEM by ANSYS software. The parameters of the circuit must be determined very precisely to take into account the skin effect and

velocity skin effect created by the current pulse and by the moving of the projectile. The mechanical behavior is also complex due to the friction between the brushes and the rails.

Despite all these uncertainties, the results obtained are satisfying. The errors on the velocities are less than 10%. This is probably in the same order as for chemical guns. Railguns are conceived for high muzzle velocities. They need high energy sources distributed on the length of the railgun as we will see in the next chapter devoted to the design of a high speed augmented railgun.

Chapter 6

Parametric Analyses for Augmented Railguns

6.1. Introduction

We have seen that railguns are electromagnetic launch systems which have the potential to accelerate projectiles to velocities higher than 2 km/s. For a conventional railgun, raising the current is the only way to increase the electromagnetic force on the projectile. Augmented railguns are able to reduce the constraints on the armature by limiting the heating of the sliding contacts between the rails and the brush armatures due to the Joule-effect and to the friction which can cause the melting of these contacts. The degrees of freedom are more important for an augmented railgun in comparison with a conventional one. Indeed, the current I_A may be defined independently in amplitude and shape. The geometry of the outer circuit has also to be defined to maximize the electromagnetic force.

In the first part, the forces on the outer rail and on the projectile will be studied. These simulations are a parametric study for the predesign of an augmenting circuit for the existing non-augmented railgun RAFIRA (RApid FIre RAilgun) according to ISL specifications. The simulations are made for another geometry and stand apart from the simulations and experiments with LARA discussed in the other chapters. RAFIRA has a square caliber of 25 mm and the inner rails have a rectangular cross-section of 25 mm x 20 mm. Therefore only a rectangular cross-section of the outer rails is considered. There are three parameters which can be varied, the distance g between the inner and the outer rails and the height and width of the last one. Three couples of currents I_R and I_A are fixed. Three methods are used to calculate the forces and will be discussed. A similar parametric study was discussed in [GAL03]. This leads to an optimized geometry. The objectives of this study are to design an augmented railgun capable of accelerating projectiles with a mass of 100 to 200 g to a velocity of 1 to 2 km/s, with the condition that the electromagnetic forces on the rails must be limited to 8 MN/m. This limit is based on the support structure used at ISL where the housing of the railgun is made of two separate blocks holding the rails, spaced by cylindrical supports and kept together with threaded rods in steel. The current in the outer rail, and thus the magnetic field, is limited by the electromagnetic forces on the rails. In § 6.2 we investigate the influence of the dimensions of the outer rail on the electromagnetic forces on the projectile and on the rails for an augmented railgun. These simulations will allow a rough design of a high power railgun. A complete design needs to examine also the global efficiency, the mechanical feasibility and the maximal current density in comparison with a conventional railgun for the same performances.

In the second part, we will optimize the projectile. The parameters we varied are the diameter of the two brushes and the distance between them. The simulations are made with the PSpice code for the LARA configuration.

In the last part we study the feeding of a railgun. Three types are considered, a classical augmented railgun for which the length of the inner rail is studied, a segmented railgun and a distributed energy storage (DES) railgun. The simulations are made with the PSpice code for the LARA geometry.

6.2. Optimization of the Position and the Dimensions of the Outer Rail [COF07]

6.2.1. Introduction

This study is based on the existing RApid FIre RAilgun RAFIRA at ISL. RAFIRA is a 3 m long conventional railgun with a square caliber of 25 mm. In the simulations, an augmenting pair of rails is added to the RAFIRA geometry. The influence of the position and the dimensions of these augmenting rails on the force on the projectile and the rails is studied. The dimensions for the inner rails are fixed and the objectives are to find a realistic optimum for the outer rail in terms of size and position to obtain a given value for the impulse and to limit the electromagnetic forces applied to the rails and especially the outer ones. In consultation with ISL, the following constraints are used:

- Muzzle velocity of 1 - 2 km/s for a projectile with a mass of 200 - 100 g; it means an impulse of 200 Ns.
- Electromagnetic forces on the rails less than 8.10^6 N/m

On one hand the electromagnetic force on the projectile must be maximum for given currents. On the other hand, forces on the rails determine the construction constraints and it is better to reduce them. As we will see later, both vary in the same way. So we will have to make a compromise.

Three geometric parameters are considered, the distance *g* between the inner and the outer rails, *b* and *h*, respectively the width and the height of the outer rail. The sizes of the inner rails are indicated on Fig. 6.1.

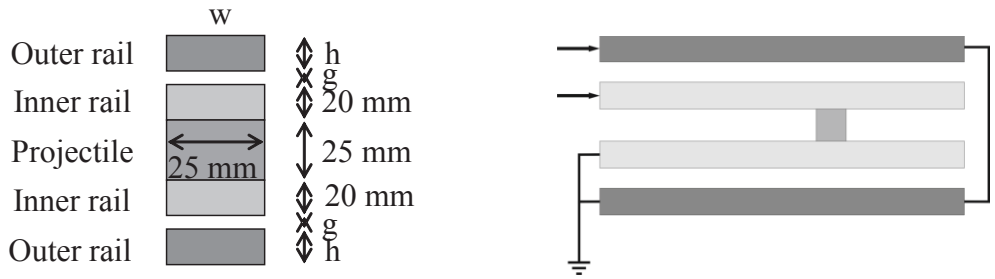

Fig. 6.1: Geometry of the augmented railgun

The current I_R is chosen arbitrarily and the amplitudes I_A are calculated to obtain the same impulse of 200 Ns on the projectile based on the railgun force equation with L'_R = 0.4 µH and M' = 0.2 µH for harmonic currents. Three couples of values are considered but the results are not all given. The currents used in the transient analyses are adapted so the maximum of the currents corresponds with the values in Table 6.1 and the impulse corresponds with 200 Ns.

Table 6.1: Couples of current in the inner and outer rails

I_R	400 kA	500 kA	600 kA
I_A	1267 kA	833 kA	511 kA

These currents are obtained by discharge of two capacitor banks with each five capacitors. So the current evolutions are like that given on Fig. 6.2. To reach the needed maximum given in Table 6.1, a coefficient is applied, i.e. the initial voltages on the capacitors are adapted.

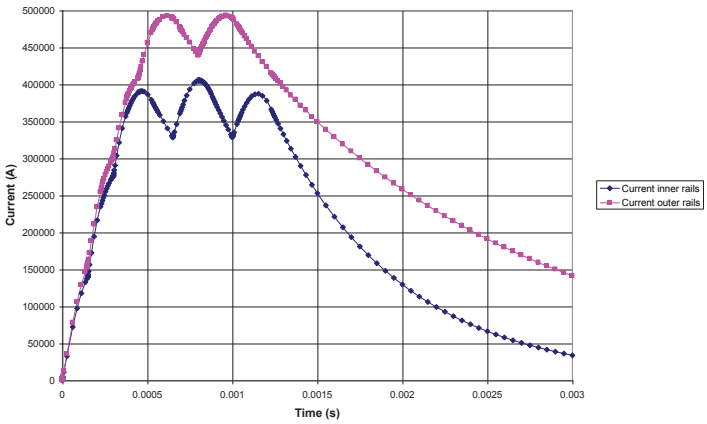

Fig. 6.2: Transient current applied to the inner and outer rails

To achieve this optimization, we will use the Finite Elements Code ANSYS. Two types of simulation will be needed:

- 2D simulations to compute the electromagnetic force on the rails. The calculation time for one case is short
- 3D-simulations to compute the force and the impulse on the projectile. Two methods are used:
  - directly with a 3D transient analysis with a fixed projectile; this takes a long time.
  - analytically with the force equation which is faster but necessitate to determine first L'_R and M'

6.2.2. Electromagnetic Forces on the Rails

6.2.2.1. Example of Electromagnetic Forces on the Rails

We propose two examples to illustrate this point. In the first case the current I_A (1267 kA) is important in comparison with the current I_R (400 kA). The geometric parameters are g = 5 mm, w = 24 mm and h = 20 mm. The outer rail is far enough from the inner rail (isolation issues) and is relatively large. All the forces are positive and the limit of 8.10^6 N/m is not reached (Fig. 6.3). The total EM force on the rails, represented by the red curve, is the sum of the electromagnetic force on the inner and outer rail and corresponds with the force on the housing of the rails.

In the second example the outer rail is thin and small (w = 2 mm and h = 2 mm) and near to the inner rail; the current impulses are the same. It can be observed in Fig. 6.4 that the electromagnetic force on the inner rail (black curve) is negative for a long time. Moreover the values exceed largely the fixed constraint of 8.10^6 N/m. The current densities in the rails for these geometries with current ratio 400 kA/1267 kA, show that the negative currents induced in the inner rail by the outer rail current are well spread at the surface of the inner rail towards the outer rail in the case of a large outer rail (Fig. 6.5a). For a small outer rail (Fig. 6.5b), the induced current is concentrated at the middle of the surface of the inner rail close to the outer rail with current densities higher than those of the injected current concentrated in the corners at the side of the projectile. Since the magnetic field is inversely proportional to the square of the distance, this explains why the magnetic force on the inner rails is negative (inwards). For construction reasons, negative forces on the inner rails have to be avoided.

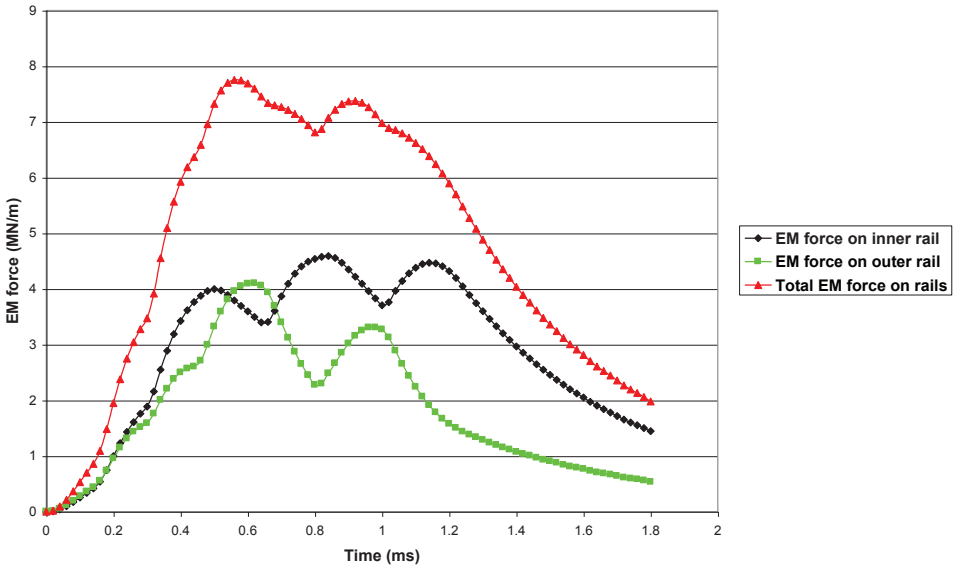

Fig. 6.3: Electromagnetic forces on the rails for a large outer rail (24 mm x 20 mm) determined with a 2D transient analysis; I_R = 400 kA and I_A = 1267 kA,

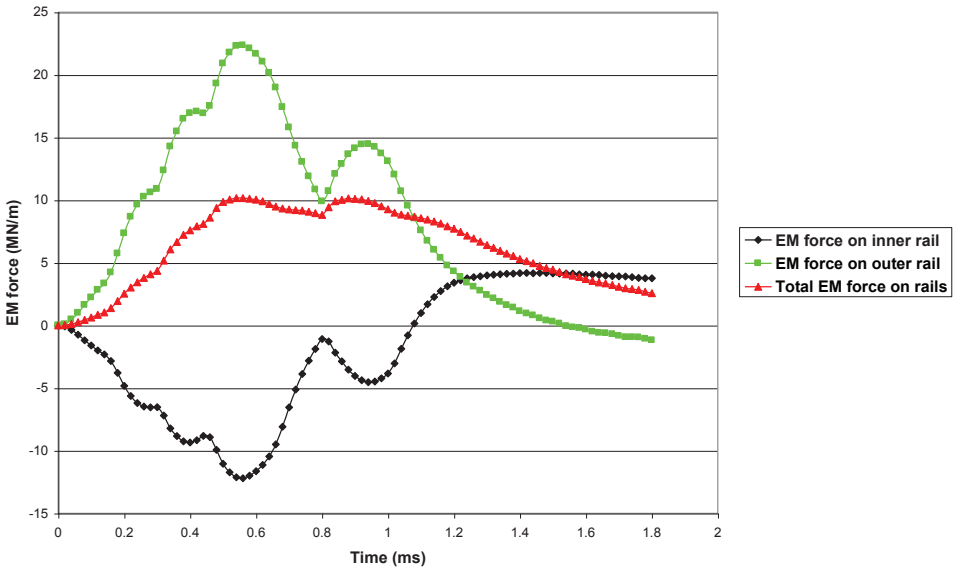

Fig. 6.4: Electromagnetic forces on the rails for a small outer rail (2mm x 2 mm) determined with a 2D transient analysis; I_R = 400 kA and I_A = 1267 kA

a b

Fig. 6.5: Model for the current distribution for a large outer rail (a) and a small outer rail (b)

6.2.2.2. Parametric Analysis

To compare the forces on the rails, we determine the maximum total force for each geometry and current ratio. Height *h* and width *w* vary first in a large domain ($2 \le w \le 40$ mm and $2 \le h \le 40$ mm) and a large area is also chosen for *g* ($1 \le g \le 15$ mm).

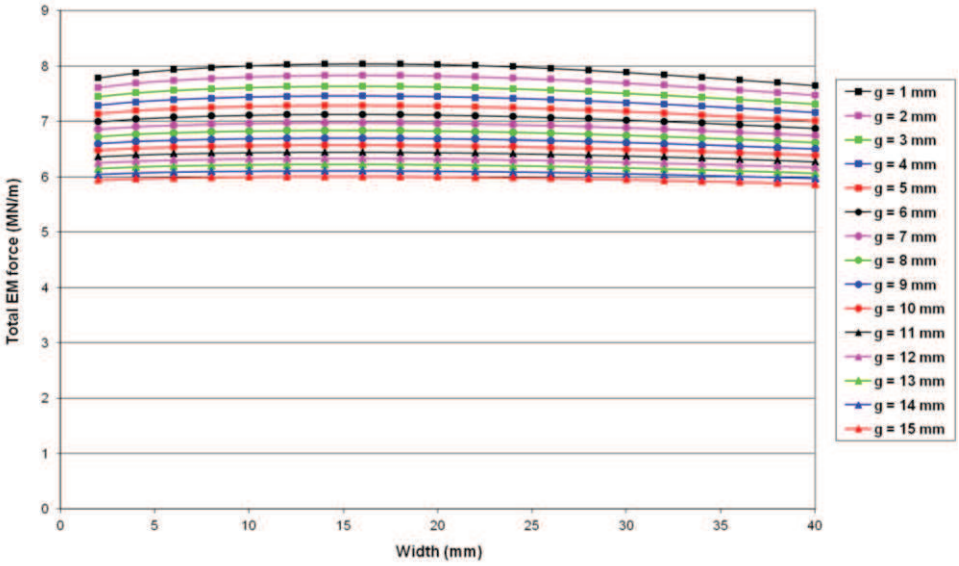

Fig. 6.6: Influence of the width of the outer rail on the total electromagnetic force
h = 24 mm (I_R = 400 kA and I_A = 1267 kA)

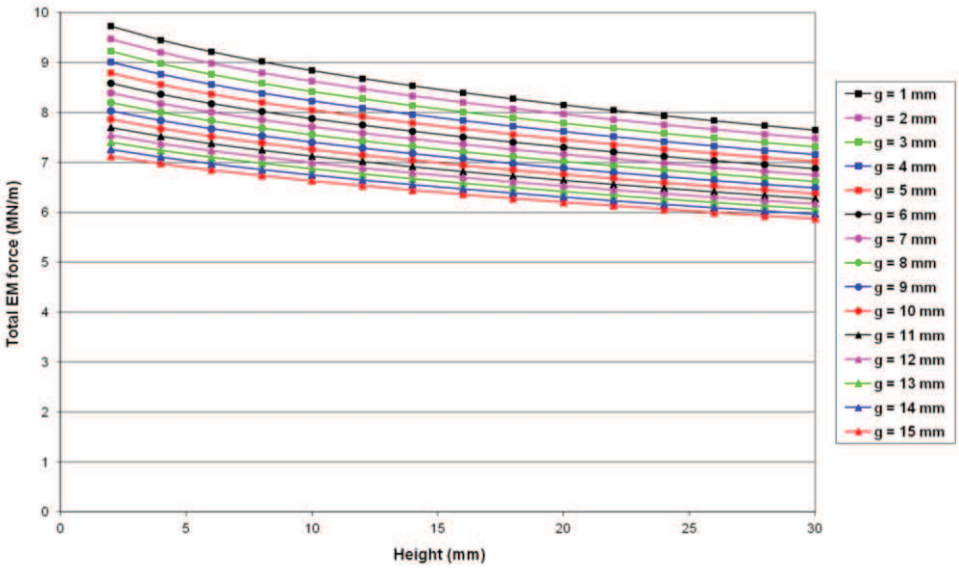

Fig. 6.7: Influence of the height of the outer rail on the total electromagnetic force
w = 25 mm (I_R = 400 kA and I_A = 1267 kA)

The maximum value depends on the maximal value of the current and on the ratio I_R/I_A. A systematic analysis has to be done. It can be observed that the width has a small influence (Fig. 6.6) and it is not necessary to enlarge the outer rail to decrease the electromagnetic force. The maximum is obtained for a width of about 20 mm.

The total electromagnetic force on the rails is decreasing with increasing height *h* and distance *g* between the rails (Fig. 6.7). For the current ratio 600 kA/511 kA the maximal total force in function of the width is found at b = 2 mm. For the two other current ratios the force curve in function of the

width goes through a maximum. This is a result of the negative electromagnetic forces on the inner rail. The overall maxima of the total magnetic force are listed in Table 6.2. The lowest maximum $4.8.10^6$ N/m is found for the highest current ratio 600 kA/511 kA. The maximum $6.8.10^6$ N/m found for 500 kA/833 kA is about 40 % higher and the maximum $10.4.10^6$ N/m for 400 kA/1267 kA is more than two times higher than the one found for the highest current ratio. But the obtained values are not realistic because a distance of 1 mm between the outer and the inner rail is too small to obtain a good isolation (e.g. LARA: g = 5 mm). Also the current density in the rails has to be considered in the determination of the cross-section of the rails. Nevertheless, this study allows reducing the range of variation for the three dimensions *g*, *h* and *w*.

Table 6.2: Maximum total force on the rails

Total Force	Maximum	Width w	Height h	Distance g
I_R = 400 kA, I_A = 1267 kA	$10,4.10^6$ N/m	14 mm	2 mm	1 mm
I_R = 500 kA, I_A = 833 kA	$6,8.10^6$ N/m	12 mm	2 mm	1 mm
I_R = 600 kA, I_A = 511 kA	$4,8.10^6$ N/m	2 mm	2 mm	1 mm

6.2.3. Electromagnetic Forces on the Projectile

6.2.3.1. 3D Finite Element Analysis

The domain of study is given on Fig. 6.8. The length of the rails is limited to 140 mm due to the too high number of nodes which have to be considered to have a good enough accuracy.

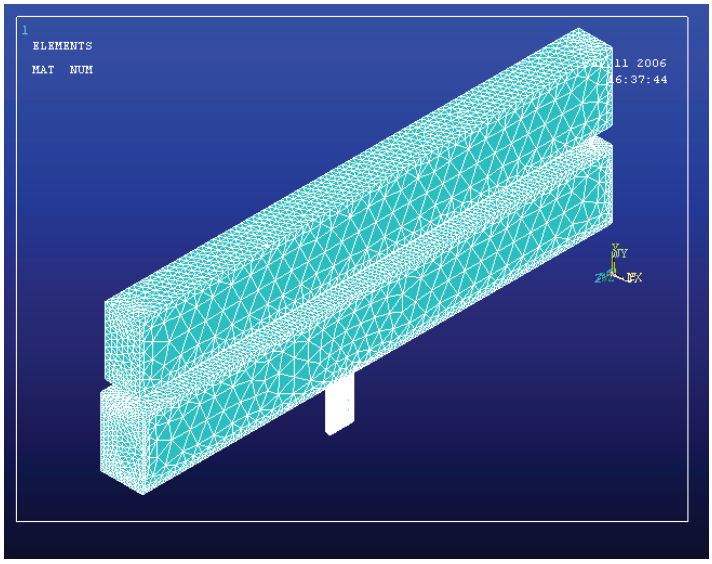

Fig. 6.8: Meshing in 3D simulation using ANSYS

6.2.3.2. Parametric Analysis for L'$_R$ and M'

To compare the electromagnetic forces on the projectile for the different geometries we need to determine *L'$_R$ and M'*. A similar method as described in § 3.4.1 is used. The analyses are made for a harmonic current with two frequencies. A harmonic current with a frequency of 10 Hz has been used instead of a dc current because a dc current could not be used for the 3D simulation in ANSYS. As said before, the best frequency would be 100 kHz to simulate the skin effect but the results could not

be processed for a 3D simulation and a frequency of 1 kHz bas been chosen. In the next paragraph we will see that the electromagnetic forces calculated with the time-dependent values for L'_R and M' based on the harmonic analyses for 10 Hz and 1 kHz show a good fit with the electromagnetic force calculated with a direct 3D transient analysis.

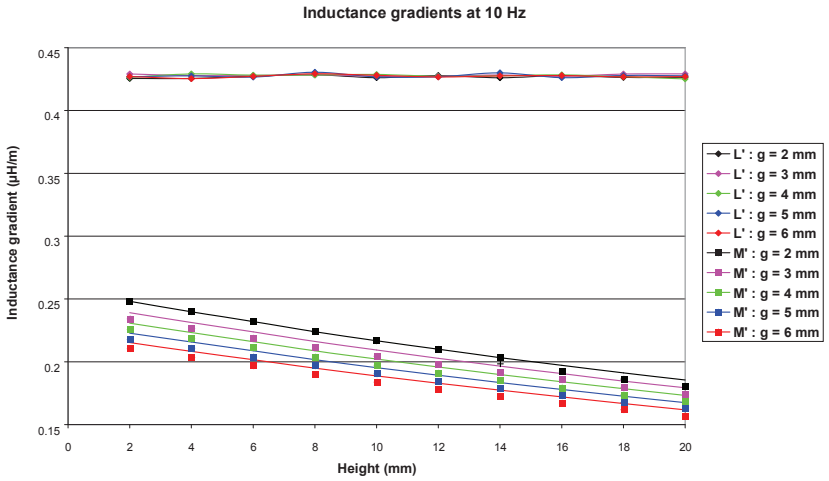

Fig. 6.9: Variation of L'_R and M' with the height for a width of 20 mm – Frequency 10 Hz

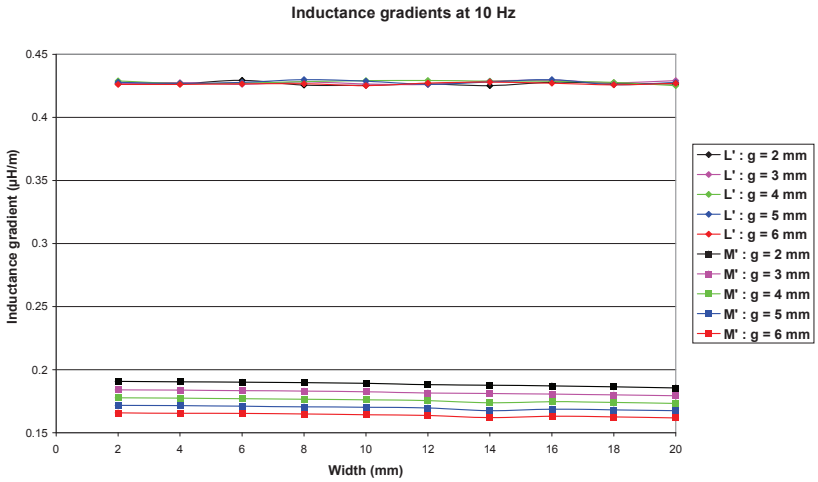

Fig. 6.10: Variation of L'_R and M' with the width for a height of 20 mm – Frequency 10 Hz

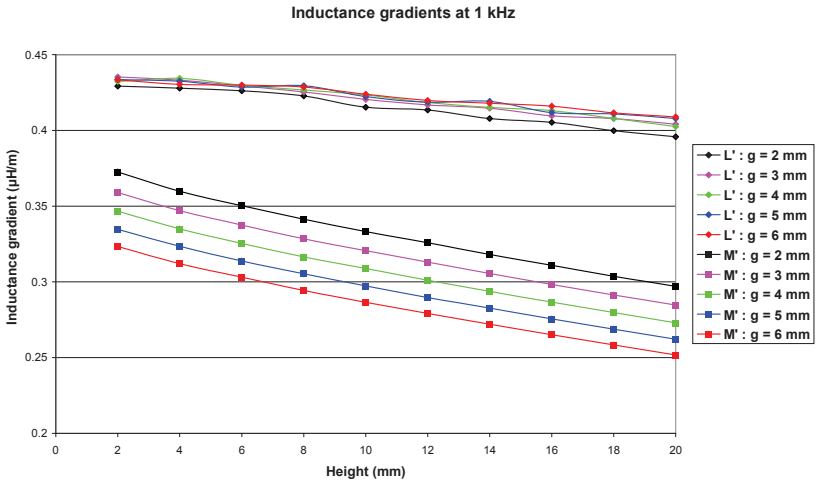

Fig. 6.11: Variation of L'_R and M' with the height for a width of 20 mm – Frequency 1 kHz

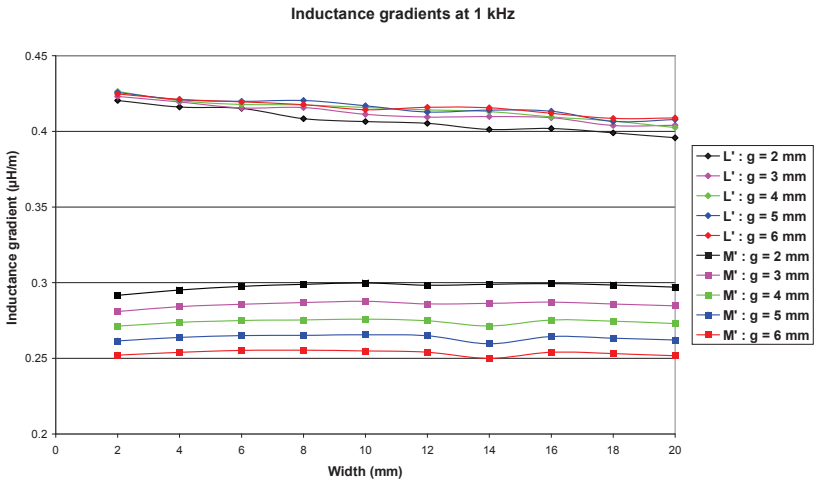

Fig. 6.12: Variation of L'_R and M' with the width for a height of 20 mm – Frequency 1 kHz

For the frequency of 10 Hz (Fig. 6.9 and Fig. 6.10), the height h and the width w have no influence on L'_R and the variation of M' with the distance g between the two rails is foreseeable. At the frequency of 1 kHz (Fig. 6.11 and 6.12), the width of the outer rail has no influence. The height must be small and it is interesting to limit the distance between the two rails but there is a necessary mechanical limit due to the electromagnetic forces.

6.2.3.3. Force on the Projectile

Before we can make a parametric analysis of the force on the projectile, we have to define the parameters L'_R and M' for which we have two different values depending on the frequency. On Fig. 6.13 we can see the variation of the force on the projectile calculated with the values obtained for the two frequencies. They are compared with a direct transient analysis for the same currents.

A good agreement can be observed at the beginning of the shot for the calculations with the values corresponding to 1 kHz and at the end with those for 10 Hz. So we propose a combination of the values to calculate the electromagnetic force on the projectile.

- values of L'_R and M' at 1 kHz till 0.3 ms
- values of L'_R and M' at 10 Hz from 1.97 ms
- L'_R and M' linearly decreasing from the values at 1 kHz to the values at 10 Hz between 0.3 And 1.97 ms

The proposed linear fitting gives very good results (Fig. 6.14); the difference between the electromagnetic forces on the projectile calculated with both methods is within 2%. We will use it for a parametric analysis of the force on the projectile.

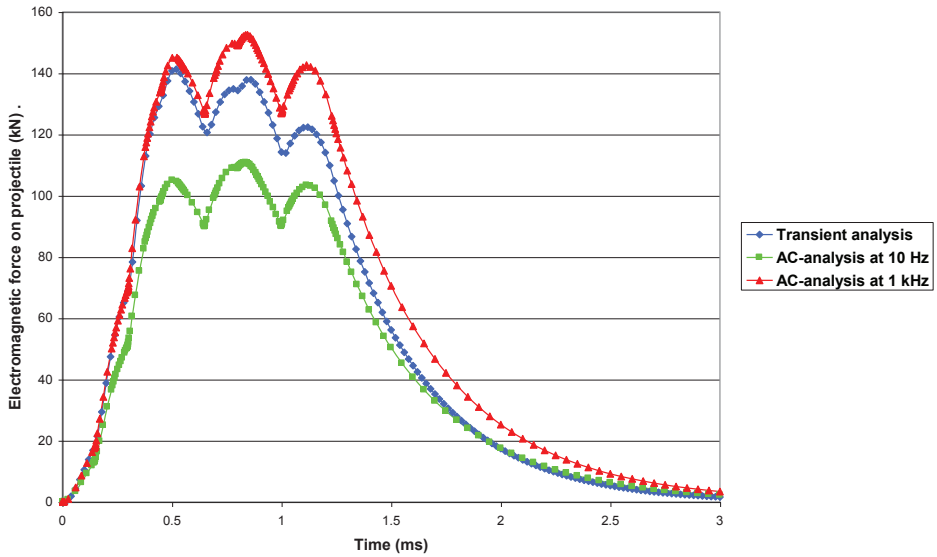

Fig. 6.13: Comparison of the electromagnetic force on the projectile between a direct computing and analytical computing knowing the values of L'_R and M'

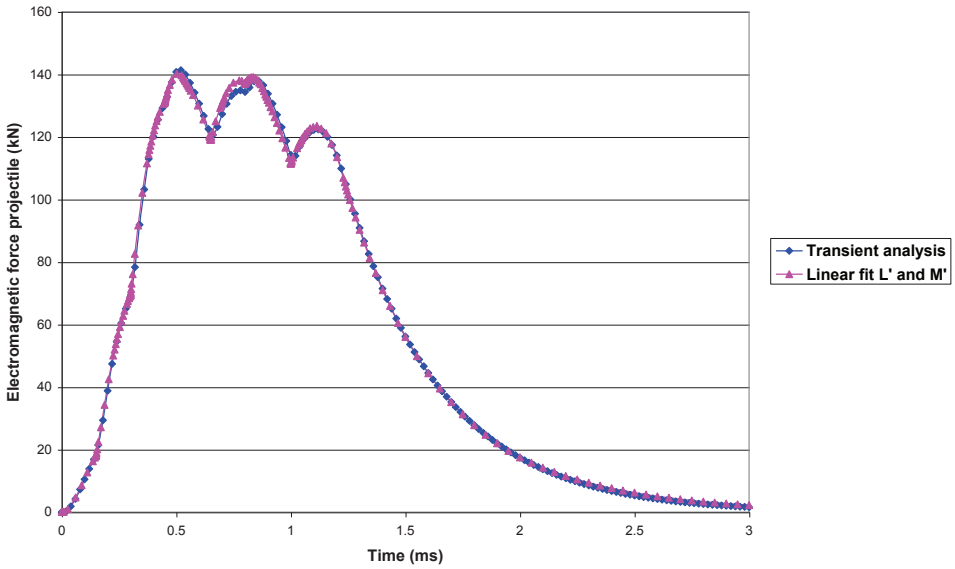

Fig. 6.14: Comparison of the electromagnetic force on the projectile between a direct computing and analytical computing with linear fitting of L'_R and M'

6.2.3.4. Parametric Analysis of the Maximum Force on the Projectile

Once the inductance gradients are determined we can calculate analytically the electromagnetic force on the projectile. The fitted values for M' and L'_R and the currents for the transient analyses are used. To compare the results, we determine the maximum electromagnetic force on the projectile for each geometry and each current ratio. Notice that we can calculate the electromagnetic force on the projectile for any current ratio we want.

The maximum electromagnetic force on the projectile is decreasing with increasing height h and distance g for all current ratios (Fig. 6.15). The values in function of the width w, shown in Fig. 6.16, go through a maximum and show a dip at w = 14 mm like the values for M' at 1 kHz.

The overall maxima are presented in Table 6.3. The lowest maximum is found for 600 kA/511 kA. The maxima found for 400 kA/1267 kA and 500 kA/833 kA are respectively 13 % and 6 % higher.

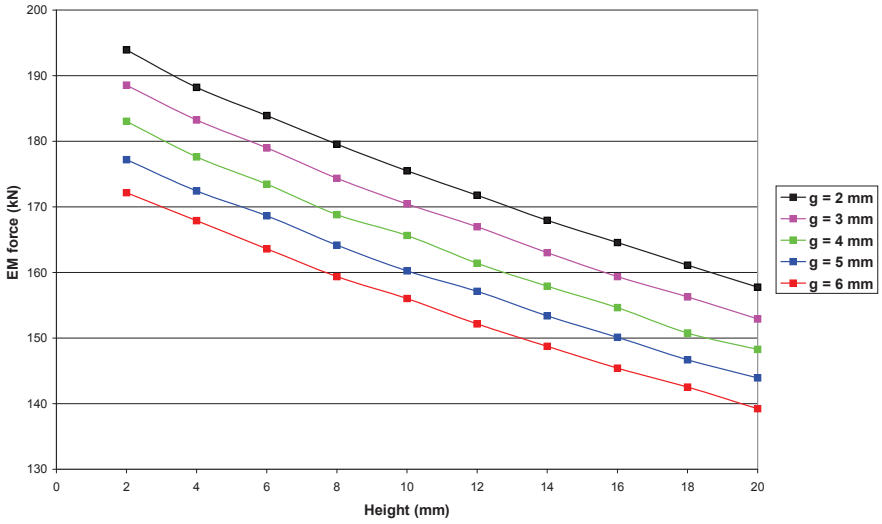

Fig. 6.15: Influence of the height of the outer rail on the electromagnetic force on the projectile w = 20mm (I_R = 400 kA and I_A = 1267 kA)

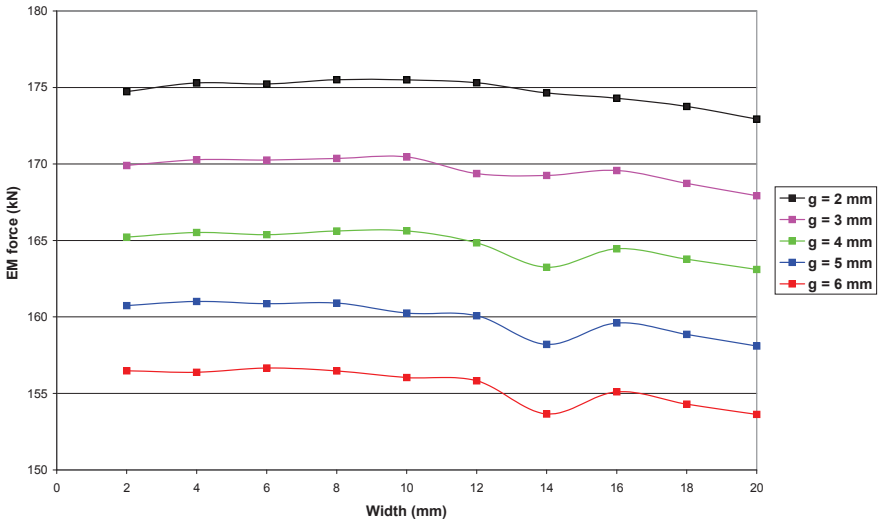

Fig. 6.16: Influence of the width of outer rail on the electromagnetic force on the projectile w = 20 mm (I_R = 400 kA and I_A = 1267 kA)

Table 6.3: Values and positions of the overall maxima for the electromagnetic force on the projectile

EM force on projectile	Maximum	w	h	g
I_R = 400 kA, I_A = 1267 kA	195 kN	8 mm	2 mm	2 mm
I_R = 500 kA, I_A = 833 kA	184 kN	8 mm	2 mm	2mm
I_R = 600 kA, I_A = 511 kA	173 kN	8 mm	2 mm	2 mm

6.2.4. Impulse and Determination of the Theoretically Best Geometry

The impulse can be calculated by integration of the analytically determined force curve. The objective is to get an impulse of 200 Ns. For a chosen impulse, the outer rail current can be calculated if the inner rail current is fixed.

With the theoretically best geometry we mean the best geometry found based upon the electromagnetic forces on the rails and on the projectile. To obtain the impulse mentioned above we have to maximize the force on the projectile. But high electromagnetic forces on the projectile mean also high electromagnetic forces on the rails. We fix the limit for the electromagnetic force on the rails at 8.10^6 N/m for construction reasons. Therefore we have to find a balance between the electromagnetic forces on the rails and the electromagnetic force on the projectile.

The electromagnetic forces on the rails just as the electromagnetic force on the projectile are increasing with decreasing distance between the rails *g* and height *h*. The force on the projectile is decreasing faster for *g* and *h* than the force on the rails. The best ratio of the force on the projectile and the forces on the rails is found at a distance between the rails of g = 2 mm and a height of h = 2 mm.

The optimal width *w* is not so easy to find. The maximal electromagnetic force on the projectile for g = 2 mm and h = 2 mm is found at 8 mm for all three current ratios. The maximum of the electromagnetic force on the rails depends on the current ratio. The best ratio of the force on the projectile and the forces on the rails is found at w = 8 mm for the current ratios 600 kA/511 kA and 500 kA/833 kA and at w = 2 mm for 400 kA/1267 kA. Another point of interest is the electromagnetic forces on the inner rail. If the width w is chosen too small, we will need a high current in the inner rail to avoid negative electromagnetic forces in the inner rails. We have chosen w = 8 mm to optimize the electromagnetic force on the projectile.

6.2.5. 3D Transient Analysis of the Theoretical Solution

6.2.5.1. Determination of the Current Ratios

We first have to optimize the current ratios needed to obtain the desired impulses for the best theoretical geometry. For an impulse of 200 Ns, we vary the inner current between 300 and 600 kA and calculate the corresponding outer current as in § 6.2.1. but based on the values for L'_R and M' for the optimized geometry. For these current ratios a 2D transient analysis was carried out to determine the corresponding electromagnetic forces on the rails. The results of these calculations are listed in Table 6.4.

Table 6.4: Current ratios calculated to determine an impulse on the projectile of 200 Ns for the theoretically best geometry and the corresponding maximum total electromagnetic forces on the rails

I_R (kA)	300	350	400	450	500	550	600
I_A (kA)	1518	1243	1030	857	713	589	480
F (MN/m)	11,9	9,2	7,5	6,3	5,5	4,9	4,5

The electromagnetic forces on the rails decrease with an increasing current in the inner rails. Since limiting the current in the inner rails is the main reason why we want to design an augmented railgun, we choose the current ratio with the lowest inner current wherefore the electromagnetic force on the rails is smaller than 8.10^6 N/m. But for the current ratio 400 kA/1030 kA there is a significant negative force on the inner rails. The results for 450 kA/857 kA show only a low negative electromagnetic force on the inner rail at the very beginning of the analysis and therefore this current ratio is chosen as solution.

6.2.5.2. Electromagnetic Force and Impulse on the Projectile

A 3D transient analysis was carried out for the best theoretical geometry for the current ratio 450 kA/857 kA. The current ratio 450 kA/857 kA was optimized to obtain an impulse of 200 Ns. The impulse based on the results of the 3D transient analysis, calculated as control, is 202 Ns.

6.2.6. Conclusion

For the construction of an augmented railgun, the influence of the geometry of the outer rail on the magnetic forces on the projectile was studied. The objective is a muzzle velocity of 1-2 km/s for a projectile with a mass of 100-200 g and electromagnetic forces on the rails lower than 8.10^6 N/m.

A 2D transient analysis was carried out for the determination of the electromagnetic force on the rails. The total electromagnetic force on the rails decreases with increasing height *h* and distance *g*. The lowest overall maximum is found for the current ratio with the highest inner rail current. The width w where the overall maxima are found is depending on the current ratio.

The electromagnetic force on the projectile was analytically calculated with the force-equation. The coefficients of this force-equation L'_R and M' were determined with 3D AC analyses at 10 Hz and 1 kHz. The force on the projectile decreases with increasing height *h* and distance *g*. The overall maxima were found at w = 8 mm. The electromagnetic force on the projectile is increasing with decreasing current ratio.

To determine the theoretically best geometry a balance between the electromagnetic forces on the rails and on the projectile has to been found. The electromagnetic force on the projectile is faster decreasing with the distance *g* and the height *h* than the electromagnetic force on the rails. The width *w* was optimized to obtain a maximum force on the projectile. The theoretically best geometry is then g = 2 mm, h = 2 mm and w = 8 mm.

Then we determined the best current ratio for this geometry to obtain an impulse of 200Ns. A 3D transient analysis was carried out for the theoretically best geometry. The difference between the directly determined and the analytically calculated force on the projectile is within 2 % and the determined impulse is 202 Ns. The maximum total electromagnetic force on the rails is $6.3.10^6$ N/m for this configuration. For an impulse of 400 Ns the limit of 8.10^6 N/m for the electromagnetic force on the rails was not achieved for an acceptable inner current.

The obtained solution for an impulse of 200 Ns is a theoretical solution based upon the electromagnetic forces on the rails and on the projectile. Other criteria have to be considered for the final construction, like the mechanical feasibility and the maximal current density.

6.3. Projectile Optimization [COF08a]

The current distribution between the brushes of a projectile is influenced by the augmenting field because the current brushes and the rails form a closed loop. To study the influence of the geometry of the projectile on the current distribution, a parametric study with PSpice for different radius *r* of the current brushes and different distances *a* between the current brushes is carried out. The study of the current distribution in the projectile is important because we want to obtain a balanced distribution to postpone contact transition as long as possible. A better balanced load also leads to lower tensile and compressive stresses in the projectile and this allows to reduce the death mass of the projectile.

Fig. 6.17 represents the current profiles calculated with PSpice for a projectile with a distance between the current brushes a = 15 mm and for different values for the radius *r* of the current brushes. A higher radius *r*, results in a lower temperature T_h and thus in a lower resistance of the current brushes and higher currents. This has an effect on the current profiles during the whole duration of the shot. The simulations are carried out for the railgun LARA

Fig. 6.18 represents the current profiles calculated with PSpice for an augmented railgun for a projectile with two current brushes with radius r = 3mm and for different distances between the brushes. A higher distance *a* between the current brushes results in a higher influence of the augmenting field because the surface defined by the closed contour formed by the current brushes and the part of the inner rails in between is bigger. The influence of the augmenting field is high when the derivative dI_A/dt of the current in the outer rails is high. At the beginning of the shot a clear difference between the current profiles is found, at the end of the shot the difference is small.

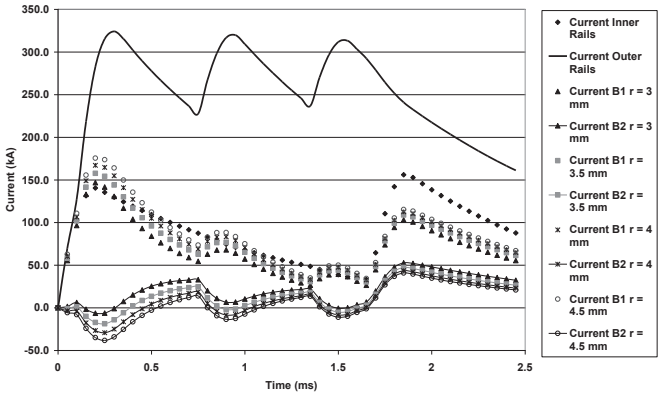

Fig. 6.17: Current profiles calculated with PSpice for an augmented railgun.
Projectile with two current brushes with different radius *r* and distance between the brushes a = 15 mm.

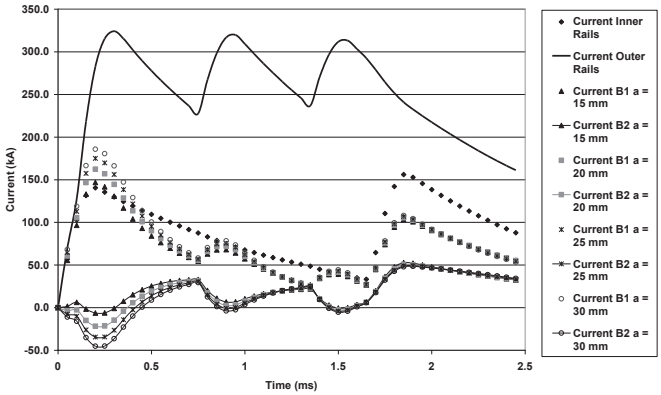

Fig. 6.18: Current profiles calculated with PSpice for an augmented railgun.
Projectile with two current brushes with radius r = 3mm and different distances *a* between the brushes.

6.4. Analysis of Different Types of Feeding [COF07a][GAL07]

For the optimization of the augmenting circuit, three different configurations for the outer rails were compared. The PFN for the inner circuit consists of two capacitor banks with U_0 = 7 kV. The PFN for the outer circuit has four capacitor banks with U_0 = 10 kV. The discharging times of the capacitor banks were altered to obtain a muzzle velocity of 1000 m/s. The efficiency of the railgun was determined for these cases. The simulations are made with the PSpice code for the LARA geometry.

6.4.1. Parallel Augmented Railgun

The length of the inner and outer rails of the parallel augmented railgun LARA is 1.5 m (Fig. 6.19). The current injection is at the breech of the rail gun. The weight of the projectile was altered

from 15 to 25 g. For each mass three different cases were studied. In case a, all the capacitor banks of the outer circuit are discharged at t = 0 ms. In case b, the first two capacitor banks are discharged at t = 0 ms and the other two banks of the outer circuit were grouped around the discharge of the second capacitor bank of the inner circuit. The discharges of the banks in case c, were optimized to have a more or less constant current. The currents are given on Fig. 6.20.

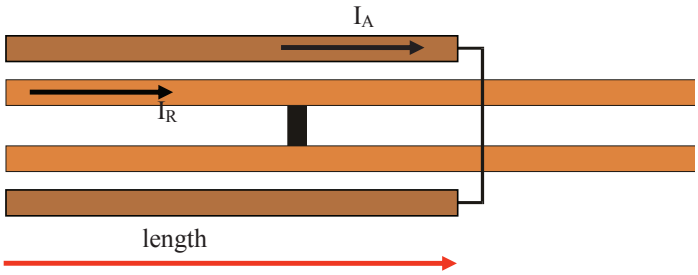

Fig. 6.19: Influence of the length

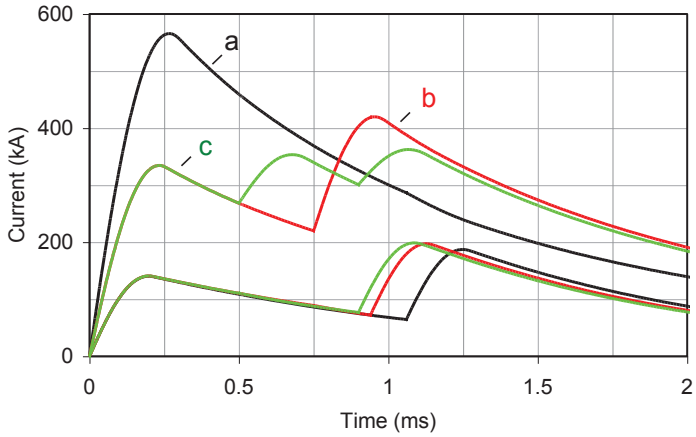

Fig. 6.20: Current evolution for the 3 cases

The highest velocity is obtained when all banks are launched at t = 0 ms. The discharging times, the muzzle velocity v and the efficiency η for the different cases are represented in Table 6.5. The efficiency η is defined as the ratio of the kinetic energy at the muzzle and the initial energy stored in the capacitors. The best efficiency is found for case c. The efficiency is overall very low (2-5 %). More than 80 % of the energy is dissipated due to the resistance of the outer rails.

Table 6.5: Muzzle velocity, efficiency and discharging time t_1 of the second bank in the inner circuit and t_2, t_3 and t_4 of the second, third and fourth bank in the outer circuit for different masses of the projectile

m (g)	t_1 (ms)	t_2 (ms)	t_3 (ms)	t_4 (ms)	Case	v (m/s)	η (%)
15	1.80	0.00	0.00	0.00	a	999.7	2.15
15	1.70	0.00	1.65	1.65	b	999.7	3.32
15	1.67	0.10	0.75	1.35	c	1000.0	3.37
20	1.06	0.00	0.00	0.00	a	1001.0	2.88
20	0.94	0.00	0.75	0.75	b	999.3	4.03
20	0.90	0.00	0.50	0.90	c	1001.8	4.10
25	0.50	0.00	0.00	0.00	a	999.5	2.47
25	0.45	0.00	0.30	0.30	b	1000.7	4.36
25	0.21	0.00	0.45	0.90	c	1000.7	5.03

Table 6.6: Muzzle velocities and efficiencies for a parallel augmented railgun with optimized length for the outer rails for different masses of the projectile.

m (g)	Case	Length (m)	v (m/s)	η (%)
15	a	1.5	999.7	2.15
20	a	1.2	1000.7	3.13
20	b	1.2	1000.0	4.39
20	c	1.2	999.7	4.44
25	a	0.9	999.9	4.44
25	b	0.9	1000.7	5.43
25	c	1.1	999.5	5.65

In order to reduce these energy losses we first try to optimize the length of the outer rails. We determined the length where the highest velocity was obtained for the cases and masses described in Table 6.6. Then we adapted the discharging times of the capacitor banks to obtain a velocity v of approximate 1000 m/s for the new adapted length of the outer rails, for the different masses and cases and calculated the efficiency η. For a mass of 15 g the maximum is found at 1.5 m. This is due to the high discharging time of the second capacitor bank in the inner circuit. For the other masses the maximum velocity is found at a shorter length of the outer rails and the efficiency has increased. A general optimal length of the outer rails cannot be defined.

6.4.2. Segmented Parallel Augmented Railgun

The second parallel augmented railgun has outer rails that are segmented (Fig. 6.21). This railgun has current injection points at the beginning of each segment. To optimize the length of the first segment, we calculated the position of the projectile at the moment the third and fourth banks (case b) are discharged. The length of the segments is adapted so the projectile has just entered the second segment when the current in this section is injected and we calculated v_1 and η_1. Then the discharging times were adapted to obtain a velocity of approximate 1000 m/s (v_2) to be able to compare the efficiency η_2 (Table 6.7) with the efficiency of the normal parallel augmented railgun.

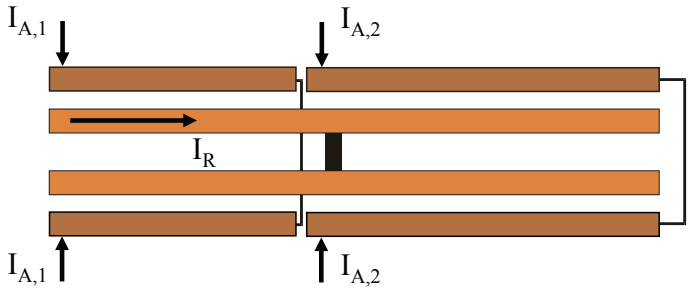

Fig. 6.21: Schematic of a segmented parallel augmented railgun.

Table 6.7: Velocities and efficiencies for a segmented parallel augmented railgun with optimized length *L* of the first segment, for different masses of the projectile.

	m (g)	L (m)	v_1 (m/s)	η_1 (%)	v_2 (m/s)	η_2 (%)
SEG	15	0.77	1088.9	3.29	1000.3	2.78
	20	0.19	882.2	4.53		
	20	0.25			940.8	3.29
DES	15	0.75	1051.5	4.37	999.7	4.00
	20	0.18	1043.5	4.53	1000.5	4.16

6.4.3. DES Parallel Augmented Railgun

The DES (Distributed Energy Storage) parallel augmented rail gun has outer rails in one piece and has besides a current injection point at the breech of the outer rails a second injection point along the outer rails (Fig. 6.22). Again the position of the projectile was determined at the moment that the third and fourth banks are discharged. The injection points were located at these positions. The efficiencies η_1 and η_2 were determined at maximum velocity v_1 and at v_2 approximately 1000 m/s. A DES parallel augmented railgun has no problems with current loss and the projectile of 20 g reaches a velocity of 1043.5 m/s with a current injection point at 0.18 m. For a projectile of 20 g the DES railgun reaches a lower velocity than the segmented but it has a higher efficiency.

Table 6.8 represents the velocities obtained for a normal, a segmented and a DES parallel augmented railgun with two capacitor banks for the inner circuit and two for the outer circuit. The second bank of the outer circuit is discharged at the moment that the projectile reaches distance *x*. For the segmented railgun this is also the distance where the second segment starts and for the DES railgun the position of the second current injection point. The highest velocity is reached with the segmented railgun except for x = 25 cm because there is no current recuperation between the segments. The DES railgun reaches a higher velocity than the normal parallel augmented railgun in all cases.

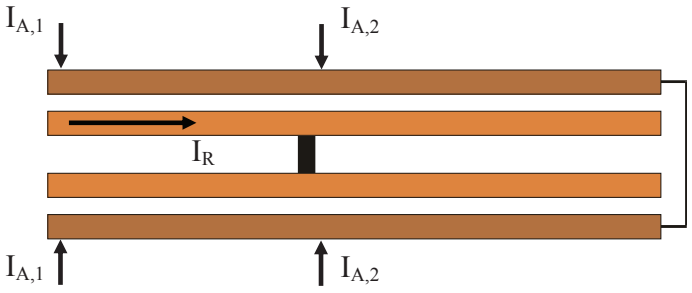

Fig. 6.22: Schematic of a DES parallel augmented railgun

Table 6.8: Muzzle velocity reached for the three different configurations with current injection at the moment the projectile reaches distance *x*.

Distance *x*	0.25 m	0.50 m	0.75 m	1.00 m
Normal	967 m/s	889 m/s	854 m/s	830 m/s
Segmented	835 m/s	944 m/s	903 m/s	861 m/s
DES	996 m/s	923 m/s	878 m/s	845 m/s

6.4.4. Conclusion

The efficiency of a normal parallel augmented railgun is low because of the energy losses in the outer rails. First we adapted the length of the outer rails but no optimal length for all cases could be found. A segmented railgun reaches, for the same conditions, the highest velocity except for a distance of 25 cm. But the segmented railgun has a low efficiency. The DES railgun finally reaches always a higher velocity than the normal segmented railgun under the same conditions and has a higher efficiency than both the normal parallel augmented railgun and the segmented railgun. The DES railgun seems thus the best solution. The downside of this type of railgun is the complexity and the cost of the construction.

6.5. Conclusion

For the construction of an augmented railgun, the influence of the geometry of the outer rail on the electromagnetic forces on the rails and on the projectile was studied. The objective is a muzzle velocity of 1-2 km/s for a projectile with a mass of 100-200 g and electromagnetic forces on the rails lower than 8 MN/m.

A 2D transient analysis was carried out for the determination of the electromagnetic forces on the rails. The total electromagnetic force on the rails decreases with increasing height h and distance between inner and outer rails g. The lowest overall maximum is found for the current ratio with the highest inner rail current. The width w where the overall maxima are found depends on the current ratio.

The electromagnetic force on the projectile was analytically calculated with the force-equation. The coefficients of this force-equation L'_R and M' were determined with 3D AC analyses at 10 Hz and 1 kHz. The force on the projectile decreases with increasing height h and distance g. The overall maxima were found at w = 8 mm. The electromagnetic force on the projectile is increasing with decreasing current ratio.

To determine the theoretically best geometry a balance between the electromagnetic forces on the rails and on the projectile has to been found. The electromagnetic force on the projectile is faster decreasing with the distance g and the height h than the electromagnetic forces on the rails. The width w was optimized to obtain a maximum force on the projectile. The theoretically best geometry is then g = 2 mm, h = 2 mm and w = 8 mm.

Then we determined the best current ratio for this geometry to obtain an impulse of 200Ns. A 3D transient analysis was carried out for the theoretically best geometry. The difference between the directly determined and the analytically calculated force on the projectile is within 2 % and the determined impulse is 202 Ns. The maximum total electromagnetic force on the rails is 6.3 MN/m for this configuration. For an impulse of 400 Ns the limit of 8 MN/m for the total electromagnetic force on the rails was not achieved for an acceptable inner current.

The obtained solution for an impulse of 200 Ns is a theoretical solution based upon the electromagnetic forces on the rails and on the projectile. Other criteria have to be considered for the final construction, like the mechanical feasibility and the maximal current density.

The second part is a parametric study of the projectile for LARA with PSpice. It shows the influence of the distance a between the brushes and the radius r of the brushes on the current profile in these brushes.

In the last part, a parametric analysis of three different types of railgun feeding with PSpice is presented. The DES augmented railgun has the best efficiency compared with the normal parallel augmented railgun and the segmented railgun.

Conclusions and Perspectives

The initial goal of this work was studying the current distribution in the armature of a railgun projectile with two current brushes. In a conventional railgun the current will flow mainly through the current brush on the breech side which corresponds with the path of the lowest resistance. Railguns are designed to obtain a high muzzle velocity. To obtain these velocities high currents are required. However the current density in the current brushes must be limited: the heating of the sliding contacts between the rails and the brush armatures due to the Joule losses and to the friction can cause the melting of these contacts and can result in contact transition. Contact transition leads to an increase of the armature resistance and the deterioration of the rails.

One way to increase the force on the projectile without raising the current in the inner circuit and thus through the armature is by adding an extra pair of rails in order to establish an augmenting magnetic field. In this work we study the influence of the additional external field of a parallel augmented railgun on the current distribution between the two current brushes of the projectile. The brushes and the parts of the rails between them form a loop. The changing augmenting field will induce a current in this loop and influence the current distribution between the brushes.

Two simulation methods are used to study the current distribution. In the first one electric circuits are used to model the railgun. We can distinguish two parts. The first part is an electric model of the capacitor banks, the pulse forming network, the rails and the projectile. The second part simulates the kinematics of the projectile through equivalent electric networks. PSpice was used for this global model of the railgun that allows us to predict the global currents in the rails and in the brushes. Also the average temperature in the brushes, the force on the projectile and the position and the velocity of the projectile can be estimated. The determination of the parameters of this model is difficult. The skin effect due to the pulsed shape of the current and the velocity skin effect due to the movement of the projectile have to be modeled. Also the heating of the brushes caused by the Joule losses is calculated because their resistance is temperature-dependent. The different components of the friction force require special attention as well as the time-dependent coefficients of the electromagnetic force.

The second method is a finite element simulation with ANSYS. This method permits the coupling of an electromagnetic and a thermal analysis and allows a local study of the current and temperature distribution in the armature. The global currents are used as input for the model which allows calculating among others the current distribution in and between the current brushes, the electromagnetic forces on the rails and the projectile and the average and maximum temperatures in the current brushes. It is used to determine the time-dependent coefficients of the force equation used in the PSpice-model. One of the drawbacks is that only a part of the rails can be modeled. The main drawback of the finite element method is that the movement of the projectile is not simulated. When the projectile moves it “sees” continuously another part of the rails and the diffusion in the rails starts after the passing of the projectile. So the current diffusion in the rails near to the armature will be erroneous except for the beginning of the shot. Nevertheless, we find a good correspondence between the global and local models.

The experiments are carried out with the LARC and LARA railgun at ISL. We worked with, for railgun standards, low currents and low velocities and no transition was detected. For the measurement of the current distribution between the brushes, a method developed at ISL was used. During the exploitation of the results we established that this method cannot be applied because of the presence of eddy currents in front of the projectile. We have exploited ten shots with the conventional railgun LARC and only two with the augmented railgun LARA. During the third shot with the augmented

configuration a problem with the third capacitor bank occurred which put an end to the experiments. We have proposed another method to obtain information about the current distribution between the brushes based on the signal measured with the loop in the measurement device. This method still needs improvement. Nonetheless, the comparison between the experiments and the simulation methods is interesting.

If we compare the different methods for the current ratio I_l/I_R for the non-augmented railgun the results are inconclusive. With ANSYS we obtain that approximately 31 % of the current flows through the brush on the muzzle side. We find almost no difference for the current ratio I_l/I_R between the first and second measurement point. This can be explained by the simulation method. To obtain a better approach of the current diffusion in the rails, we adapted the currents used as input in ANSYS. If we would simulate the whole shot, the diffusion into the rails would be further evolved at the moment the projectile passes. Therefore we delay the simulation. We used the original current profile from the moment the projectile passes the measurement point until 2 ms later. To simulate the rising part, we used the first part of the original current profile until the first maximum is reached. The rising time is respected. By using this method the current diffusion in the rails after the rising part of the current is the same in the simulations for both measurement points. The results obtained with PSpice show a better correspondence with the experimental results for I_l/I_R. However we must conclude that the results obtained for the current ratio during the experiments allow only making qualitative conclusions. The currents calculated with Spice show a good correspondence with the experiments until the maximum of the current is reached but they decrease faster. The comparison for the velocities is satisfactory.

For an augmented rail gun, the analytical method for the calculation of the current distribution takes into account the current i_{loop} induced by the augmenting field. ANSYS does take into account the influence of the augmenting field and the results for the current ratio show a better correspondence than for a non-augmented rail gun. For the PSpice simulations the same conclusion as for the non-augmented railgun can be made. This model always underestimates the current ratio compared to the experimental results. Although the analytic method allows estimating the current ratio, the results are not what we expected. We hoped to obtain an accurate current ratio from the experiments and to demonstrate the influence of the augmenting magnetic field. It appeared that the used measurement technique was not well adapted for low speeds.

The last part of this work discusses a preliminary design for an augmented railgun with high muzzle velocity. A parametric study with ANSYS was carried out. The impulse aimed for in the simulations was 200 Ns. The inductance gradients were determined for different geometries of the outer rails and also the distance between the inner and outer rails was varied. Then the electromagnetic forces on the projectile were determined. Higher electromagnetic forces on the projectiles mean also higher electromagnetic forces on the rails. For the forces on the rails a limit of 8.10^6 N/m must be respected. The best results were found for outer rails with a width of 8 mm, a height of 2 mm and a distance of 2 mm between the rails. This result is the best theoretical result only based upon the forces on the rails and the projectile and does not consider mechanical feasibility or a maximum current density.

The influence of the geometry of the projectile on the current distribution and the temperature was examined with the distance a between the brushes and the radius r of the brushes as parameters. This simulation was made with the PSpice code for LARA. Higher values for r result in lower temperatures while low values for a limit the influence of the augmenting magnetic field.

Finally, different types of railgun feeding for the LARA configuration are analyzed. The efficiency of a normal parallel augmented railgun, a DES parallel augmented rail gun and a segmented parallel augmented railgun was compared. The best results were found for a DES augmented railgun.

This work opens perspectives. The solution of an augmented railgun deserves to be further examined. A first step would be a more extensive experimental study. The method discussed in [SCH09] for the determination of the current distribution shows promissing results for high velocities. Although the interpretation of the signals was not straightforward during our experiments, we could make an estimation of the current distribution based on the signal measured with the loop in the measurement device. This method should be further explored. Special attention should be given to the quality of the signal. The signal shows a lot of noise and the treatment of the signal with a FFT-filter can cause loss of information. Also the combination with other measurement techniques is an interesting option. Hereby we like to mention the method discussed in [ZUR11], [LIE09], [LIE11] and [SCH09a] to measure the magnetic field with a CMR-based sensor.

A second step would be the adaptation of the feeding of the railgun. A distributed energy storage for both the inner and outer circuit, so the injection of the current can be adapted to the position of the projectile, would have a positive influence on the efficiency. The downside of this type of railgun is the cost and the complexity of the construction.

Another path forward is to improve the simulation methods. Comparison between the results obtained with PSpice for the currents and the kinematics and the experiments show that the accuracy of the parameters of this model must be improved. Special attention should be given to the model for the forces on the projectile. A better estimation of the mechanical component of the friction force and of the coefficients of the electromagnetic force equation is in order. The coefficients of the electromagnetic force were obtained with a local model using ANSYS. Adapting the FEM analysis so the movement of the projectile could be simulated correctly would make a huge difference. Also the model for the contact layer between the brushes and the rails needs finetuning.

Bibliography

ASO09 Y. Aso, T. Hashimoto, T. Abe and S. Yamada, "Inductive Pulsed-Power Supply with Marx Generator Methodology", IEEE Trans. Magn., vol. 45, no. 1, Jan. 2009, pp. 237-240

BAR91 J. Barber, D. Bauer, K. Jamison, J. Parker, F. Stefani and A. Zielinski, "Observations on the Limits of Plasma Armatures", IEEE Trans. Magn., vol. 27, 1991, p. 323-325

BAR93 J.P. Barber, A. Challita,"Velocity effects on metal armature contact transition (railguns)", IEEE Trans. Magn., vol. 29, 1993, p. 733-738

BAR95 J.P. Barber, Y.A. Dreizin,"Model of contact transitioning with realistic armature-rail interface", IEEE Trans. Magn., vol. 31, 1995, p. 96-100

BAR03 J. Barber, D. Bauer, K. Jamison, J. Parker, F. Stefani and A. Zielinski, "A survey of armature transition mechanisms", IEEE Trans. Magn., vol. 39, Jan. 2003, pp. 47–51

BEC09 G. Becherini, S. Di Fraia, M. Schneider, R. Ciolini, B. Tellini, "Shielding of High Magnetic Fields", IEEE Trans. Magn., vol. 45, no. 1, Jan. 2009, pp. 604-609

CHA91 R. Charon, H. Peter, W. Wenning, "Description d'une unité de stockage d'énergie capacitive de 170 kJ destinée à la préétude PEGASUS", Rapport ISL N604, 1991

CIO09 R. Ciolini, M. Schneider, B. Tellini, "The Use of Electronic Components in Railgun Projectiles", IEEE Trans. Magn., vol. 45, no. 1, Jan. 2009, pp. 578 – 583

COF06 M. Coffo, J. Gallant, "Preliminary design of an augmented rail gun", 17th EEMLS Meeting Bruxelles, Sept. 2006

COF07 M. Coffo, J. Gallant, "Modelling of a Parallel Augmented Railgun with Pspice. Validation of the Model and Optimization of the Augmenting Circuit," 16th IEEE Pulsed Power Conference, vol. 2, 2007, pp. 1814-1818

COF07a M. Coffo, J. Gallant, "Preliminary design of an augmented railgun. Influence of the dimensions of the outer rails on the forces acting on the projectile and the rails", EEEJ Transactions on Fundamentals and Materials, vol. 127-A, no. 11, Nov. 2007, pp. 704-708

COF08 M. Coffo, J. Gallant, "Simulation of the Current Distribution and the Heat Load of a Multiple Brush Projectile in a Non-Augmented and a Parallel Augmented Railgun with the Finite Element Code Ansys. Comparison with the Heat Load Observed During Experiments", 2nd Euro-Asian Pulsed Power Conference 2008**,** 22-26 Sept. 2008, Vilnius, Lithuania

COF08a M. Coffo, J. Gallant, "Modeling and Analysis of the Current Distribution between the Brushes of a Multiple Brush Projectile in a Parallel Augmented Railgun", Proceedings of the 2008 IEEE International Power Modulators and High Voltage Conference, 2008, pp. 419-422

COF09 M. Coffo, J. Gallant, "Simulation of the current distribution and the heat load of a brush projectile in a railgun with the finite element code ANSYS", Acta Physica Polonica A, vol. 115, no. 6, 2009, pp. 1112-1114

COF09a M. Coffo, J. Gallant, "Modeling of the contact resistance and the heating of the contact of a multiple brush projectile for railguns with the final element code ANSYS", Power Pulsed Conference 2009, Washington DC, United States, 28 June-2 July 2009

COF10 M. Coffo, J. Gallant, M. Schneider, J.M. Kauffmann, "Study of the current distribution between the brushes of a projectile launched by an augmented railgun", Research Meeting, Electrical Engineering, Saint Louis, France, 10 -11 May 2010

CWT02 "CWT Application Notes, Power Electronic Measurements Ltd, Nottingham, UK, Sept. 2002"

DAR86 K. Darée, "Caractéristiques fondamantales d'un lanceur à rails avec accumulation de l'énergie et formage de l'impulsion par induction ", Rapport ISL N610, 1986

DED08 P. Dedié, S. Scharnholz, V. Brommer, "ICCOS Counter-Current Thyristor High-Power Opening Switch for Currents up to 28 kA", IEEE Trans. Magn., vol. 45, no. 1, Jan. 2009, pp. 536-539

DRE95 Y. Dreizin, J. Barber, "On the origins of muzzle voltage", IEEE Trans. Magn., vol. 31, 1995, pp. 582-586

EGE89 M. Egeland,"Birkelands Electromagnetic Gun: A Historical Review", IEEE Trans. Plasma Science, vol. 17, 1989, pp. 73-82

EML10 Proceedings of the 15th Electromagnetic Launch Symposium, 2010, Brussels, Belgium. IEEE Trans. Plasma Sci., vol. 39, issue 1, Feb. 2011

FAI01 H. Fair, "The Science and Technology of Electric Launch", IEEE Trans. Magn., vol. 37, 2001, pp. 25-32

FAI09 H. Fair, "Advances in Electromagnetic Launch Science and Technology and Its Applications", IEEE Trans. Magn., vol. 45, 2009, pp. 225-230

FIK84 D. Fikse, J. Wu and Y Thio, "The ELF-I augmented electromagnetic launcher", IEEE Trans. Magn., vol. 20, no. 1, 1984, pp. 287-290

FUL91 R. Fuller, J. Kitzmiller and M. Ingram, "Design and testing of a 0.60 caliber augmented railgun", IEEE Trans. Magn., vol. 27, no. 1, 1991, pp. 45-49

GAL03 J. Gallant, "Parametric Study of an Augmented Railgun," IEEE Trans. Magn., vol. 39, no. 1, Jan. 2003

GAL04 J. Gallant, "Le lanceur électromagnétique à rails augmenté : modélisation et validation expérimentale', PhD Thesis, Université de Franche–Comté, 2004

GAL05 J. Gallant, P. Lehmann, "Experiments with brush projectiles in a parallel augmented railgun," IEEE Trans. Magn., vol. 41, Jan. 2005, pp. 188-193

GAL07 J. Gallant, M. Coffo, "Modelling of a parallel augmented railgun with Pspice: Validation of the model and optimization of the augmenting circuit", 18th Topical EEMLS Meeting, Brighton, 11-12 Sept. 2007

GAL11 J. Gallant, P. van de Maat, "Efficiency of a railgun against anti-ship missiles. First results", ISL Symposium on Electric Engineering, Saint-Louis, Mar. 2011

GAU94 Gauthier C., "Mesure de la répartition des lignes de courant dans les lanceurs à rails avec des sondes magnétiques. Analyse des limites de la méthode." Rapport ISL RT505, 1994

GER99 L. Gernandt, H. Nett,"Historique de l'accéleration élecromagnétique par bobines", Rapport ISL RT512, 1999

GRO99 H. Grosch, "All electric combat vehicle (AECV) – Vision and reality". Military Technology, 1999, vol. 9, p. 37-47

IND11 J. Boone, "Accidental explosion at Yemen arms factory kills 100", The Independent, 29 Mar. 2011, www.independent.co.uk

KEE93 D. Keefer, J. Taylor and R. Crawford, "The Electromagnetic Force in Railguns", 4th EEML Symposium, 1993

KEE95 D. Keefer, R. Crawford and J. Taylor, "Inductance gradient scaling experiments in an augmented railgun," IEEE Trans. Magn., vol. 31, Jan. 1995, pp. 326–331

KES09 A. Keshtkar, S. Bayati, A. Keshtkar, "Derivation of a Formula for Inductance Gradient Using Intelligent Estimation Method", IEEE Trans. Magn., vol. 45, no. 1, Jan. 2009, pp. 305-308

KLI92 G. Klingenberg, J. Heimerl, "Gun muzzle blast and flash", Reston (Virginia, United States) : AIAA Progress in astronautics and aeronautics, 1992, 551 p.

KOL76 H. Kolm, K. Fine, F. Williams, P. Mongeau, "Electromagnetic Guns, Launchers and Reaction Engines", Proceedings of the 2nd IEEE International Pulsed Power Conference, 1976, pp. 42-48

LEH03 P. Lehmann, E. Spahn, "The pulse power generation for weapon systems", Groupe de travail OTAN AVT 047 & 098, 2003

LEH03a P. Lehmann, H. Peter en J. Wey, "Overview of the electric launch activities at the French-German research institute of Saint-Louis (ISL)", IEEE Trans. Magn., vol. 39, pp. 24-28

LEH91 P. Lehmann, H. Peter, "Etude expérimentale de différents types de ponts de courant d'un lanceur électromagnétique à rails", Rapport ISL RT502, 1991

LIE09 Liebfried O., Löffler M., Schneider M., Balevičius S., Stankevič V., Žurauskienė N., Abrutis A. and Plaušinaitienė V., "B-Scalar Measurements by CMR-Based Sensors of Highly Inhomogeneous Transient Magnetic Fields", IEEE Trans. On Magnetics, vol. 45, no. 12, Dec. 2009, p 5301-5306

LIE11 Liebfried O., Schneider M. and Balevičius S.,"Current Distribution and Contact Mechanisms in Static Railgun Experiments With Brush Armatures", IEEE Trans. On Plasma Science, vol. 39, no. 1, Jan. 2011, p 431-436

LIU09 H.-P. Liu, M. Lewis, "3-D Electromagnetic Analysis of Armatures and Rails for High Launch Energy Applications", IEEE Trans. Magn., vol. 45, no. 1, Jan. 2009, pp. 322-326

MAR01 R. Marshall, "Railgunnery : where have we been ? Where are we going ?", IEEE Trans. Magn., vol. 37, 2001, p. 440-444

MAR04 R. Marshall, Wang Ying, "Railguns: their science and technology", China machine Press

MAR84 R. Marshall, "Current Flow Patterns in Railgun Rails", IEEE, Trans. Magn., vol. 20, no. 2, 1984, pp. 243-244

MCF03 J. McFarland, I. McNab, "A Long-Range Naval Railgun", IEEE Trans. Magn., vol. 39, no. 1, Jan. 2003, pp. 289-294

MCN97 I. McNab, "Pulsed Power for Electric Guns", IEEE Trans. Magn., vol. 3, no. 1, Jan. 1997, pp. 453-460

MCN99 I. McNab, "Early Electric Gun Research", IEEE Trans. Magn., vol. 35, no. 1, Jan. 1999, pp. 250-261

MCN07 I. McNab, F. Beach, "Naval Railguns", IEEE Trans. Magn., vol. 43, no. 1, Jan. 2007, pp. 463-475

MCN09 I. McNab, "Progress on Hypervelocity Railgun Research for Launch to Space", IEEE Trans. Magn., vol. 45, no. 1, Jan. 2009, pp. 381-388

MEI07 C. Meinel, "For Love of a Gun", Spectrum IEEE, vol. 44, no. 7, 2007, pp. 40-46

NEX11 "Nexter industries", Mar. 2011, www.giat-industries.fr

PAR90 P.B. Parks, "Current melt-wave model for transitioning solid armature", Journal of Applied Physics, vol. 67, no. 7, 1990, pp. 3511-3516

PAR99 Parker J. V., "Experimental Observation of the Rail Resistance Contribution to Muzzle Voltage", IEEE Trans on Magnetics, vol. 35, no. 1, Jan. 1999, p 437-441

PET95 H. Peter, R. Charon, "Le contact entre rail et pont de courant solide dans un lanceur électromagnétique à rails," Rapport ISL R111, 1995

PFL03 G. Pflieger,"Simulation numérique du comportement mécanique des projectiles lors d'un tir avec un lanceur électromagnétique à rails", Rapport ISL R105, 2003

REC09 B. Reck, P. Lehmann, E. Spahn, W. Wenning and M. D. Vo, "A Model for Predicting Transition in Railgun Fiber Brush Armatures", IEEE Trans. on Magn., vol. 45, no. 1, Jan. 2009, pp. 620-625

ROD86 W. Rodgers, "Report of the Presidential Commission on the Space Shuttle Challenger Accident", 1986, http://science.ksc.nasa.gov/

RUT09 P. Rutberg, I. Kumkova, G. Shvetsov, "New Steps in EML Research in Russia", IEEE Trans. on Magn., vol. 45, no. 1, Jan. 2009, pp. 231-236

SCH93 B. Schulman et al., "HART hypervelocity augmented railgun test facility", IEEE Trans. On Magn., vol. 29, no. 1, Jan. 1993, pp. 505-510

SCH98 A.-G. Schmitt, "Evaluation des forces exercées sur des projectiles accélérés par un lanceur électromagnétique à rails," PhD thesis, Université de Haute Alsace, 1998, pp. 87-89

SCH02 M. Schneider, D. Eckenfels and F. Hatterer, "Kontaktmechanismen multipler elektrischer Bürstenkontakte in Schienenbeschleunigern" (in German), ISL, Saint Louis, France, Rep. ISL-R 120, 2002

SCH03 M. Schneider, D. Eckenfels and F. Hatterer, "Doppler-radar: a possibility to monitor projectile dynamics in railguns", IEEE Trans. Magn., vol. 39, 2003, p. 183-187

SCH03a M. Schneider, D. Eckenfels and S. Nezirevic, "Transition in Brush Armatures", IEEE Trans. Magn., vol. 39, 2003, pp. 76-81

SCH05 M. Schneider, R. Schneider, "Sliding contact performance of multiple brush armatures", IEEE Trans. Magn., vol. 41, 2005, pp. 432-436

SCH05a M. Schneider, R. Schneider and D. Eckenfels, "Experiments with brush armatures: new technical solutions", IEEE Trans. Magn., vol. 41, 2005, pp. 231-234

SCH09 M. Schneider, R. Schneider, "Measurement of the Current Distribution between Multiple Brush Armatures during Launch", IEEE Trans. Magn., vol. 45, no. 1, Jan. 2009, pp. 436-441

SCH09a M. Schneider, O. Liebfried, V. Stankevic, S. Balevicius, N. Zurauskiene, "Magnetic Diffusion in Railguns: Measurements Using CMR-Based Sensors", IEEE Trans. Magn., vol. 45, no. 1, Jan. 2009, pp. 430-435

SCH09b M. Schneider, M. Woetzel, W. Wenning, D. Walch, "The ISL rapid fire railgun project RAFIRA. Part I: Technical aspects and design considerations", vol. 45, no. 1, Jan. 2009, pp. 442-447

SCH09c M. Schneider, M. Woetzel, W. Wenning, "The ISL rapid fire railgun project RAFIRA. Part II: first results", vol. 45, no. 1, Jan. 2009, pp. 448 – 452

SCH11 M. Schneider, O. Božić, T. Eggers, "Some Aspects Concerning the Design of Multistage Earth Orbit Launchers Using Electromagnetic Acceleration", IEEE Trans. Plasma Sci., vol. 39, issue 2, Feb. 2011, pp. 794-801

SPA92 E. Spahn, W. Wenning, "L'emploi de diodes semi-conductrices pour la commutation dite « de crowbar » dans les lanceurs électriques", Rapport ISL RT517, 1992

SPA05 E. Spahn, V. Zorngiebel, G. Buderer, K. Sterzelmeier, A. Welleman, "Novel 13.5 kV Multichip Thyristor with an Enhanced di/dt for Various Pulsed Power Applications", 15th IEEE Pulsed Power Conference, 2005, pp. 824-827

SPA05a E. Spahn, G. Buderer, V. Brommer, K. Sterzelmeier, V. Brommer, "50 kJ ultra-compact pulsed power supply unit for various applications", 11th European Conference on Power Electronics and Applications, 2005, pp. 824-827

STE04 H. Stewart, "The impact of the USS Forrestal's 1967 fire on United States Navy shipboard damage control," Master's thesis, U.S. Army Command and General Staff College, 2004

SIA11 T. Siaenen, M. Schneider, M. Löffler, "Railgun Muzzle Velocity Control with High Accuracy", IEEE Trans. Plasma Sci., vol. 39, issue 1, Feb. 2011, pp. 133-137

SIA T. Siaenen, private communication, 2009

TAY93 J. Taylor, R. Crawford, D. Keefer,"Experimental comparison of conventional railguns and trans-augmented railguns", IEEE Trans. Magn., vol. 29, no. 1, 1993, pp. 523-528

THO89 L. Thornhill, J. Batteh and J. Brown, "Armature Options for Hypervelocity Railguns", IEEE Trans. Magn., vol. 25, no. 1, 1989, pp. 552-557

WAT11 T. Watt, K. Chakravarthy, D. Bourell, "The use of high-speed video as an in-bore diagnostic for electromagnetic launchers", IEEE Trans. Plasma Sci., vol. 39, issue 2, Feb. 2011, pp. 809-814

WEY97 J. Wey, E. Spahn, and M. Lichtenberger, "Railgun modeling with the P-Spice Code", IEEE Trans. Magn., vol. 33, 1997, pp. 619-624

WEY99 J. Wey, P. Lehmann, R. Charon, D. Eckenfels et C. Gauthier, "First measurements of current distribution in moving fiber-armatures in railguns", IEEE Trans. Magn., vol. 35, 1999, pp. 107-111

WOO97 L.C. Woods,"The Current Melt-Wave Model", IEEE Trans. Magn., vol. 33, 1997, pp. 152-156

YOU82 F. Young and W. Hughes, "Rail and Armature Current Distributions in Electromagnetic Launchers", IEEE Trans. Magn., vol. 18, no. 1, Jan. 1982, pp. 33-41

ZIE01 A. Zielinski and J. Parker, "Demonstration of a hypervelocity mass-efficient integrated launch package," IEEE Trans. Magn., vol. 39, Jan. 2001, pp. 56–61

ZOR09 V. Zorngiebel, E. Spahn, G. Buderer, A. Welleman, and W. Fleischmann, "Compact high voltage IGBT switch for pulsed power applications", vol. 45, no. 1, Jan. 2009, pp. 531-535

ZUR11 Žurauskienė N., Balevičius S., Stankevič V., Keršulis S., Schneider M., Liebfried O., Plaušinaitienė V., and Abrutis A., "B-Scalar Sensor Using CMR Effect in Thin Polycrystalline Manganite Films", IEEE Trans. on Plasma Science, vol. 39, no. 1, Jan. 2011, p 411-416

Annex

Analytic approach to calculate the loop voltage

A.1 Principle

An exact computation of the loop voltage is difficult because it is necessary to know the real current distribution in the rails at each moment, i.e. at each position of the projectile. We propose an approximation taking into account that the current, due to skin effect, is concentrated as it appears in figure A.1. Three principal approximations are made:

- the rails are represented with a filiform conductor,
- the surface of the loop is considered small compared with the other dimensions
- the magnetic induction B is considered constant on the loop

The voltage is calculated by derivation of the flux through the loop. For the calculation of the magnetic induction B we use the BIOT-SAVART law and more especially the expression for a segment. We have also to take into account the angle between B and the normal direction of the loop to calculate the flux. The axis of the loop is parallel with the y-axis of the figure which corresponds with the axes of the brush current. Therefore there is only a contribution of the horizontal current in the rails and not from the current on the armatures.

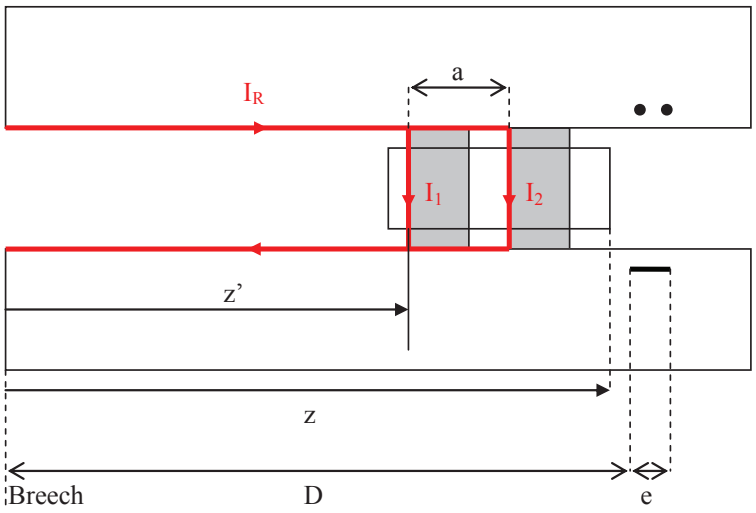

Fig. A.1: Geometry of the measurement of the current distribution between the brushes of the projectile

A.2 Non-augmented railgun

The magnetic induction is depending on the current and thus on the position of the projectile. Fig A.3. shows the configurations for the upper and lower rail of the non-augmented railgun. I_R represents the total current in the rails. D is the distance between the breech and the point where the voltage between the pins and the voltage in the loop is measured and z' is the distance between the breech and the current brush towards the breech. The factor α represents the fraction of the total current that runs through the current brush towards the muzzle. It is related to λ introduced in Chapter 1 by: $\alpha = 1 - \lambda$

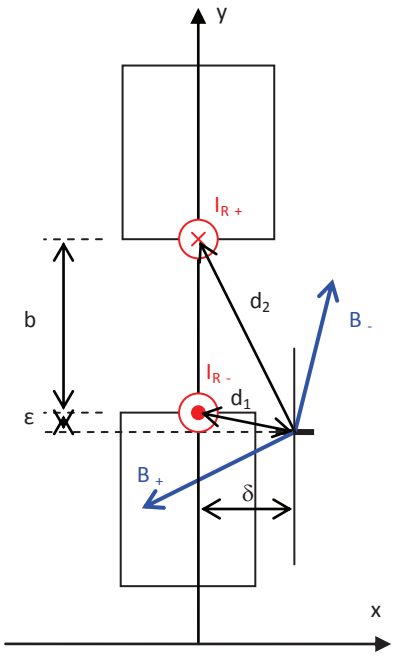

Fig.A.2: Geometry for a non-augmented railgun, cross-section of the rails.

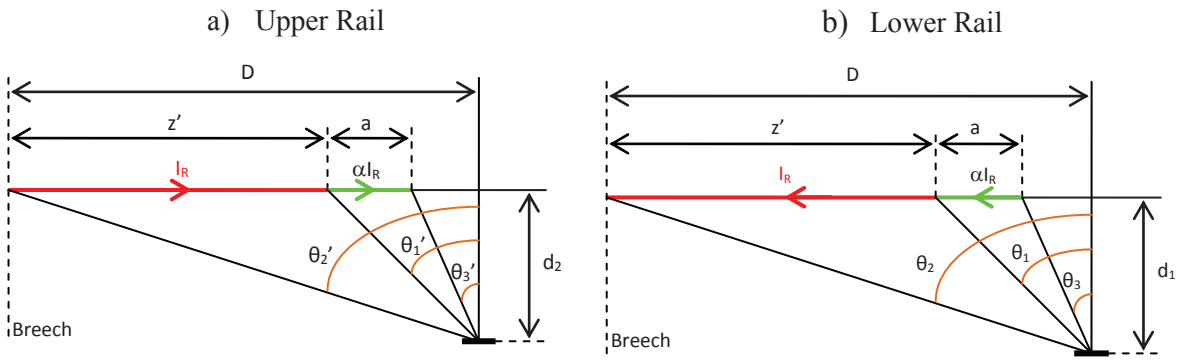

Fig.A.3. Configurations for the upper and lower rail for the non-augmented railgun.

Application of the Biot-Savart Law and flux calculation results in:

$$\Phi_{loop} = \frac{\mu_0 s \delta I_R}{4\pi}\left[\frac{(\sin\theta_2 - \sin\theta_1) + \alpha(\sin\theta_1 - \sin\theta_3)}{d_1^2} - \frac{(\sin\theta_2' - \sin\theta_1') + \alpha(\sin\theta_1' - \sin\theta_3')}{d_2^2}\right]$$

$$\Phi_{loop} = \frac{\mu_0 s \delta}{4\pi} C(D, z', \lambda, v, t) \cdot I_R(t)$$

with:

$$d_1 = \sqrt{\delta^2 + \varepsilon^2} \qquad d_2 = \sqrt{\delta^2 + (\varepsilon + b)^2}$$

$$\sin\theta_1 = \frac{D - z'}{\sqrt{(D - z')^2 + d_1^2}} \qquad \sin\theta_1' = \frac{D - z'}{\sqrt{(D - z')^2 + d_2^2}}$$

$$\sin\theta_2 = \frac{D}{\sqrt{D^2 + d_1^2}} \qquad \sin\theta_2' = \frac{D}{\sqrt{D^2 + d_2^2}}$$

$$\sin\theta_3 = \frac{D - z' - a}{\sqrt{(D - z' - a)^2 + d_1^2}} \qquad \sin\theta_3' = \frac{D - z' - a}{\sqrt{(D - z' - a)^2 + d_2^2}}$$

A.3 Augmented railgun

For an augmented railgun two additional terms for the magnetic induction induced by the current in the outer rails have to be calculated. The augmenting current I_A runs through the total length of the augmenting rails and the induced magnetic induction independent of the position of the projectile. The configuration for the lower and upper augmenting rails is shown in Fig. A.4. *D'* is the distance between the measurement point and the muzzle.
The flux in the loop due to the outer rails is:

$$\Phi_A = \frac{\mu_0 s \delta I_A}{4\pi}\left[\frac{(\sin\theta_4 - \sin\theta_5)}{d_1'^2} - \frac{(\sin\theta_4' - \sin\theta_5')}{d_2'^2}\right] = C'(D) I_A$$

with:

$d_1' = \sqrt{\delta^2 + (c - \varepsilon)^2}$	$d_2' = \sqrt{\delta^2 + (b + c + \varepsilon)^2}$
$\sin\theta_4 = \frac{D}{\sqrt{D^2 + d_1'^2}}$	$\sin\theta_4' = \frac{D}{\sqrt{D^2 + d_2'^2}}$
$\sin\theta_5 = -\frac{D'}{\sqrt{D'^2 + d_1'^2}}$	$\sin\theta_5' = -\frac{D'}{\sqrt{D'^2 + d_2'^2}}$

The global flux in the loop is given by:

$$\Phi_{loop} = \frac{\mu_0 s \lambda}{4\pi}\left[C(D, z', \lambda, v, t) \cdot I_R(t) + C'(D) I_A(t)\right]$$

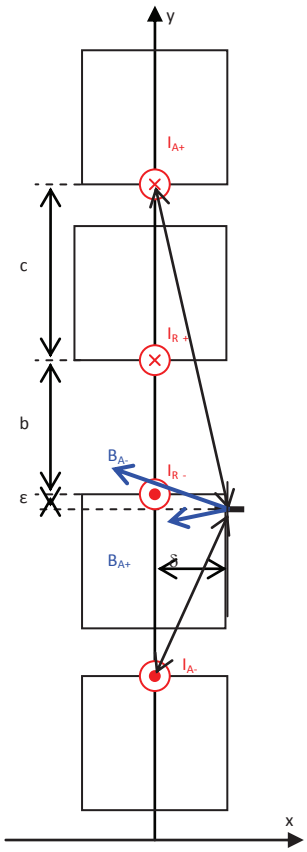

Fig. A.4: Geometry for a non-augmented railgun, cross-section of the rails.

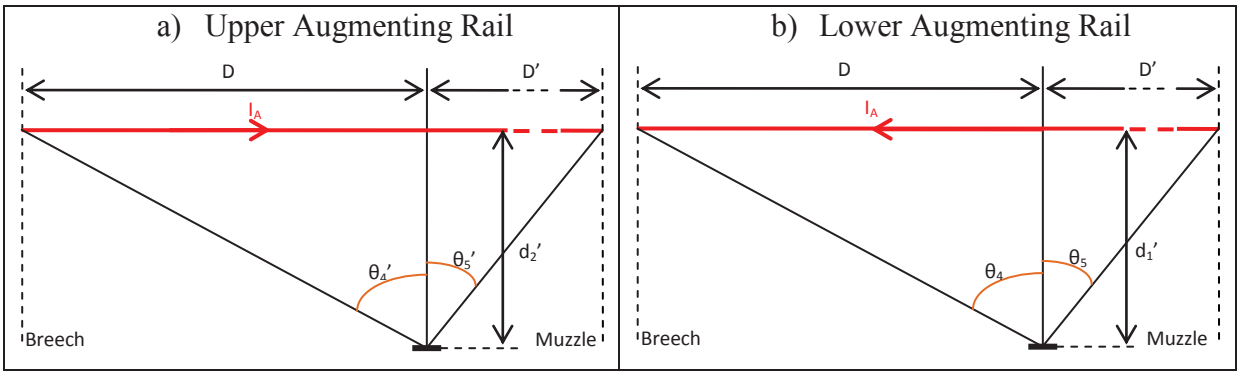

Fig. A.5: Configurations for the upper and lower rail for the augmented railgun.

A.4 Influence of the circulating current between the brushes

The current i_{loop} is solution of the differential equation

$$R_c i_{loop} + L_c \frac{di_{loop}}{dt} = -M'a \frac{dI_A}{dt}$$

with $R_c = R_R' a + 2R_b$; $L_c = L'_R a + 2L_b$ and $\tau_c = \frac{L_c}{R_c}$

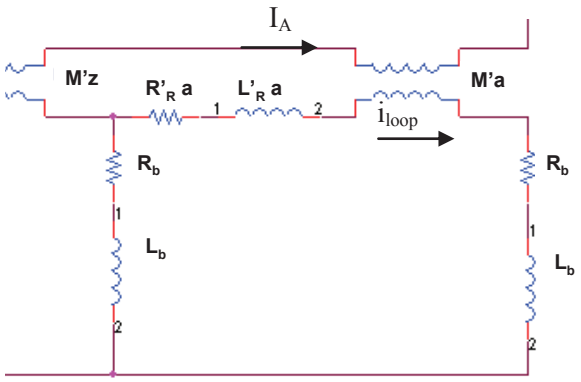

Fig. A.6: Electrical scheme for the circuit with two armatures.

Current I_A can be expressed with a good approximation by:

for $0 \le t \le t_{0A}$ $\quad I_A = I_{MA} \sin\left(\frac{\pi}{2}\frac{t}{t_{0A}}\right)$

$t_{0A} \le t$ $\quad I_A = I_{MA} \exp\left(-\frac{t - t_{0A}}{\tau_A}\right)$

i_{loop} is given by following relations for the two time domains.

$0 \le t \le t_{0A}$ $\quad i_{loop1} = C_1 \exp\left(-\frac{t}{\tau_c}\right) + D_1 \cos\left(\frac{\pi}{2}\frac{t}{t_{0A}} - \varphi_c\right)$

with $D_1 = -\frac{M'aI_{MA}}{R_c}\frac{\pi}{2t_{0A}}\frac{1}{\sqrt{1+tg^2\varphi_c}}$ and $tg\varphi_c = \tau_c\frac{\pi}{2t_{0A}}$

$t_{0A} \le t$ $\quad i_{loop2} = C_2 \exp\left(-\frac{t - t_{0A}}{\tau_c}\right) + D_2 \exp\left(-\frac{t - t_{0A}}{\tau_A}\right)$

with $D_2 = \frac{M'aI_{MA}}{R_c}\frac{1}{\tau_A - \tau_c}$

The two constants are determined using limit conditions:

At $t = 0$ $\quad i_{loop1} = 0$ $\quad C_1 = -D_1 \cos\varphi_c$

and for $t = t_{0A}$ $\quad i_{loop1} = i_{loop2}$ $\quad C_2 = -D_1 \cos\varphi_c \exp\left(-\frac{t_{0A}}{\tau_c}\right) + D_1 \sin\varphi_c - D_2$

In conclusion:

$0 \le t \le t_{0A}$ $\quad i_{loop1} = D_1\left[-\cos\varphi_c \exp\left(-\frac{t}{\tau_c}\right) + \cos\left(\frac{\pi}{2}\frac{t}{t_{0A}} - \varphi_c\right)\right]$

$t_{0A} \le t$ $\quad i_{loop2} = \left[-D_1 \cos\varphi_c \exp\left(-\frac{t_{0A}}{\tau_c}\right) + D_1 \sin\varphi_c - D_2\right]\exp\left(-\frac{t - t_{0A}}{\tau_c}\right) + D_2 \exp\left(-\frac{t - t_{0A}}{\tau_A}\right)$

All parameters, *R'*, R_b, L'_R and *M'* may depend on time t and some on temperature. There is a very good agreement with Pspice simulation. It has been verified in the case of $I_R = 0$. The different parameters are considered not varying.

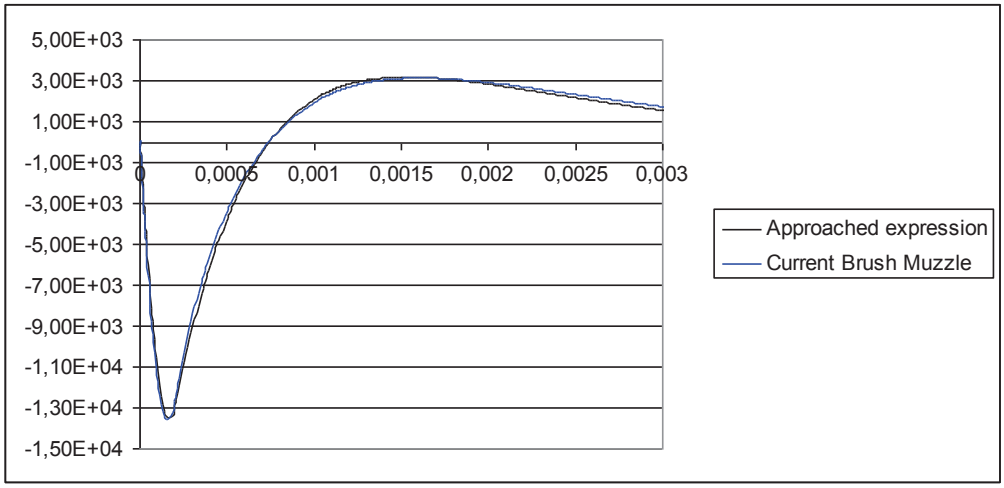

Fig. A7: Comparison between analytical and simulated values

In the exponential decreasing of the current, the second term of i_{loop2} becomes rapidly the principal part.

$$t_{0A} << t \qquad i_{loop2} \cong D_2 \exp\left(-\frac{t-t_{0A}}{\tau_A}\right) = \frac{M'aI_{MA}}{R_c}\frac{1}{\tau_A-\tau_c}\exp\left(-\frac{t-t_{0A}}{\tau_A}\right) = \frac{M'a}{L_c}\frac{\tau_c}{\tau_A-\tau_c}I_A$$

In these previous conditions $i_{loop} \cong k_A \frac{M'}{L'_R} I_A = K_A I_A$ with $k_A = 0{,}236$. The circulating current represents about 20% of I_A and cannot be neglected. We have to take it into account in the emf induced in the voltage loop.

c) Upper Rail

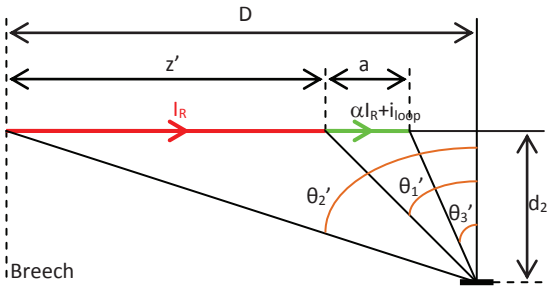

d) Lower Rail

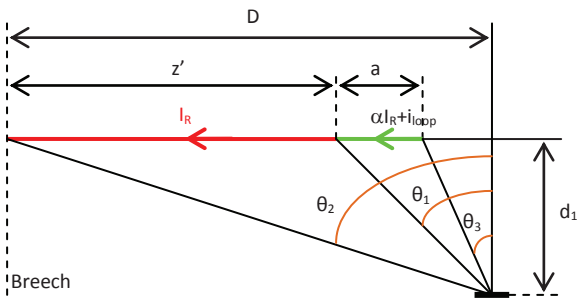

Fig. A8: Configurations for the upper and lower rail with loop current influence

The flux created by the current i_{loop} is given by:

$$\Phi\ "= \frac{\mu_0 s\delta}{4\pi}\left[\frac{(\sin\theta_1-\sin\theta_3)}{d_1^2}-\frac{(\sin\theta_1'-\sin\theta_3')}{d_2^2}\right] i_{loop} = \frac{\mu_0 s\delta}{4\pi} C''(D,z',v,t) i_{loop}$$

Therefore the total flux in the measurement loop is the sum of the three terms.

$$\Phi_{loop} = \frac{\mu_0 s \delta}{4\pi}\left[C(D,z',\lambda,v,t)\cdot I_R(t) + C''(D,z',v,t)\cdot i_{loop} + C'(D)I_A(t)\right]$$

If we satisfy $t >> t_{0A}$ the flux in the voltage loop is therefore given by

$$\Phi_{loop} = \frac{\mu_0 s \delta}{4\pi}\left[C(D,z',\lambda,v,t)\cdot I_R(t) + C'(D)I_A(t) + C''(D,z',v,t)\cdot K_A I_A(t)\right]$$